Temporal and Spatial Variability of Surface Solar Radiation over the South-West Indian Ocean and Reunion Island : Regional Climate Modeling

Peng Li

Temporal and Spatial Variability of Surface Solar Radiation over the South-West Indian Ocean and Reunion Island: Regional Climate Modeling

By

PENG LI

TO EARN THE TITLE OF DOCTOR OF THE UNIVERSITY OF REUNION

December 8, 2015

PhD Examination Board:

Pr. Frédéric CADET	**President**
Pr. Miloud BESSAFI	**Supervisor**
Dr. Béatrice MOREL	**Supervisor**
Dr. Philippe DROBINSKI	**Reviewer**
Dr. Babatunde ABIODUN	**Reviewer**
Dr. Fabien SOLMON	**Member**
Pr. Yves RICHARD	**Member**

Temporal and Spatial Variability of Surface Solar Radiation over the South-West Indian Ocean and Reunion Island: Regional Climate Modeling

By

PENG LI

TO EARN THE TITLE OF DOCTOR OF THE UNIVERSITY OF REUNION

December 8, 2015

PhD Examination Board:

Pr. Frédéric CADET	**President**
Pr. Miloud BESSAFI	**Supervisor**
Dr. Béatrice MOREL	**Supervisor**
Dr. Philippe DROBINSKI	**Reviewer**
Dr. Babatunde ABIODUN	**Reviewer**
Dr. Fabien SOLMON	**Member**
Pr. Yves RICHARD	**Member**

Contents

Acknowledgements

Carrying out a PhD research is an intellectual and physical power challenge with a good deal of hard work. One could learn the specialized knowledge of a relatively narrow discipline during the PhD project. Three years ago, I just started the PhD study at the University of Reunion, but now I am writing these acknowledgements at my desk. Thesis writing is a truly transformative process, making me organize all the work done before. At this point, I would like to show my appreciation for all the great, knowledgeable and kind people I have been working with during these three years in the Reunion Island.

First and foremost, I would like to thank my supervisors from LE2P laboratory, Dr. Béatrice Morel and Pr. Miloud Bessafi, for supporting me during these past three years. It has been an honor to be their first Chinese PhD student. I am grateful for the opportunity they have given me to work with them and learn from them. Béatrice is someone you would instantly love and never forget once you have met her. She is calm and nice to all the people and she is my role model for a scientist, mentor, and teacher. She is the reason why I decide to pursue a career in research in the future. Pr. Bessafi has been supportive and has given me the freedom to pursue various research directions without objection. He has also provided insightful discussions about my research work. As the leader of our research group, he always encourages and expects from us more independently thinking about our experiments and results. He pushes us in the right direction, in order to avoid us getting lost in the research.

I also thank the director of LE2P, Jean-Pierre Chabriat for accepting me as a PhD student in his laboratory. As the first Chinese PhD student at the University of Reunion, he helped me to come from China and get used to the life in Reunion. He managed to convince the university to organize French lessons for me. I also want to show my respect to Pr. Frédéric Cadet, vice-president of the Regional Council. He made me feel that I am not just a PhD student, but also a person representing Chinese people and that I was participating to the strengthening of the relationship between Reunion and China.

I am grateful for all the model support I received from the ICTP, especially Fabien Solmon. He guided my work on RegCM4 model and the analyses of the radiation subject. I would also like to give a heartfelt, special thanks to Benjamin Pohl and Yves Richard from the CRC. They initiated me into the world of climate variability on which they are working and suggested me the necessary reading for pursuing my PhD work on that topic. The conversations I had with them enlightened my way of thinking, and Benjamin's patience, flexibility, genuine caring and concern, and faith in me during the dissertation process enabled me to be more confident on my thesis. When I went to work with them at the University of Bourgogne, Dijon, they gave me a lot of suggestions that were really helpful in my PhD work.

I also thank LE2P laboratory as a whole for giving me ideal environment. With such an environment, I would feel free and could concentrate on my PhD research. I was lucky to be a member of this laboratory, and thank all its present members. In particular, I would like to acknowledge Patrick for being helpful and friendly to me. He gave me a great help about the equipment and material for my research. I also thank Kelly. She is so nice and pretty. She answered lots of the questions I would asked her, and solved many problems regarding the documents I had to prepare for conferences and academic institutes. I also thank Methieu, a smart and nice guy. We can share the idea about our research, and he gave me some advices. And I never forget: he picked us to watch the volcano eruption at night.

I gratefully acknowledge the Regional Council for providing financial support for three years. Without that support, I couldn't have been able to live in Reunion, and focus all my energy on the PhD research and complete it in time. Indeed, I would like to thank the French government and the European Union for supporting a Chinese student.

I also thank my friends (too many to list here but you know who you are) for providing support and friendship I needed. My time at the University of Reunion was made enjoyable in large part due to the many friends and groups that became a part of my life. I would like to thank Carole for being supportive throughout my time in the laboratory. I think of her as a sister. When I was confused with French language problems, she would explain things to me and helped me to fill lots of documents. I am grateful for the time spent with my colleagues and friends, Zaki, Elisa, Jerome, Ludovic, Max, Sebastian, Pauline, Farid…. all of them gave me a great help to adapt to the life in Reunion. The time we played and laughed together will be a memorable part of my life. I would like to thank them as my best friends.

I especially thank my mom, dad, and sisters. Their understanding and loves encourage me to work hard and continue pursuing a PhD study aboard. I love them so much, and I would not have made it this far without them. My sisters have been my best friends all my life and I love them dearly and thank them for all their advice and support. Lastly, special thanks to my husband, Qi Li, as well as his wonderful family who all have been supportive and caring. Qi Li is my husband, best friend and soul mate during these past three years. When I was irritable and depressed, he was always beside me. His love and support without any complaint or regrets to enable me complete my PhD study. There is no word to convey how much I love him.

Abstract

This work documents the temporal and spatial variability of surface solar radiation (SSR) over the southwest Indian Ocean (SWIO) and Reunion Island using two complementary Regional Climate Models (RCMs): RegCM4 and WRF. The first part of the work is dedicated to the analysis of the temporal variability of SSR based on RegCM4 over the SWIO at a moderate spatial resolution (50km). Because RegCM4 is the first RCM that focuses on the solar radiation research over the SWIO region, a first series of test experiments with this model to illustrate the model performance and its sensitivity to the choice of the physical parameterizations (radiation, convection), the domain size, and the spatial resolution, are performed. The default CCM radiative and the mixed convective scheme: Grell scheme over land and Emanuel scheme over ocean, give better performance over the SWIO compared to the other available options. The interannual, intraseasonal and synoptic climate variability is then examined through the climate indices and several ERA-Interim parameters (U, V, T and RH) are firstly analyzed along with the corresponding RegCM4 output data to check whether the RegCM4 model forced by ERA-Interim reanalyses is able to maintain the El-Nino Southern Oscillation (ENSO), the Indian Ocean Dipole (IOD), the Madden-Julian Oscillation (MJO) and the Tropical Temperate Trough (TTT) signals. Secondly, simulated SSR in association with the different modes of variability is examined. In the second part, SSR spatial variability over Reunion Island is analyzed based on WRF simulations at very fine resolution (750m) for seasonal, intraseasonal, and daily time scales. Clustering classification is applied to WRF simulated SSR over Reunion and the effect from the atmospheric circulation is checked together. Météo France observations and CM SAF are used to validate the results of the model. The results indicate that regional climate models have the ability to present the temporal and spatial variability of SSR over Reunion.

Keywords

Regional climate model; temporal variability; spatial variability; surface solar radiation; cloud cover; atmospheric circulation; climate index; clustering

Chapter 1

Introduction

1.1 Scientific context

All societies require energy services to meet basic human needs, for example, lighting, cooking, and communication, and to serve productive processes. The demand for energy and associated services to meet social and economic development and improve human welfare and health, is increasing. Since approximately 1850, global use of fossil fuels (coal, oil and gas) has increased to dominate energy supply, leading to a rapid growth in carbon dioxide (CO_2) emissions, which is the main component part of greenhouse gases (GHG). GHG emissions resulting from the provision of energy services have contributed significantly to the historic increase in atmospheric GHG concentrations. Most of the observed increase in global average temperature since the mid-20th century is likely due to the observed increase in anthropogenic GHG concentrations. The anthropogenic warming has a discernible influence on many physical and biological systems, including sea level rise, increased frequencies and severities of some extreme weather events, loss of biodiversity and regional changes in agricultural productivity. There are multiple options for lowering GHG emissions from the energy system while still satisfying the global demand for energy services, such as energy conservation and efficiency, fossil fuel switching, renewable energy, nuclear and carbon capture and storage. As it has a large potential to mitigate climate change, renewable energy could provide wider benefits and the development of renewable energy has been increasing rapidly in recent years. Renewable energy can help decouple the strong correlation between economic development and increasing energy use and growth of GHG emissions, contributing to sustainable development. Renewable energy, which is derived from natural processes that are replenished constantly, includes solar energy, wind energy, geothermal energy, biofuel, hydropower, etc., and replaces conventional fuels in four distinct areas: electricity generation, hot water/space heating, motor fuels and rural (off-grid) energy services. Renewable energy resources exist over wide geographical areas, in contrast to other energy sources, such as coal, natural gas, petroleum, nuclear materials and so on, which are concentrated in a limited number of countries (Dincer 2000; Omer 2008).

Most renewable energy resources come either directly or indirectly from the sun. Sunlight, or solar energy, can be used directly for heating and lighting homes and other buildings, for generating electricity, and for hot water heating, solar cooling, and a variety of commercial and industrial uses (Boyle 1996; Garci 2003). The sun's heat also drives the winds, whose energy is captured with wind turbines. The winds and the sun's heat then cause water to evaporate. When the water vapor turns into rain or snow and flows downhill into rivers or streams, its energy can be captured using hydroelectric power (Kaunda et al. 2012). Along with the rain and snow, sunlight causes plants to grow. The organic matter that makes up those plants is known as biomass, which can be used to produce electricity, transportation fuels, or chemicals. The use of biomass for any of these purposes is called bioenergy (Field et al. 2008; Slade et al. 2014). Hydrogen also can be found in many organic compounds, as well as water. Though it is the most abundant element on the Earth, it doesn't occur naturally as a gas, and is always combined with other elements, such as with oxygen

to make water. Once separated from another element, hydrogen can be burned as a fuel or converted into electricity. Not all renewable energy resources come from the sun. Geothermal energy (Barbier 1997, 2002; Baldacci et al. 1998) taps the Earth's internal heat for a variety of uses, including electric power production, and the heating and cooling of buildings. The energy of the ocean's tides come from the gravitational pull of the moon and the sun upon the Earth. Ocean energy comes from a number of sources. In addition to tidal energy, there's the energy of the ocean's waves, which are driven by both the tides and the winds. The sun also warms the surface of the ocean more than the ocean depths, creating a temperature difference that can be used as an energy source. All these forms of ocean energy can be used to produce electricity (Avery & Wu 1994; Pelc & Fujita 2002).

Solar radiation incident at the Earth's surface is the principal energy source for life on the planet, and largely determines the climatic conditions of our habitats. It has also major practical implications, including solar energy technologies and agricultural productivity (Wild 2009). Knowledge of the local solar radiation is then essential as it is a critical input parameter for the designing, performance, prediction, and monitoring of solar energy devices (Hussain et al. 1999; Davy & Troccoli 2012; Monforti et al. 2014).

In general, there are different ways to evaluate the solar resource.

1) *Statistical interpolation of ground-based measurements.* Direct measurements of solar radiation from radiometers deployed at ground stations are the most accurate source of solar radiation data, provided that the equipment is well maintained and regularly calibrated. Information about the solar resource is based upon measured data when available. The best database would be the long-term measured data at the site of the proposed solar system. Various methods have been developed to obtain solar radiation estimates for locations where it is not directly measured. The simplest solution is to assign measured values from a nearby station (Hunt et al. 1998) or to use spatial interpolation methods (Bechini et al. 2000; Ertekin & Evrendilek 2007). However, the density of solar radiation measurements (Wild et al. 2013) is often not sufficient for reliable interpolation. Figure 1.1 shows geographical distribution of surface radiative fluxes observation sites from the Global Energy Balance Archive (GEBA, Gilgen et al. 1998; Ohmura et al. 1989), and the database of the Baseline Surface Radiation Network (BSRN, Ohmura et al. 1998). In the absence of direct measurements, solar radiation can be estimated by means of empirical models using other available meteorological observations (Yohanna et al. 2011; Ulgen & Hepbasli 2009; Li et al. 2011; Karakoti et al. 2012). However, accurate solar radiation measurements or estimates from weather stations alone are often insufficient to perform statistical interpolation and create accurate gridded solar radiation time series at high spatial resolutions (Bojanowski 2014).

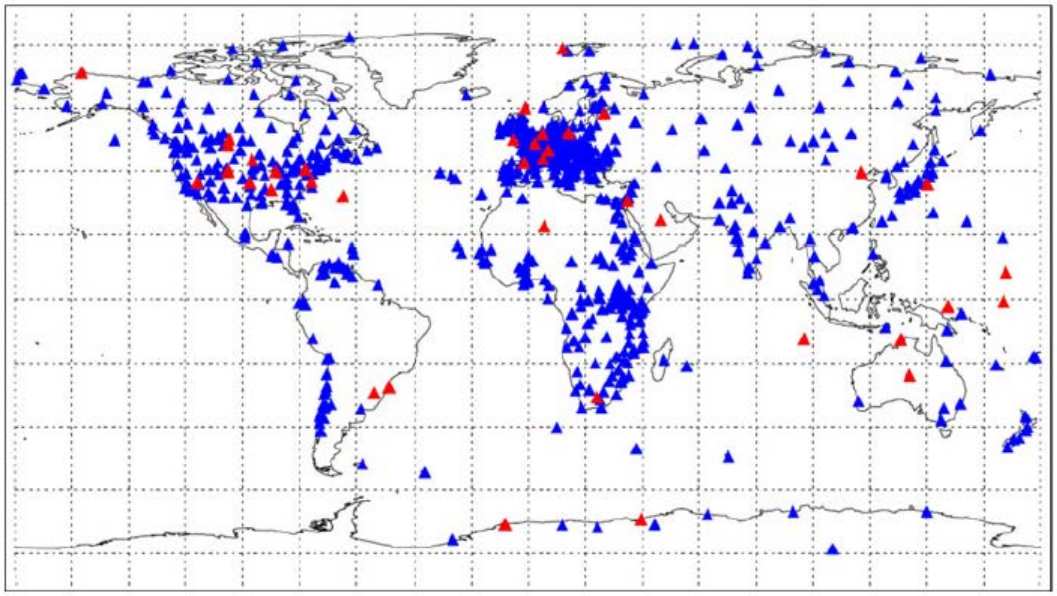

Figure 1.1 Geographical distribution of surface radiative fluxes observation sites from GEBA (760 sites in blue) and from BSRN (42 sites in red). From Wild et al. 2013.

2) *Satellite-derived solar radiation products*. During recent decades, satellite-based techniques have become the standard method for solar resource assessment at regional, continental or global scale (Brisson et al. 1999; Laszlo et al. 2008; Posselt et al. 2012a; Gueymard & Myers 2008b). However, these methods still suffer from limitations, originated partly from the still insufficient three-dimensional description of the microphysical and optical properties of clouds. This fact is particularly limiting for the computation of direct normal irradiance. In addition, the availability of historic satellite records suitable for solar radiation assessment is often rather short (Ruiz-Arias et al. 2015), limiting the study of temporal variability on the longer terms. Finally, the rather limited spatial resolution cannot allow taking into account the topography effects at very fine scales.

3) *Atmospheric models*. Both Numerical Weather Prediction (NWP) models (Ruiz-Arias et al. 2011b; Ruiz-Arias et al. 2013a) and Regional Climate Models (RCMs), represent an alternative to the satellite-based approaches for the regional assessment of solar radiation. Though the accuracy of these models at computing surface solar radiation is still significantly less than what is achievable with the current satellite-based techniques (Lohmann et al. 2006; Kennedy et al. 2011; Jia et al., 2013; Bojanowski et al. 2014), they have some other potential advantages over satellite methods, such as the possibility to evaluate solar radiation over longer periods than satellites – up to several decades backward, and the fact that NWP models and RCMs perform a comprehensive simulation of the whole atmospheric system, including ancillary variables such as wind, temperature or relative humidity. Finally, some of these models can produce solar radiation data at a higher resolution (of less than 1 km) than satellites, then accounting for the high spatial variability by

locally formed clouds (e.g. Morel et al. 2014).

In the subtropical regions, and especially the SWIO where the solar resource is abundant, solar energy appears to be a real alternative to the conventional energy sources. In this regard, several island countries in the SWIO including Reunion Island (Praene et al. 2012) are actively engaged in the development of solar energy technologies such as solar thermal or photovoltaic conversion systems. Because of the range of spatial and temporal scales over which solar radiation incident at the surface varies (Bishop & Rossow 1991; Perez & Hoff 2013), a detailed examination of the solar resource availability and space-time variability over the SWIO region is then needed. This necessitates the development of high-resolution gridded solar products with spatially- and temporally-continuous coverage. Because the South West Indian Ocean (SWIO) region (Figure 1.2) consists mainly of ocean surfaces, availability of measurements is very scarce (Figure 1.1). Other solar radiation data sources providing high-resolution information with continuous spatial and temporal coverage will have to be considered.

Figure 1.2 SWIO area. The star indicates the position of Reunion Island. From Google Maps.

Reunion Island is a French overseas territory. It lies in the SWIO at 20.8°South and 55.5°East, about 800km east of Madagascar (Figure 1.2). Reunion Island is a small mountainous island (2512 km^2) with very complex terrain that drives several microclimates. Reunion Island has a tropical maritime climate marked by two seasons (austral summer: November to April; austral winter: May to October) depending on the behavior of the southern Hadley cell and the Walker circulation (Baldy et al. 1996). The prevailing winds blow from the east and south-east to the west coast and the east coast has more rain than the west: average annual rainfall amounts present a marked west-east gradient, reaching cumulated values larger than 10-12m in the elevated sectors facing the dominant moisture fluxes associated with the trade winds (Morel et al. 2014). Winter seasons are characterized by large-scale atmospheric subsidence and broken low-level cloudiness, while in summer, clouds are found both at low and high altitudes (Badosa et al. 2013).

Figure 1.3 Map of Reunion Island. From Google Maps.

As it is a small territory, Reunion Island's development is closely related to its geographical situation, energy production and municipal solid waste management. In addition, it is far away from any European or continental territories, which makes it impossible to link the island to any energy production network. Based on these limitations, the use of renewable energy as a sustainable alternative is a better way to produce energy and support its development. Due to its geographical location, solar energy is an abundant energy resource in Reunion. The availability of this resource makes the development of all solar technologies particularly interesting. Annual sunshine is in the range of 1400-2500 h and can reach the value of 2900 h, for an altitude lower than 400m. Daily insolation is characterized by strong spatio-temporal variability due to orographic cloud formations on the mountains (Badosa et al. 2013). The monthly daily radiation reaches more than 6.5 kWh/m^2 during the wet season in some parts of the coastal region (altitude < 300 m) (Soler 2000). In terms of direct solar energy use, the two main applications in Reunion are solar water heating and photovoltaic. Thanks to its solar energy potential, Reunion is actively engaged in the development and promotion of solar thermal and photovoltaic energy through various action plans and programs (GERRI: Green Energy Revolution, PRERURE: Plan Régional des Energies Renouvelables et de l'Utilisation Rationnelle de l'Energie) in the context of sustainable development. Therefore, thorough knowledge of the solar

resource is especially important for the design, dimensioning and building of solar energy systems. In Reunion, one basic need of the photovoltaic industry in regard to electricity production is the mapping of solar resources at high spatial and temporal resolutions. Such a mapping is needed to produce precise estimates of photovoltaic electricity generation from solar systems implemented at any point of the island. For Reunion area characterized by steep topography that results in strong micro climatic differences, and where the observation network as in many places in the world, is very sparse, mapping at high spatial and temporal resolutions is currently difficult to obtain. In this study, regional climate models are used to regionalize solar energy at high resolution.

1.2 Climate models

Climate models (North et al. 1981; Randall et al. 2007; Kemp 2011) use quantitative methods to simulate the interactions of the atmosphere, oceans, land surface, and ice. They are used for a variety of purposes from study of the dynamics of the climate system to projections of future climate. Various types of models are used to analyze different aspects of the climate. They can be relatively simple one-, two- or three dimensional, and can be applied to a single physical feature of climatic relevance, or they may contain fully interactive, three-dimensional processes in all three domains: atmosphere, ocean and land surface. Global Climate Models (GCMs) and Regional Climate Models (RCMs) are most applied climate models and also utilized in this study.

GCMs have evolved from the Atmospheric General Circulation Models (AGCM; Gates 1992) widely used for daily weather prediction. GCMs have been used for a large range of applications, including investigating interactions between processes of the climate system, simulating evolution of the climate system, and providing projections of future climate states under scenarios that might alter the evolution of the climate system (Solomon et al. 2007). The most widely recognized application is the projection of future climate states under various scenarios of increasing atmospheric carbon dioxide (CO_2) as performed (Flato 2011; Heavens et al. 2013), for instance, in the Climate Model Intercomparison Project (CMIP; http://cmip-pcmdi.llnl.gov). For this, Earth System Models (ESMs) are often used. These are composed of model components that simulate individual parts of the climate system (such as the atmosphere, ocean, land, and sea ice) and the exchange of energy and mass between these parts. Limitations in computing power frequently result in the inability of GCMs to resolve important climate processes. Low-resolution models fail to capture many important phenomena of regional and lesser scales, such as clouds; downscaling to higher-resolution models introduces boundary interactions that can contaminate the modeling area and propagate error.

Modeling climate and Earth system processes on a regional scale is essential for projecting the impacts of climate change on society and our natural resources. Only by assessing what the real impact will be on different countries will it be possible to

justify difficult social and economic policies to avert a dangerous deterioration in the global climate. Furthermore, understanding processes on the regional scale is a crucial part of global research. Processes acting on local or regional scales, such as mountain ranges blocking air flow or dust clouds interacting with radiation, will ultimately have impacts at the global level. One technique used to overcome the coarse spatial resolution of coupled GCMs is that of nested modeling, depicted in Figure 1.4. This involves the linking of models of different scales within a global model to provide increasingly detailed analysis of local conditions while using the general analysis of the global output as a driving force for the higher resolution model. Results for a particular region from a coupled GCM are used as initial and boundary conditions for the RCM, which operates at much higher resolution and often, with more detailed topography and physical parameterizations. This enables the RCM to be used to enhance the detailed regional model climatology and this downscaling can be extended to even finer detail in local models (Giorgi & Mearns 1999; Murphy 1999; Christensen & Christensen 2007). This procedure is particularly attractive for mountain regions and coastal zones, as their complexity is unresolved by the coarse structure of a coupled GCM grid (Pierce et al. 2009; Rummukainen 2010).

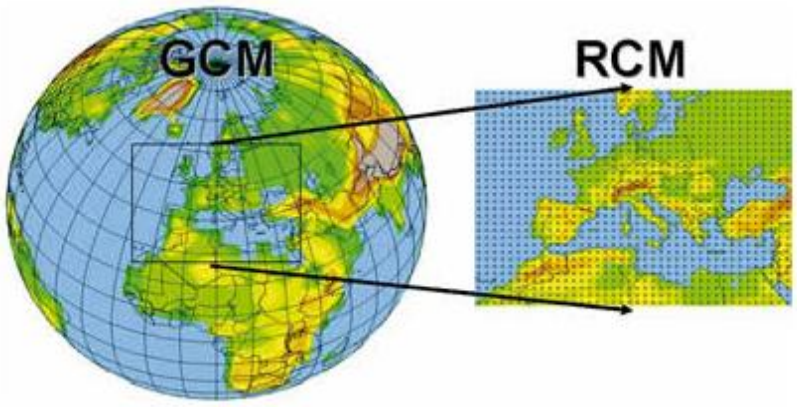

Figure 1.4 Global climate model nesting approach (Giorgi 2008).

According to the recent earth energy budget estimates by Wild et al (2013; Figure 1.5), 22% (76 W/m^2) of solar radiation reaching the top of the earth's atmosphere is reflected back to space. 23% (79 W/m^2) is absorbed by the clouds, gases and aerosols in the atmosphere. Only 54% (185 W/m^2) of solar radiation reaches the earth's surface, which is referred as the surface solar radiation (SSR) in this thesis. SSR depends on the geographic location, orientation of the surface, time of the day, time of the year, and atmospheric components (Boes 1981). Indeed, many factors and processes interact to determine the amount of solar radiation received at a given point on the Earth's surface – primarily the clouds (Chiacchio & Vitolo 2012) and the topography (Bessafi et al. 2013). To overcome the lack of solar radiation data over the SWIO region, we then propose to apply dynamical interpolation or downscaling with a RCM. The principal factor behind regional climate modelling includes representations of physical processes (i.e., radiation, clouds) and a high spatial resolution, which

resolves complex topography, land-sea contrast, and land use. A limited-area model can generate realistic regional climate information consistent with the driving large-scale circulation supplied by either global reanalysis data or a GCM (Wang et al. 2004).

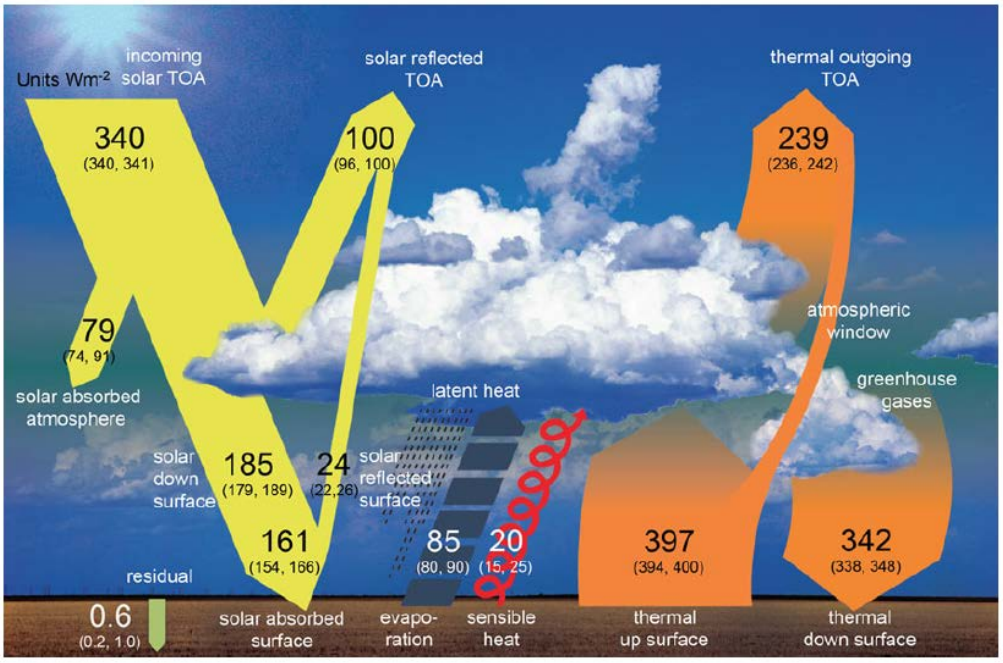

Figure 1.5 Schematic diagram of the global mean energy balance of the Earth. The numbers (W/m^2) indicate best estimates for the magnitudes of the globally averaged energy balance components together with their uncertainty ranges, representing present day climate conditions at the beginning of the twenty first century (from Wild et al. 2013).

A number of researchers previously evaluated the ability of high-resolution (~0.5°) RCM to estimate the mean state and variability of the Surface Radiation Budget (SRB) over the Arctic (Wyser et al. 2008), North America (Markovic et al. 2008), Europe (Kothe et al. 2011) and West Africa (Kothe et al. 2010). They did this with the aim to identify aspects of the physical processes that would require refined representation in order to better simulate the SRB, improving then the overall performance of the RCM. Other studies documented the capability of high-resolution (a few kilometers) mesoscale models to provide global horizontal irradiance short-term forecasts at some locations in the United States (Zamora et al. 2005) and in Spain (Lara-Farengo et al. 2012).

In this study, the capability of two complementary current state-of-the-art RCMs are assessed to study the variability of SSR at different space-time scales. In a first step, and because it runs rapidly, is computationally efficient, and can be used for long-term simulations, we use Regional Climate Model Version 4 (hereafter refereed to as RegCM4; Giorgi et al. 2012) to document the temporal variability of SSR at different

time scales (intraseasonal, interannual) over the SWIO. Because it is a hydrostatic model, RegCM4 is only run at a moderate resolution (50 km). At this spatial resolution, the complex topography Reunion Island (roughly 50 km x 50 km) is however not resolved at all. In a second step, we thus use the non-hydrostatic Weather Research and Forecasting/Advanced Research WRF (ARW) model, version 3.5 (WRF hereafter, Skamarock et al. 2008) to document the spatial variability of SSR at local scales (750-m spatial resolution) over Reunion Island. Such a non-hydrostatic approach allows simulating the complex regional climate and associated topography effects accurately.

The RegCM and WRF models have been run for various domains around the world and for different research applications, from model validation to climate change and impact studies. These models have also been used in several RCM intercomparison projects including the North American Regional Climate Change Assessment Program (NARCCAP; Mearns et al. 2012), or the World Climate Research Programme (WCRP) Coordinated Regional Downscaling Experiment (CORDEX; Giorgi et al. 2009) for 13 land-regions worldwide (see, e.g. Nikulin et al. (2012) for a comparison of the performance of several RCMs including RegCM and WRF for the precipitation climate over CORDEX-Africa domain; for more details on the RegCM4 model and preliminary tests on multiple CORDEX domains along with examples of applications of the previous version RegCM3, we also refer the reader to the Climate Research Special Issue, 'The regional climate model RegCM4' (Giorgi & Anyah 2012)).

Several studies performed with either Version 3 or 4 of the RegCM model were conducted with a focus on many African domains [East Africa: Anyah & Semazzi 2007; Otieno & Anyah 2012; West Africa: Abiodun et al. 2008; Sylla et al. 2010; Solmon et al. 2012; Southern Africa: Kgatuke et al. 2008; Sylla et al. 2012], or the whole of Africa (Mariotti et al. 2011). None of them, however, were carried out over a domain including the whole SWIO region. Even in those performed over either the southern or the entire African (CORDEX) domain, the region of interest was too close to the lateral boundaries. In addition, apart from Sylla et al. (2012) who investigated the influence of surface radiative fluxes in controlling rainfall and surface temperature biases as produced by RegCM3 over southern Africa at high resolution (25km) during the austral summer season, none of the aforementioned studies focused on the SRB itself.

Many studies were also performed with different versions of the WRF model over the neighboring regions of Southern Africa [e.g. rainfall variability (Crétat et al. 2012), Pohl et al. 2014), tropical-temperate troughs development (Macron et al. 2014)], and the SWIO. Indeed, the WRF model was used very recently over Reunion Island itself to regionalize rainfall with a resolution of 680 m (Morel et al. 2014). The model was also used over Reunion but in NWP mode to forecast day-ahead solar irradiance with a horizontal resolution of 3 km (Diagne et al. 2014). This resolution is however not sufficient to account for the effect of topography on the formation of local clouds.

1.3 Objectives and strategy of the thesis

Tropical islands, such as Reunion Island in the SWIO, have significant solar resource that is highly variable in both spatial and temporal scales because of heterogeneous and rapidly changing cloudiness. The characterization of this variability is essential to improve solar energy investment. This work focuses on the regional-scale (over the SWIO) and local-scale (over Reunion Island) variability of surface solar irradiance at different temporal scales using two complementary RCMs.

In a first step, we analyze the relationship between simulated SSR and the structures of inter-annual, intra-seasonal and synoptic climate variability, which are expected to modulate solar energy primarily through the cloud patterns. This is done by calculating the correlation between RCM RegCM4 data including SSR, and several climate indices of interannual [El Niño Southern Oscillation (ENSO; Trenberth & Caron 2000), Indian Ocean Dipole (IOD; Saji et al. 1999)], intraseasonal [Madden–Julian oscillation (MJO; Madden & Julian 1971; 1972; Zhang 2005)], and synoptic [Tropical Temperate Trough (TTT; Cook 2000; Macron et al. 2014] climate variability. RegCM is meant to participate to the CORDEX program, in which future climate projections using GCM forcing data from CMIP will be produced. To evaluate the anthropogenic-forced SSR changes in these projections, it is thus important to understand how SSR is affected by the natural climate variability.

In a second step, we propose to assess the capability, usefulness, and limitations of a nonhydrostatic RCM, the WRF model, to regionalize SSR locally over Reunion Island with a very high resolution (a few hundreds of meters). Time scales considered in this work range from seasonal differences between two contrasted rainy seasons on the one hand, to daily SSR on the other hand. Seasonal means and intraseasonal variability are also documented. WRF SSR is compared to ground-based measurements and satellite-derived products. This study should be seen as a preliminary work, based on hindcast simulations that aim to document how large-scale circulation patterns over the SWIO modulate the amounts and spatial distribution of rainfall, at local-terrain scale, over Reunion. An ensemble approach using 5 members has been used in both steps.

1.4 Outline of the thesis

The core of this thesis is composed of Chapters 2, Chapters 3 and Chapters 4, and each chapter explains and links to the overall objective of the thesis.

Chapter 2 introduces the study area, reference data used and the regional climate models which are applied in this thesis: RegCM4 and WRF, including the experimental design and the sensitivity tests performed for achieving a satisfactory representation of the climate of the SWIO.

Chapter 3 studies the temporal variability of surface solar radiation over the SWIO

centered on Reunion Island by ensemble member simulations of RegCM4 through the climate indices.

Chapter 4 analyzes the spatial variability of surface solar radiation at Reunion Island by ensemble member simulations of WRF.

Finally, Chapter 5 gives a general summary and critique of the main results.

Chapter 2

Implementation Strategy

As the objective of the thesis is to study the temporal and spatial variability of Surface Solar Radiation (SSR) over the South West Indian Ocean (SWIO) and over Reunion Island by ensemble-member simulations of RegCM4 and WRF, respectively, the basic characteristics of these two regional climate models are presented here. In addition, the related climate theories are described here for the implementation in the following. The datasets used as models' inputs and for the validation of simulation results are listed in this part.

2.1 Study area

Reunion Island (55°E-21°S, red box in Figure 2.1) is a small mountainous island with very complex terrain (Figure 2.2). It is a hotspot volcano with three major central depressed areas: the Cirques of Mafate (north-west), Salazie (north-east) and Cilaos (south-west) (Figure 1.3). These Cirques are enormous collapses of Reunion's oldest volcano, with edges that are practically vertical walls, more than 1000 m high (Oehler et al. 2008). In addition, Reunion is characterized by two coalescent volcanic peaks, Piton des Neiges (about 3070 m above the sea level) and Piton de La Fournaise (about 2632 m above the sea level). There are more than 300 inhabitants per km² with a majority of the population living close to the coast of the island. This is because there are several zones of complex topography, many of which are remote and inaccessible resulting in an observational network that is not regularly spatially distributed. Because of the small size (2512 km²) of Reunion Island and its complex topography, mapping SSR over the island at very high resolution is difficult. In this work, we have chosen a dynamical downscaling approach based on two complementary Regional Climate Models (RCMs): RegCM and WRF, to study the temporal and spatial variability of SSR at regional and local scales for a large range of temporal scales.

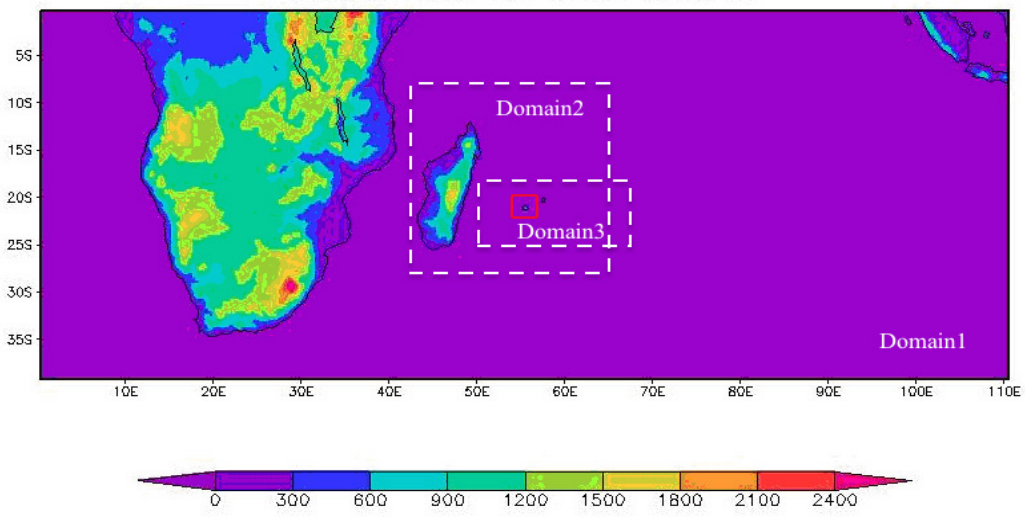

Figure 2.1 Surface elevation (m) over the SWIO as given by RegCM4. The location of Reunion Island is indicated by the red box. Domain 2 and 3 are in the white box.

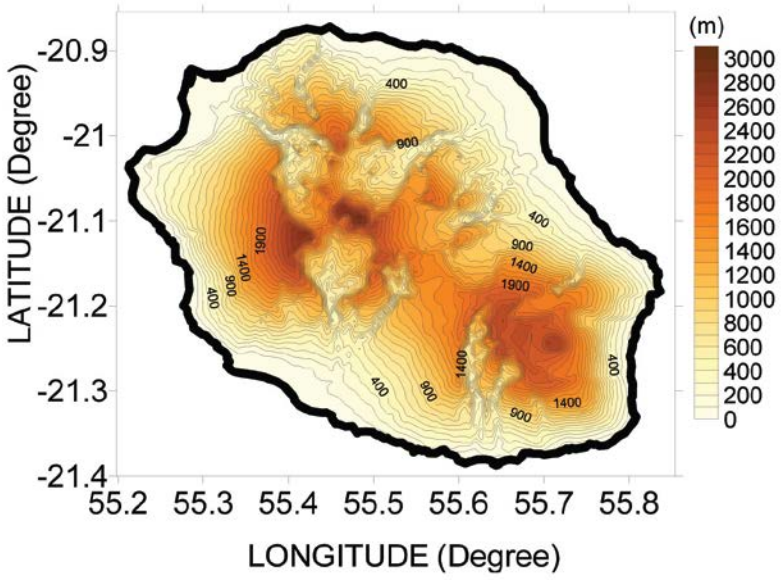

Figure 2.2 250-m DEM topographic data for Reunion.

Figure 2.1 shows the domain chosen for all RegCM4 simulations, which covers Southern Africa and the SWIO including Madagascar, Mauritius, Reunion Island (0°-40°S, 0°-100°E). The choice of this domain has been motivated by the fact that there is no sharp topography near the domain boundaries. A strength of this choice is that high mountains too close from the boundaries can cause many problems in RCMs. However, the boundaries lie rather far from continents most of the time, and thus of observational networks, so that the reliability of reanalyses there is probably weaker than over continents (because there are fewer observations to assimilate).

WRF is used to study the spatial variability of SSR over the Reunion with very high resolution. The regional domains consist of three nested domains, at 18.75km, 3.75km and 750m horizontal resolutions, all centered on Reunion Island (Figure 2.3); the model utilize two-way nesting in the inner domains. Domain #1 covers Madagascar, Reunion, Mauritius and the SWIO area in which the effect of the large-scale atmospheric circulation locally on SSR over Reunion will be examined. Figure 2.4 and Figure 2.5 presents, respectively, domains #1 and #3 with the topography elevation.

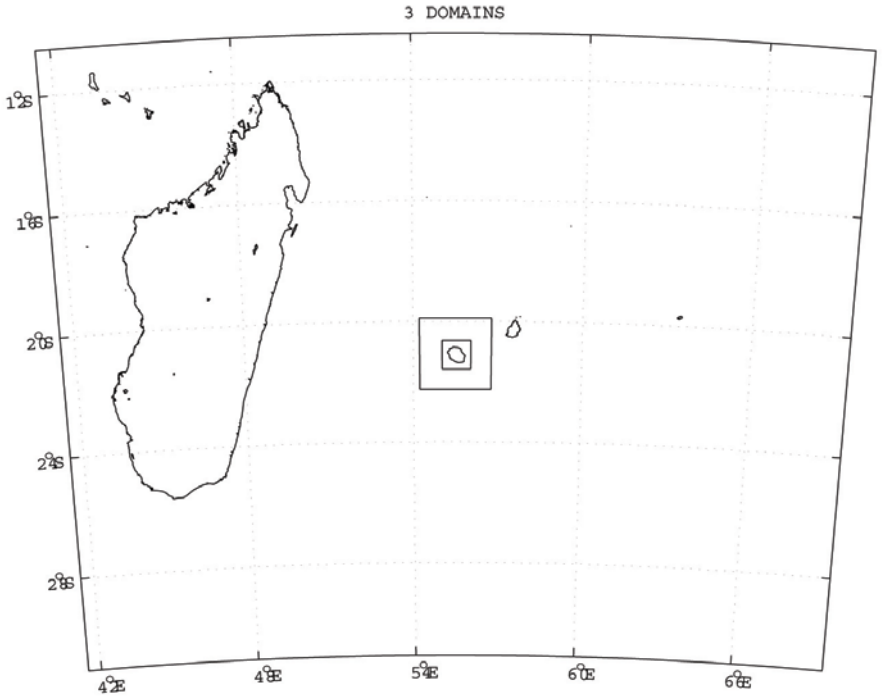

Figure 2.3 WRF domains.

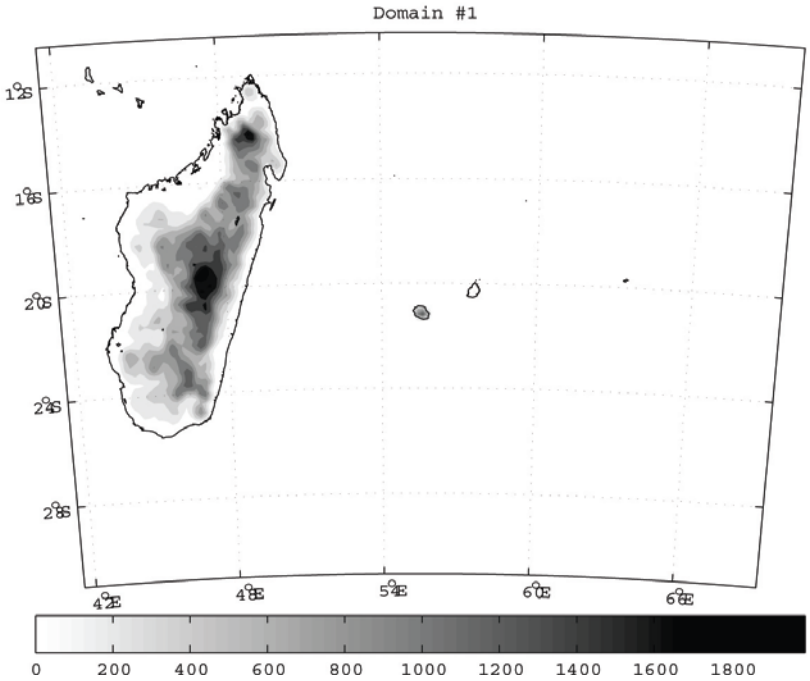

Figure 2.4 WRF domain #1 with the elevation of topography (m).

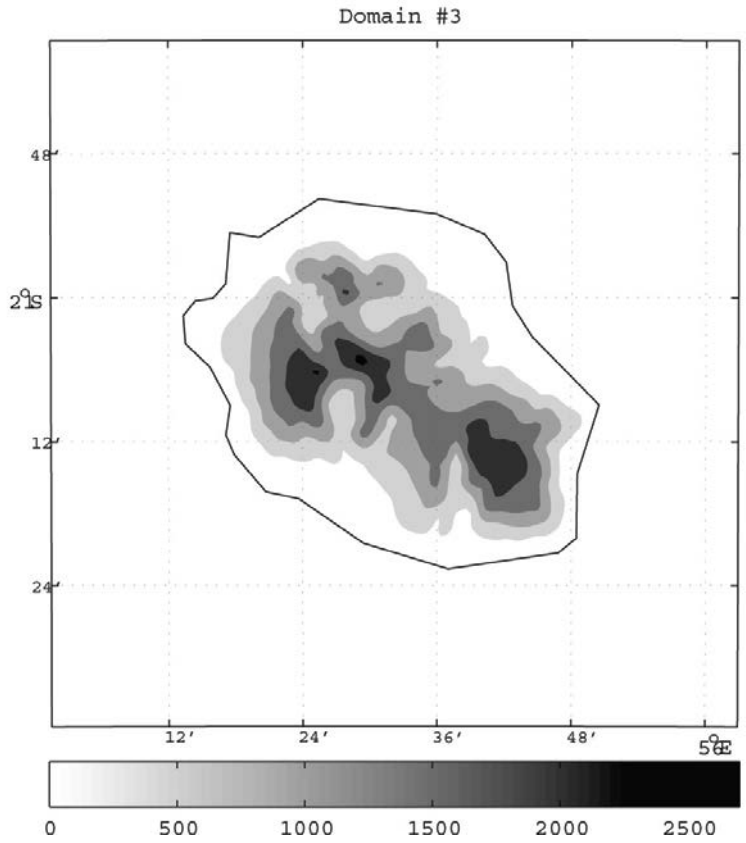

Figure 2.5 WRF domain #3 with the elevation of topography (m).

2.2 Reference data used

2.2.1 Strategy

Because we use here an uncommon RegCM domain, we first need to check that the model is able to reproduce the mean climate (not only the radiative fluxes but also the temperature and the precipitation) of the region before using it for the analysis of the temporal variability. This has been done using different types of datasets: ground-based SSR measurements over Reunion Island, satellite-derived radiative fluxes (both the LW and the SW at the surface and the top of atmosphere), estimates of precipitation, reanalysis surface temperature, cloud cover and surface albedo. In addition, to study RegCM4's ability to reproduce the temporal variability of SSR at different time scales over the SWIO, several parameters from the input (reanalyses) and output (RegCM4) datasets: SSR, and relative humidity (RH), air temperature (T), zonal (U) and meridional (V) components of wind at different pressure levels throughout the troposphere, are related to different climate indices.

In this study, WRF is run over the same time periods (two contrasted austral summer periods: 2000-2001 and 2004-2005) and with the same physical package in Morel et al. (2014). Because of the good performances of the model in that previous work, we focus here solely on the validation of WRF SSR outputs using ground-based and satellite-derived SSR data.

2.2.2 Météo France data

In this work, model outputs are validated by comparison to ground-based observations when available. In Chapter 3, monthly SSR data for 10 years (1999-2008) from a limited number of solar radiation stations (40; Figure 2.6) belonging to Météo-France network are compared to RegCM4 SSR outputs. The stations are not uniformly distributed across the covered altitude range (~0-2500 m), with about 80% of them being situated below 1000 m. This feature could pose big bias when comparing to the simulated data because about 40% of the territory is located over 1000 m. In Chapter 4, daily SSR data for two austral summer seasons (2000-2001 and 2004-2005) are used to validate WRF SSR results.

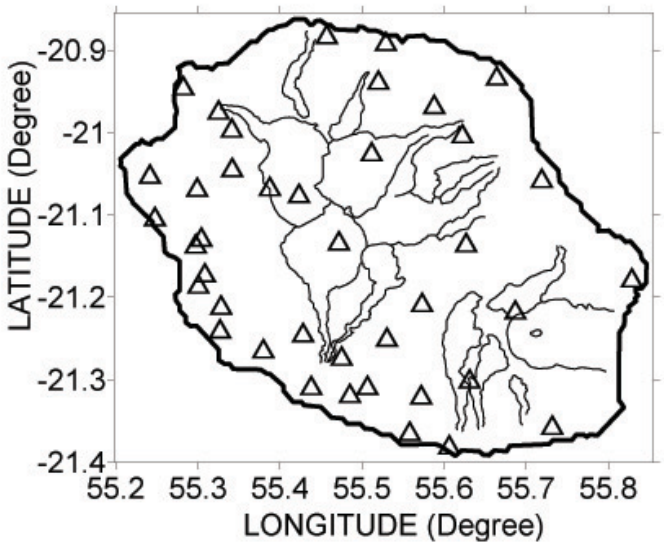

Figure 2.6 Solar irradiation observing station network over Reunion Island as provided by Météo-France.

2.2.3 Satellite data

As direct observations of surface radiation fluxes are not available, the Clouds and Earth's Radiant Energy System (CERES; *http://ceres.larc.nasa.gov/*) Energy Balanced and Filled (EBAF) products (hereafter referred to as CERES) are used for RegCM4 model validation. CERES provides satellite-based datasets of short-wave (SW), long-wave (LW) and net radiation fluxes at the earth's surface and at the top of atmosphere (TOA) in clear- and all-sky conditions, on 1° × 1° resolution and monthly scales. Kato et al. (2013), analyzing the bias [root-mean-square difference (RMSD)] between CERES data and surface observations from a number of sites for 10 years, found values of 4.7(13.3) W/m^2 for downward SW and -2.5(7.1) W/m^2 for downward LW irradiances over ocean, and -1.7(7.8) W/m^2 for downward SW and -1.0(7.6) W/m^2 for downward LW irradiances over land. Monthly dataset from Global Precipitation Climatology Project (GPCP) (Version 2.1; Adler et al. 2003) with a resolution of 2.5°×2.5° is also used to validate precipitation results simulated by RegCM4.

The daily outgoing longwave radiation (OLR) datasets (Liebmann & Smith 1996) from National Oceanic and Atmospheric Administration (NOAA) for the austral summer months (November to February) 1999-2008 on a 2.5°×2.5° regular grid is regarded as the reference to examine the performance of ERA-Interim reanalyses (input to RegCM4) and RegCM4 with regard to the synoptic climate variability.

WRF results for austral summers 2000-2001 and 2004-2005 are validated against the data from the Satellite Application Facility on Climate Monitoring (CM_SAF; Posselt et al. 2011; *http://www.cmsaf.eu*) which processed a 23-year long (1983-2005) continuous surface incoming solar (SIS) and surface incoming direct (SID) radiation climate data record from Meteosat's first generation satellites at 0.03°×0.03°. Those datasets have been validated using ground based observations from the Baseline Surface Radiation Network (BSRN; Dehne & Wild 1998) as a reference. The results demonstrated that the target accuracy is achieved for monthly and daily means. In Chapter 4, SSR data from WRF domain #3 are compared to the daily SIS data.

2.2.4 Reanalyses data

The ERA-Interim reanalyses data are used as input to both RegCM4 and WRF, and for the validation of RegCM4 outputs. Lateral forcing of RegCM4 and WRF is provided every 6h by ERA-Interim reanalyses (Simmons et al. 2007; Dee et al. 2011) at a 1.5° and 0.75° horizontal resolution, respectively. In addition, we use daily OLR at a 1.5° horizontal resolution during NDJF 1999 to 2008 to derive the clusters in the analysis of the synoptic climate variability of SSR, as well as monthly surface air temperature with a resolution of 1.5°×1.5° and monthly total cloud cover and surface albedo with a resolution of 0.125°×0.125° to assess the ability of RegCM4 to reproduce the mean climate of the SWIO region during the period 1999 to 2008.

2.2.5 Climate indices

In this work, we study the temporal variability of surface solar radiation through simulation data from the regional climate model RegCM4 in relation to some indices of the interannual (ENSO, IOD), intraseasonal (MJO) and synoptic (TTT) climate variability. These are described hereafter.

2.2.5.1 Interannual variability

2.2.5.1a ENSO

The ENSO develops due to the redistribution of heat and momentum in the tropical Pacific Ocean, presenting irregular fluctuations between its warm (El Niño-EN) and cold (La Niña-LN) sea surface temperature (SST) anomalies over the eastern-central tropical Pacific Ocean (Allan 2000). ENSO is the most important coupled atmospheric-oceanic phenomenon responsible for inter-annual variability on a global scale, and it also has strong impact on the regional scale. Many studies have shown a close relationship between the variability of precipitation of southern African region with ENSO (Rocha & Simmonds 1997a; Latif et al. 1999; Makarau & Jury 1997;

Ropelewiski & Halpert 1989; Janowiak 1988). Cook (2000) examines the influence of ENSO on rainfall interannual variability in southern Africa by using a GCM simulation. Nicholson (2003) suggested that Indian Ocean SST anomalies could shift atmospheric convection and rainfall eastwards during El Niño events. Misra (2003) examined the influence of ENSO by the Pacific SST on the precipitation over southern Africa diagnosed from an AGCM. Philippon et al. (2012) studied the influence of ENSO on winter rainfall in South Africa.

There are different climate indices to account for the ENSO signal, such as Nino3, Bivariate ENSO Timeseries (BEST), Nino 3.4, Multivariate ENSO Index (MEI) (Wolter & Timlin 1993, 1998) and so on. In this study, we use the MEI to determine the correlation between ENSO and SSR because it is often used and appears to be more appropriate to express the coupled nature of ENSO. Indeed, the MEI is determined as the first principal component of six different parameters: sea level pressure, zonal and meridional components of the surface wind, sea surface temperature, surface air temperature and cloudiness of the South Pacific Ocean. The MEI values are computed for every month based on the two preceding calendar months, thus MEI values are bimonthly. 1999-2008 NDJF (10 years) of MEI data are applied to calculate the correlation coefficient with ERA-Interim (forcing data for RegCM4)) and RegCM4 output data during the same period.

2.2.5.1b IOD

IOD is a similar ocean-atmosphere interaction causing interannual climate variability. IOD is an irregular oscillation of sea-surface temperatures (SST) in which the western Indian Ocean becomes alternately warmer and then colder than the eastern part of the ocean. IOD is a coupled ocean-atmosphere phenomenon in the Indian Ocean. It is a similar ocean-atmosphere interaction causing inter-annual climate variability as ENSO. IOD is normally characterized by anomalous cooling of SST in the southeastern equatorial Indian Ocean and anomalous warming of SST in the western equatorial Indian Ocean. Associated with these changes the normal convection situated over the eastern Indian Ocean warm pool shifts to the west and brings heavy rainfall over the east part of Africa and severe droughts/forest fires over the Indonesian region (Figure 2.7; Saji et al. 1999).

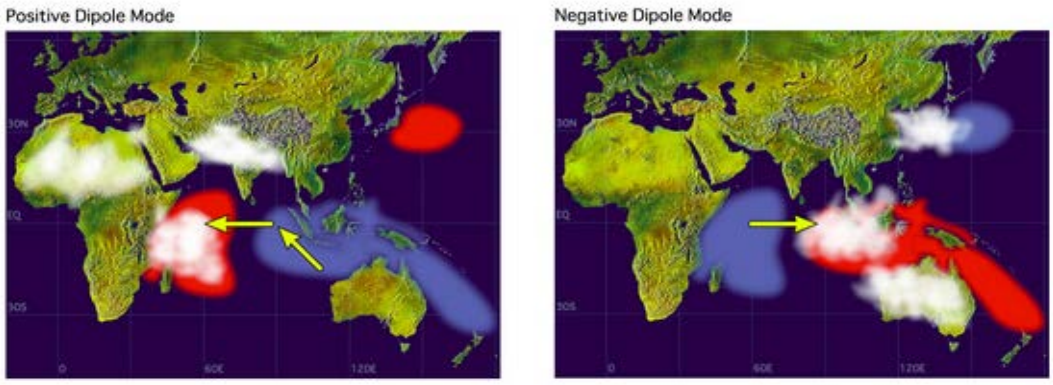

Figure 2.7 Schematic of positive and negative IOD events. SST anomalies are shaded (red color is for warm anomalies and blue is for cold ones). White patches indicate increased convective activities and arrows indicate anomalous wind directions during IOD events (Source: the Japan Agency for Marine-Earth Science and Technology)

About 50% of the IOD events in the past 100 years have co-occurred with ENSO and the other half independently (Vinayachandran et al. 2009). Luo et al. (2010) studied the interaction between El Niño and extreme IOD events. Reason (2001) studied the relationship between subtropical Indian Ocean SST dipole events and southern African rainfall. Rao et al. (2002) examined the interannual subsurface variability in the tropical Indian Ocean with an emphasis on the IOD. Marchant et al. (2007) reviewed the causes of the IOD in the Indian Ocean, the relationships with ENSO, and the consequences for East African climate dynamics.

The Dipole Mode Index (DMI) is an indicator of the east-west temperature gradient across the tropical Indian Ocean, linked to the IOD. It is defined as the difference between SST anomalies in the west and east (Saji et al. 1999). 1999-2008 NDJF (10 years) of DMI data are thus applied to calculate the correlation coefficient with ERA-Interim and RegCM4 output data during the same period.

2.2.5.2 Intraseasonal variability

The MJO is the largest mode of the intraseasonal (30-90 days) variability in the tropical atmosphere. It was first discovered in the early 1970s by Roland Madden and Paul Julian when they were studying tropical wind and pressure patterns (Madden and Julian 1971; 1972). It is a large-scale coupling between atmospheric circulation and tropical deep convection (Zhang 2005). Unlike ENSO, MJO is a traveling pattern that propagates eastward at approximately 4 to 8 m/s through the atmosphere above the warm parts of the Indian and Pacific Oceans.

Usually, the strong MJO activity consists in two parts: one within the enhanced convective phase and the other in the suppressed convective phase. These two phases produce opposite changes in clouds and rainfall, then opposite solar radiation. In the enhanced convective phase, winds at the surface converge, and air is pushed up

throughout the atmosphere. At the top of the atmosphere, the winds diverge. Such rising air motion in the atmosphere tends to increase condensation and rainfall. In the suppressed convective phase, winds converge at the top of the atmosphere, forcing air to subside and to diverge at the surface later (Rui & Wang 1990). As air sinks from high altitudes, it warms and dries, which suppresses convection. This entire dipole structure is illustrated in Figure 2.8, which moves west to east with time in the tropics, causing more cloudiness, rainfall, and even storminess in the enhanced convective phase, and more downward solar radiation and dryness in the suppressed convective phase. The MJO can produce impacts similar to those of ENSO, but which appear only in weekly averages before changing, rather than persisting, therefore appearing in seasonal averages.

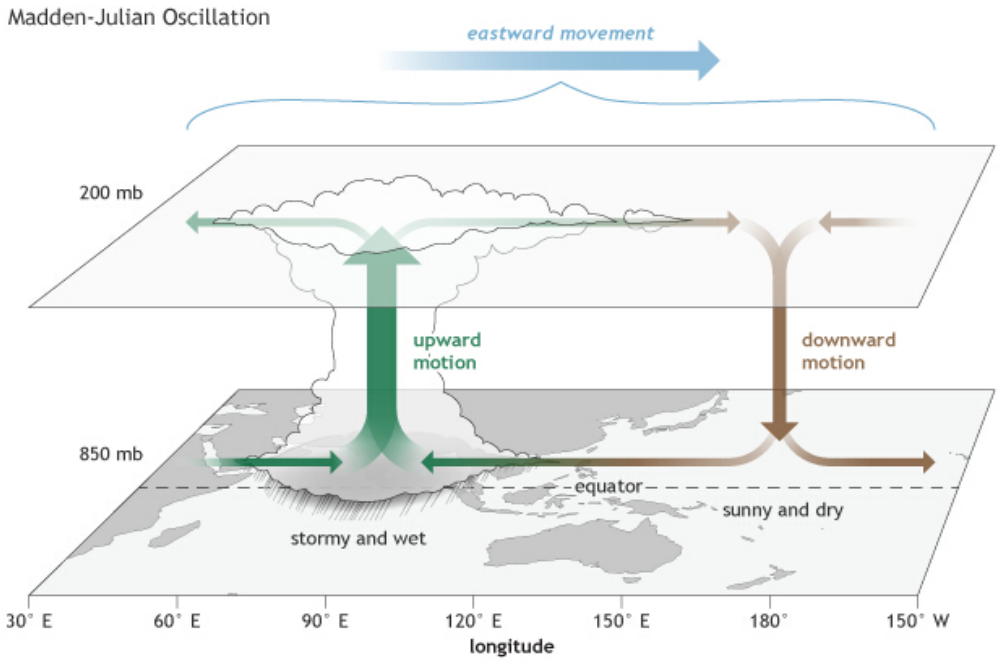

Figure 2.8 The surface and upper-atmosphere structure of the MJO for a period when the enhanced convective phase (thunderstorm cloud) is centered across the Indian Ocean and the suppressed convective phase is centered over the west-central Pacific Ocean. Horizontal arrows pointing left represent wind departures from average that are easterly, and arrows pointing right represent wind departures from average that are westerly. The entire dipole shifts eastward over time. (Climate.gov drawing by Fiona Martin)

There are several kinds of time series data that quantify current and historic MJO activity, which are referred to as MJO indices (Kiladis et al. 2014; Ventrice et al. 2013). Only the All-season Real-time Multivariate MJO (RMM) index which uses an objectively-defined index to monitor and predict the climate and weather variations related to the MJO (Wheeler & Hendon 2004), is used here to examine the intraseasonal variability of SSR. This index is based on the first two Empirical Orthogonal Functions (EOFs) of the combined fields of near-equatorially-averaged

850hPa zonal wind, 200hPa zonal wind, and satellite-observed OLR data. Projection of the daily observed data onto such multiple-variable EOFs, with the annual cycle and components of inter-annual variability removed, yields principal component (PC) time series that vary mostly on the intraseasonal time scale of the MJO only. This projection thus serves as an effective filter for the MJO without the need for time filtering, making the PC time series an effective index for real time use. The two PC time series that form the index are called the Real-time Multivariate MJO series 1 (RMM1), and RMM2. RMM1&RMM2 index provides 8 phases to descript the life cycle of oscillation.

2.2.5.3 Synoptic variability

In southern Africa and the SWIO area, cloud bands oriented from the northwest to the southeast and linking the tropics to mid-latitude circulation, initially revealed from satellite data (Harangozo & Harrison 1983), are referred to as TTTs. TTTs are embedded in the south Indian Ocean convergence zone (Cook 2000), develop at the synoptic scale and are responsible for significant amounts of rainfall during austral summer (Harrison 1984, 1986; Crimp et al. 1998; Todd & Washington 1999; Washington & Todd 1999; Tyson & Preston-White 2000; Hart et al. 2012). TTTs are regarded as an interaction between tropical convection and mid-latitude transient perturbations (Todd et al. 2004; Macron et al. 2014). The TTTs connect synoptic disturbances in the tropics and mid-latitudes and the cloud band formation is triggered by the arrival of an upper-level trough over the southern Africa associated with a band of divergence east of its leading edge (Ratna et al. 2012). TTTs are associated with an increase in the intensity of the African Walker cell with enhanced moisture convergence over tropical southern Africa (Todd et al. 2004) and poleward moisture transport along the cloud bands of TTTs. Hart et al. (2010) suggested that tropical-extratropical interactions over southern Africa may be related to planetary waves. Fauchereau et al. (2009) and Pohl et al. (2009) showed that TTTs tend to propagate eastward from southern Africa to the Mozambique Channel and southern Madagascar. Harrison (1984) analyzed the significance of TTTs over southern Africa and SWIO in the transfer energy and momentum between the tropics and the mid-latitudes. Because TTTs are the major expression of the synoptic climate variability over the SWIO and therefore Reunion Island, we analyze the synoptic variability of SSR in connection with the TTTs. Though Macron et al. (2014) already studied how TTTs form and develop over Southern Africa, we still need to re-study the characterization and the form of TTTs in our domain, which covers a larger part of the Indian Ocean including Reunion Island in the center of the domain.

The analysis of TTTs through OLR patterns is conducted with the objective to investigate the spatial response of the SSR to the synoptic climate variability over the region. The dynamical clustering (K-means clustering) is applied on the daily OLR anomalies over the SWIO and Southern Africa. K-means clustering here essentially follows that of Cheng and Wallace (1993) and Michelangeli et al. (1995). Given a previously fixed number of regimes, k, the aim of the regime analysis algorithm is to

obtain a partition, P, of the observations (days) into k regimes that minimizes the sum of the intra-regime variances, V. The Euclidean distance is used to measure the similarity between two observations, X and Y. The overall minimum of the function V(P) corresponds to the partition that best separates the different points. When the classification is applied to large samples, climatological series as we use, this overall minimum cannot be found in practice because of the huge number of different possibilities to explore. The algorithm defines n iterative partitions, P(n), for which V[P(n)] decreases with n and eventually converges to a local minimum of the Function, V(P). The overall minimum of V(P) is surrounded by many local minima that differ from it by only a few observations, exchanged from one regime to another and essentially found at the periphery of them. The latter may largely depend on the analyzed sample, the algorithm being initialized by a random draw of the k regimes. The reproducibility of the obtained partitions should therefore be tested. If the distribution of the climatological dataset is uniform, the final partition is assumed to be largely dependent on the initial randomly chosen seeds. In contrast, when the dataset is distributed into well-defined regimes, two different initial draws should theoretically lead to roughly similar final partitions. The dependence of the final result on the initial random draw may thus be sued as an indicator of the degree of classifiability of the dataset into k regimes (Fauchereau et al. 2009).

Following Michelangeli et al. (1995) and Moron and Plaut (2003), 100 different partitions of the OLR anomaly patterns are performed, and each time initialized by a different random draw. Classifiability of the original dataset consists of comparing several final partitions for a given number of regimes k. Then we retain the partition having the highest mean similarity with the 99 other ones. A classifiability index, c (Cheng & Wallace 1993), is defined to measure the average similarity within the 150 sets of regimes: its value would be 1 if all the partitions were identical. If the OLR anomaly patterns gather into k regimes in a natural way, one would expect the classibiability of the actual maps to be significantly better than that of an ensemble of artificial datasets generated through a first-order Markov process having the same covariance matrix as the true atmospheric data (Moron & Plaut 2003). The red-noise test operates as follows: 100 samples of the same length as the atmospheric dataset are generated, providing 100 values of the classifiability index, which are ranked to find the 10 and 90% confidence limits. The value c for the atmospheric dataset is then compared with these limits: a value above the 90% confidence limit indicates, for the corresponding value of k, a classifiability significantly higher than that of the red-noise model. The operation is repeated for k varying from two to ten: in most cases the best choice for the number of regimes appears quite unambiguously (Michelangeli et al. 1995). Same regimes as in Fauchereau et al. (2009), Vigaud et al. (2012) and Macron et al. (2014) are chosen for they are robust and were already successfully used in previous work.

2.3 Regional climate simulations

2.3.1 Overview

The RCM approach, which was proposed to achieve high resolution climate simulations at an affordable computational cost (Dickinson et al. 1989; Giorgi & Bates 1989; Giorgi & Marinucci 1996), is now applied in a number of climate researches. Hydrostatic and non-hydrostatic approximations are two kinds of RCM normally used now. The hydrostatic approximation is a simplification of the equation governing the vertical component of velocity. It simply says that the pressure at any point in the atmosphere (ocean) is due to the weight of the air (water) above it. When vertical accelerations are small compared to the gravitational acceleration, the hydrostatic approximation is valid as the case for RegCM4. Orlanski (1981) showed that the hydrostatic approximation was not valid when the grid size is smaller than about 8 km. The non-hydrostatic solver is more computationally expensive than a hydrostatic solver, and is often found in higher resolution models which themselves are more computationally expensive than coarse grids, such as WRF. The use of non-hydrostatic models is important in simulating highly convective flows and may be important in getting the details right for flows associated with high frequency internal waves.

Based on these (non-) hydrostatic characters of regional climate modeling, RegCM4 is used to run long-term (10-year) simulations at lower resolution (50 km) over SWIO, and WRF to perform short-term (6-month) simulations at very high resolution (750 m) over a smaller domain centred on Reunion Island.

In the RCM approach, the physics is described based on several schemes to take into account the different processes in the atmosphere, especially radiative transfer, cumulus convection, land surface processes, ocean-air exchanges, planetary boundary layer, ocean fluxes, aerosols and atmospheric chemistry.

The radiation schemes provide atmospheric heating due to radiative flux divergence and surface downward longwave and shortwave radiation for the ground heat budget.

Cumulus schemes are responsible for the sub-grid-scale effects of convective or shallow clouds in RCM. These schemes are intended to represent vertical fluxes due to unresolved updrafts and downdrafts and compensating motion outside the clouds. They operate only on individual columns where the scheme is triggered and provide vertical heating and moistening profiles. Cumulus parameterizations are theoretically only valid for coarser grid sizes, (e.g., greater than 10 km), where they are necessary to properly release latent heat on a realistic time scale in the convective columns. While the assumptions about the convective eddies being entirely sub-grid-scale break down for finer grid sizes, sometimes these schemes have been found to be helpful in triggering convection in 5–10 km grid applications. Generally, they should not be used when the model can resolve the convective eddies itself (e.g., $\leqslant$ 5 km grid).

The planetary boundary layer (PBL) is responsible for vertical sub-grid-scale fluxes due to eddy transports in the whole atmospheric column, not just the boundary layer. Thus, when a PBL scheme is activated, explicit vertical diffusion is de-activated with the assumption that the PBL scheme will handle this process.

The land-surface models (LSMs) use atmospheric information from the surface layer scheme, radiative forcing from the radiation scheme, and precipitation forcing from the microphysics and convective schemes, together with internal information on the land's state variables and land-surface properties, to provide heat and moisture fluxes over land points and sea-ice points. These fluxes provide a lower boundary condition for the vertical transport done in the PBL schemes. The land-surface models have various degrees of sophistication in dealing with thermal and moisture fluxes in multiple layers of the soil and also may handle vegetation, root, and canopy effects and surface snow-cover prediction. The land surface model provides no tendencies, but does update the land's state variables which include the ground (skin) temperature, soil temperature profile, soil moisture profile, snow cover, and possibly canopy properties.

For all these processes, there are several options available in both RegCM and WRF. In the following, we will only describe the packages that have been used.

2.3.2 RegCM4

2.3.2.1 Description

The Regional Climate Model system RegCM, originally developed at the National Center for Atmospheric Research (NCAR), is maintained in the Earth System Physics (ESP) section of the International Centre for Theoretical Physics (ICTP). The first version of the model, RegCM1 (Dickinson et al. 1989, Giorgi & Bates 1989), was developed at the NCAR, and was the first regional climate model (RCM) documented in the literature. It was based on the Mesoscale Model MM4 (Anthes et al. 1987) with suitable augmentations in the radiative transfer and land surface process parameterizations. While Dickinson et al. (1989) had carried out ensembles of short (3 to 5 d) simulations, Giorgi & Bates (1989) and Giorgi (1990) presented the first month-long simulations driven at the lateral boundaries by reanalysis of observations and General Circulation Model (GCM) data, respectively. The first major upgrade to the RegCM system, which led to the development of the second generation version (RegCM2), was implemented in the early 1990s (Giorgi et al. 1993). RegCM2 was based on the hydrostatic version of the mesoscale modeling system MM5 (Grell et al. 1994), and compared to RegCM1 it included upgrades not only in the model dynamics, but also in all aspects o the model physics packages. An intermediate upgrade (RegCM2.5) was prepared in the late 1990s (Giorgi & Mearns 1999). In addition to several upgrades to the physics components, RegCM2.5 included the first attempts to interactively couple the atmospheric component of RegCM to other Earth system components, such as a lake model (Hostetler et al. 1993; Small et al. 1999) and a simple aerosol module (Qian & Giorgi 1999). In the mid-2000s a third major upgrade of the model was conducted (Pal et al. 2007). RegCM3 was more portable,

easy to use, and aimed at simulating tropical climates, reflecting the greater emphasis placed by ICTP on fostering the growth of scientific research in developing countries. The main upgrades and developments in the RegCM4 include a complete recoding of the model to increase its flexibility, portability, ease of use and parallelization efficiency and the interactive online coupling with chemistry/aerosol, lake, ocean and biosphere model components (Giorgi et al. 2012). The model grid spacing has spanned the 10 to 100 km range, with simulations ranging from seasonal to centennial periods, over domains covering all land regions of the world (except for the polar regions) with sizes going from sub-regional to continental. The RegCM model can be driven by lateral boundary conditions from analyses of observations (ERA40, NCEP, ERA-Interim) as well as different GCMs (MPI-ECHAM5, NCAR-CCSM, HC-HadCM/HadGEM). A new feature of RegCM4 is that it can be run in full tropical band mode (Coppola et al. 2012).

RegCM4 is an evolution of its previous version and the latest version as well. In this part, we summarize the basic features of RegCM4. Table 2.1 presents a list of the options available in the model that can be used for the simulations. RegCM4 is a hydrostatic, compressible, sigma-p vertical coordinate model run on an Arakawa B-grid in which wind and thermodynamical variables are horizontally staggered. A time-splitting explicit integration scheme is used in which the 2 fastest gravity modes are first separated from the model solution and then integrated with smaller time steps. This allows the use of a longer time step for the rest of the model. Essentially, the model dynamics are the same as that of the hydrostatic version of MM5 (Grell et al. 1994).

Because RegCM4 has not been run over the SWIO yet, we perform here a series of sensitivity tests on the schemes that are the most relevant for SSR, essentially the radiative transfer and the cumulus convection schemes. All the schemes used for the simulations are described in detail as follow:

Table 2.1 Model options available in RegCM4

Model aspects	Available options
Dynamics	* Hydrostatic, σ -vertical coordinate (Giorgi et al. 1993a)
Radiative transfer	*** Modified CCM3 (Kiehl et al. 1996)**
PBL	* Modified Holtslag (Holtslag et al. 1990)
	* UW-PBL (Bretherton et al. 2004)
Cumulus convection	* Simplified Kuo (Anthes et al. 1987)
	*** Grell (Grell 1993)**
	*** MIT (Emanuel & Zivkovic-Rothman 1999)**
	*** Tiedtke (Tiedtke 1989)**
Resolved scale precipitation	* SUBEX (Pal et al. 2000)
Land surface	* BATS (Dickinson et al. 1993)
	* Sub-grid BATS (Giorgi et al. 2003)
	* CLM(Stenier et al. 2009)
Ocean fluxes	* BATS (Dickinson et al.1993)
	* Zeng (Zeng et al.1998)
	* Diurnal sea surface temperature (Zeng & Beljaars 2005)
Interactive aerosols	* Organic and black carbon, SO_4 (Solmon et al. 2006)
	* Dust (Zakey et al. 2006)
	* Sea salt (Zakey et al. 2008)
Interactive lake	* 1D diffusion/convection (Hostetler et al. 1993)
Tropical band	* Coppola et al. (2012)
Coupled ocean (not in public version)	* MIT (Artale et al. 2010)
	* ROMS(Ratnam et al.2009)

*Those in bold font have been tested in this work (see the text for a detailed description of corresponding schemes).

2.3.2.1.1 Radiative transfer

Radiative transfer calculations in RegCM4 are carried out with two radiative transfer schemes currently available: The default modified Community Climate Model (CCM3; Kiehl et al. 1996, Giorgi et al. 2012), and the newly implemented Rapid Radiative Transfer Model (RRTM; Mlawer et al. 1997) for GCM applications

(hereafter referred to as RRTM), which has not been so far tested yet within the RegCM4 framework. CCM3 scheme includes calculations for the short-wave and infrared parts of the spectrum, including both atmospheric gases and aerosols. The scheme includes contributions from all main greenhouse gases, i.e. H_2O, CO_2, O_3, CH_4, N_2O, and CFCs, and solar radiative processes are treated using a delta-Eddington formulation (Briegleb 1992). Scattering and absorption of solar radiation by aerosols are also included based on the aerosol optical properties (absorption coefficient and single scattering albedo). Concerning cloud radiation calculations, the solar spectrum optical properties are based on the cloud liquid water amount prognostically calculated by the model, cloud fractional cover, which is calculated diagnostically as a function of relative humidity, and effective cloud droplet radius, which is parameterized as a function of temperature and land sea mask for liquid water and as a function of height for ice phase. In addition, the scheme diagnostically calculates a fraction of cloud ice as a function of temperature. In the infrared spectrum, the cloud emissivity is calculated as a function of cloud liquid/ice water path and cloud infrared absorption cross sections depending on effective radiation for the liquid and ice phases.

The main features of RRTM are described in Clough et al. (2005) and are summarized here. RRTM utilizes the k-correlated method to calculate shortwave (SW) fluxes, longwave (LW) fluxes and heating rates efficiently and accurately. The absorption coefficients used to build the relevant k-distributions are obtained from the Line-By-Line Radiative Transfer Model (LBLRTM; Clough et al. 1981), which includes the MT_CKD water vapor continuum model (Mlawer et al. 2003), and the HITRAN line parameter database. RRTM is divided into sixteen contiguous bands in the LW (hereafter referred to as RRTM-LW) from 10 to 3250 cm^{-1}, and fourteen bands in the SW (hereafter referred to as RRTM-SW; Mlawer et al. 1998) from 820 to 50000 cm^{-1}. Spectral bands were chosen based on the major absorption features of the active gaseous species. Modeled absorbers in RRTM-LW include water vapor, carbon dioxide, ozone, nitrous oxide, methane, oxygen, nitrogen, and the common halocarbons. Modeled sources of extinction in RRTM-SW include water vapor, carbon dioxide, ozone, methane, oxygen, aerosols, and Rayleigh scattering. In addition to clear sky radiative transfer, parameterizations of the radiative effects of water clouds (Hu & Stamnes 1993) and ice clouds (Fu et al. 1998) are available in RRTM. RRTMG further includes the Monte-Carlo Independant Column Approximation (McICA) capability to represent sub-grid cloud variability with random, maximum-random and maximum options for cloud overlap (Barker et al. 2003; Pincus et al. 2003).

2.3.2.1.2 Planetary boundary layer

In RegCM4, the planetary boundary layer (PBL) scheme that is currently available, is of Holtslag et al (1990). This scheme underwent various modifications and a second new PBL scheme, the University of Washington PBL (Grenier & Bretherton 2001, Bretherton et al. 2004), was implemented in the model. In the Holtslag scheme, a PBL

height is first diagnostically calculated based on an iteration procedure employing a bulk critical Richardson number formulation. Then a non-local vertical profile of eddy diffusivity for heat, moisture, and momentum is specified from the surface to the PBL height, and a countergradient transport term is added for temperature and moisture. The eddy diffusivity depends on the friction velocity, height, Monin-Obhukov length, and PBL height.

2.3.2.1.3 Cumulus convection

Convective precipitation in RegCM4 is computed using one of the four following schemes: (1) Modified-Kuo scheme (Anthes 1977); (2) Grell scheme (Grell 1993); (3) MIT-Emanuel scheme (Emanuel 1991; Emanuel & Zivkovic-Rothman 1999); (4) Tiedtke scheme (Tiedtke 1989). In addition, the Grell parameterization is implemented using one of two following closure assumptions: (1) the Arakawa and Schubert closure (AS74, Grell et al 1994); (2) the Fritsch and Chappell (1980) closure (FC80). And the new version of RegCM4 has the capability of running different convection schemes over land and ocean, which is referred as mixed convection schemes. A series of preliminary test experiments showed that different schemes have different performance over different regions, particularly over land and ocean areas (Giorgi & Shields 1999; Martínez-Castro et al. 2006; Sylla et al. 2012). In this study, we conduct sensitivity tests with the 6 following schemes: 1) Emanuel, 2) Grell with the AS74, 3) Grell with the FC80 closure, 4) Grell over land and Emanuel over ocean, 5) Emanuel over land and Grell over ocean, 5) Tiedtke. These are described hereafter.

Grell Scheme: The Grell scheme (Grell 1993) considers clouds as two steady-state circulations: an updraft and a downdraft. No direct mixing occurs between the cloudy air and the environmental air except at the top and bottom of the circulations. The mass flux is constant with height and no entrainment or detrainment occurs along the cloud edges. The originating levels of the updraft and downdraft are given by the levels of maximum and minimum moist static energy, respectively. The Grell scheme is activated when a lifted parcel attains moist convection. Condensation in the updraft is calculated by lifting a saturated parcel. The downdraft mass flux (m_0) depends on the updraft mass flux (m_b) according to the following relation:

$$m_0 = \frac{\beta I_1}{I_2} m_b \qquad \text{(Eq. 2.1)}$$

where I_1 is the normalized updraft condensation, I_2 is the normalized downdraft evaporation, and β is the fraction of updraft condensation that re-evaporates in the downdraft. β depends on the wind shear and typically varies between 0.3 and 0.5. Rainfall is given by

$$P^{CU} = I_1 m_b (1-\beta) \qquad \text{(Eq. 2.2)}$$

Heating and moistening in the Grell scheme are determined both by the mass fluxes and the detrainment at the cloud top and bottom. In addition, the cooling effect of moist downdraft is included. Due to the simplistic nature of the Grell scheme, several

closure assumptions can be adopted. RegCM4's earlier version directly implements the quasi-equilibrium assumption of AS74. It assumes that convective clouds stabilize the environment as fast as non-convective processes destabilize it as follows:

$$m_b = \frac{ABE'' - ABE}{NA\Delta t} \qquad \text{(Eq. 2.3)}$$

where ABE is the buoyant energy available for convection, ABE'' is the amount of buoyant energy available for convection in addition to the buoyant energy generated by some of the non-convective processes during the time interval Δt, and NA is rate of change of ABE per unit m_b . The difference ABE'' – ABE can be thought of as the rate of destabilization over time Δt. ABE'' is computed from the current fields plus the future tendencies resulting from the advection of heat and moisture and the dry adiabatic adjustment.

In the RegCM4, a stability-based closure assumption, the FC80 type closure assumption is used by default and it is assumed that convection removes the ABE over a given time scale as follows:

$$m_b = \frac{ABE}{NA\tau} \qquad \text{(Eq. 2.4)}$$

where τ is the ABE removal time scale.

The fundamental difference between the two assumptions is that the AS74 closure assumption relates the convective fluxes and rainfall to the tendencies in the state of the atmosphere, while the FC80 closure assumption relates the convective fluxes to the degree of instability in the atmosphere. Both schemes achieve a statistical equilibrium between convection and the large-scale processes.

MIT-Emanuel Scheme: This scheme (Emanuel 1991; Emanuel & Zivkovic Rothman 1999) assumes that the mixing in clouds is highly episodic and inhomogeneous and considers convective fluxes based on an idealized model of sub-cloud-scale updrafts and downdrafts. Convection is triggered when the level of neutral buoyancy is greater than the cloud base level. Between these two levels, air is lifted and a fraction of the condensed moisture forms precipitation while the remaining fraction forms the cloud. The cloud is assumed to mix with the air from the environment according to a uniform spectrum of that ascend or descend to their respective levels of neural buoyancy. The mixing entrainment and detrainment rates are functions of the vertical gradients of buoyancy in clouds. The fraction of the total cloud base mass flux that mixes with its environment at each level is proportional to the undiluted buoyancy rate of change with altitude. The cloud base upward mass flux is relaxed towards the sub-cloud layer quasi equilibrium. In addition to a more physical representation of convection, the MIT-Emanuel scheme offers several advantages compared to the other RegCM4 convection options. For instance, it includes a formulation of the auto-conversion of cloud water into precipitation inside cumulus clouds, and ice processes are accounted for by allowing the auto-conversion threshold water content

to be temperature dependent. Additionally, the precipitation is added to a single, hydrostatic, unsaturated downdraft that transports heat and water. Lastly, the MIT-Emanuel scheme considers the transport of passive tracers.

Tiedtke Scheme: This scheme is a bulk model based on the mass flux concept. It considers shallow, midlevel and penetrative convection, as well as the effects of cumulus-scale downdrafts. Stratocumulus convection is parameterized as an extension of the model's vertical diffusion scheme (Tiedtke et al. 1988). The closure assumption for midlevel/penetrative convection is that large-scale moisture convergence determines the bulk cloud mass flux; for shallow convection, the mass flux is maintained instead by moisture from surface evaporation. Entrainment and detrainment of mass in convective plumes occurs both through turbulent exchange and organized inflow and outflow. Momentum transport by convective circulations is also included, following Schneider and Lindzen (1976).

2.3.2.1.4 Land surface processes

The Biosphere-Atmosphere Transfer Scheme (BATS) of Dickinson et al. (1993) has been used in the RegCM since the earliest versions. It includes a 1-layer vegetation module, a 1-layer snow module, a force-restore model for soil temperatures, a 3-layer soil scheme, and a simple surface runoff parameterization. This land surface scheme includes 20 surface types and 12 soil color and soil texture types. In addition, a sub-grid land surface configuration can be used by which each model grid point is divided into a regular sub-grid, and land surface processes are calculated at each sub-grid point taking into account the local land-use and topography (Giorgi et al. 2003). The latter scheme was shown to be especially useful in improving the simulation of the surface hydrologic cycle in mountainous areas (Giorgi et al. 2003). There are two major augmentations for land surface processes in RegCM4. First is, 2 new land use types were added to BATS to represent urban and suburban environments. Urban development not only modifies the surface albedo and alters the surface energy balance, but also creates impervious surfaces with large effects on runoff and evapotranspiration. These effects can be described by modifying relevant properties of the land surface types in the BATS package.

2.3.2.1.5 Ocean flux parameterization

Zeng et al. (1998) ocean flux scheme has been used in RegCM4 for our simulations. Pal et al. (2007) implemented the scheme of Zeng et al. (1998), which is based on a Monin-Obhukov turbulence representation for improving the excessive evaporation over warm tropical oceans found in the BATS option. Sea surface temperatures (SST) are prescribed every 6h from temporally interpolated weekly or monthly SST products by default in RegCM. These products, which are produced from satellite retrievals and in situ measurements, are representative of the mean temperature in the top few meters of the ocean. However, the actual SST can differ significantly from this mean temperature due to the cool-skin and warm-layer effects described by Fairall et al. (1996). To improve the calculation of diurnal fluxes over the ocean, the

prognostic SST scheme described by Zeng & Beljaars (2005) was implemented in RegCM4. The scheme is based on a 2-layer, 1-dimensional heat transfer model, with the top layer representing the upper few millimeters of the ocean which is cooled by net longwave radiation loss and surface fluxes. The bottom layer is 3 m thick, is warmed by solar radiation, and exchanges heat with the top layer. This diurnal SST scheme appears to provide significant, although not major, effects on the model climatology mostly over tropical oceans, for example the Indian Ocean, and now it is used as default in RegCM4.

2.3.2.1.6 Large-scale precipitation scheme

Subgrid Explicit Moisture Scheme (SUBEX, Pal et al. 2000) is used to handle nonconvective clouds and precipitation resolved by the model. SUBEX accounts for the subgrid variability in clouds by linking the average grid cell relative humidity to the cloud fraction and cloud water following the work of Sumdqvist et al. (1989). It first calculates fractional cloud cover at a given grid point based on the local relative humidity. Then, in the cloudy fraction it uses a Kessler-type bulk formulation in which cloud water is turned into precipitation via an autoconversion and an accretion term. Below-cloud evaporation of falling raindrops is also accounted for based on the local relative humidity and an evaporation rate coefficient. Key sensitivity parameters in this scheme are the in-cloud liquid water threshold for the activation of the autoconversion term (Oth) and the rate of sub-cloud evaporation (Cevap). Greater values of Qth and Cevap lead to decreased precipitation amounts.

2.3.2.2 Experimental design

Because RegCM4 has never been used over the SWIO region before, we perform a series of sensitivity tests to find the optimal configuration of the physical package, essentially on the radiative scheme (CCM, default; RRTM) and the convection schemes (MIT-Emanuel convective scheme (Emanuel); Grell convective scheme with AS74 closure assumption (Grell_A); Grell convective scheme with FC80 closure assumption (Grell_F); Grell convective scheme implemented over land and Emanuel convective scheme implemented over ocean (Grell_Emanuel); Emanuel convective scheme implemented over land and Grell convective scheme implemented over ocean (Emanuel_Grell); Tiedtke convective scheme (Tiedtke)).

We also document the influence of the domain size and the spatial resolution. Three different domains are tested: 0°-40°S, 0°-100°E (Domain 1, default; Figure 2.1); 12°-28°S, 42°-65°E (Domain 2; Figure 2.1); 17°-25°S, 50°-67°E (Domain 3; Figure 2.1), and two spatial resolutions: 20 km and 50 km.

All the simulations performed are summarized in Table 2.2. For all them, we use modified Holtslag et al. (1990) PBL scheme, BATS land surface package (Dickinson et al. 1993), Zeng et al. (1998) ocean flux scheme, SUBEX moisture scheme (Pal et al. 2000) which are incorporated as default options in the RegCM4 code (Giorgi et al. 2012). Lateral boundary conditions are provided every 6h from the ERA-Interim

reanalyses (Simmons et al. 2007; Dee et al. 2011) at a 1.5° resolution and 37 pressure levels. SST fields are prescribed every 6 h after a linear interpolation of weekly NOAA OA-V2 SST at a 1° resolution (Reynolds et al. 2002). The buffer zone area for the model's simulation is not shown in the figures for it close to the Equator boundary which gives different behavior.

Table 2.2 Summary of the simulations performed with RegCM4

Simulation	**Radiation scheme**		**Convection scheme**						**Spatial resolution**		**Domain**			**Period**	
	CCM	RRTM	E	G_A	G_F	G_E	E_G	T	50 km	20 km	1	2	3	.00-.01	.98-.08
#1	✓		✓						✓		✓			✓	
#2		✓	✓						✓		✓			✓	
#3	✓		✓							✓	✓			✓	
#4		✓	✓							✓	✓			✓	
#5	✓		✓						✓		✓				✓
#6	✓			✓					✓		✓				✓
#7	✓				✓				✓		✓				✓
#8	✓					✓			✓		✓				✓
#9	✓						✓		✓		✓				✓
#10	✓		✓					✓	✓		✓				✓
#11	✓		✓							✓		✓		✓	
#12	✓		✓							✓			✓	✓	

E: Emanuel scheme; G_A: Grell scheme with AS74 closure assumption; G_F: Grell scheme with FC80 closure assumption; G_E: Grell over land and Emanuel over ocean; E_G: Emanuel over land and Grell over ocean; T: Tiedtke scheme. The setting in simulation #8 (blue color) is conducted for ensemble simulations.

The simulations are all carried out with 18 sigma levels in the vertical, and over domain 1 (including a 12-grid point buffer zone to prescribe lateral boundary conditions) centered on Reunion island (21.0°S; 55.0°E) and covering Southern Africa, Madagascar and the SWIO (Figure 2.1), with the exception of simulations #11 and #12 which are carried out over domain 2 and domain 3, respectively.

They are all carried out with the CCM radiative scheme, except for simulation #2 and #4, which utilizes RRTM.

Simulations for the radiation (#1-#2), domain (#1-#11-12) and resolution tests (#1-#4) start on January 1st, 2000, and end on December 31st, 2001, with the first year discarded for spin-up.

Simulations for the convection tests (#5-10) start on January 1st, 1998, and end on December 31st, 2008, there again with the first year discarded for spin-up.

Because RegCM4 is able to run rapidly and efficiently over long time periods, 5-member ensemble simulations are performed from December 1998 to December 2008 at 50 km spatial resolution. The simulations differ only by their initial conditions (obtained from the ERA-Interim fields at various times of December 1998, starting on December the 1st). Based on the results from the sensitivity tests performed, CCM for radiative transfer and a mixed convective scheme (Grell over land and Emanuel over ocean) for atmospheric convection is set as physical package. Data are archived every 6h from the beginning to the end of the simulations. The first month of simulation (December of 1998) is the spin-up month and is discarded from the analyses.

Figure 2.9 shows the 5 members' monthly mean values of SSR at the grid point of RegCM4 closest to Reunion Island, with regard to the spatial mean of the values from 40 Météo France station data for the 10-year period 1999-2008. Firstly, this figure points out the same seasonal variability for the 5 members separately, displaying not surprisingly more SSR in austral summer (November to April) than in austral winter (May to October). Secondly, all the members have a similar temporal evolution in comparison to that from Météo France point data, though the bias is kind of big and systematic (> 50 W/m^2 in austral summer; <50 W/m^2 in austral winter). This may be due 1) the model's internal variability itself or to the fact that; 2) there are not enough stations to record SSR and 3) all these stations are distributed only over a limited area and even don't cover the highest altitudes. Other datasets are then needed to assess the performance of the model. In this study, we use the CM SAF (satellite) data, though they don't cover the whole time period of the simulation. Over the time period covered by the CM SAF dataset, RegCM4 seems to perform similarly. Figure 2.11 represents the daily evolution of SSR at Gilot (Météo France) station over the north coast of Reunion Island which displays values close to those from RegCM4 for 5 members (Figure 2.10).

Figure 2.10 is the same as Figure 2.9, but for the daily data. Daily data of the 5 members during 10 years obviously gives same seasonal variability pattern. Each member of the model simulation almost shows approximately maximum values in summer. However individual members provide different minimum value in winter. These signals relate to the IV of the model and also the topography (Figure 2.1), which are important information for making decision on the site of photovoltaic equipment.

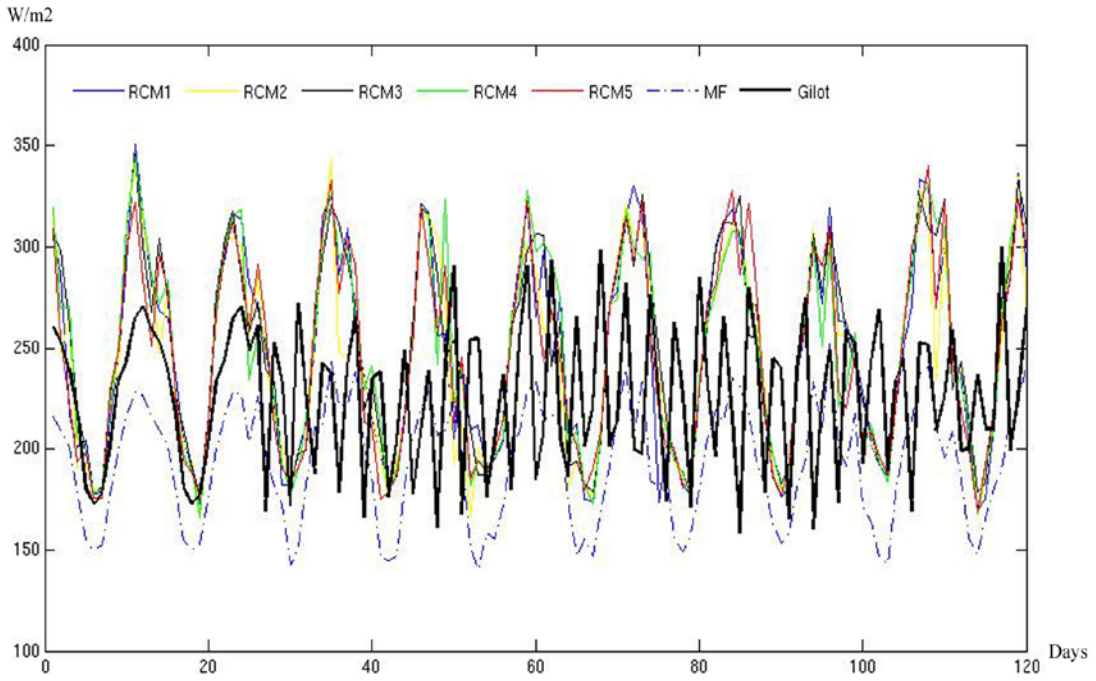

Figure 2.9 Monthly mean values of SSR from the 5-member ensemble simulations by RegCM4 (grid point closest to Reunion Island) in comparison to the corresponding values from Météo France (spatial average over all MF stations) and the monthly value from the Gillot station (Saint Denis; altitude:8m).

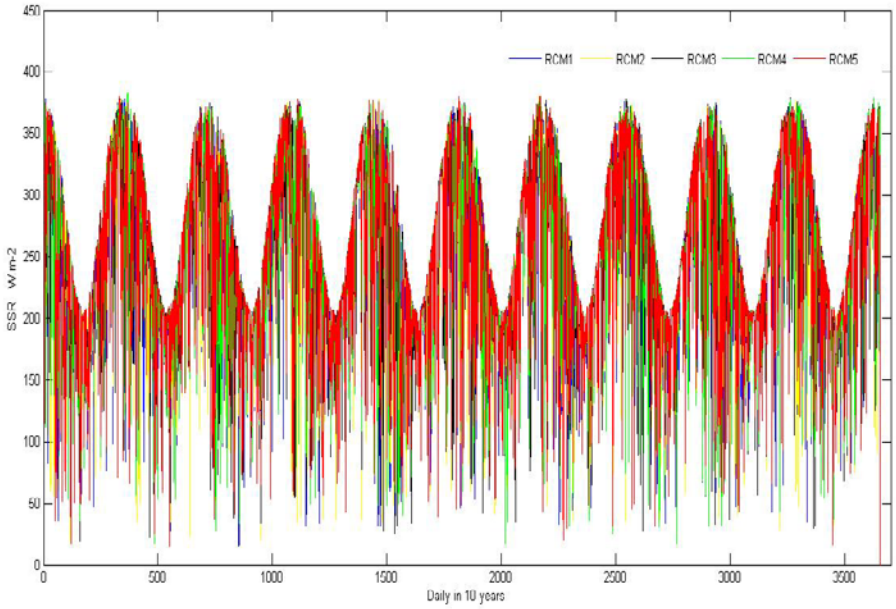

Figure 2.10 Same as Figure 2.9 but for RegCM4 daily data.

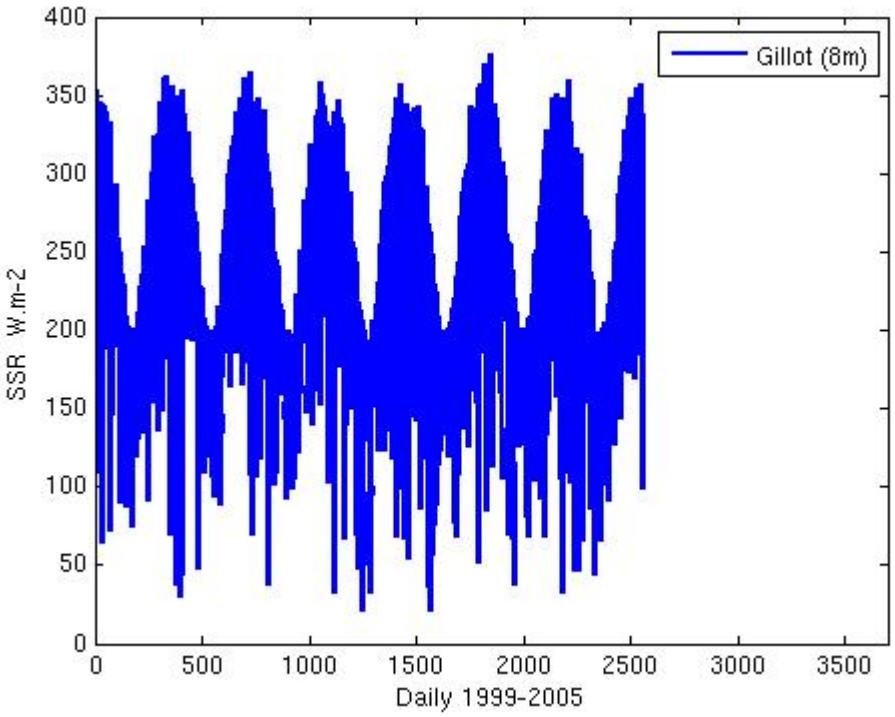

Figure 2.11 CM SAF daily data at Gillot station for 1999-2005.

In addition, the coefficient of variation (CV) is computed at each grid point to quantify the ratio between the uncertainty and the signal. CV is a measure of the IV of the model. CV is calculated as the ratio of the inter-member variance to the ensemble mean (Crétat et al. 2011). Values range from 0 (less reproducible) to 1 (most reproducible). Figure 2.12 shows that the largest uncertainties (i.e., less reproducible SSR amounts) concentrate at the tropical latitudes in the Indian Ocean, on the western part of Madagascar and in the northwest of southern Africa. This pattern is partly due to the regional modeling methodology itself. Regional climate models are known to produce largest uncertainties in the central parts of their domain or near the outflow boundary. In Chapter 3, our aims are to analyze how climate variability of SSR is distributed temporally at different time scales (interannual, intraseasonal, synoptic). Knowing that the largest uncertainties concentrate in the center of the domain, how is RegCM4 able to produce the temporal variability associated to climate signals (ENSO, IOD, etc.), on condition that those signals are present in the lateral forcing data (ERA-Interim).

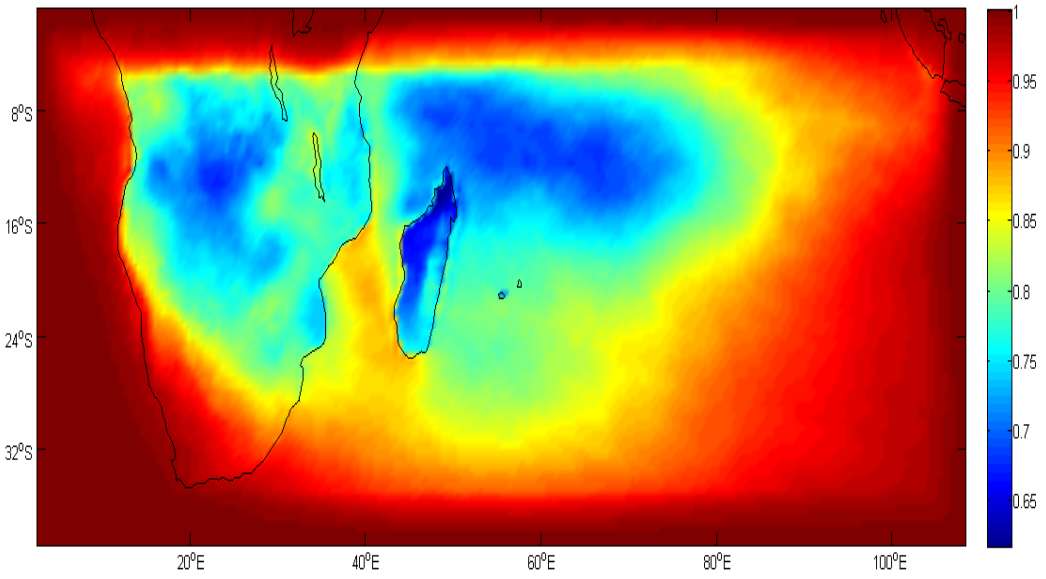

Figure 2.12 Inter-member CV of simulated seasonal SSR in RegCM4.

2.3.2.3 Results of the sensitivity study

Because a RCM has to be tested and "customized" for a given region (e.g., Crétat et al. 2012), and given that the current modeling study with RegCM is the first one that focuses on the solar radiation research over the SWIO region, we perform several test experiments with RegCM4 to evaluate all possible sources of uncertainties, from the domain size, resolution and physics (radiation, convection) of the model to its IV (Table 2.2).

2.3.2.3.1 Domain test

As the final aim is to provide temporal and spatial variations of solar radiation over Reunion Island, the effect of different domain sizes and locations on RegCM4's radiation fluxes at the top of atmosphere (TOA) and the surface, is examined. RegCM4 simulation results over 3 different domains (Figure 2.1) for the following variables: clear-sky net upward longwave flux at the TOA (LWN(clear sky) TOA), all-sky net upward longwave flux at the TOA (LWN(all sky) TOA), downward longwave flux at the surface (LW Surface), net upward longwave flux at the surface (LWN Surface), net downward shortwave flux at the surface (SWN Surface) and all-sky net upward shortwave flux at the TOA (SWN(all sky) TOA) are shown in Figure 2.13. The bias patterns RegCM4 – CERES are displayed in Figure 2.14.

In Figure 2.13, we use the same color bar to show the different radiation patterns as simulated by RegCM4 for the 3 domain sizes. It is evident that Domains 2 and 3 have almost the same radiation patterns for the 6 aforementioned LW and SW variables at the TOA and the surface over the region covered by Domain 3. However, there are clearly differences over Madagascar and the adjacent ocean area when comparing Domains 1 and 2 over the region covered by Domain 2. More LWN (clear sky/all sky) TOA values are simulated over the coastal regions of Madagascar and the Indian Ocean area between Madagascar and Reunion Island for Domain 2 than for Domain 1. The mean difference over that area is around 5 W/m^2. There are less (more) LW Surface (LWN Surface) over the Indian Ocean area between Madagascar and Reunion from 16°S to 22°S for Domain 2 than for Domain 1, and the difference between the simulations for the two domain sizes is around 20 W/m^2 for the LW Surface and 5 W/m^2 for the LWN Surface. Over the northern part of Madagascar and its right adjacent Indian Ocean areas, RegCM4 simulates more (30 W/m^2) SWN Surface and SWN (clear sky) TOA for Domain 2 than for Domain 1. Generally, results for Domain 2 show more LWN and SWN at the TOA (clear- and all-sky) and the Surface than for Domain 1, except for LW Surface, which is less for Domain 2 than for Domain 1.

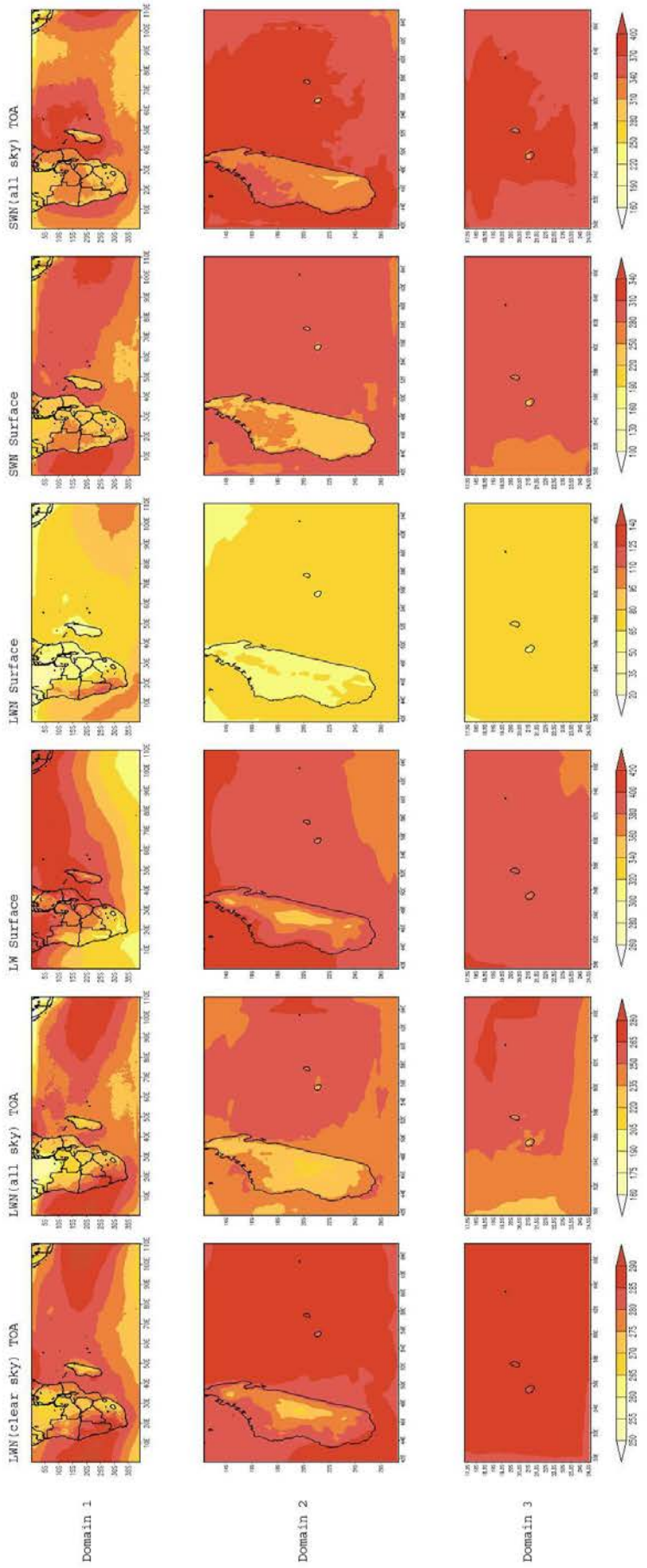

Figure 2.13 RegCM4 simulation results (W/m^2) in summer for different domain sizes tested (row) and longwave and shortwave radiative fluxes at the surface and at the top of atmosphere (column). LW: longwave flux; LWN: net longwave flux; SWN: net shortwave flux.

Anthes et al. (1989) and Giorgi and Mearns (1999) presented that different domain sizes affect the balance between the boundary and internal model forcing in the simulation. Rauscher et al. (2006) also showed that the location of boundaries related to the regional sources of forcing in a particular climatic region can also affect the regional climate model solution. To further validate this relationship over SWIO Domains 1, 2, and 3, RegCM4 results for the 3 domains are compared to CERES in Figure 2.14. Similar to Figure 2.13, the biases shown in Domain 3 have the same spatial pattern than in Domain 2 over the area covered by Domain 3. There are negative radiation fluxes biases for the 6 parameters over Reunion and Mauritius Islands in Domains 2 and 3. However, it is evident that RegCM4 simulations have substantial discrepancies for Domains 1 and 2 over the land (Madagascar) and oceanic areas. Less negative biases of LWN (clear sky/ all sky) TOA (5-10 W/m^2) are found in Domain 2 over Madagascar and its right adjacent Indian Ocean areas than in Domain 1, and more positive biases (2 W/m^2) of LWN (clear sky/ all sky) TOA are presented for Domain 2 over the Mozambique Channel. Domain 2 shows more negative biases of LW (LWN) Surface over adjacent Mozambique Channel oceanic area of northern Madagascar and Indian Ocean area than for Domain 1. Especially over the eastern Madagascar land area, Domain 2 presents more LWN Surface bias values (5-10 W/m^2). For the SWN Surface, there are obviously more positive biases over the Mozambique Channel in Domain 2 than in Domain 1. It is clear in Figure 2.14 that Madagascar as a whole has negative bias (30-40 W/m^2) of SWN (all sky) TOA in Domain 1, whereas the northern part of Madagascar has positive bias (10-30 W/m^2) in Domain 2 and the southern part has less negative biases than in Domain 1. Domain 2 presents more positive biases for SWN (all sky) TOA than Domain 1.

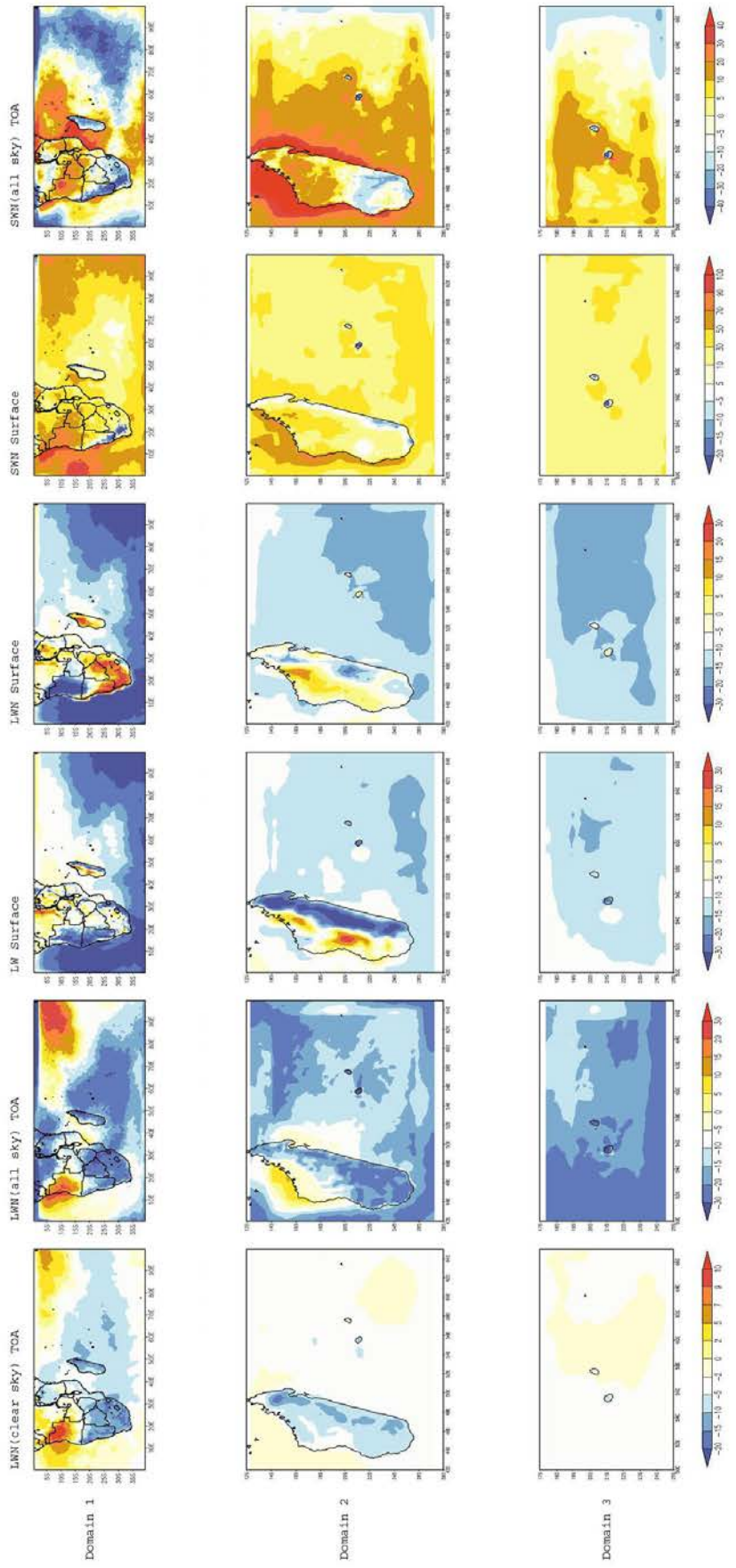

Figure 2.14 Bias of RegCM4 compared to CERES (W/m^2) in summer for different domain sizes tested (row) and longwave and shortwave radiative fluxes at the surface and at the top of atmosphere (column). LW: longwave flux; LWN: net longwave flux; SWN: net shortwave flux.

Based on the above analysis, it is clear that the domain sizes and locations have effects on the regional climate model simulation of radiation fluxes, which result from the boundary forcing for the model. Jones et al. (1995) pointed out that regional domains should be large enough to present the full development of small-scale features over the domain of interest. Leduc and Laprise (2009), Rapaić et al. (2010), Leduc et al. (2011) and Laprise et al. (2012) studied the RCM's sensitivity to domain size over Canada area, which found small-scale solution over the larger domain diverges freely from the boundary forcing in some period, and forcing the large scales throughout the domain offer definite advantages, permitting the full spin-up of small scales. Then Domain 1 is kept throughout out the remaining of the study, because that's the one for which we get the smallest biases in SW surface as compared to the satellite products.

2.3.2.3.2 Resolution test

Resolution tests for 20 km and 50 km over the domain extending from 0°S to 40°S and 0°E to 100°E (Domain 1) for two years, 2000 and 2001 in austral summer and winter are performed at the same time with the radiative scheme test in the following section. Because the results indicate that there is no obvious difference over our domain for these two resolutions, no figures are shown here. This shows that our configuration of the model is robust, and this suggests it would probably succeed in simulating regional climate variables using the protocol with the 50-km resolution. In the next sub-section, only the results at 50 km are presented.

2.3.2.3.3 Radiative scheme test

2.3.2.3.3.1 Radiation fluxes

Figures 2.15 and 2.16 present model seasonal mean longwave (LW) and shortwave (SW) fluxes for summer and winter 2001 produced with CCM3 (default in RegCM4) and RRTM radiative transfer codes at 50-km resolution at the TOA (Figure 2.15) and at the surface (Figure 2.16). These two simulations are referred as RegCM4-CCM and RegCM4-RRTM hereafter. Net LW and SW fluxes at the TOA are evaluated in both clear-sky and all-sky conditions. Figures 2.17 and 2.18 show the biases (RegCM4–CERES) in the model radiation fluxes with regard to CERES observational data at the TOA (Figure 2.17) and at the surface (satellite-derived fluxes data) (Figure 2.18).

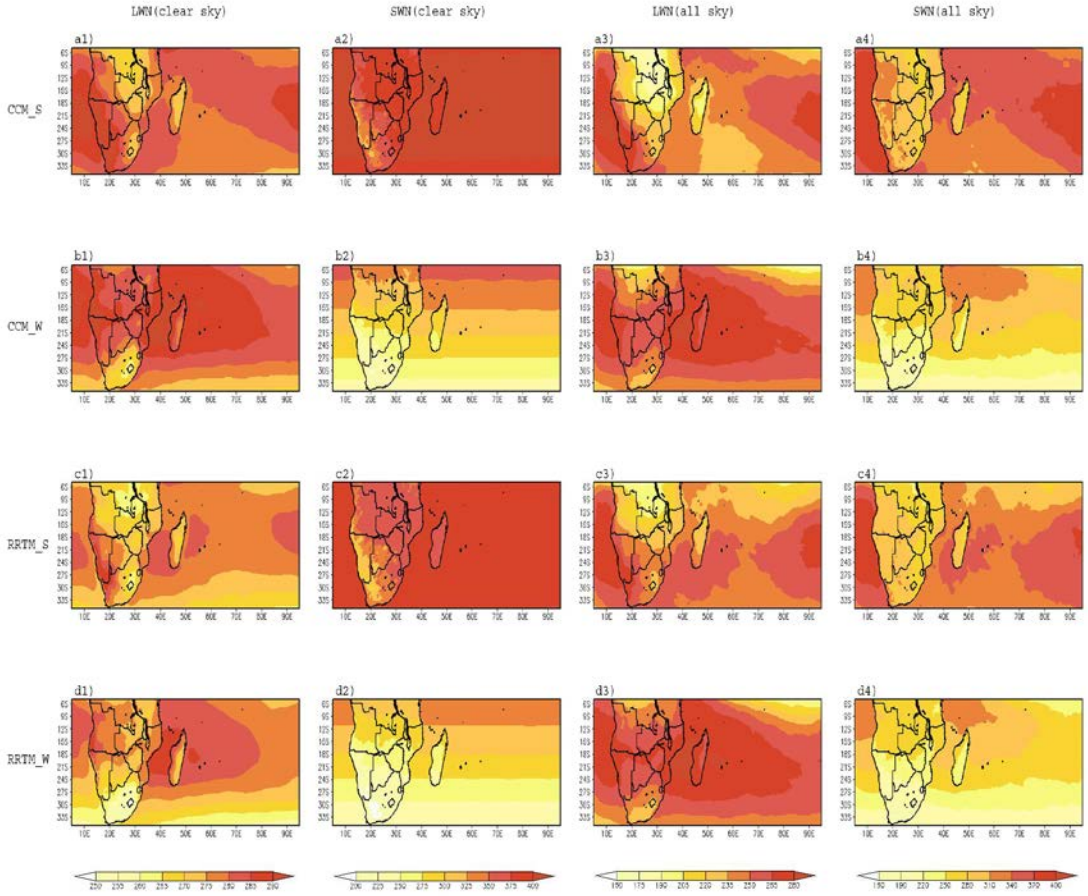

Figure 2.15 Seasonal mean LW and SW radiation fluxes (W/m^2) at TOA simulated by RegCM4-CCM and RegCM4-RRTM at 50km. CCM_S refers to summer mean of radiation fluxes as obtained with the CCM scheme; CCM_W refers to winter mean of radiation fluxes as obtained with the CCM scheme; similarly, RRTM_S and RRTM_W refer to summer mean and winter mean of radiation fluxes with RRTM; LWN and SWN refer to net LW and net SW fluxes separately.

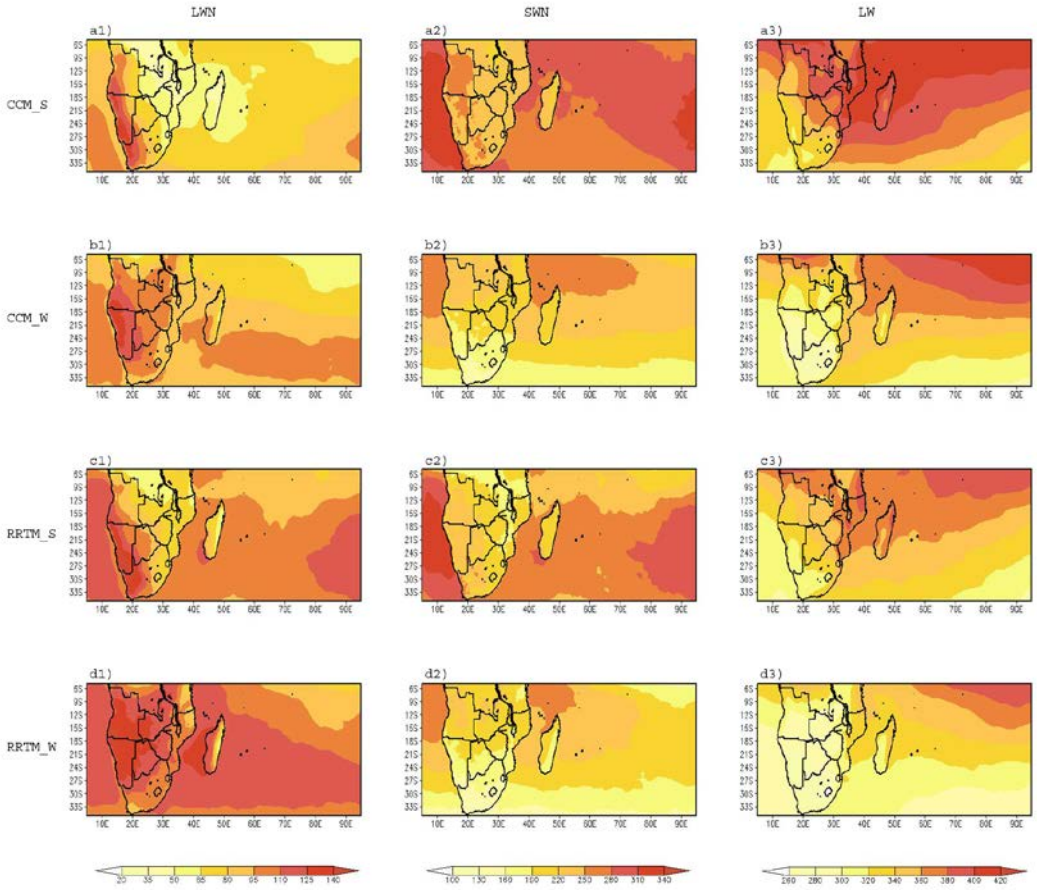

Figure 2.16 Same as in Figure 2.15 but for the surface.

2.3.2.3.3.1*a Shortwave fluxes*

At the TOA (Figure 2.15), clear-sky net SW (SWN) flux simulated by RegCM4-CCM displays a strong seasonal contrast, with, not surprisingly, larger values in summer than in winter, and larger values over ocean than over land. In the longitudinal zone 30°-90°E, that is essentially the SWIO, values can reach as much as 400 W/m^2 in summer, but they are less than 300 W/m^2 in winter. Minimum values of about 220 W/m^2 in winter and 300 W/m^2 in summer are obtained over the west coast of Southern Africa including Namibia and South Africa. The all-sky radiation field is quite similar to that of the clear-sky one, with more downward SWN over the oceanic regions, and more downward SWN in summer than in winter, though values are much less for the all-sky than for the clear-sky conditions. The minimum value of all-sky SWN is 160 W/m^2 over South Africa in winter, and the maximum is 400 W/m^2 over the oceanic areas in summer. All-sky SWN at the surface (Figure 2.16) follows a similar pattern compared to the TOA in spite of quantitative differences. The minimum value of all-sky SWN is 130 W/m^2 over South Africa in winter, and the maximum value is 310 W/m^2 over the South Atlantic Ocean and at the eastern part of the SWIO in summer.

Compared to RegCM4-CCM, RegCM4-RRTM produces similar seasonal average

spatial patterns of SWN fluxes, although with a substantial and quasi-systematic reduced magnitude. In all-sky conditions, for instance, the maximum value of SWN at the TOA (Figure 2.15) is around 400 W/m^2 over the Atlantic Ocean in summer, and the minimum value is about 160 W/m^2 over Namibia in winter; the minimum value of all-sky SWN at the surface (Figure 2.16) is around 100 W/m^2 over South Africa in winter, and the maximum value is 310 W/m^2 over the South Atlantic Ocean in summer.

Comparing RegCM4 and CERES observations at the TOA (Figure 2.17), we find that in clear-sky conditions, RegCM4-CCM tends to overestimate SWN all year around over the whole domain, with the exception of a small region covering Namibia and the west part of South Africa where the model underestimates the flux by 20-30 W/m^2. Greater positive biases are evident during the summer, with the model overestimating the flux by about 5 W/m^2 over most ocean areas and by 10-20 W/m^2 over most land areas. In all-sky conditions, RegCM4-CCM also tends to overestimate SWN by 20 W/m^2 in the two seasons over most ocean areas, and by 30 W/m^2 in summer over the northwestern part of the land areas in Southern Africa and Angola. In contrast, the model underestimates SWN by 20 W/m^2 in the two seasons over most land areas, and by 30 W/m^2 in summer over the SWIO. At the surface (Figure 2.18), the all-sky SWN flux simulated by RegCM4-CCM also shows positive biases compared to the observations, especially over ocean. Despite small patches of negative biases over Namibia and the west part of South Africa, the model overestimates the flux by 30 W/m^2 over the land and ocean areas, with larger positive biases of approximately 90 W/m^2 over the Atlantic Ocean for summer and winter seasons.

Because it produces similar spatial patterns of seasonal SWN fluxes but with a reduced magnitude, RegCM4-RRTM simulates even less SWN on the mean compared to the observations than RegCM4-CCM. In contrast to RegCM4-CCM, RegCM4-RRTM shows general negative biases in the clear-sky SWN at the TOA (Figure 2.17). RegCM4-RRTM underestimates SWN in the clear sky 20-30 W/m^2 during summer and winter, especially over west of Namibia and South Africa, where negative biases are more than 40 W/m^2 compared to CERES. In all-sky conditions, RegCM4-RRTM shows the same general tendency for biases as RegCM4-CCM, from largely positive over some parts of the ocean (e.g., the South Atlantic Ocean) to largely negative over land, but with a magnitude generally shifted toward more negatives values. As a result, RegCM4-RRTM underestimates the SWN flux by 30 W/m^2 at the upper boundary of the domain (the equatorial region) where RegCM4-CCM rather displays overestimation. At the surface (Figure 2.16), RegCM4-RRTM overestimates SWN almost everywhere as for RegCM4-CCM, except over Southern Africa (Namibia and the west part of South Africa) in both seasons, but also over Eastern Africa including Mozambique, Tanzania and Madagascar, and there again over the equatorial Indian Ocean, especially in summer.

2.3.2.3.3.1.*b Longwave fluxes*

At the TOA (Figure 2.15), the clear-sky net LW flux (LWN) simulated by RegCM4-CCM seems to be larger in winter than in summer. As for clear-sky SWN, clear-sky LWN also appears to be larger over ocean than over land, with maximum values (up to 290 W/m^2) over the Atlantic Ocean in summer and over the Mozambique Channel in winter. The model shows smaller values over a region covering Congo and Zambia in summer, and over the eastern part of South Africa including Lesotho in both seasons. A minimum value of 260 W/m^2 is obtained over the latter in winter. There again, the all-sky radiation field is similar to that of the clear-sky one, with generally more LWN over the oceanic regions and more LWN during winter than summer. The minimum value of all-sky upward LWN is 175 W/m^2 over Zambia in winter, and the maximum is 280 W/m^2 over ocean for the two seasons. At the surface (Figure 2.16), LWN values simulated by RegCM4-CCM are larger over land, up to 140 W/m^2 in both seasons over the western coast of Southern Africa (Angola, Namibia, South Africa). In addition, larger values of LWN are simulated over the subtropical regions of the oceanic areas than over the equator. In contrast to LWN, downward LW is higher in summer than in winter, and decreases with increasing latitude with larger values over the equatorial region of the Indian Ocean. There are also larger values of downward LW over the eastern part of the African land areas (Congo, Tanzania, Zambia, Mozambique, Zimbabwe), and smaller values over the western part of Southern Africa (Namibia, South Africa).

Although RegCM4-RRTM also simulates more LWN over ocean than over land at the TOA (Figure 2.15) in both the clear- and all-sky conditions, some significant quantitative differences appear between RegCM4-CCM and RegCM4-RRTM. For instance, values of the clear-sky LWN are smaller for RegCM4-RRTM. In all-sky conditions, maximum values of LWN are located south of Madagascar for RegCM4-RRTM, while being located north of Madagascar for RegCM4-CCM. Radiation fluxes at the surface as produced by RegCM4-RRTM are similar to those of RegCM4-CCM (Figure 2.16), except that RegCM4-RRTM simulates much more LWN values and much lower downward LW values than RegCM4-CCM.

Compared to CERES observations (Figure 2.17), RegCM4-CCM tends to underestimate the TOA LWN flux in clear- and all-sky conditions in both seasons over most of the domain, expect in summer over the northwestern part of the domain including Angola, where RegCM4-CCM overestimates LWN by 10 W/m^2 in clear-sky conditions and by 20 W/m^2 in all-sky conditions. At the surface (Figure 2.18), the LW radiation parameters simulated by RegCM4-CCM show large negative biases compared to the observations, especially over ocean. In contrast, the model overestimates LWN by about 10 W/m^2 over land, except over the northwestern part of Southern Africa including Angola, where the model underestimates the flux by 10-20 W/m^2 for the two seasons but with a much more pronounced negative bias in summer. LW in summer displays similar biases to those of LWN compared to CERES, though the model exhibits negative biases over almost the whole domain in both seasons,

excluding the northern-east part of Africa and Madagascar in summer.

RegCM4-RRTM compared to CERES in Figure 2.17 shows a similar bias distribution for LWN in clear- and all-sky conditions at the TOA during summer and winter, except that RegCM4-RRTM shows negative biases, which are larger for the all-sky conditions than for the clear-sky condition. The largest negative bias is about 30 W/m^2 over South Africa in summer. The largest positive bias is about 6 W/m^2 over Angola in summer. At the surface (Figure 2.18), RegCM4-RRTM displays negative LWN biases over the whole domain, except over South Africa where positive biases (5 W/m^2) are found. RegCM4-RRTM also underestimates downward LW by 30 W/m^2 over the whole domain in summer and winter.

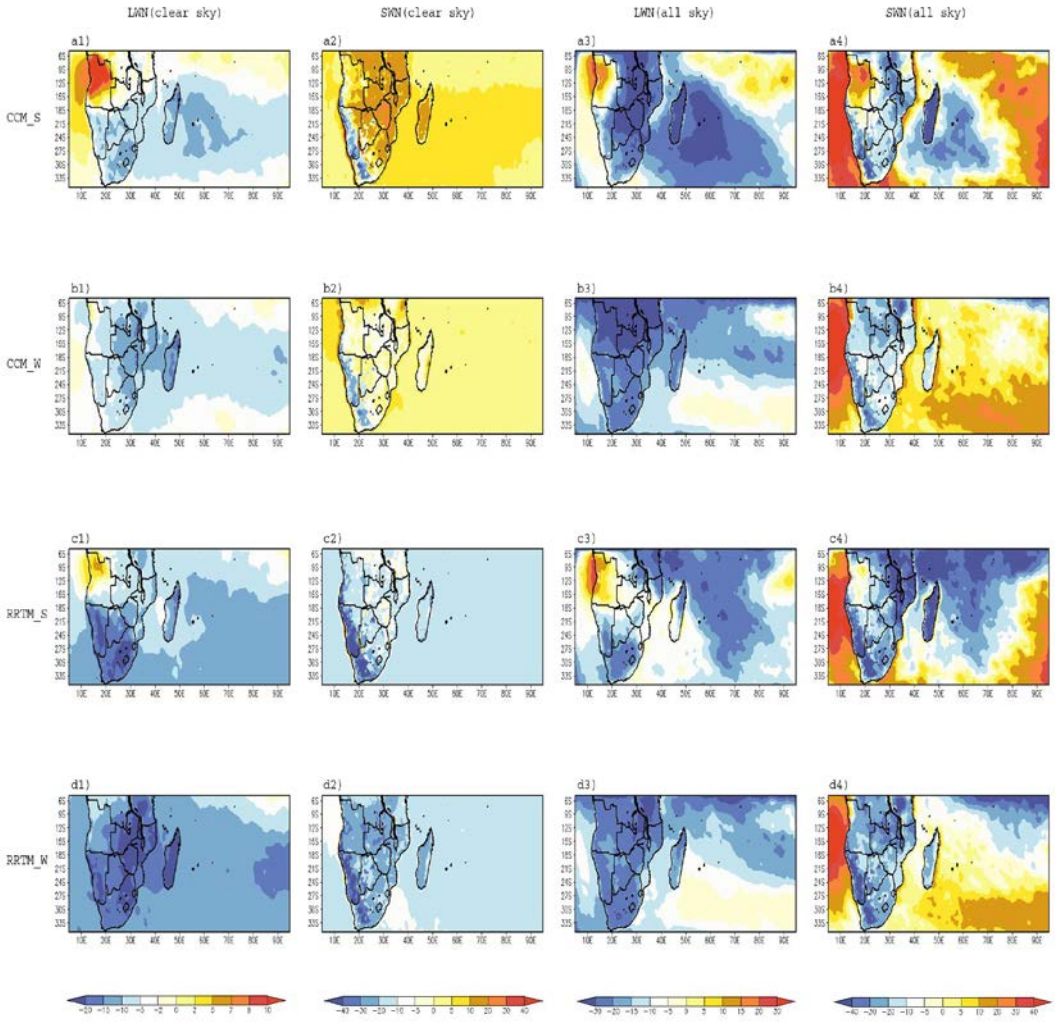

Figure 2.17 Seasonal radiation biases of RegCM4-CCM and RegCM4-RRTM with regard to CERES at 50km resolution at the top of atmosphere. CCM_S refers to summer mean of radiation fluxes as obtained with the CCM scheme; CCM_W refers to winter mean of radiation fluxes as obtained with the CCM scheme; similarly, RRTM_S and RRTM_W refer to summer mean and winter mean of radiation fluxes with RRTM; LWN and SWN refer to net LW and net SW fluxes separately.

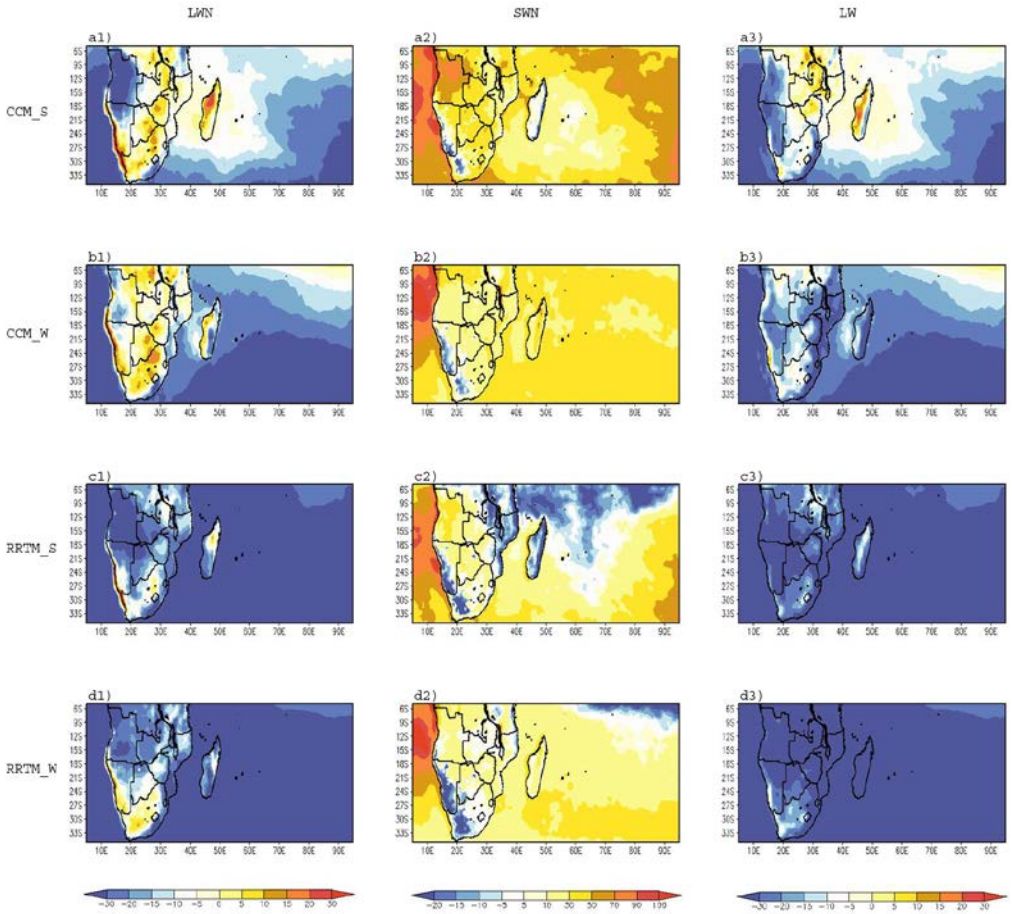

Figure 2.18 Same as in Figure 2.17 but for the surface.

2.3.2.3.3.2 Rainfall and surface air temperature

To further evaluate the performance of the two radiative schemes, precipitation and surface air temperature are examined to understand their relationship with the biases found in the radiation budget. As shown in Figure 2.19, RegCM4-CCM simulates maximum rainfall amounts over the land areas of Eastern Africa and Madagascar in summer, while RegCM4-RRTM simulates the highest rainfall amounts over the Indian Ocean. In winter, both RegCM4-CCM and RegCM4-RRTM yield more precipitation over the Indian Ocean, though RegCM4-CCM simulates more rainfall than RegCM4-RRTM in the two seasons. This result is not surprising, given the fact that RegCM4-CCM is generally warmer than RegCM4-RRTM. Comparing to the GPCP dataset (Figure 2.20), RegCM4-CCM apparently produces more precipitation than RegCM4-RRTM over the whole domain. RegCM4-RRTM has smaller absolute biases compared to the observations.

RegCM4-CCM and RegCM4-RRTM have similar spatial patterns for surface air temperature in summer and winter (Figure 2.19). RegCM4 simulations with these two radiative schemes capture the temperature maxima over the Mozambique Channel in summer, and the minima over South Africa in winter. As compared to ERA-Interim (Figure 2.20), simulations with the two radiative schemes tend to overestimate the

2-meter temperature over Angola (>2℃), and to underestimate it over the southern part of Mozambique, Botswana, South Africa and the eastern part of Namibia and the whole of Madagascar in summer. A warmer bias is produced by RegCM4-CCM over Tanzania and Mozambique in summer than by RegCM4-RRTM. However, RegCM4-RRTM produces a colder bias (2-5℃) in the same region in winter than RegCM4-CCM.

The region of cold biases in the two simulations seems to be co-located with that of the wet biases over the land areas, which emphasizes that precipitation plays an important role in affecting surface temperature. In addition, the spatial pattern in surface air temperature seems to be consistent with the surface downward LW flux (Figure 2.16). Although precipitation and surface air temperature are important climatic factors for radiation parameters in RegCM4, additional parameters should be examined such as the total cloud cover and the surface albedo.

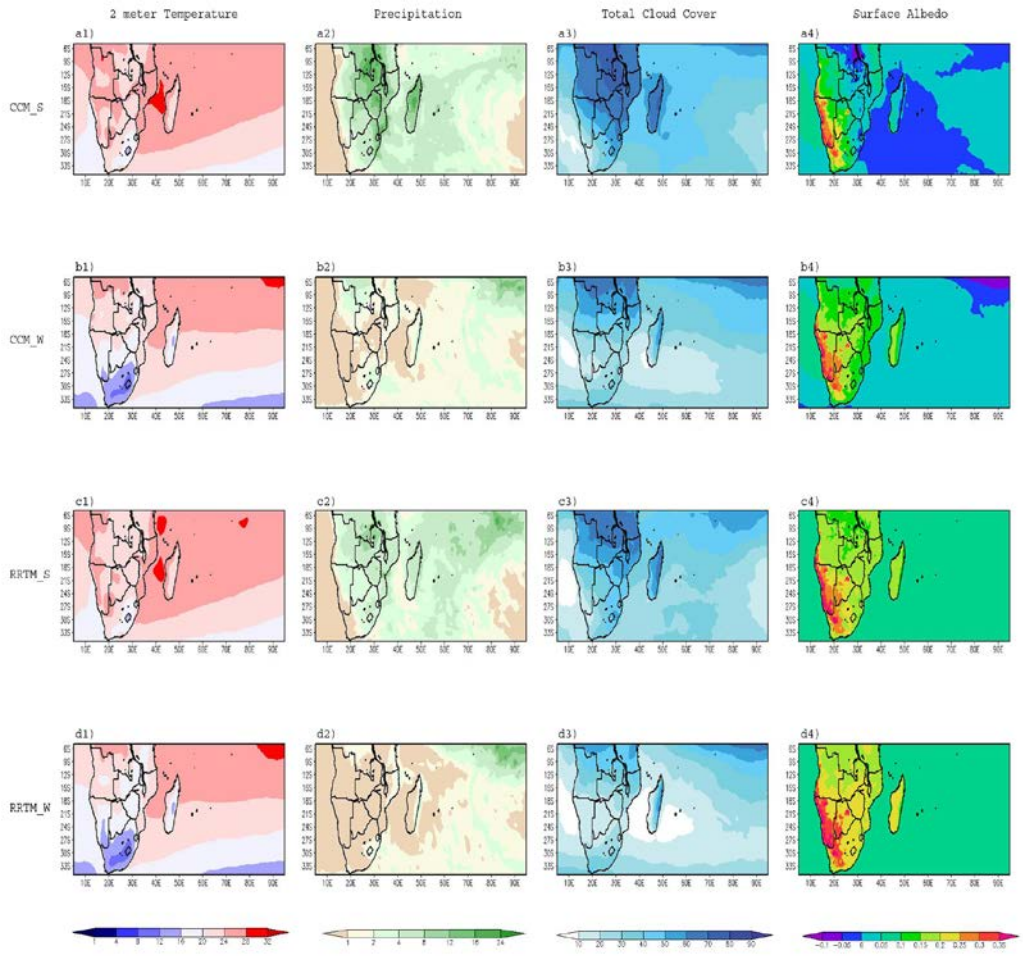

Figure 2.19 Seasonal mean 2 meter temperature (℃), precipitation (mm/day), total cloud cover (in %) and surface albedo simulated by RegCM4-CCM and RegCM4-RRTM at 50km. CCM_S refers to summer mean of radiation fluxes with the CCM scheme; CCM_W refers to winter mean of radiation fluxes with the CCM scheme; similarly, RRTM_S and RRTM_W refer to summer mean and winter mean of radiation fluxes with RRTM.

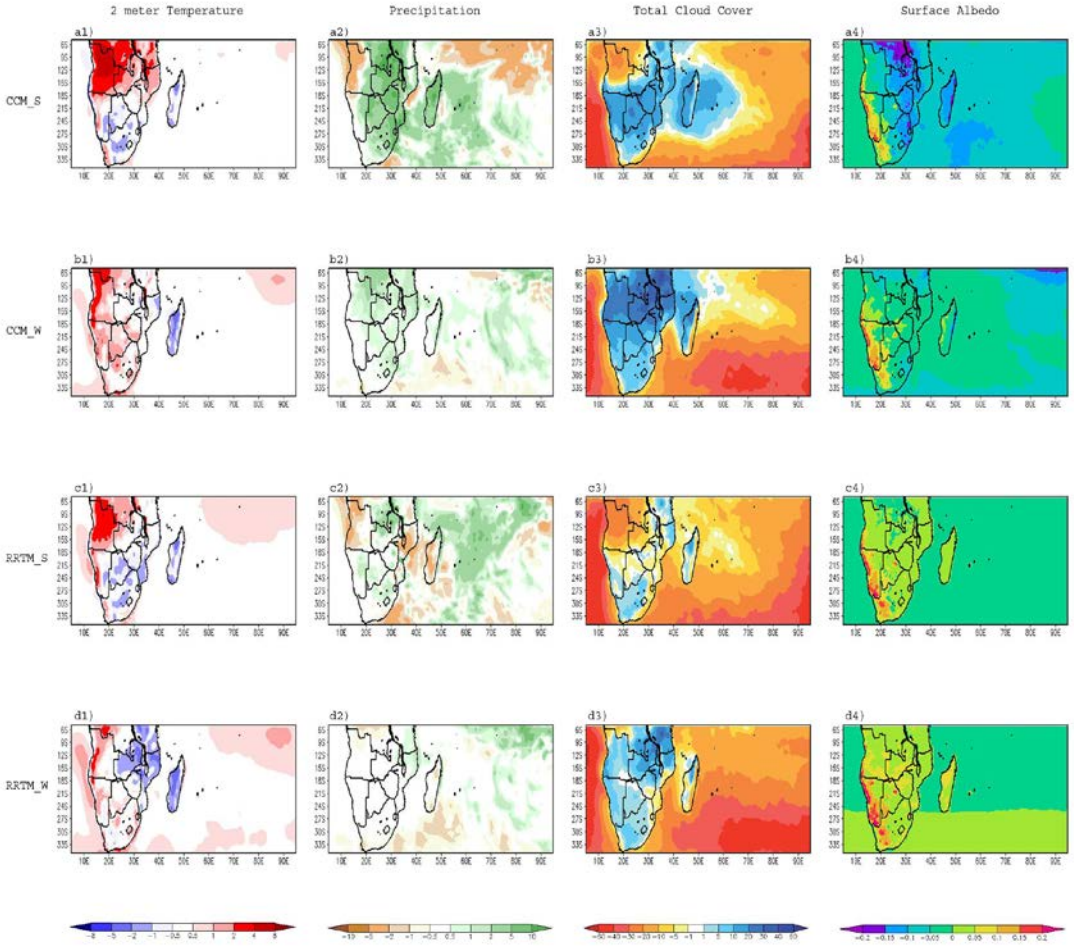

Figure 2.20 Seasonal differences for 2 meter temperature (℃), precipitation (mm/day), total cloud cover (in %) and surface albedo of RegCM4-CCM and RegCM4-RRTM with regard to ERA-Interim for the 2 meter temperature, the total cloud cover and the surface albedo, and to GPCP for precipitation. CCM_S refers to summer mean of radiation fluxes with the CCM scheme; CCM_W refers to winter mean of radiation fluxes with the CCM scheme; similarly, RRTM_S and RRTM_W refer to summer mean and winter mean of radiation fluxes with RRTM.

2.3.2.3.3.3 Total cloud cover and surface albedo

The cloud cover plays an important role in regulating the amount of energy that reaches the Earth from the Sun as well as the amount of energy that the Earth reflects and emits back into space. In Figure 2.19, RegCM4-CCM simulations yield more cloud cover in summer and winter than RegCM4-RRTM, which is consistent with the precipitation pattern, especially over the northern part of Africa land area and Madagascar. With regard to the surface radiation fluxes, RegCM4-CCM simulates more LWN (upward) and less LW (downward) over the western coast of Namibia and South Africa, where the cloud cover is reduced. Compared to RegCM4-CCM, RegCM4-RRTM simulates less cloud cover in the same area, resulting in even higher values of LWN and lower values of LW than in RegCM4-CCM. With regard to the total cloud cover from the ERA-Interim reanalyses, RegCM4-RRTM has positive bias

in summer and winter, but RegCM4-CCM has more positive bias than RegCM4-RRTM over the same region (Figure 2.20).

Surface albedo is the ratio of the reflected radiation from the surface to the incident radiation upon it. From Figure 2.19, it is clear that surface albedo is higher over the western part of Namibia and South Africa, which results in more upward shortwave surface radiation and less net shortwave flux (SWN in Figure 2.16). When comparing RegCM4-CCM and RegCM4-RRTM to ERA-Interim, the positive bias in surface albedo over this area seems to be consistent with the negative bias of SWN there (Figure 2.18). There is one thing needed to point out that: normally the surface albedo pattern in these two radiative schemes should be similar over the ocean, and the results in our other tests with new version of RegCM4 give almost the same behavior for surface albedo.

According to the analysis above, RegCM4 simulations with the two different radiative schemes, CCM and RRTM, generally capture the spatial pattern of surface radiation budget, with regard to the impact factor of the total cloud cover and the surface albedo.

2.3.2.3.3.4 Statistic analysis

The respective skills of all model experiments with the two radiation schemes at 50-km resolution in summer and winter, are compared and summarized using Taylor diagrams (Taylor 2001). These diagrams provide a way of graphically summarizing how closely a pattern (or a set of patterns) matches observations. The similarity between two patterns is quantified in terms of their correlation, their centered RMSD and the amplitude of their variations (represented by their Standard Deviation – SD). The simulated results which coincide with the observations best are those having the highest values of the correlation coefficient values and the lowest root mean square deviation. The statistics in this paper are computed over the spatial dimension, including the whole simulation domain for 2001 in summer and winter. LWN and SWN in all-sky conditions at the TOA and the surface in summer and winter are shown in Figure 2.21, and precipitation and the 2-meter temperature in Figure 2.22.

At the TOA, RegCM4-CCM and RegCM4-RRTM perform similarly in both summer and winter, though RegCM4-RRTM achieves lower RMSD and higher correlation values (0.8-0.9 in both seasons) for LWN according to CERES than RegCM4-CCM. In contrast, RegCM4-CCM performs lower RMSD for SWN than RegCM4-RRTM in summer and winter, achieving higher correlation in winter (0.9) than summer (0.7), as displayed in Figure 2.21.

At the surface, both RegCM4-CCM and RegCM4-RRTM have low correlation values (0.4-0.6) in summer and winter for LWN, but for SWN, the two radiative schemes achieve higher correlation with CERES, around 0.6-0.7 in summer and 0.7-0.9 in winter. In addition, RegCM4-CCM has lower RMSD than RegCM4-RRTM with CERES in both seasons, which means that the CCM scheme gives better performance.

Considering the precipitation and the 2-meter temperature for analyzing the radiation fluxes, RegCM4-CCM and RegCM4-RRTM both agree well with GPCP for precipitation, with SD close to 0 and high correlation especially in winter, though RegCM4-RRTM achieves higher correlation (0.79 in summer up to 0.92 in winter) than RegCM4-CCM (0.61 in summer up to 0.87 in winter) in both seasons. According to ERA-Interim dataset for the 2-meter temperature, RegCM4-RRTM has higher correlation (>0.9) and lower RMSD (<1.5 ℃) than RegCM4-CCM in summer. In winter, RegCM4-CCM and RegCM4-RRTM agree well with each other, and have high correlation with the ERA-Interim dataset (～0.95), and low RMSD (～1.25).

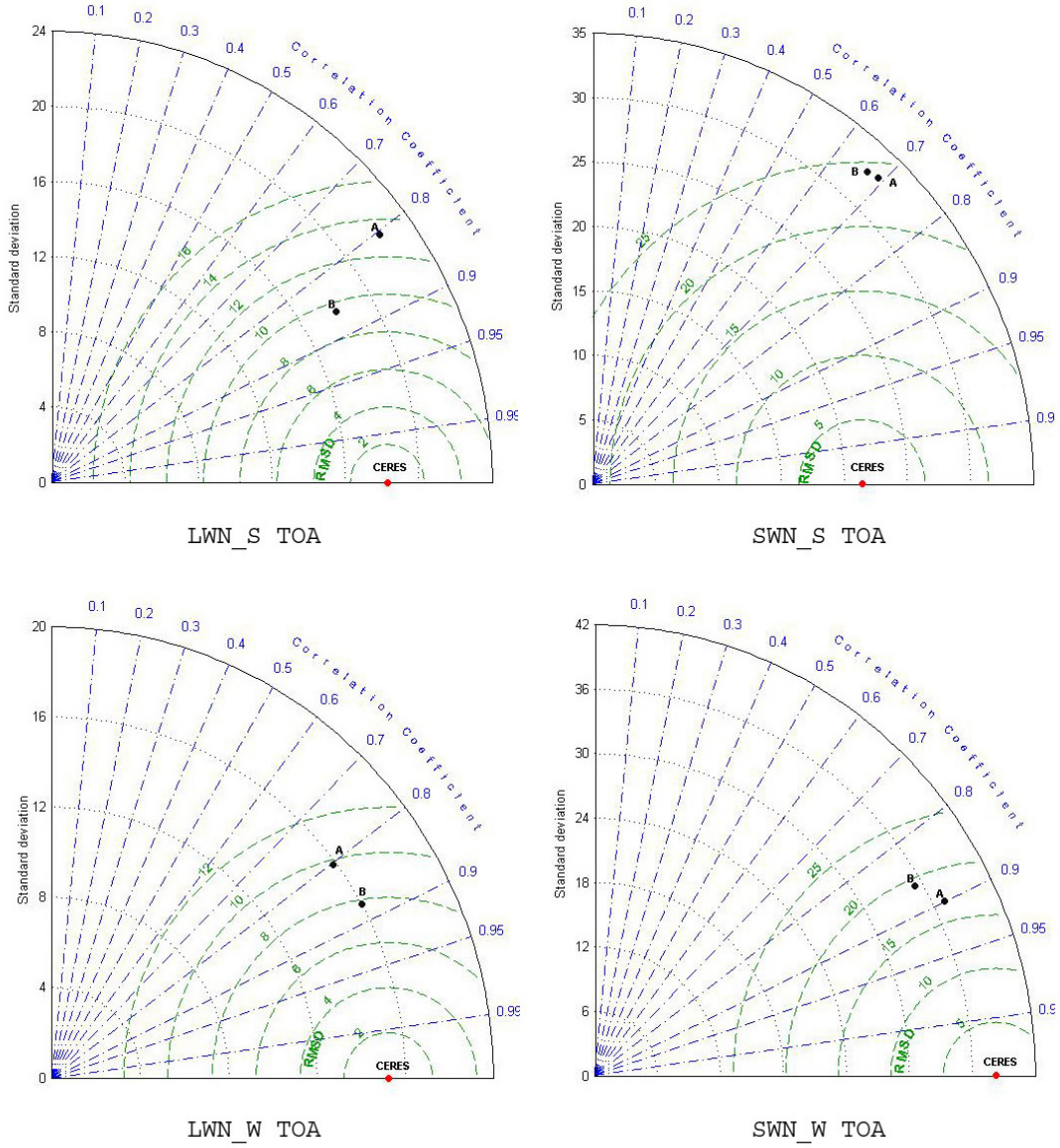

Figure 2.21a Taylor diagram showing simulated LW and SW radiation spatial correlation coefficient, root mean square deviation (RMSD) and standard deviation (SD) calculated with regard to CERES datasets for summer and winter at TOA (A: RegCM4-CCM, B: RegCM4-RRTM; LWN_S and SWN_S refer to net LW and SW fluxes in summer; LWN_W and SWN_W refer to net LW and SW fluxes in winter).

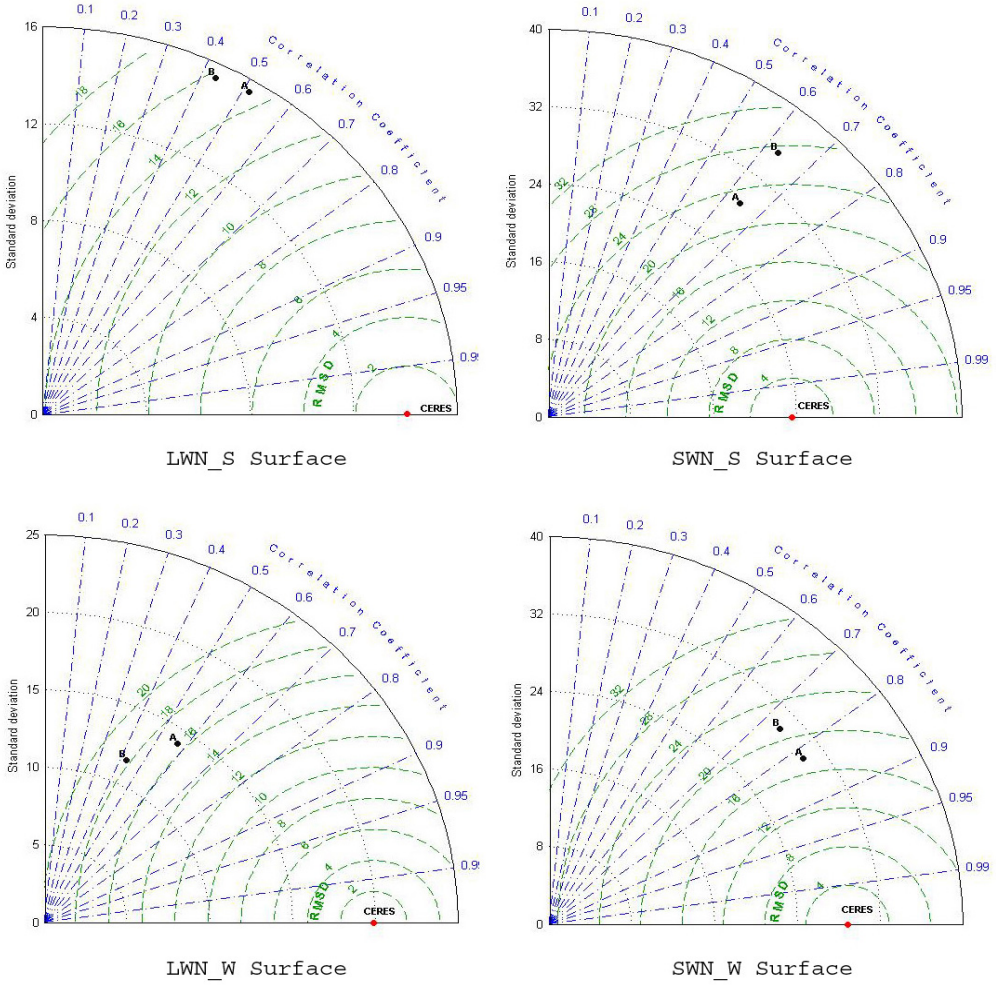

Figure 2.21b Taylor diagram showing simulated LW and SW radiation spatial correlation coefficient, root mean square deviation (RMSD) and standard deviation (SD) calculated with regard to CERES datasets for summer and winter at the surface (A: RegCM4-CCM, B: RegCM4-RRTM; LWN_S and SWN_S refer to net LW and SW fluxes in summer; LWN_W and SWN_W refer to net LW and SW fluxes in winter).

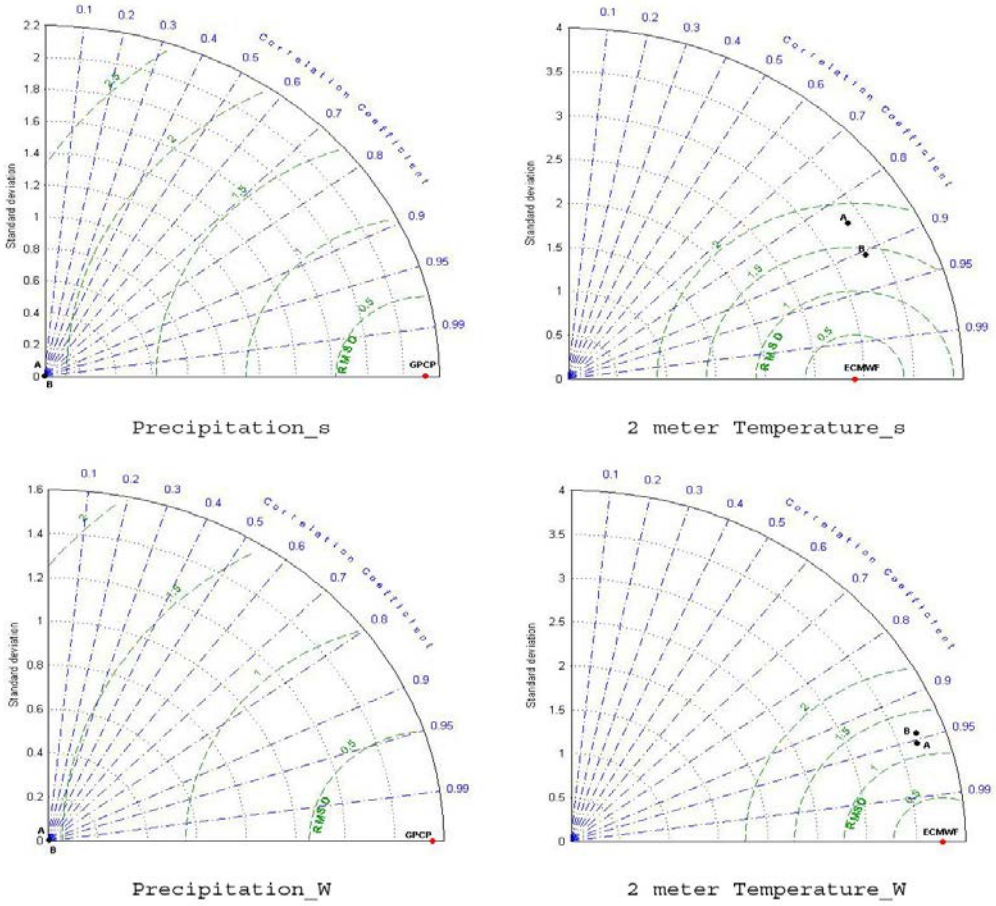

Figure 2.22 Taylor diagram showing precipitation and 2-meter temperature spatial correlation coefficient, root mean square deviation and standard deviation calculated with regard to GPCP (precipitation) and ERA-Interim (2-m temperature) datasets for summer and winter (A: RegCM4-CCM, B: RegCM4-RRTM; Precipitation_S and 2 meter Temperature_S refer to precipitation and temperature in summer; Precipitation_W and 2 meter Temperature_W refer to precipitation and temperature in winter).

In general, RegCM4 with CCM radiative scheme seems to give better performance for the radiation parameters and related variables over the SWIO domain than RegCM4 with RRTM scheme at 50-km resolution for the two seasons.

2.3.2.3.4 Convective scheme test

In this part, the model's biases, averaged over the summer period (November to April) for various radiative parameters with regards to different convection schemes are shown in Figure 2.23. The results for the winter period (May to October) are similar to the summer in general, and are not shown here. The average model biases for precipitation and the temperature at 2 meters, are shown in Figure 2.24.

LWN (clear/all Sky) TOA have a bipolar structure for all schemes with positive values

in the sub-equatorial region, and negative in areas south of 20° S. Grell (Grell_A and Grell_F) and Emanuel convection schemes tend to produce contrasting effects: the model clearly overestimates (underestimates) more LWN (all sky) TOA flux in the sub-equatorial region (subtropical) with a bias of 30 W/m^2 (-30 W/m^2) over large areas than the CERES data. Mixed convection schemes (Grell_Emanuel and Emanuel_Grell) can mitigate these contrasts.

LW Surface has different structures depending on the schemes. There is positive bias over the Indian Ocean and negative bias over southern African with the Grell convection scheme (Grell_A and Grell_F), and obvious negative bias for the Emanuel scheme over almost the whole area. The mixed schemes reproduce the bias over the areas in which the Grell scheme and the Emanuel scheme are enabled. For the Tiedtke scheme, reduced positive bias area is noticed in the southeast Indian Ocean. For LWN Surface, biases on oceanic regions are similar to those for the LW surface flux. For all the schemes, positive bias is found over the most eastern regions of land surfaces (on the east of Africa, Western Cape Town to Mozambique, and on the eastern side of Madagascar).

The model overestimates largely SWN Surface (50W/m^2 beyond the boundary of the domain for all schemes, but also the western boundary of the domain patterns for Emanuel and Grell_Emanuel). The model underestimates slightly more solar flux incident on the surface than the CERES data, especially on a reduced southwestern seaboard of South Africa for all schemas, and over a wider area covering the Indian Ocean patterns with the convective schemes: Grell (Grell_A and Grell_F), Emanuel_Grell and Tiedtke. Biases shown for SWN (all sky) TOA are rather positive on the African continent and the western Indian Ocean, and negative elsewhere. It should be noted that the simulations produced in this work do not include aerosol forcing, which would induce an increased atmospheric absorption and scattering, reducing the solar flux incident on the surface. Data archiving every 6 hours for parameters strongly influenced by the path of the sun, could also partly explain the strong biases identified here.

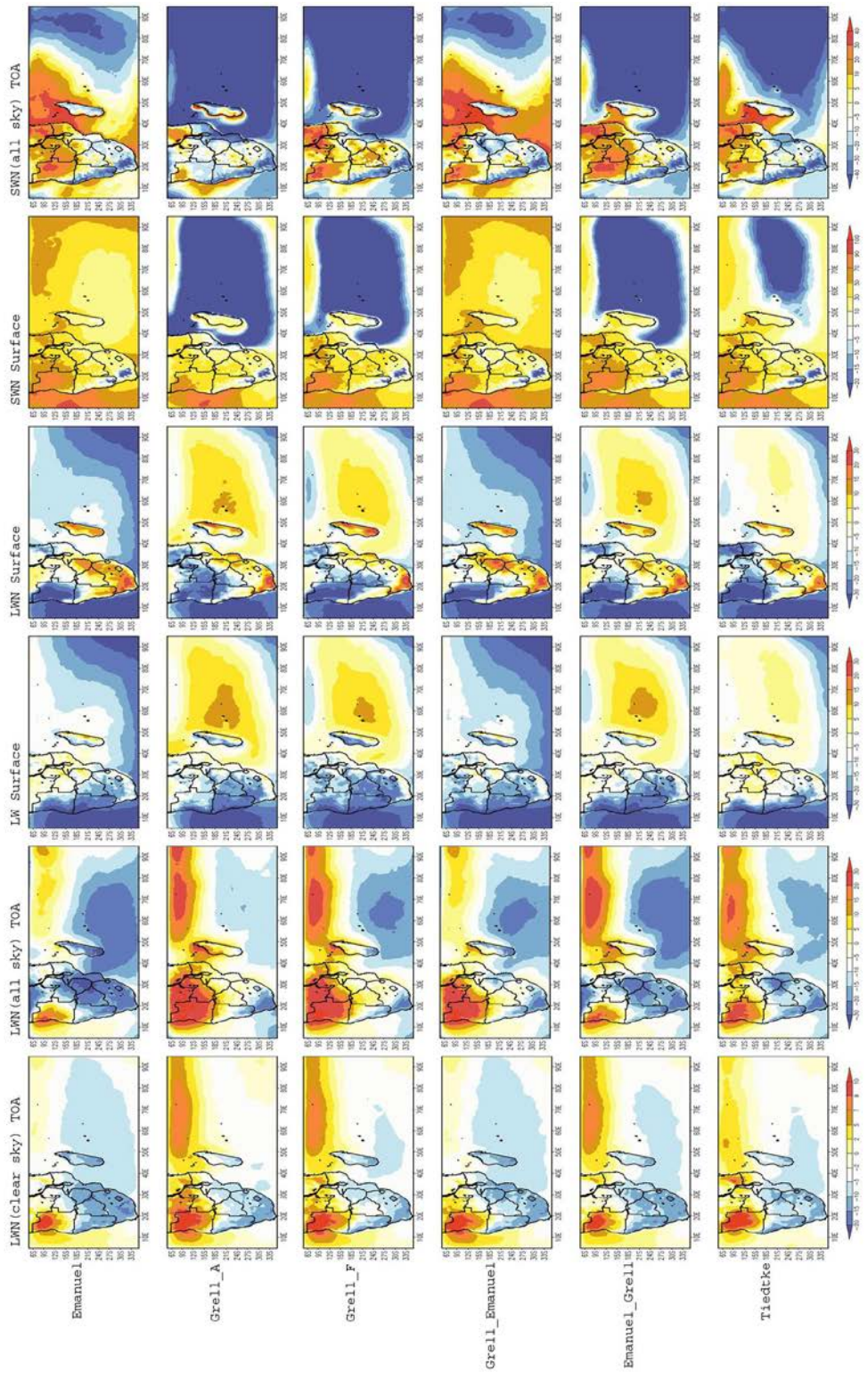

Figure 2.23: Bias of RegCM4 compared to CERES (W/m^2) in summer for different convection schemes tested (row) and long-wave and shortwave radiative fluxes at the surface and at the top of atmosphere (column). LW: long-wave flux; LWN: net long-wave flux; SWN: net shortwave flux.

To demonstrate the different performance of these convective schemes, precipitation and surface air temperature are examined to capture the relationship between them with radiation budget. Bias for the surface air temperature (2 meter Temperature as shown in Figure 2.24) can be related to LWN Surface fluxes: cold (hot) biases are located in the areas where the model overestimates (underestimates) the LWN surface fluxes. Most cold biases are found over the Indian Ocean with the convective schemes: Grell (Grell_A and Grell_F) and Emanuel_Grell, which produce similar spatial bias patterns with negative biases for SWN Surface. The model simulates much more surface air temperature (bias values > 8°C) over the Angola area for the Tiedtke scheme. All schemes underestimate rainfall (Figure 2.24) in the north-eastern Indian Ocean, particularly Grell_A, Grell_F and Emanuel_Grell. All schemes except Grell_A overestimate rainfall over land area (excluding the Angola and eastern part of Tanzania and Mozambique) and underestimate precipitation on the Atlantic and Indian facades in the latitude band 5°-20°S.

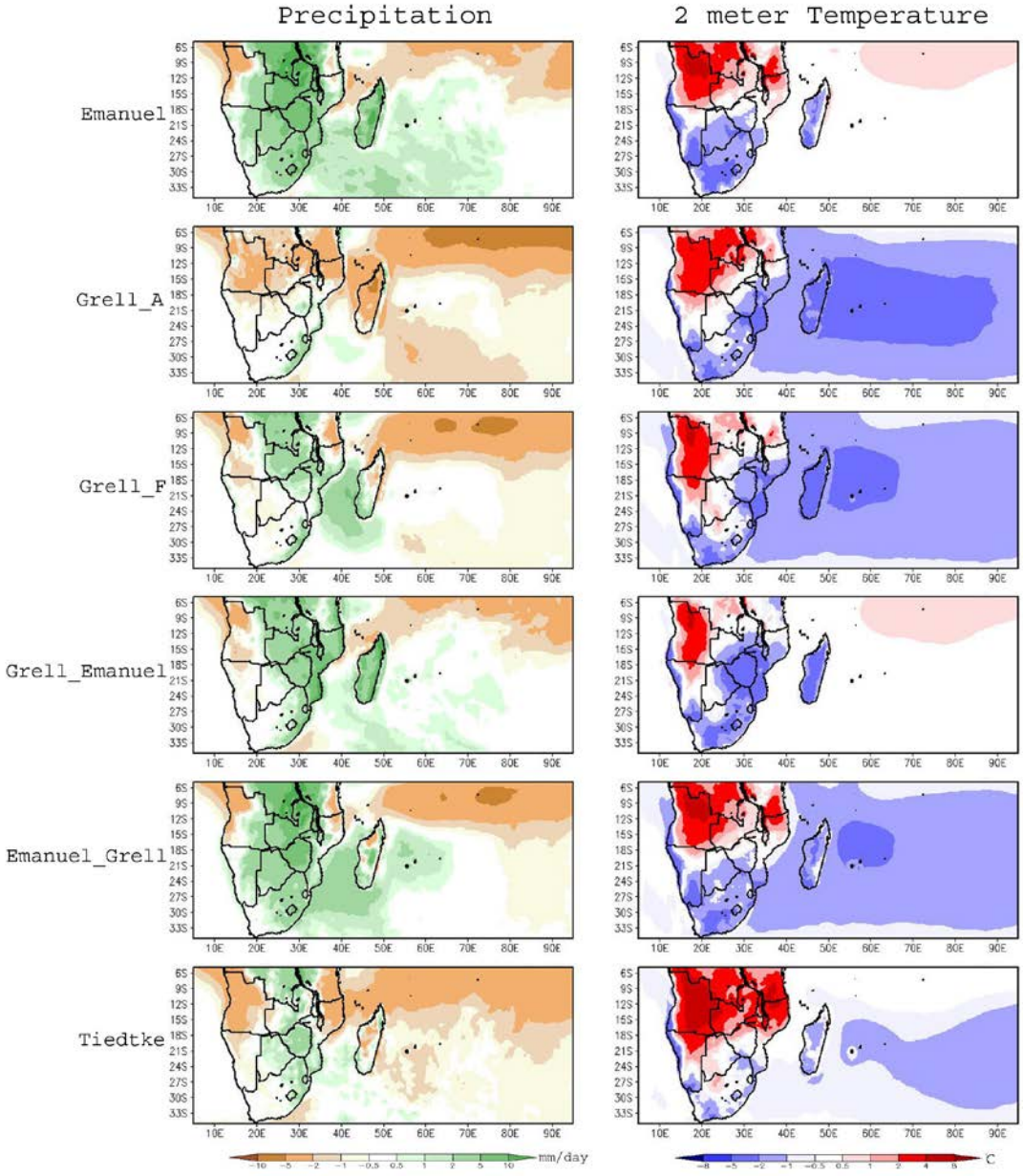

Figure 2.24: Bias of RegCM compared to GPCP for precipitation (mm/day), and reanalyses ERA-Interim for the temperature (°C) in summer for different convection schemes tested.

The respective skills of all model experiments with the 6 convective schemes at 50km resolution in summer, are compared and summarized using Taylor diagrams (Taylor, 2001). The statistics in this paper are computed over the spatial dimension including the whole simulation domain for 10 years in summer. LWN and SWN in all-sky conditions at the TOA and the surface in summer and winter are shown in Figure 2.27, and precipitation and the 2-meter temperature are shown in Figure 2.25 and 2.26, respectively.

Taylor diagrams in Figures 2.25 and 2.26 summarize the ability of the RegCM4 model to reproduce the spatial structures with regard to the observation, of, respectively, the 2-meter temperature and the precipitation for different convection schemes. From these 2 figures, they show that for both parameters: 2-meter temperature and precipitation, the scheme Grell_Emanuel is the one giving the highest values of the correlation coefficient (r slightly above 0.75 for precipitation r≈0.95 for 2-meter temperature). For this mixed scheme, the values of the root mean square deviation between simulation and observation for precipitation are close to the standard deviation values for the observations (SD = 2.1-2.2 mm/day; RMSD = 2.0 mm/day). For the 2-meter temperature, however, the model with the same mixed convective scheme (Grell_Emanuel), has a lower spatial variability than the observations (SD = 2.8-2.9°C; observation SD > RMSD = 1.0°C).

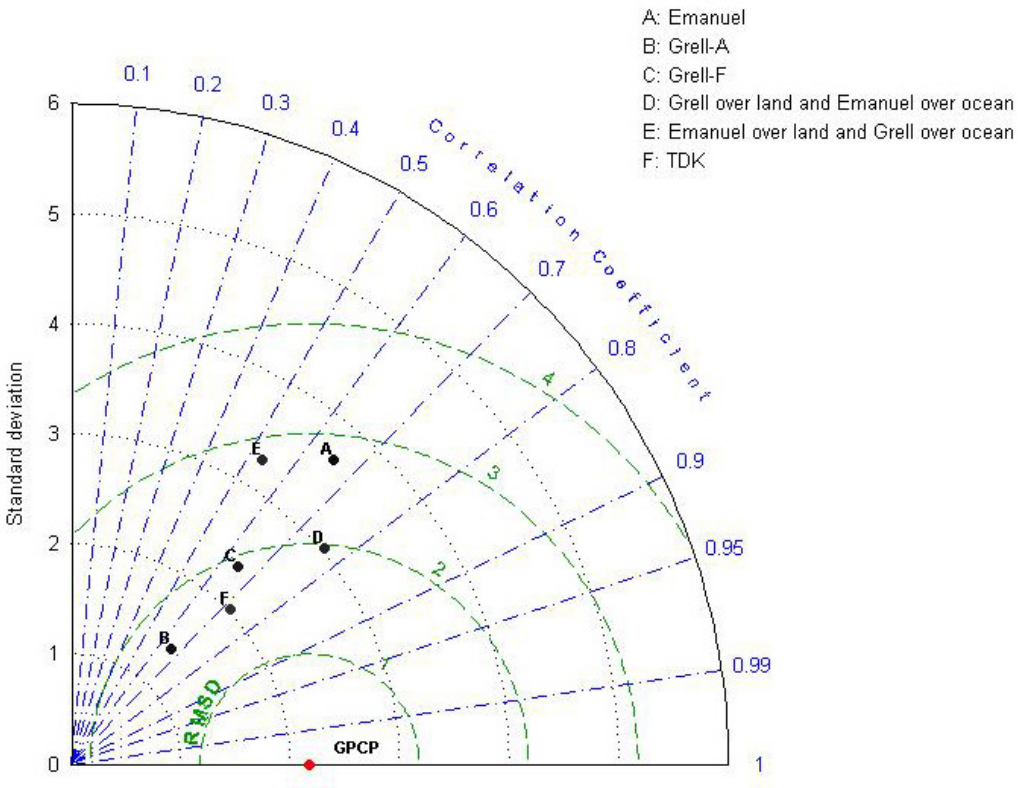

Figure 2.25: Taylor diagram showing simulated austral-summer 2000-2009 precipitation spatial correlation coefficient r, root mean square deviation (RMSD, mm/day), and stand deviation (SD, mm/day) calculated with regards to GPCP data.

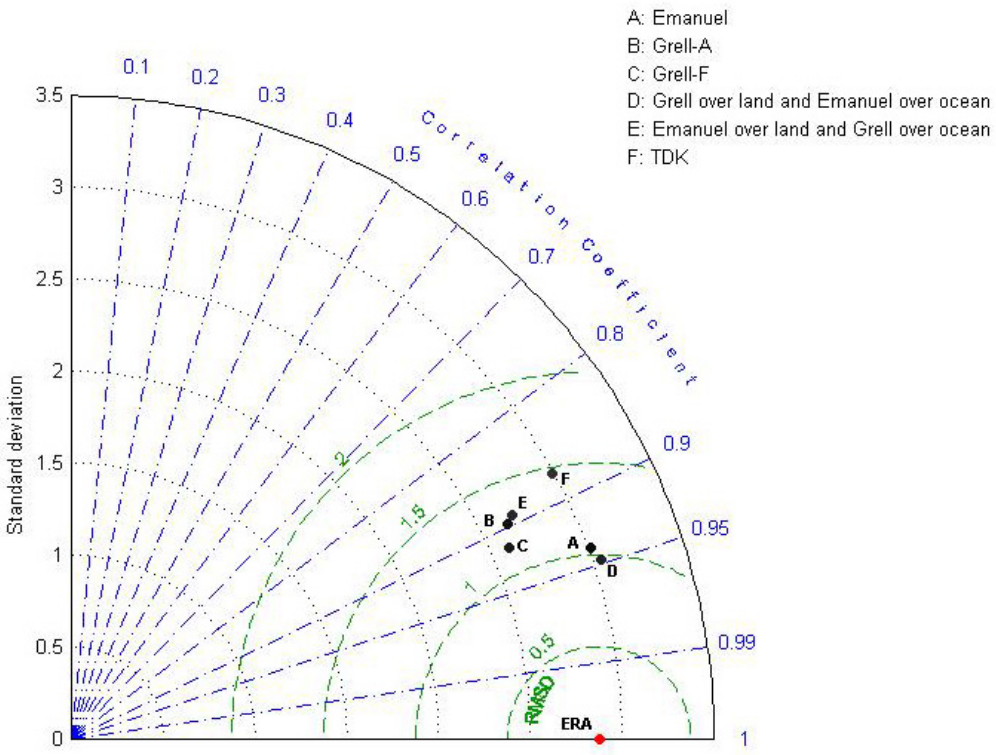

Figure 2.26: Taylor diagram showing simulated austral-summer 2000-2009 temperature spatial correlation coefficient r, root mean square deviation (RMSD, °C), and stand deviation (SD, °C) calculated with regards to ERA-Interim reanalysis data.

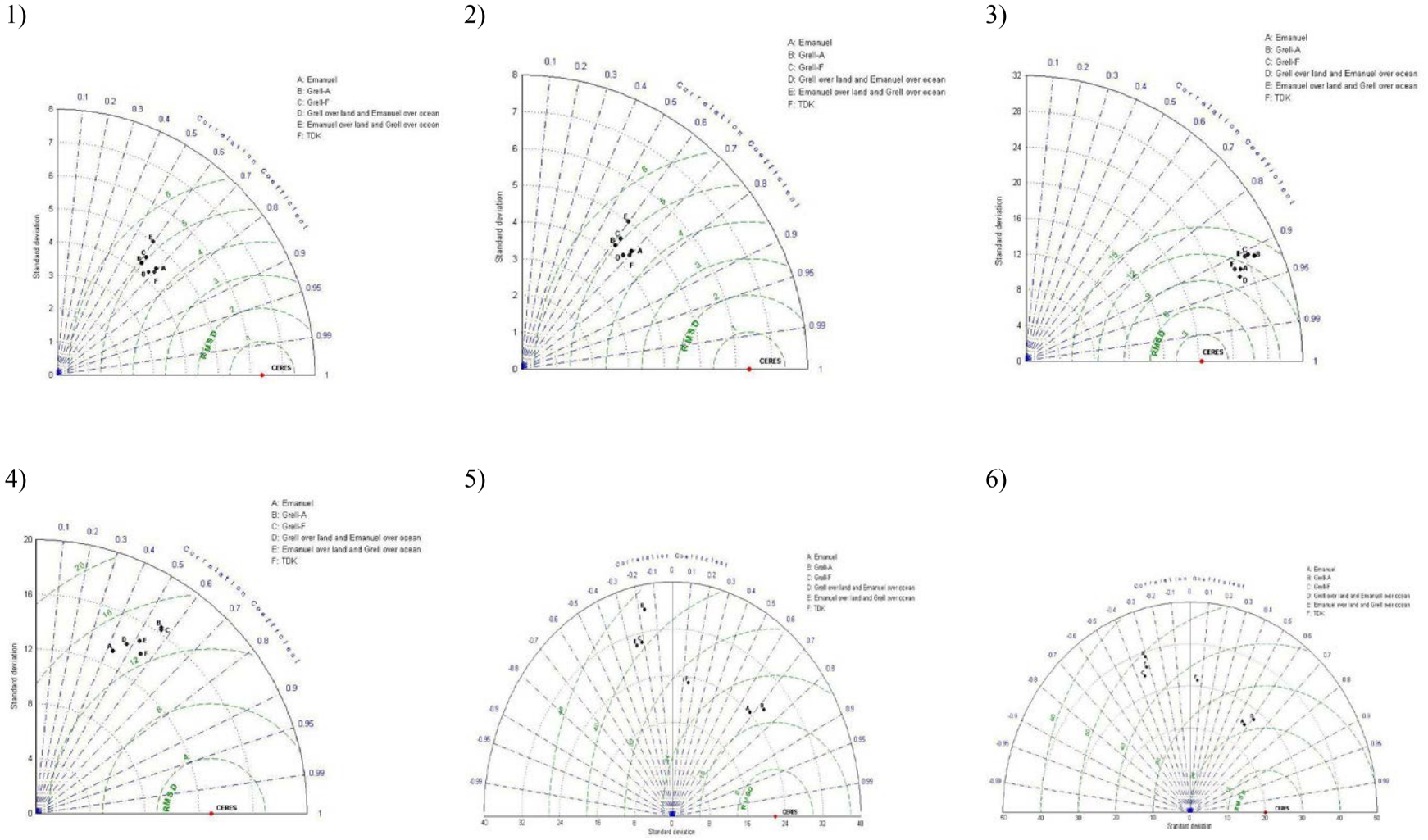

Figure 2.27 : Taylor diagram showing simulated austral-summer 2000-2009 1)LWN (clear sky) TOA; 2)LWN (all sky) TOA; 3)LW Surface; 4)LWN Surface; 5)SWN Surface; 6)SWN (all sky) TOA spatial correlation coefficient r, root mean square deviation (RMSD, W/m2), and standard deviation (SD, W/m^2) calculated with regards to CERES data.

Figure 2.27 presents statistic summary for long-wave and short-wave radiation fluxes according to observations at the TOA and the surface. The Tiedtke scheme gives the highest correlation coefficient (r=0.7) and the lowest root mean square deviation (RMSD≈4.5 W/m^2) for LWN (clear sky) TOA (r=0.7, RMSD≈4.5 W/m^2) and LWN Surface (r≈0.57, RMSD≈13 W/m^2), but at the same time, the mixed scheme Grell_Emanuel showed the similar patterns for these two parameters (r≈0.68, RMSD ≈4.6 W/m^2 for LWN (clear sky) TOA; r≈0.48, RMSD≈14.2 W/m^2 for LWN Surface). The mixed scheme Grell_Emanuel for other radiation parameters simulated in this study, LWN(all sky) TOA, LW Surface, SWN Surface and SWN (all sky) TOA, all show best coincidence with the observation.

Based on the above analysis, it appears that the mixed scheme Grell_Emanuel gives the best performance with the RegCM4 simulation setting over the SWIO domain in general. This scheme generally captures the spatial pattern of surface radiation budget, with regard to the impact factor of the precipitation and 2 meter temperature. The model could perform simulations with Grell_Emanuel scheme for SSR analysis over SWIO region

2.3.3 WRF3.5

2.3.3.1 Description

The Weather Research and Forecasting (WRF) Model is a next-generation mesoscale numerical weather prediction system designed to serve both atmospheric research and operational forecasting needs. It features two dynamical cores, a data assimilation system, and a software architecture facilitating parallel computation and system extensibility. The model serves a wide range of meteorological applications across scales from tens of meters to thousands of kilometers.

WRF allows to generate atmospheric simulations based on real data (observations, analyses) or idealized conditions. WRF offers operational forecasting a flexible and computationally-efficient platform, while providing advances in physics, numeric, and data assimilation contributed by developers in the broader research community. The current applications include meteorological investigations, real-time NWP, idealized atmospheric simulations, data assimilation studies and development, coupling with other earth system models, modeling and model use instruction and training. As the simulations are performed using the WRF/Advanced Research (ARW), version 3 (WRF hereafter, Skamarock et al. 2008), the main physics parameters of this version are described. The WRF physics options fall into 5 categories: (1) micro-physics, (2) cumulus parameterization, (3) planetary boundary layer (PBL), (4) land-surface model, and (5) radiation. In the following, all the options are listed out and only the options used for the simulations are introduced in detail.

The physical package used in this study is the same as in Morel et al. (2014), which includes the Kain-Fritsch scheme for atmospheric convection (Kain 2004) using the

trigger function developed by Ma and Tan (2009), the WSM 6-class graupel scheme for cloud microphysics (Hong & Lim 2006) and the Yonsei University parameterization of the Planetary Boundary Layer (PBL; Hong et al. 2006). Radiative transfer is parameterized with the RRTM (Mlawer et al. 1997) for long waves and Dudhia (1989) scheme for short waves. Over the continents WRF is coupled with the 4-layer NOAH land surface model (Chen & Dudhia 2001a,b). Except for elevation data, which are from the Shuttle Radar Topography Mission (SRTM), all other surface data are taken from United States Geological Survey (USGS) database, which describes a 24-category land-use index based on climatological averages and a 17 category United Nations Food and Agriculture Organization soil data.

2.3.3.1.1 Microphysics

Microphysics includes explicitly resolved water vapor, cloud, and precipitation processes. In all the WRF simulations for the analysis of spatial variability performed in this work, the WRF single-moment microphysics scheme 6-class (WSM6) is used as the microphysics scheme. WSM scheme follows Hong et al. (2004) including ice sedimentation and other new ice-phase parameterizations. A major difference from other approaches is that a diagnostic relation is used for ice number concentration that is based on ice mass content rather than temperature. WSM6 scheme is extended to include graupel and its associated processes. Some of the graupel-related terms follow Lin et al. (1983), but its ice-phase behavior is much different due to the changes of Hong et al. (2004). A new method for representing mixed-phase particle fall speeds for the snow and graupel particles by assigning a single fall speed to both that is weighted by the mixing ratios, and applying that fall speed to both sedimentation and accretion processes is introduced (Dudhia et al. 2008). WSM6 works much differently on cloud-resolving grids compared to WSM3 and WSM5, and it is the most suitable for cloud-resolving grids, considering the efficiency and theoretical backgrounds (Hong & Lim 2006).

2.3.3.1.2 Cumulus parameterization

The modified version of the Kain-Fritsch scheme (Kain 2004) is chosen as the convective scheme in all the WRF simulations here. It is based on Kain and Fritsch (1990; 1993), but has been modified based on testing within the Eta model. Differing from the original KF scheme, the modified one has the changes as follows: 1) a minimum entrainment rate is imposed to suppress widespread convection in marginally unstable, relatively dry environments; 2) shallow convection is allowed for any updraft that does not reach minimum cloud depth for precipitating clouds and this minimum depth varies as a function of cloud-base temperature; 3) the entrainment rate is allowed to vary as a function of low-level convergence; 4) source layer is the entire 150-200mb deep layer just above cloud base; mass flux is specified as a fraction of updraft mass flux at cloud base; detrainment is specified to occur in updraft source layer and below.

2.3.3.1.3 Planetary Boundary Layer

WRF contains 12 PBL scheme options, and the Yonsei University (YSU) PBL (Hong et al. 2006) is set in the simulations. The YSU PBL is the next generation of the Medium Range Forecast (MRF) PBL, also using the countergradient terms to represent fluxes due to non-local gradients. This adds to the MRF PBL (Hong & Pan 1996) an explicit treatment of the entrainment layer at the PBL top. The entrainment is made proportional to the surface buoyancy flux in line with results from studies with large-eddy models (Noh et al. 2003). The PBL top is defined using a critical bulk Richardson number of zero (compared to 0.5 in the MRF PBL), so is effectively dependent on the buoyancy profile, in which the PBL top is defined at the maximum entrainment layer (compared to the layer at which the diffusivity becomes zero). A smaller magnitude of the counter-gradient mixing in the YSU PBL produces a well-mixed boundary-layer profile, whereas there is a pronounced over-stable structure in the upper part of the mixed layer in the case of the MRF PBL. Details are available in Hong et al. (2006), including the analysis of the interaction between the boundary layer and precipitation physics. In version 3.0, an enhanced stable boundary-layer diffusion algorithm (Hong 2007) is also devised that allows deeper mixing in windier conditions.

2.3.3.1.4 Land-Surface Model

There is no horizontal interaction between neighboring points in the LSM, so it can be regarded as a one-dimensional column model for each WRF land grid-point, and many LSMs can be run in a stand-alone mode. In the WRF simulations, we use the 5-layer thermal diffusion option as the LSM. This simple LSM is based on the MM5 5-layer soil temperature model. Layers are 1,2,4,8 and 16 cm thick. Below these layers, the temperature is fixed at a deep-layer average. The energy budget includes radiation, sensible, and latent heat flux. It also allows for a snow-cover flag, but the snow cover is fixed in time. Soil moisture is also fixed with a landuse- and season-dependent constant value, and there are no explicit vegetation effects.

2.3.3.1.5 Atmospheric Radiation

All the radiation schemes in WRF currently are column (one-dimensional) schemes, so each column is treated independently, and the fluxes correspond to those in infinite horizontally uniform planes, which is a good approximation if the vertical thickness of the model layers is much less than the horizontal grid length. This assumption would become less accurate at high horizontal resolution. The radiation schemes include two parts: longwave schemes and shortwave schemes.

In the WRF simulations, RRTM is chosen for the treatment of the LW and Dudhia scheme for that of the SW. Rapid Radiative Transfer Model (RRTM) Longwave scheme has been described previously in the section dedicated to RegCM4. Dudhia SW scheme is base on Dudhia (1989) and is taken from the MM5 model. It has a simple downward integration of solar flux, accounting for clear-air scattering, water vapor absorption (Lacis & Hansen 1974), and cloud albedo and absorption. It uses

look-up tables for clouds from Stephens (1978). In Version 3, the scheme has an option to account for terrain slope and shadowing effects on the surface solar flux.

2.3.3.2 Experimental design

WRF simulations are carried out over two contrasted austral summer seasons (Morel et al. 2014): November through April 2000-2001 and 2004-2005 as shown in Table 2.3. Integrations are initialized on the 15th of October for each year, allowing for a 15-day-long spin-up period. Data are archived from October 15th to April 30th. 5 ensemble simulations are performed for these two summer seasons over three domains (Figure 2.3). Lateral forcings are provided every 6h by ERA-Interim reanalyses (Simmons et al. 2007; Dee et al. 2011) at a 1.5° horizontal resolution and 19 pressure levels. SST fields are prescribed every 24h after a linear interpolation of monthly ERA-Interim SST.

Table 2.3 Summary of the simulations performed with WRF3.5

Time Period	Start Date
15/10/2000-31/04/2001	**2000-10-15 00:00:00**
	2000-10-15 06:00:00
	2000-10-15 12:00:00
	2000-10-15 18:00:00
	2000-10-16 00:00:00
15/10/2004-31/04/2005	**2004-10-15 00:00:00**
	2004-10-15 06:00:00
	2004-10-15 12:00:00
	2004-10-15 18:00:00
	2004-10-16 00:00:00

2.4 Clustering method

The ascending hierarchical clustering (AHC) has been successfully applied to rainfall data (Ramos 2001; Tennant & Hewitson 2002; Mufioz-Diaz & Rodrigo 2004, 2006; Crétat et al. 2012, 2014). Here it is also used to classify the SSR over domain 3 (Figure 2.5). AHC creates a nested sequence of partitions of the patterns from a dissimilarity matric, and proceeds by series of fusions of the n objects into groups (Gong & Richman 1995). It produces a series of partitions of the data, P_n, P_{n-1}, …, P_1. In this study, P_n consists of 905 single object clusters, and P_1 consists of a single group containing the 905 days (5 ensemble simulations x 181 days for a summer period, 2000-2001 or 2004-2005). At each stage, the AHC regroups the two clusters that are closest according to a Euclidean distance metrics. Consider a matric X containing 905 days × 19600 (140×140) grid points in domain 3 of WRF, then the Euclidean distance between entities X_{day1} and X_{day2} is given by:

$$d_{day1,day2} = \sum_{i=1}^{19600} [(X_{day1} - X_{day2})'(X_{day1} - X_{day2})]^{1/2} \quad \text{(Eq. 2.5)}$$

The Ward's method (Ward, 1963) is used for merging two clusters including more

than one day, or a cluster of one day with a cluster including more than one day. It minimizes the within-group variance at each stage of merging and optimizes an objective statistic. At each step, the intra-cluster sum of squares is minimized over all partitions obtainable by merging two clusters from the previous step. If C_K and C_L are two clusters that are merged to form cluster C_M, the combinatorial formula that defines the distance between the new cluster and another cluster C_J is:

$$d_{J,M} = \frac{(n_J + n_K)d_{JK} + (n_J + n_L)d_{JL} - n_J d_{KL}}{n_J + n_M} \qquad \text{(Eq. 2.6)}$$

where n_J, n_K, n_L and n_M are the number of objects in clusters J, K, L and M, and d_{JK}, d_{JL}, d_{KL} are the distances between JK, JL and KL, respectively (Ramos 2001). In general, the AHC procedure is able to obtain partitions of SSR patterns based on objective distance computations.

Chapter 3

Temporal Variability of Surface Solar Radiation over the South West Indian Ocean

There have been several studies on inter-annual variability of solar radiation over different areas, but with almost not similar researches over the SWIO and Reunion Island. Our objective here is to study surface solar radiation at different temporal and spatial scales over Reunion. This chapter focuses on the analysis of SSR temporal variability by considering the effects of modes of large-scale climate variability known to affect the cloud cover over the region. Indeed, we check whether RegCM4 forced by the large-scale in which such modes of variability are present, is able to reproduce them as well: does it suppress or amplify the effects at regional scales? In that regard, we first analyze input data to RegCM4 (U, V, T, RH) taken from the reanalyses, and then corresponding RegCM4 outputs from the ensemble simulations over the SWIO area along with SSR.

3.1 Inter-annual variability of surface solar radiation

Rising interest in large-scale solar energy applications requires reliable information on the solar resource and its stability. Knowledge of the variability of incoming solar radiation is required for estimates of the worst-case scenarios in solar power project development. The inter-annual variability of SSR at a site is an important factor to assess the uncertainty of energy yielded from solar plants, such as flat-plate photovoltaic. Inter-annual variability is both determined by the climatic and topographic conditions. Reliable long-term radiation measurements are rare, especially in areas that are interesting for solar energy applications. Lohmann et al. (2006) studied long-term variability of solar direct (DNI) and global radiation (GHI) derived from the International Satellite Cloud Climatology Project (ISCCP) data for 18 years in comparison with some reanalyses data (ERA40 & NCEP/NCAP), which showed that inter-annual variability for DNI is very strong and sometimes exceeds 20% of the annual mean. Changes in GHI are much smaller and less significant. Perdigão et al. (2011) examined the variability and trends of surface radiation over the Iberian Peninsula using ERA40 reanalysis data from the European Centre for Medium-Range Weather Forecasts (ECMWF) and analyzed the relation between the inter-annual variability of solar radiation and the cloud cover over the same area. Christian and Stephen (2011) did a research on the spatial and temporal variability of the solar resource in the United States. They calculated the coefficient of variation (COV) from eight annual values of the National Solar Radiation Database (NSRDB) to analyze the inter-annual variability of DNI and global tilt irradiance (GTI).

Here we first relate the input data to RegCM4 (U, V, T, RH) taken from the reanalyses, and then the corresponding output data from RegCM4 to several climate indices. Finally, we study the SSR with regard to those parameters (U, V, T, RH).

3.1.1 Mean state of surface solar variability

Figure 3.1 presents the ensemble seasonal mean of RegCM4 SSR during NDJF 1999-2008 over the SWIO. It shows the average spatial distribution of SSR. There are more SSR over the Indian Ocean and the west part of Southern Africa. ENSO and IOD’s impacts on that are examined in this section.

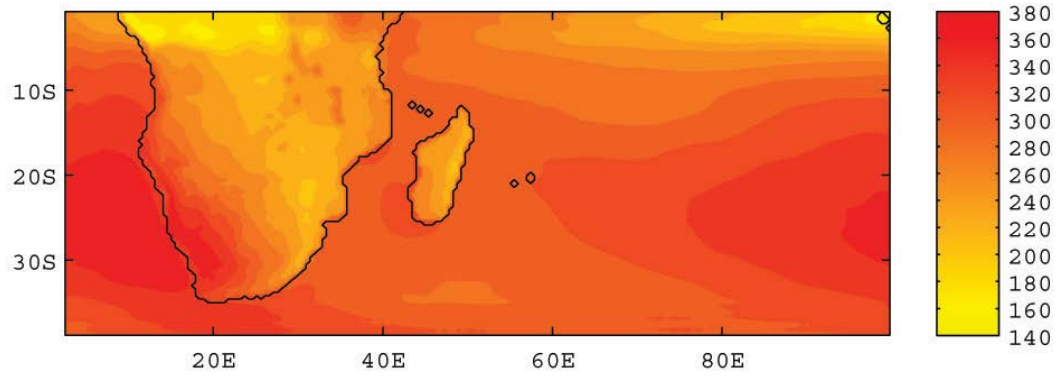

Figure 3.1 SSR ensemble mean in RegCM4 during austral summer NDJF 1999-2008 over the SWIO (W/m^2).

3.1.2 ENSO

The MEI is first correlated with the ERA-Interim reanalyses data and then with RegCM4 outputs.

Correlation coefficients between the MEI and U, V, RH, T at 5 different pressure levels covering the whole troposphere (1000hPa, 850hPa, 700hPa, 500hPa, 300hPa) are calculated based on monthly data for each of the 10 austral summers (Nov to Feb) over the period 1999-2008. Figures 3.2, 3.3, 3.4 and 3.5 display correlation coefficients between the MEI and those parameters with the 95% significance level indicated as the black contour for ERA_Interim data. For RegCM4 outputs, correlation coefficients are calculated for each member separately, and averaged together for the comparison to ERA-Interim. Based on the analysis of the impact from atmospheric circulation, correlation coefficients between the MEI and surface solar radiation are calculated (Figure 3.6).

3.1.2.1 Zonal and Meridional wind components

Meridional flow is the atmospheric flow in which north south component (V), and the Zonal flow is the east west (U). ERA-Interim U has high significant negative correlation with the MEI (~-0.75) over the subequatorial Indian Ocean at all studied pressure levels (1000hPa to 300hPa; Figure 3.2a). In addition, there is positive correlation over South Africa, south Atlantic Ocean and south Indian Ocean at 1000hPa, 850hPa and 700hPa. Moreover, negative correlation patterns are shown over the Angola, Zambia and Zimbabwe at 1000hPa, 850hPa and 700hPa. At 500hPa, negative correlation is mainly found over the subequatorial and northern parts of southern Africa. At 300hPa, significant positive correlation (~0.5) is found over Madagascar, the Mozambique Channel and the subtropical Indian Ocean, with the exception of the subequatorial area where there is negative correlations.

With regard to ERA-Interim, RegCM4 results (Figure 3.2b) presents similar correlation patterns in the lower and higher troposphere, though the patches of negative correlation cover larger areas. The subequatorial Indian Ocean and northern of southern Africa (excluding South Africa) are all covered by negative correlation values at all pressure levels and the degree of negative correlation coefficient is a little larger (~0.1) than for ERA-Interim (Figure 3.2b).

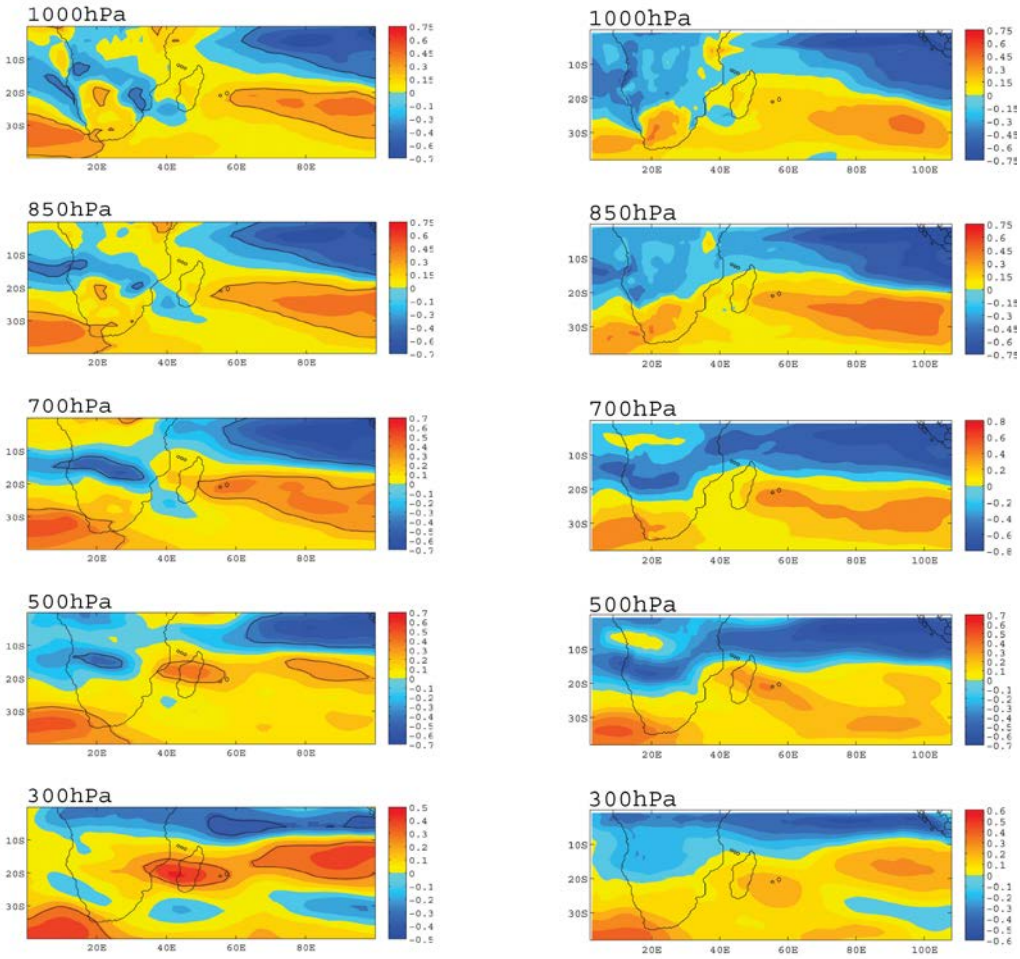

Figure 3.2 Correlation coefficients between (a) ERA-Interim (left) and (b) RegCM4 (right) U at 5 pressure levels, and the MEI during Nov to Feb 1999-2008. For ERA-Interim, correlations that are significant at 95% level are plotted as black contours (left).

ERA-Interim V shows high negative correlation with the MEI over the subtropical Indian Ocean and the south Atlantic Ocean at 1000hPa, 850hPa and 700hPa. There are high positive correlation with the MEI over the Mozambique and Mozambique Channel at 1000hPa, 850hPa and 700hPa (Figure 3.3a). At 500hPa, there is significant positive correlation value with the MEI (~0.5) over Mozambique, Zimbabwe, part of northern South Africa and the Mozambique Channel at 500hPa, and over the subtropical Indian Ocean at 300hPa.

Correlation of RegCM4 V with the MEI has a similar behavior (Figure 3.3b) with high negative (positive) correlation over the subtropical Indian Ocean and the south Atlantic Ocean (Mozambique and Mozambique Channel) at 1000hPa, 850hPa and 700hPa; negative values reach as much as -0.7. At 500hPa and 300hPa, the correlation pattern is similar to that from ERA-Interim, though with smaller values of the correlation coefficients.

At the low-pressure level, U and V of RegCM4 have larger correlation coefficient with the MEI. Both U and V of RegCM4 have spatial patterns of correlation with the MEI similar to those from ERA-Interim, which indicates RegCM4's ability to simulate the large-scale climate variability at the inter-annual time scales.

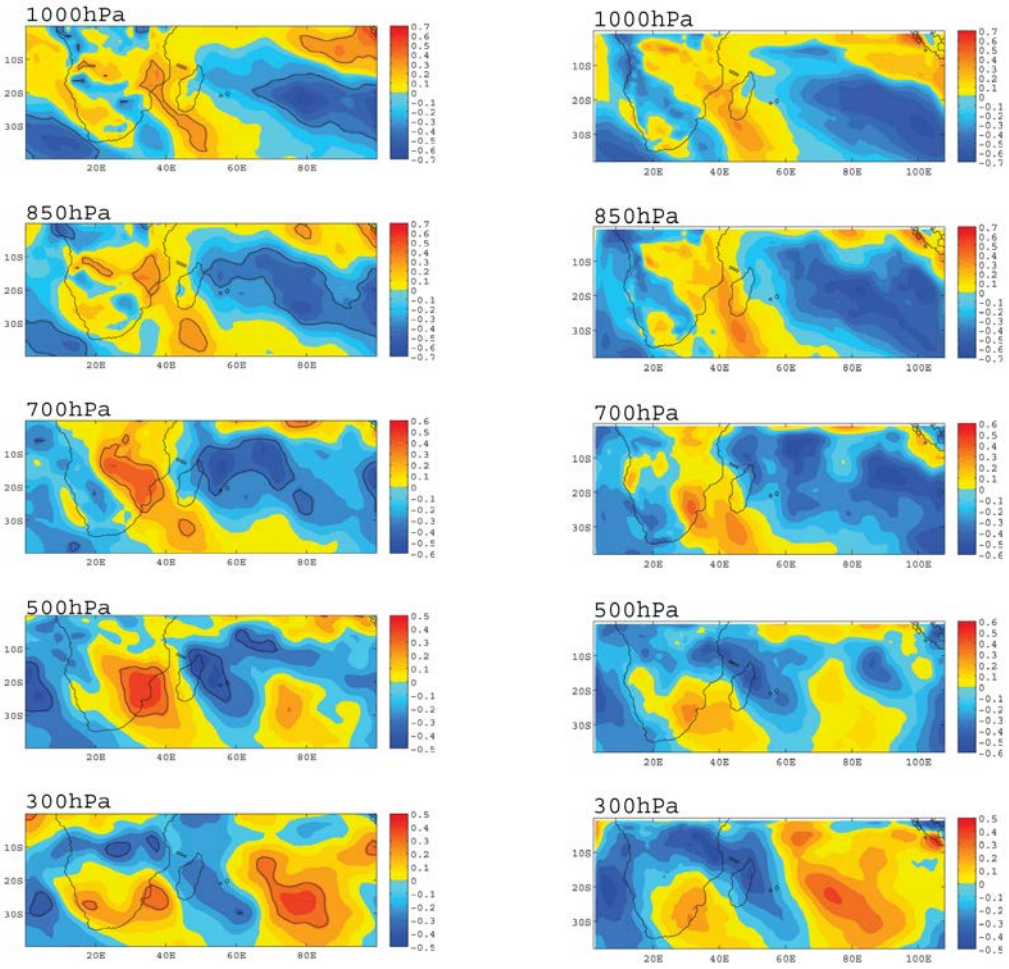

Figure 3.3 a) and b) Same as Figure 3.2 but for the meridional wind component V.

3.1.2.2 Air temperature

In Figure 3.4a, air temperature at mid to high troposphere (300hPa/500hPa) has high positive correlation (~0.7) with the MEI over the area (0°-10°S). At 1000hPa and 850hPa (low troposphere), there is significant correlation only over Mozambique, Zimbabwe, Zambia and Namibia for ERA-Interim data; elsewhere the correlation is not so big and obvious (<0.2). At 700hPa, the whole land area in the simulation

domain, including Africa and Madagascar, and the subequatorial Indian Ocean, is covered by positive correlation values.

RegCM4 gives similar spatial patterns of correlation between temperature and the MEI at each pressure level (Figure 3.4b). We find obvious positive correlation between T and the MEI over most of the domain, especially at low troposphere. Some differences with ERA-Interim appear over Angola at 1000hPa, 850hPa and 700hPa, where the correlation is negative in RegCM4 results and positive in ERA-Interim ones. In addition, there is a negative (positive) band pattern for ERA-Interim (RegCM4) T at 500hPa over Botswana and South Africa. However, the negative correlation is very small for both of these two datasets, most of the domain is covered by positive correlation coefficient value.

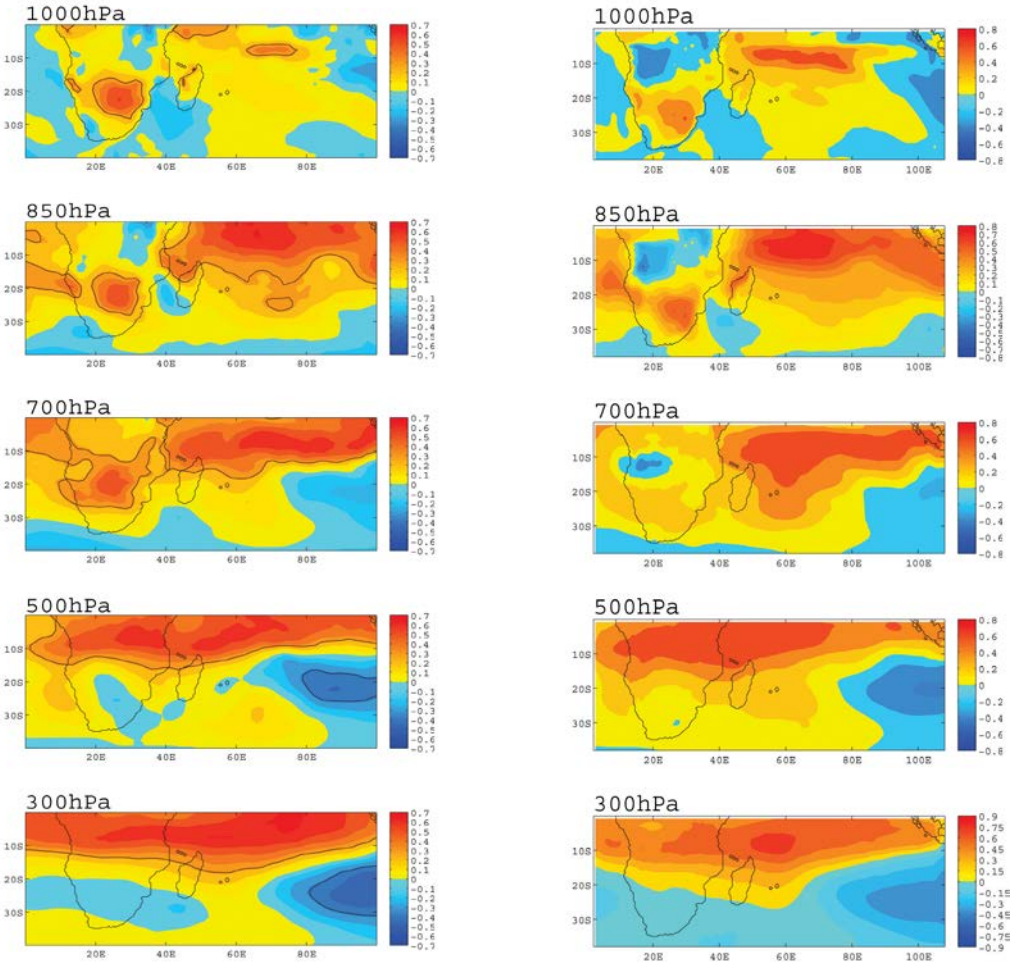

Figure 3.4 Same as Figure 3.3 but for air temperature T.

3.1.2.3 Relative humidity

In Figure 3.5a, ERA-Interim RH at 1000hPa (surface) displays high significant positive correlation with the MEI (up to 0.7) over the subequatorial and subtropical (0-30°S) Indian Ocean and Atlantic Ocean adjacent to the African land, and negative correlation over southern African, including Mozambique, Zimbabwe, Zambia,

Namibia, Botswana and South Africa; values can reach as much as -0.7 in some areas. At 850hPa (low troposphere), RH shows a negative correlation with the MEI over most of the domain with large significant negative values up to -0.7 over southern Mozambique, Zimbabwe, northern South Africa and eastern Indian Ocean, with the exception of the subequatorial (0-10°S) Indian Ocean, DR Congo and Tanzania where the correlation is positive. From 700hPa to 300hPa (mid to upper troposphere), the correlation patterns between RH and the MEI are similar, with positive (negative) values mainly over the Indian Ocean (southern Africa, the Mozambique Channel and the eastern part of the Indian Ocean). It seems as if the negative correlation coefficient patterns are slowly moving easterly from the high-pressure level (1000hPa) to the low-pressure level (300hPa).

In comparison to the results from ERA-Interim, the correlation coefficient values from the ensemble mean of the 5-member ensemble simulations by RegCM4 (Figure 3.5b) give almost the same patterns at each pressure level (1000hPa to 300hPa). Obvious positive and negative correlation of RH with the MEI, and negative correlation patterns moving easterly from the higher-pressure level (surface) to the lower-pressure level (high troposphere) are observed.

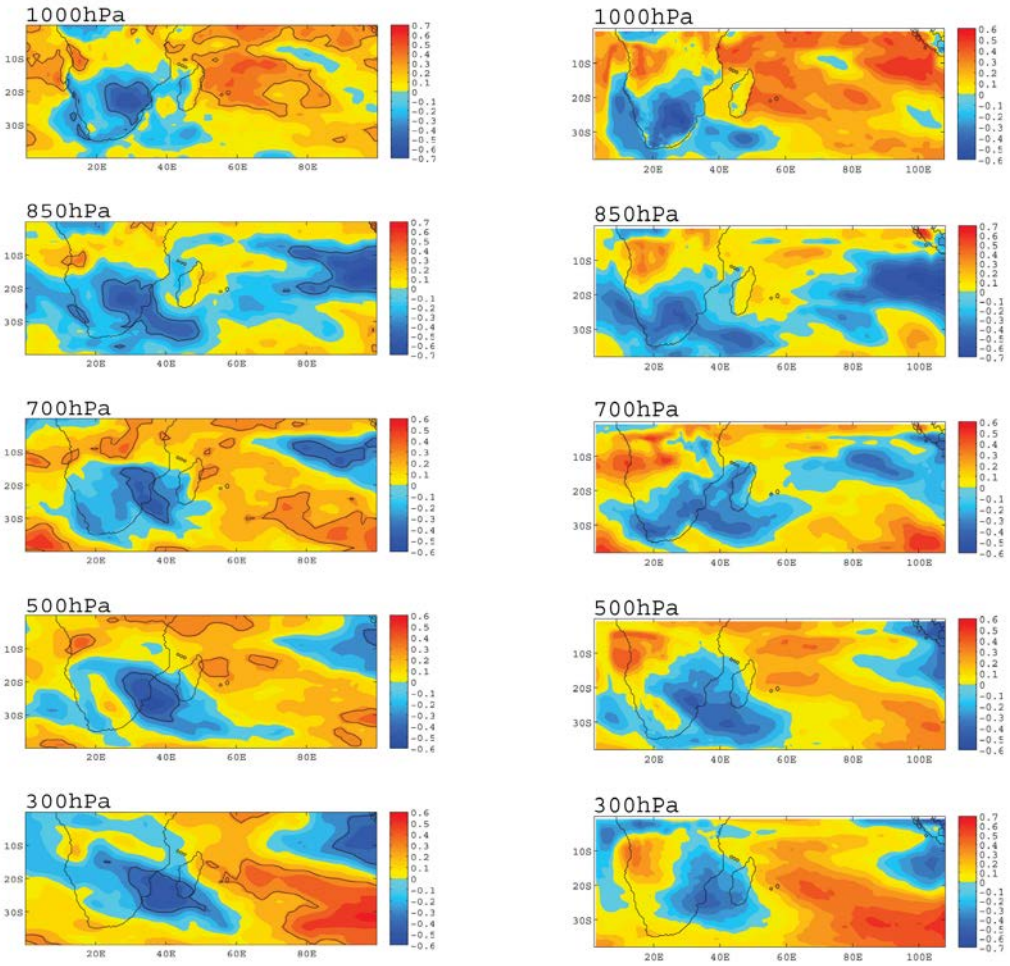

Figure 3.5 Correlation coefficients between (a) ERA-Interim and (b) RegCM4 RH at 5 pressure levels, and the MEI during Nov to Feb 1999-2008. As in Figure 3.2, for ERA-Interim, correlations that are significant at 95% level are plotted as black contours.

3.1.2.4 Surface solar radiation

ERA-Interim SSR has high positive correlation coefficients with the MEI (~0.6) over Mozambique, Zimbabwe and the northeastern part of South Africa, as well as above the eastern part of the Indian Ocean, and over some part of the southern Atlantic Ocean adjacent to the African continent Southern Africa (Figure 3.6). Regions of high negative correlation coefficients (-0.6) are located mainly over northern Angola, southern DR Congo and the subequatorial part of the Indian Ocean (0°-10°S). SSR data from RegCM4 (bottom panel) gives a similar correlation pattern compared to ERA-Interim except over northern Namibia (Mozambique, Tanzania and Malawi), where RegCM4 displays negative (positive) correlation coefficients in contrast to ERA-Interim. This result indicates that the model forced by the large scales, doesn't suppress or amplify the relationship between the inter-annual variability and SSR at regional scales.

The correlation patterns should be related to the mean distribution of SSR over the

10-year period, with areas of positive (negative) correlation coefficients being coincident with those receiving more (less) SSR (Figure 3.1).

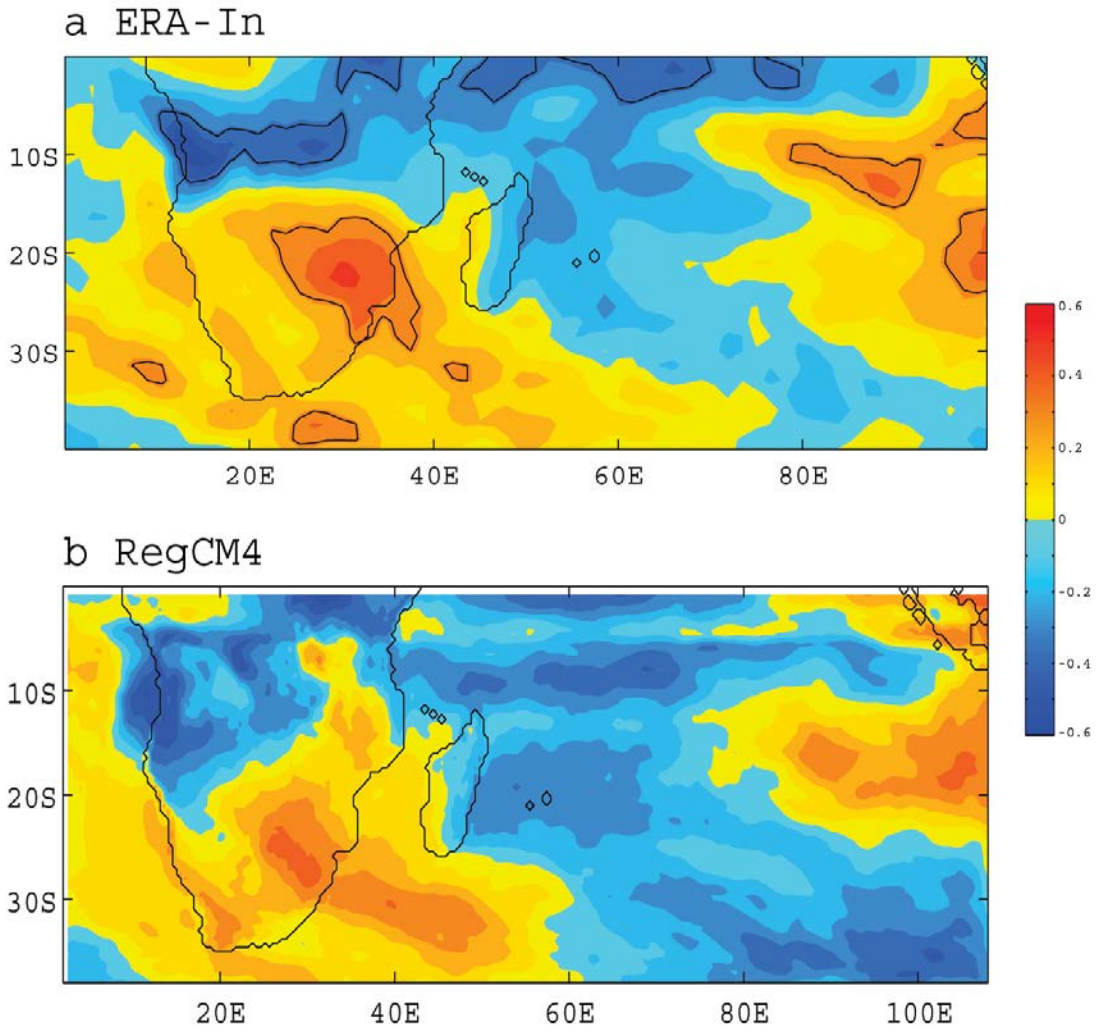

Figure 3.6 Correlation coefficients between SSR and the MEI during Nov to Feb 1999-2008 as computed from (a) ERA-Interim and (b) RegCM4 (mean of the values calculated for each simulation separately). For ERA-Interim, correlations that are significant at the 95% level are also plotted as black contours.

With regard to SSR mean state for the 10-year period, the negative (positive) correlation coefficient values are found over areas with more (less) SSR, for both ERA-Interim and RegCM4.

The results here are consistent with ENSO-like conditions. The positive correlation between V and the MEI over the Mozambique Channel is associated with southerly wind over the Mozambique Channel, while the negative correlation between V and the MEI over the eastern part of Southern Africa is associated with northerly wind over Southern Africa. These patterns simulated by RegCM4 induce an anticyclonic

circulation over Southern Africa in the lower levels, associated with lower-air level divergence there. Similarly, by looking at the correlation fields in the upper levels, we find upper-air level convergence over Southern Africa, with suppressed convection. This is also the region where we find negative correlation between RH and the MEI, that is a decrease in the RH in comparison to neutral conditions. Because of this drier air subsiding there, the cloud cover is reduced and more SSR can reach the surface and warm it. The positive correlation between the surface air temperature and the MEI is consistent with the latter. As expected, the situation is reversed over the SWIO, with enhanced convection there over a warmer ocean that releases more latent heat to the atmosphere, that is an increase in the RH, more clouds and less SSR.

Note that even the period over which the simulations were performed doesn't include any major ENSO event, the plot showing the correlation between SSR and the MEI here is very similar to that from Faucherau et al. (2009) which presents El Nino composites OLR anomalies.

3.1.3 IOD

The DMI is correlated here first with the ERA-Interim reanalyses data and then with RegCM4 output data. Correlation coefficients between the DMI and U, V, RH, T at 5 different pressure levels covering the whole troposphere (1000hPa, 850hPa, 700hPa, 500hPa, 300hPa) are calculated based on monthly data for each of the 10 austral summers (Nov to Feb) over the period 1999-2008. Figures 3.7, 3.8, 3.9 and 3.10 display correlation coefficients between the DMI and those parameters with the 95% significance level indicated as the black contour for ERA_Interim data. For RegCM4 outputs, correlation coefficients are calculated for each member separately, and averaged together for the comparison to ERA-Interim. Based on the analysis of the impact from atmospheric circulation, correlation coefficients between the DMI and surface solar radiation are calculated (Figure 3.11).

3.1.3.1 Zonal and Meridional wind components

Figure 3.7a shows the correlation patterns of ERA-Interim U with the DMI. U has significant negative correlation with the DMI over the subequatorial Indian Ocean (~-0. 5) at the 5 pressure levels (1000hPa to 300hPa), with values of the correlation coefficients bigger at the high-pressure level (1000hPa). At 500hPa and 300hPa, we find negative correlation over the whole subequatorial area (0°-20°S), and positive correlation elsewhere, though the correlation is not high and significant. At 1000hPa, there is significant positive correlation over Angola, Namibia, DR Congo and South Atlantic Ocean.

In comparison to ERA-Interim, RegCM4 produces similar correlation patterns at low- and high-pressure levels, though negative correlation is found over larger areas (Figure 3.7b). At 1000hPa and 850hPa, there is negative correlation over western Namibia and central Angola, in contrast to ERA-Interim. In addition, in RegCM4, the negative correlation with the DMI is larger at the surface (1000hPa) over the

subequatorial Indian Ocean.

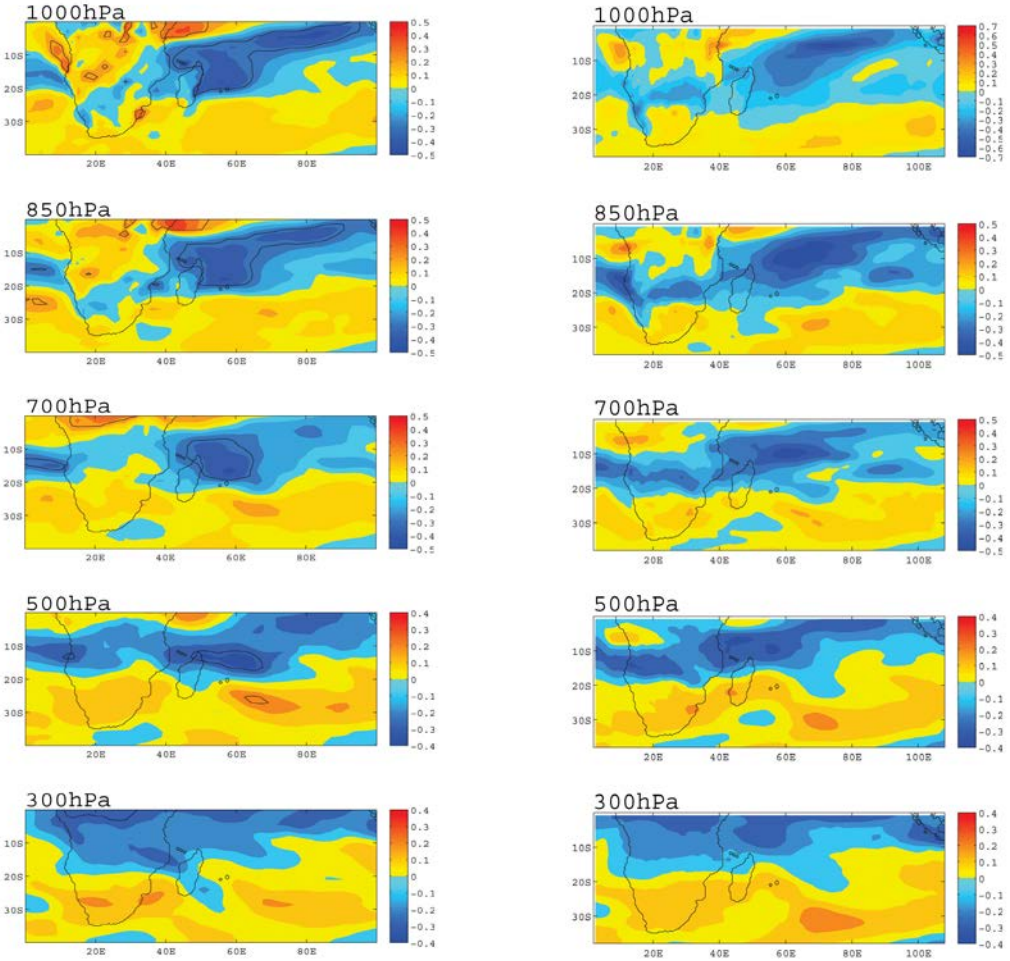

Figure 3.7 Correlation coefficients between (a) ERA-Interim (left) and (b) RegCM4 (right) U at 5 pressure levels, and the DMI during Nov to Feb 1999-2008. For ERA-Interim, correlations that are significant at 95% level are plotted as black contours (left).

As Figure 3.7, Figure 3.8 displays results for the meridional wind component V. ERA-Interim V (Figure 3.8a) shows high significant negative (positive) correlation with the DMI over DR Congo, Tanzania, northern Mozambique, Madagascar and Mozambique Channel (subtropical and northeast Indian Ocean and South Atlantic Ocean) at 1000hPa and 850hPa. At 700hPa, there is significant negative correlation of V with the DMI only over Madagascar, the Mozambique Channel and adjacent Indian Ocean (~-0.5), and small positive correlation elsewhere. At 500hPa, there is negative (positive) correlation between V and the DMI over the subequatorial area and positive correlation patterns over the subtropical area. At 300hPa, significant negative correlation is found over the subequatorial Indian Ocean and South Atlantic Ocean. Positive correlation patterns are shown over the Madagascar and eastern Indian Ocean area at 300hPa.

Results for RegCM4 (Figure 3.8b) display quite a different behavior for the correlation patterns as ERA-Interim. RegCM4 V has positive correlation with the DMI over Mozambique and Mozambique Channel at 1000hPa and 850hPa, but ERA-Interim show negative patterns over the same area. At 700hPa, RegCM4 V has negative correlation with the DMI over South Africa and part of the eastern Indian Ocean, in contrast to ERA-Interim. At 300hPa, Madagascar is covered by negative correlation values for RegCM4 V with the DMI, once again in contrast to ERA-Interim.

In general, both RegCM4 U and V produce similar correlation patterns with the DMI as ERA-Interim, which indicates RegCM4's ability to simulate the interannual variability. In the low troposphere, U and V have larger correlation with the DMI, which means that IOD would mainly impact the climate near the surface.

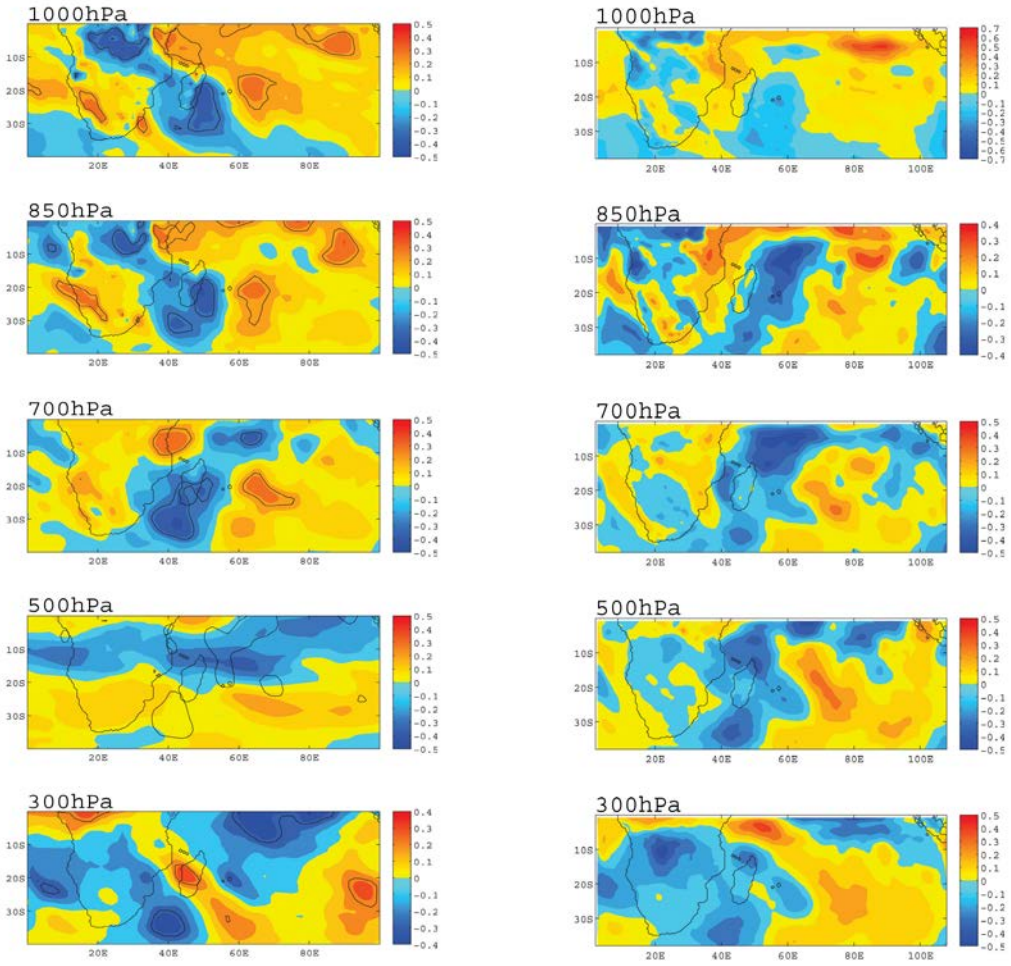

Figure 3.8 Same as Figure 3.7 but for the Meridional wind component V.

3.1.3.2 Air temperature

As shown in Figure 3.9a, ERA-Interim T has negative correlation with the DMI over almost the whole domain, except over the subequatorial Indian Ocean and part of southern Africa (Mozambique, Zimbabwe, Botswana and Namibia). T shows larger

negative correlation at high pressure levels (1000hPa/850hPa/700hPa) than low pressure levels (300hPa/500hPa). The latter one is smaller than -0.4. There is even no significant correlation for ERA-Interim T at 300hPa with the DMI. The largest negative correlation coefficient (~-0.5) mainly appears over the northern African area and the adjacent Atlantic Ocean (0°-10°S).

RegCM4 gives similar patterns at each pressure level for T, with negative correlation with the DMI over the domain (Figure 3.9b). The differences with ERA-Interim appear over the subequatorial Indian Ocean at 1000hPa, 850hPa and 700hPa, where RegCM4 T shows larger amplitudes for the correlation. The negative correlation over the whole subequatorial area at 500hPa and 300hPa is not as strong and big as for ERA-Interim. At 300hPa, even though the correlation between RegCM4 T and the DMI is small (<0.3), the patterns differ largely, which would indicate that either RegCM4 may tend to have temperature biases at high pressure levels, or T at high pressure level doesn't have any correlation with the DMI.

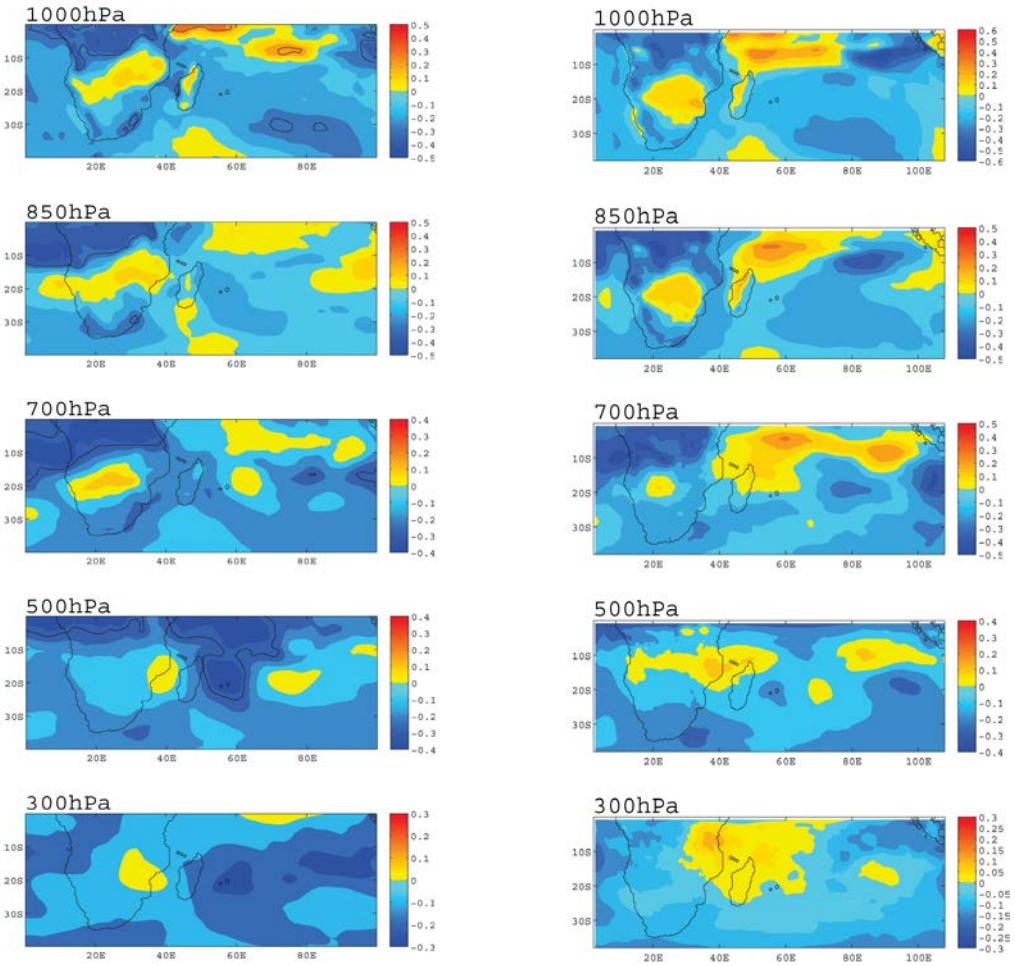

Figure 3.9 Same as Figure 3.8 but for the air temperature T.

3.1.3.3 Relative humidity

In Figure 3.10a, ERA-Interim RH at 1000hPa displays significant positive correlation with the DMI over northern Africa (Angola, DR Congo and Tanzania) and the southeastern Indian Ocean where the largest value achieves 0.5. In addition, negative correlation coefficient values mainly appear over southern Africa, including Mozambique, Zimbabwe, Zambia, Namibia, Botswana and South Africa. At 850hPa, RH shows negative correlation with the DMI over most of the domain, up to -0.7 over the eastern Indian Ocean. There is also positive correlation between RH at 850hPa and the DMI over the subequatorial area, though values remain small (<0.5). The spatial pattern of correlation between RH at 700hPa and the DMI is similar to that at 850hPa, though at this level the area of significant negative correlation over the Indian Ocean is of a lesser extent. At 500hPa, there are significant positive (negative) correlation coefficient patterns between RH and the DMI over subequatorial area and negative correlation coefficient patterns over the subtropical Indian Ocean. The correlation pattern of RH at 300hPa is similar to that at 500hPa, though less significant.

The correlation patterns derived from RegCM4 outputs (Figure 3.10b) are similar to those from ERA-Interim at all pressure levels, with positive correlation of RH with the DMI over northern Africa and the subequatorial Indian Ocean area adjacent to the African continent and the negative correlation patterns over the Angola, DR Congo and Tanzania.

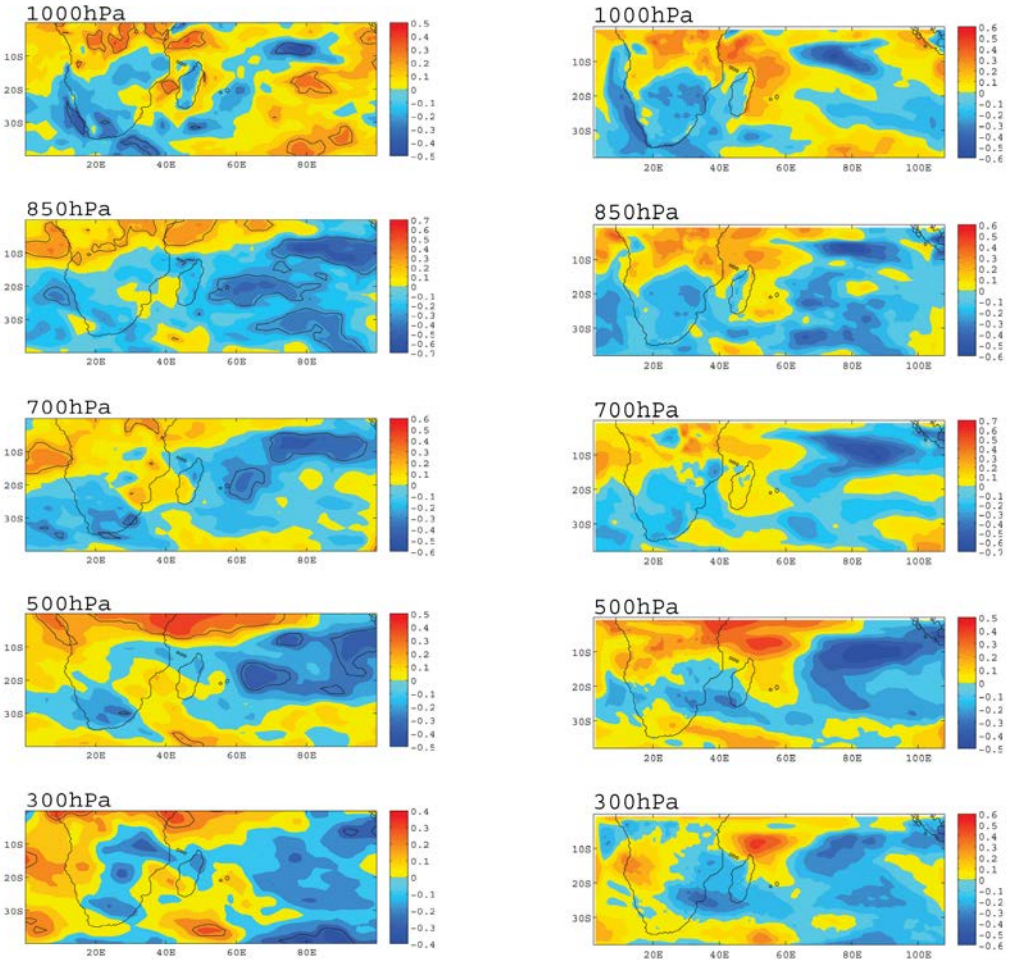

Figure 3.10 Same as Figure 3.8 but for the relative humidity RH.

3.1.3.4 Surface solar radiation

ERA-Interim SSR has positive correlation with the DMI over the Indian Ocean, the northern part of Madagascar and the southern part of South Africa, though values are not very high (<0.4). Negative correlation coefficients are found essentially over Africa, the southern Atlantic Ocean and the southern Indian Ocean. As shown on Figure 3.11a, correlation coefficients between ERA-Interim SSR and the DMI are not significant at the 95% level. RegCM4 SSR (Figure 3.11b) shows higher correlation with the DMI than ERA-Interim. Positive correlation appears over Zimbabwe, Mozambique, Botswana, Namibia, South Africa, Mozambique Channel and the eastern part of the Indian Ocean. Negative correlation is found over DR Congo, Angola, the eastern part of Madagascar and the subequatorial part of the Indian Ocean. In general, the variance of DMI during these 10 years is very weak (correlation coefficient values < 0.4).

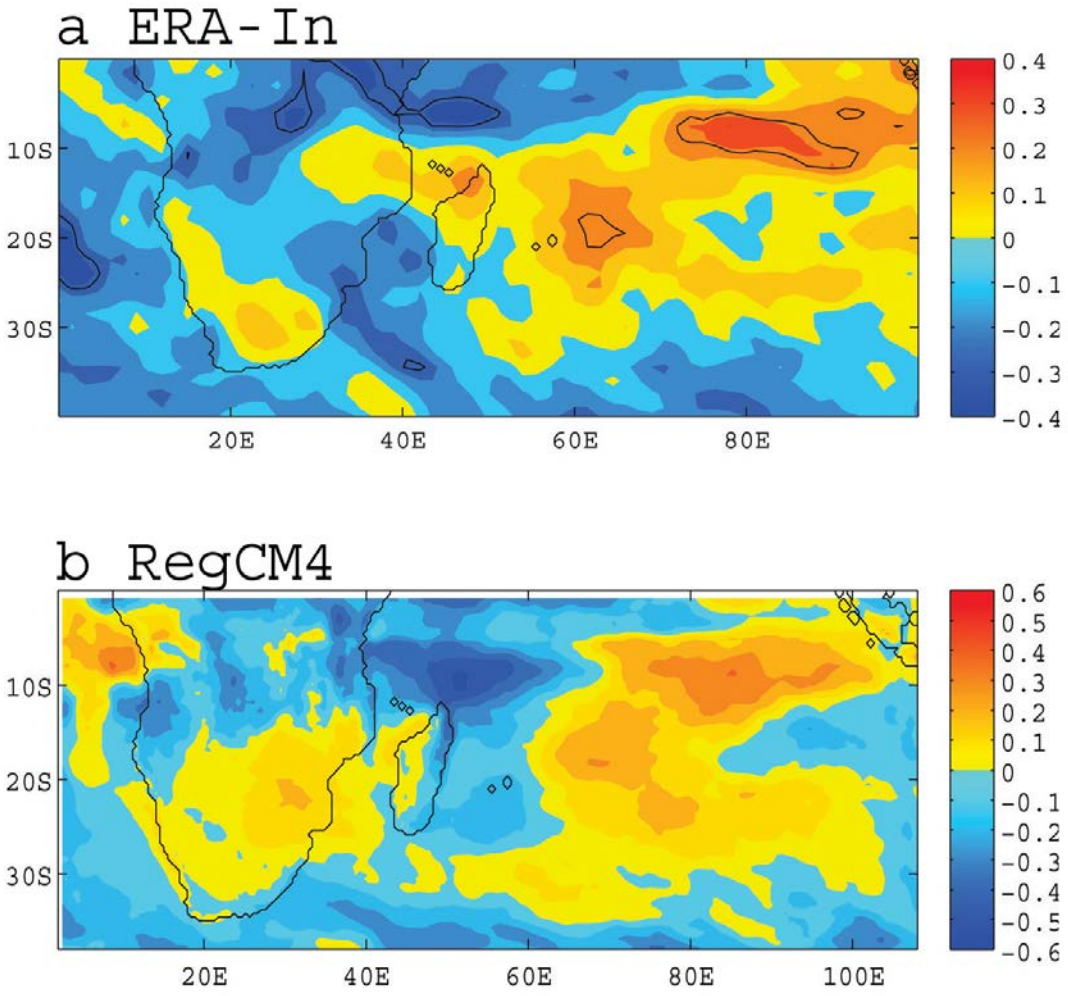

Figure 3.11 a) Correlation coefficients of ERA-Interim SSR with the DMI for the austral summers Nov to Feb 1999-2008. Correlations that are significant at the 95-% level are superimposed in black contours. b) Correlation coefficients of RegCM4 SSR with the DMI during austral summers Nov to Feb 1999-2008. These are the ensemble mean values of the correlation coefficients' values for the 5 simulations.

SSR simulated by RegCM4 and DMI have positive correlation over the Southern Africa and Indian Ocean where found has more radiation with regard to the SSR mean state. U and V have larger correlation with the DMI at the low troposphere, related to the convection effect on the SSR. Strong negative correlation between RH and DMI over the east of Southern Africa where we find less SSR is due to the fact that RH is related to more clouds and then less solar radiation reaching the surface. Note that the correlation between those parameters and DMI is not so strong, the IOD signal over the period is not so obvious, but RegCM4 is able to give the interannual variability considering the similar patterns as reanalyses data.

3.2 Intraseasonal variability of surface solar radiation

In the first sections, we analyzed the relationship between two modes of interannual

climate variability (ENSO, IOD) and SSR over the SWIO considering related atmospheric parameters. In this section, we relate SSR over the SWIO to an intraseasonal mode of variability, the MJO. Firstly, RH and T with wind at different pressure levels (1000hPa, 850hPa, 700hPa, 500hPa, 300hPa) from ERA-Interim reanalyses data are examined to search for the MJO patterns, then the output data from RegCM4 for the same atmospheric parameters. SSR of ERA-Interim and RegCM4 are related to those parameters to create SSR, U and V anomaly composites for different MJO phases through RMM1 & RMM2 index. These phases are constructed from the daily data for austral summer months (Nov to Apr) over the 10-year period 1999-2008. Superimposed on the figure are composites of wind vectors anomalies at low troposphere (850hPa) and high troposphere (300hPa). Results for the other pressure levels (1000hPa, 700hPa, 500hPa) are shown in the appendix (Figure A1-A18).

3.2.1 Relative humidity with wind

Figures 3.12a and 3.12b show ERA-Interim RH along with the wind vector anomalies in the upper atmosphere (300hPa) and low troposphere (850hPa) for the 8 MJO phases constructed from the RMM1 & RMM2 index. At the low troposphere (Figure 3.12b), RH anomalies ([-5 5]; %) are smaller than in the upper atmosphere ([-12 12]; %).

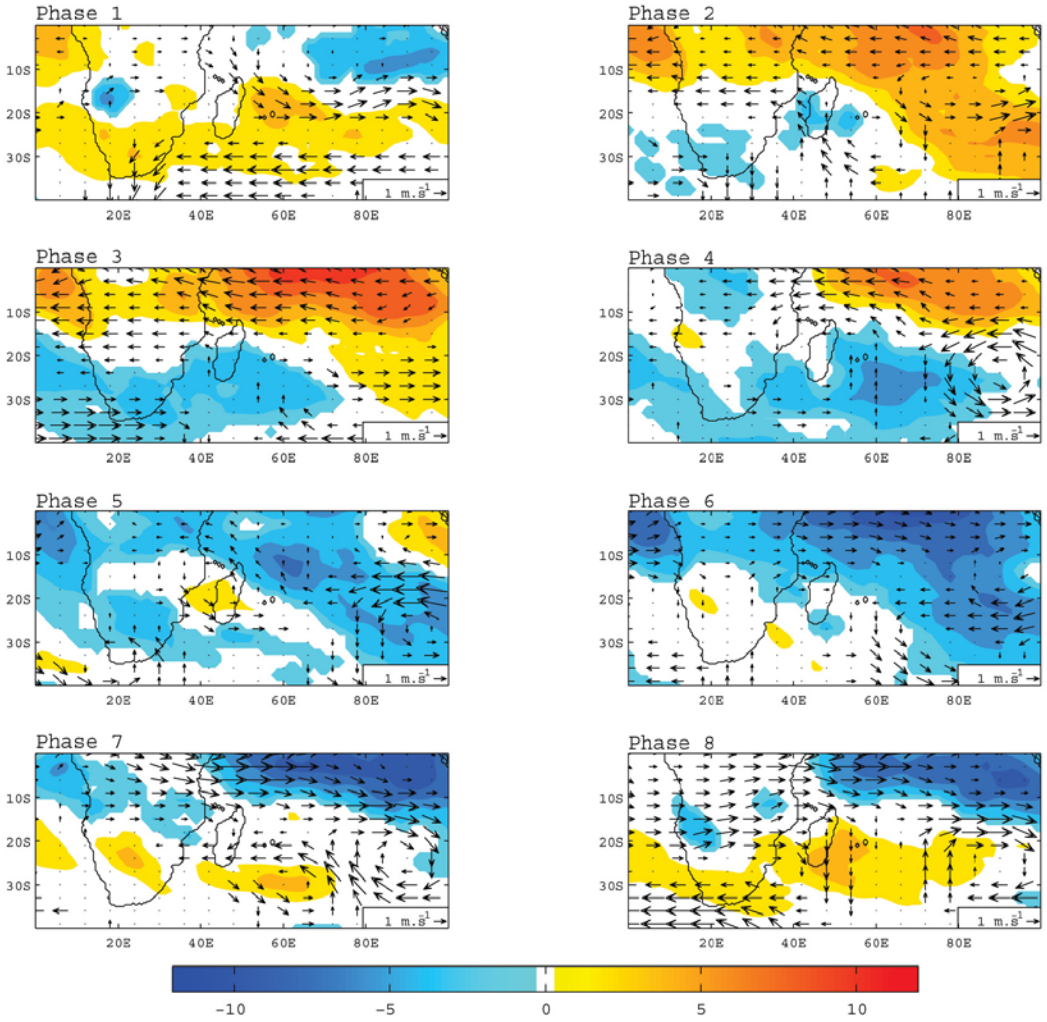

Figure 3.12 a) Composites of ERA-Interim NDJFMA RH anomalies (in %) as a function of the 8 MJO phases for the period 1999-2008. Superimposed are 300-hPa wind vector anomalies (in m/s).

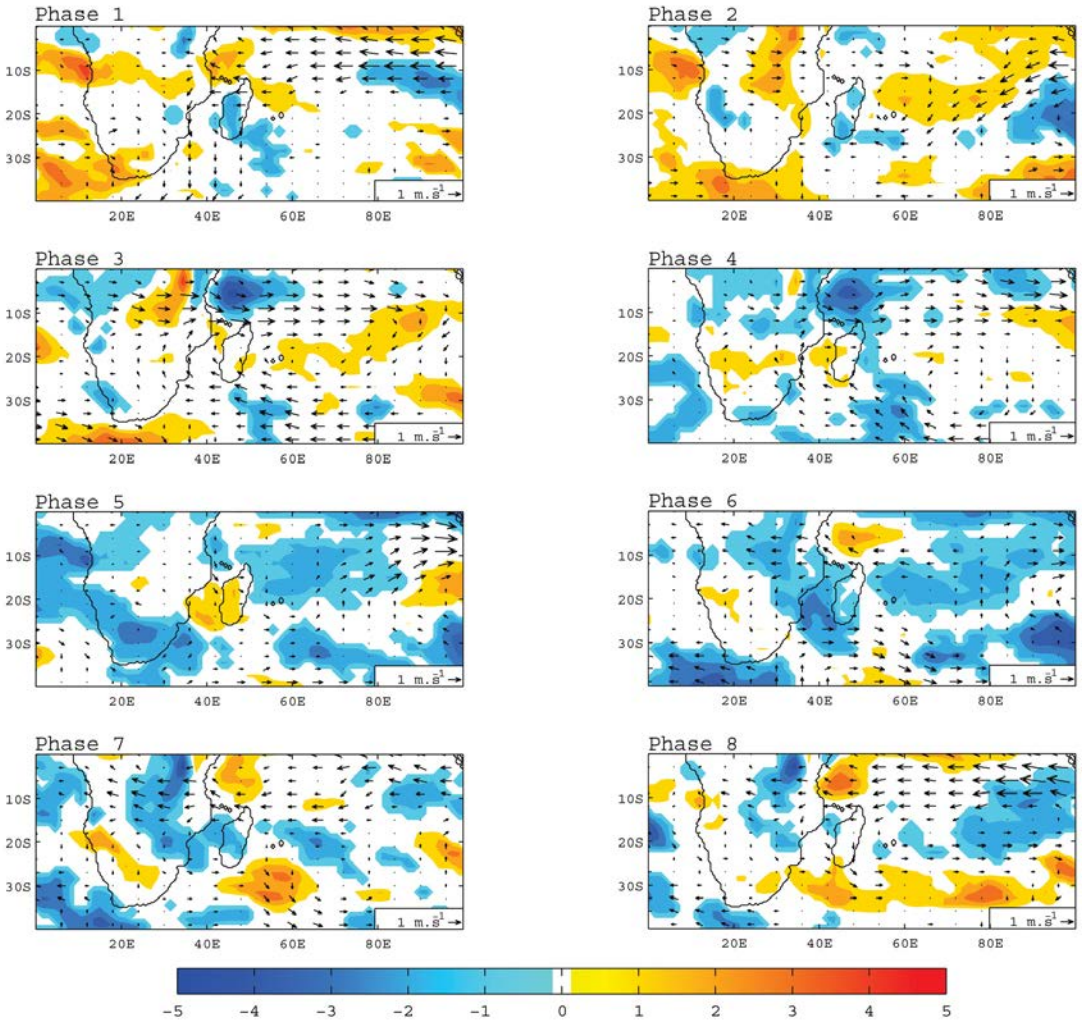

Figure 3.12 b) As Figure 3.12a but for the 850hPa wind vector.

Figures 3.13a and 3.13b show RegCM4 RH anomaly composites for the 8 MJO phases. In the upper atmosphere (Figure 3.13a), there is obvious easterly moving of positive RH anomalies from phase 1 to 8 over the subequatorial area. Near the surface (Figure 3.13b), the easterly (westerly) moving of positive (negative) RH anomalies is also evident, though the patterns for all MJO phases show reversed spatial distribution as compared to the upper level. For example, in phase 6, we find positive anomalies in the upper atmosphere and negative ones near the surface over South Africa, while in phase 7 we find positive anomalies in the upper atmosphere and negative ones near the surface over the Indian Ocean.

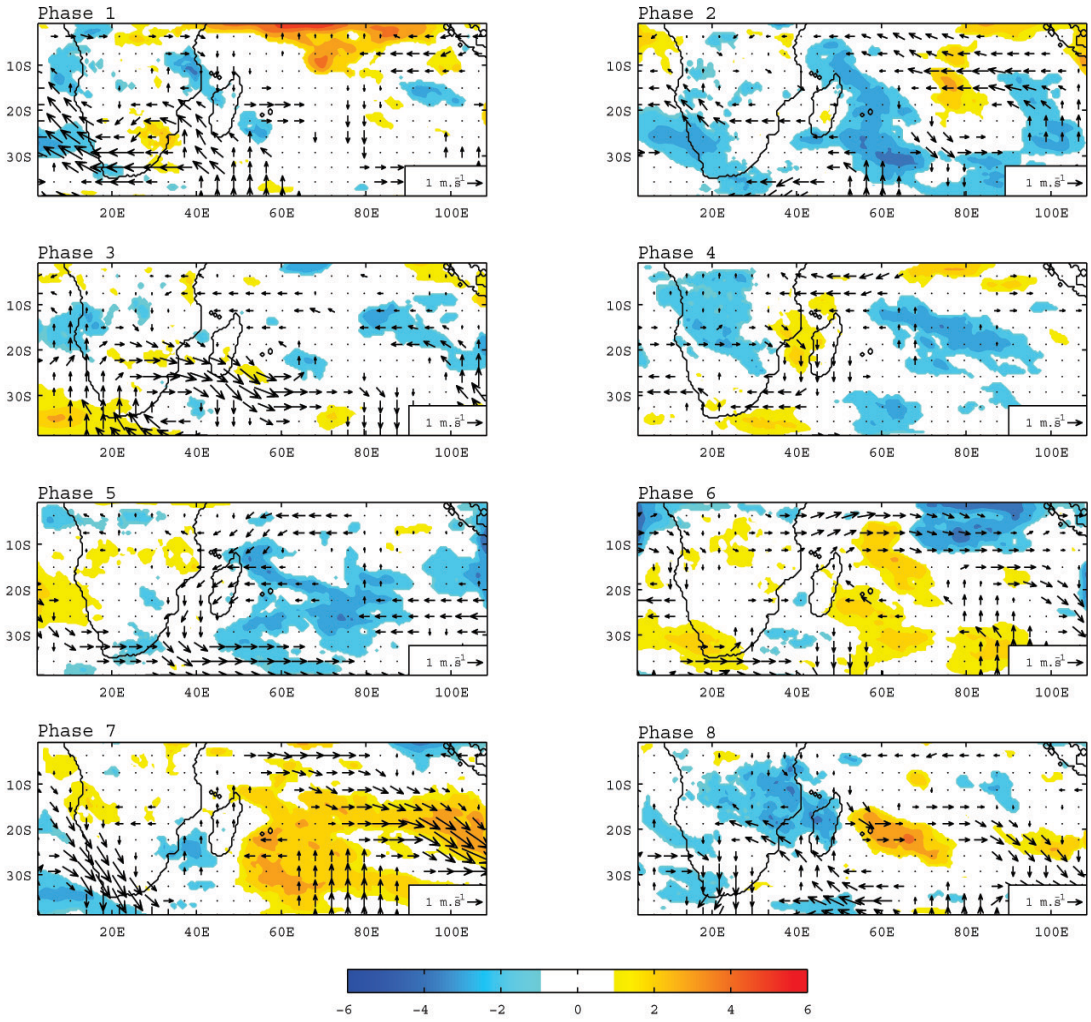

Figure 3.13 a) Same as Figure 3.12a but for RegCM4.

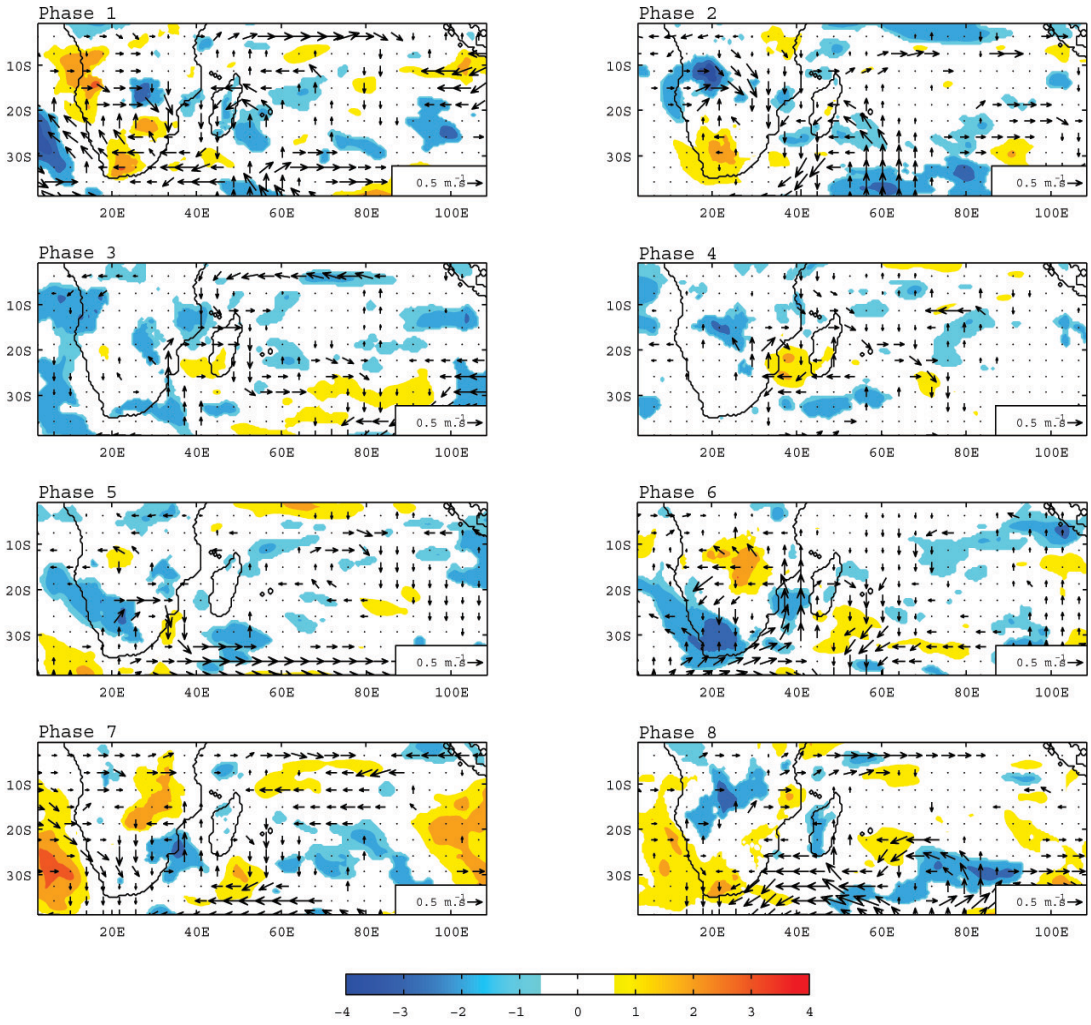

Figure 3.13 b) Same as Figure 3.12b but for RegCM4.

3.2.2 Air temperature with wind

Figures 3.14a and 3.14b shows ERA-Interim T anomaly composites along with the wind vector anomalies in the low (300hPa) and high (850hPa) pressure level for the 8 MJO phases. In the upper atmosphere (Figure 3.14a), even though the T anomalies are small ([-0.8 0.8] Kelvin), strong negative (positive) anomalies patterns are shown in phases 1, 7 and 8 (3, 4 and 5) over the subtropical area. At 850hPa (Figure 3.14b), the T anomalies are also small ([-0.7 0.7]; K), with the largest negative (positive) values over the Atlantic and Indian oceans in all phases.

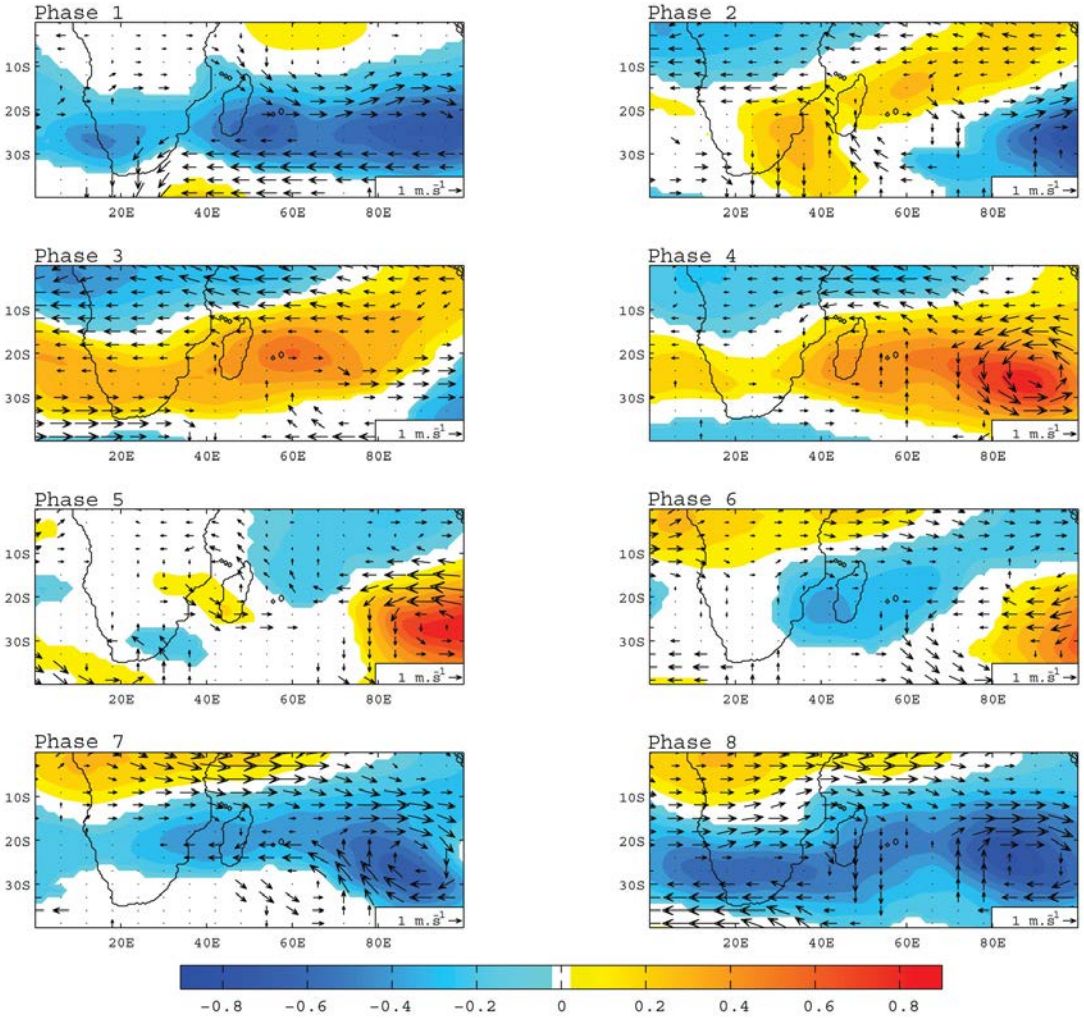

Figure 3.14 a) Composites of ERA-Interim NDJFMA T anomalies (in K) as a function of the 8 MJO phases at 300hPa. Superimposed are 300hPa wind vector anomalies (in m/s).

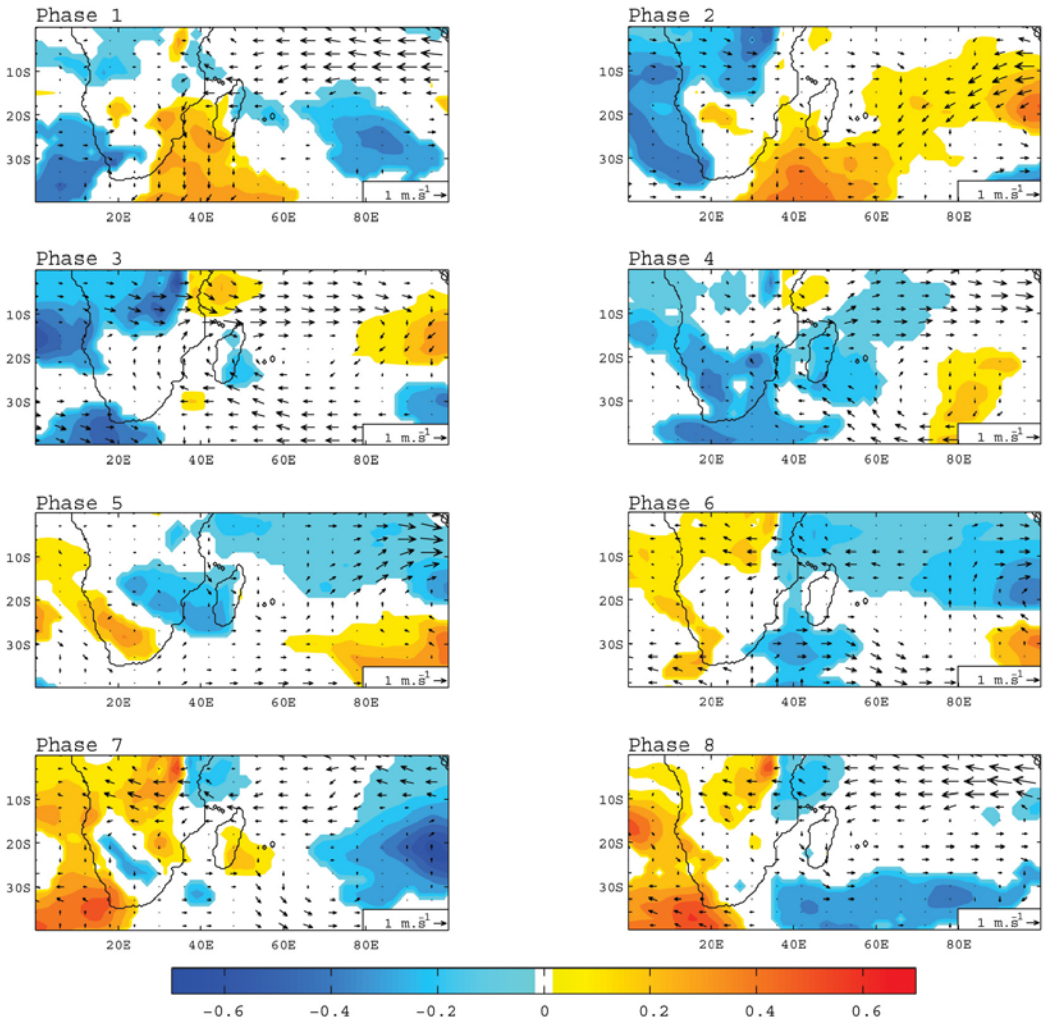

Figure 3.14 b) As Figure 3.14a but for the 850hPa wind vector.

Similarly, we examine RegCM4 T anomaly composites for the different phases of the MJO index (Figure A13-A15 in the Appendix A). The anomalies are small both in the upper atmosphere and near the surface, and it is hard to distinguish any moving of the patterns.

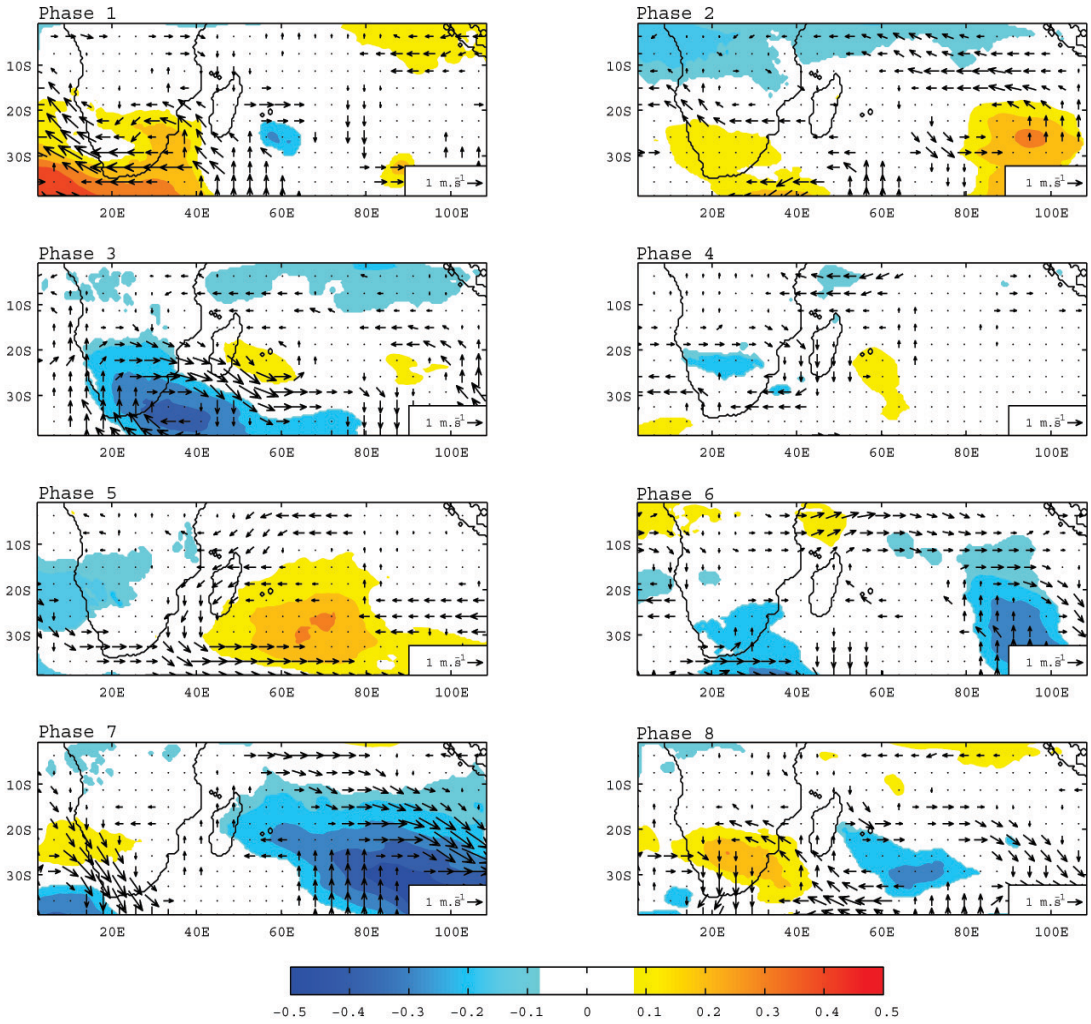

Figure 3.15 a) As Figure 3.14a but for the RegCM4.

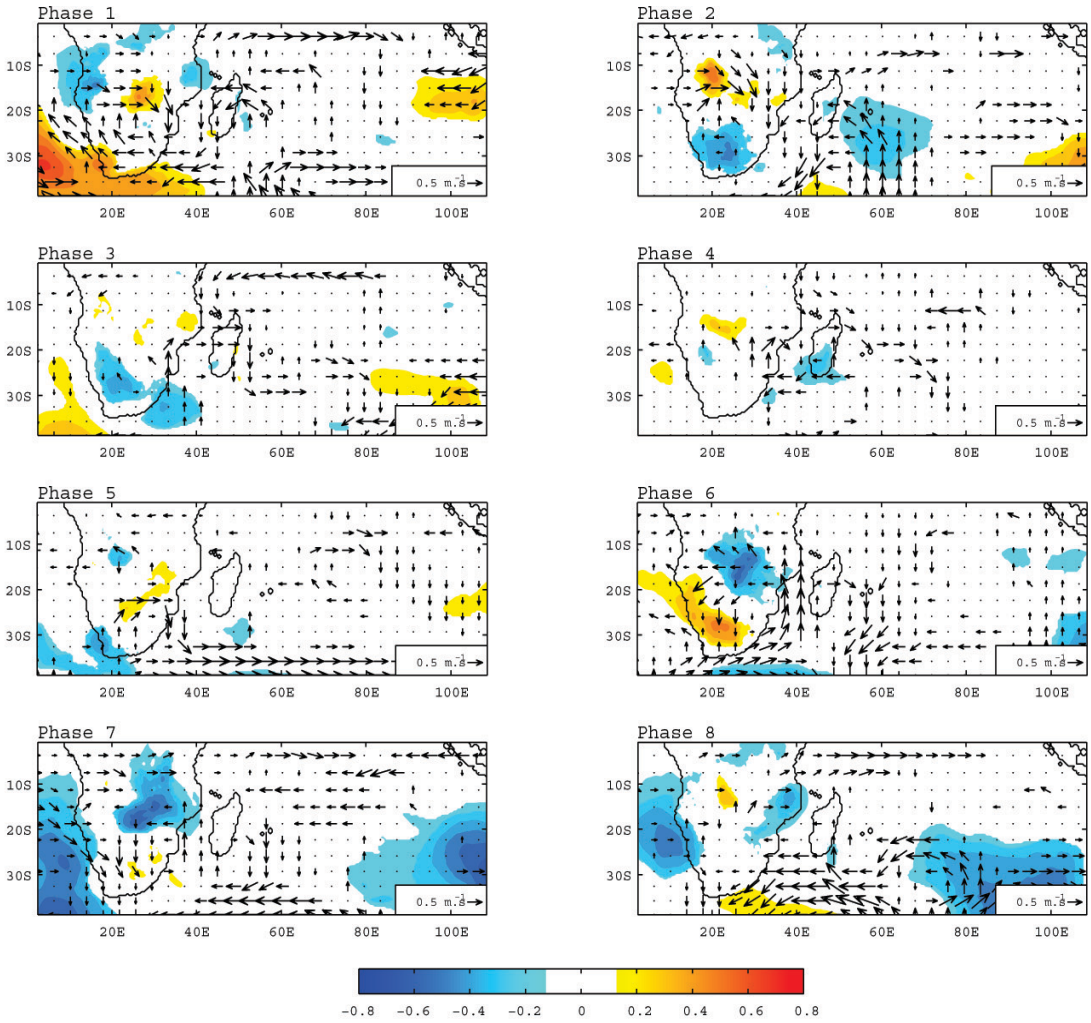

Figure 3.15 b) As Figure 3.14b but for the RegCM4.

3.2.3 Surface solar radiation

Figures 3.16a and 3.16b (Figures 3.17a and 3.17b) show composites of ERA-Interim (RegCM4) SSR anomalies as a function of the 8 MJO phases. These are constructed from the daily data for austral summer months (Nov to Apr) over the 10-year period 1999-2008. Superimposed on the figure are composites of wind vectors anomalies at low troposphere and high troposphere. Results for the other pressure levels (1000hPa, 700hPa, 500hPa) are shown in the appendix.

ERA-Interim SSR anomaly composites for the 8 MJO phases give the similar patterns as RegCM4 (Figure 3.16), with essentially negative (positive) anomalies over the subequatorial area in phase 1 to 4 (5 to 8). Indeed, eastward moving of negative SSR anomalies from phase 1 to 8 is observed at all pressure levels (Figure 3.16a and b; Figure A7-A9 in appendix). There are strong anomalous westerly winds at low troposphere (850hPa), which are reversed at the upper troposphere (300hPa). The negative (positive) SSR anomalies are mainly located over the subequatorial area with the MJO phase moving.

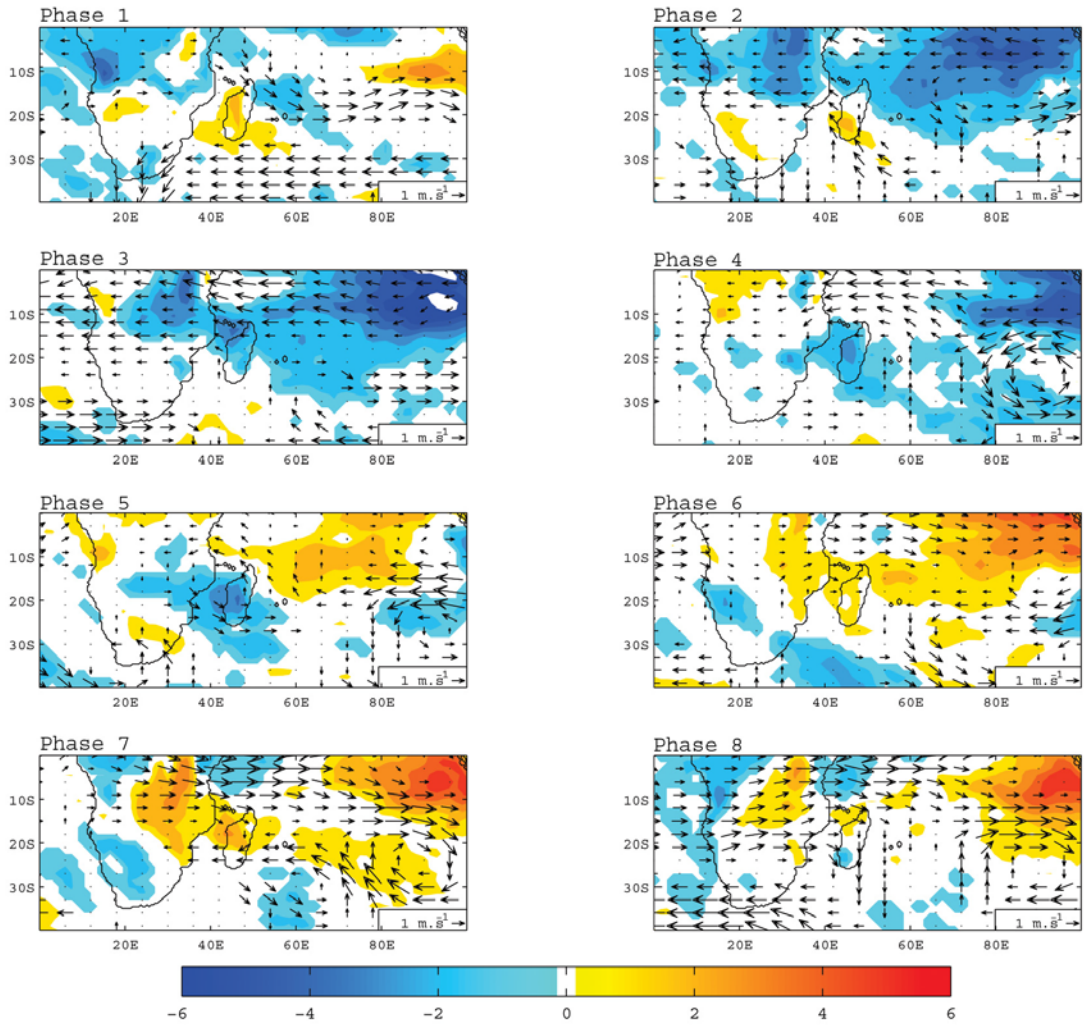

Figure 3.16 a) Composites of ERA-Interim NDJFMA SSR anomalies (in W/m^2) as a function of the 8 MJO phases. Superimposed are 300hPa wind vector anomalies (in m/s).

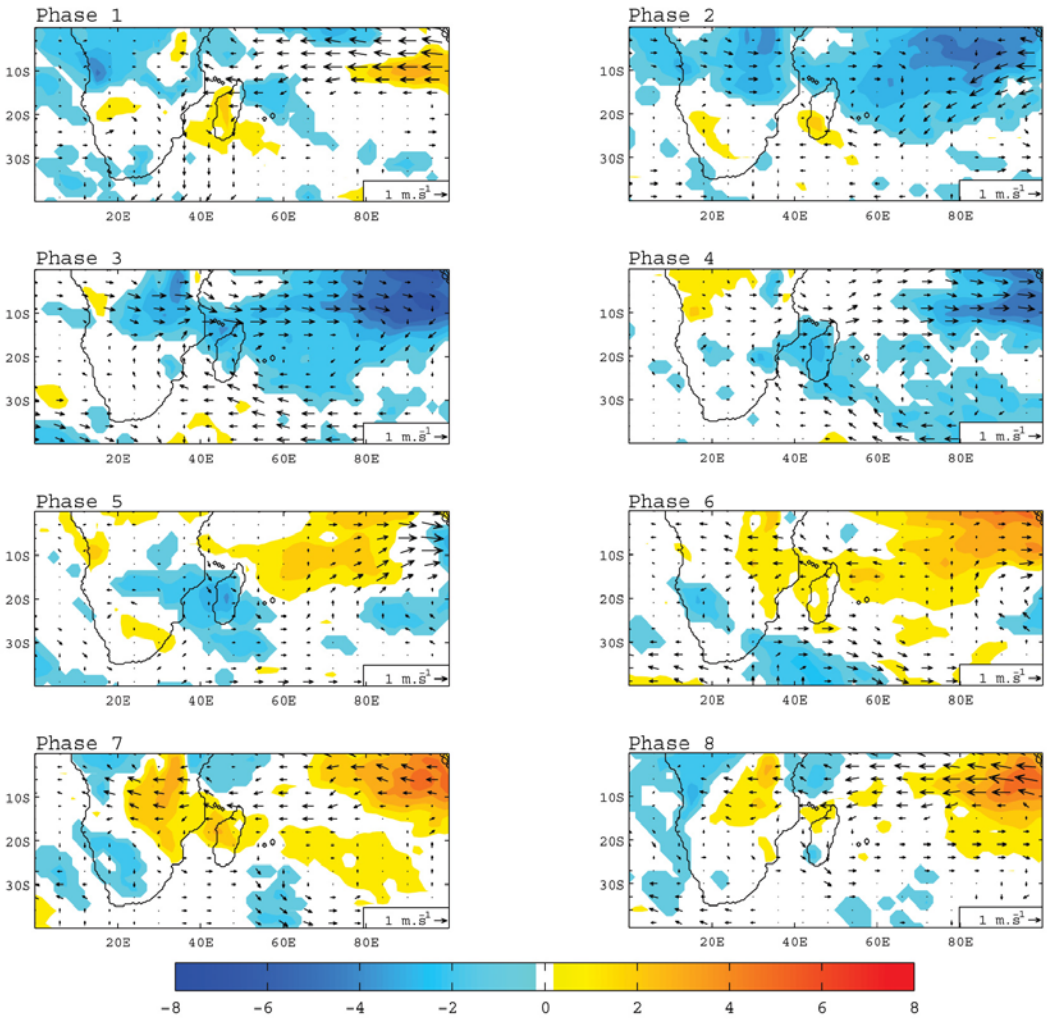

Figure 3.16 b) Same as Figure 3.16a but for the 850-hPa wind vector.

Similarly, results for RegCM4 (Figures 3.17a and 3.17b) show the eastward moving of negative anomalies from one MJO phase to another. There again, the strong negative (positive) SSR anomalies are accompanied with westerly (easterly) wind anomalies at the low troposphere (850hPa). However, the wind anomalies in some places do not completely reverse direction in the upper atmosphere compared to the surface. For example, we find strong westerly wind anomalies over South Africa and the adjacent ocean area both at the low troposphere (Figure 3.17b) and in the upper atmosphere (Figure 3.17a). The direction of the wind anomalies over the Indian Ocean is mostly reversed.

In the upper atmosphere (Figure 3.12), we find positive RH anomalies at places where we would find negative SSR anomalies (Figure 3.16). There again, these anomalies are moving eastward as the MJO shifts. This is reasonable, because the surface normally receives more solar radiation in clear sky conditions, i.e., with less cloud and convective precipitation. At the lower atmosphere, SSR anomalies can be related to the RH anomalies patterns in each phase (Figure 3.12), with obvious negative

(positive) RH anomalies over South Africa (Madagascar and Mozambique Channel) in phase 5 at places where we would find positive (negative) SSR anomalies. With regard to the air temperature, they are areas where the patterns are inverted with regard to SSR. For example, we find positive T anomalies in phases 1 and 2 over South Africa (Figure 3.14a), where we find negative SSR anomalies (Figure 3.16a).

Normally, RegCM4 should give patterns similar to those from ERA-Interim. Here, RegCM4 SSR anomalies are a little bit larger and the patterns are different in each phase compared to ERA-Interim. However, RegCM4 still manages to maintain the MJO signal. In general, RCMs or GCMs have some difficulties in maintaining the MJO signal. The good performance here may be due to the fact that the lateral forcing itself was containing the MJO signal, and the relatively reduced size of the domain in comparison to the scale at which this phenomenon occurs (Lin et al. 2006; Zhang et al. 2006; Kim et al. 2009).

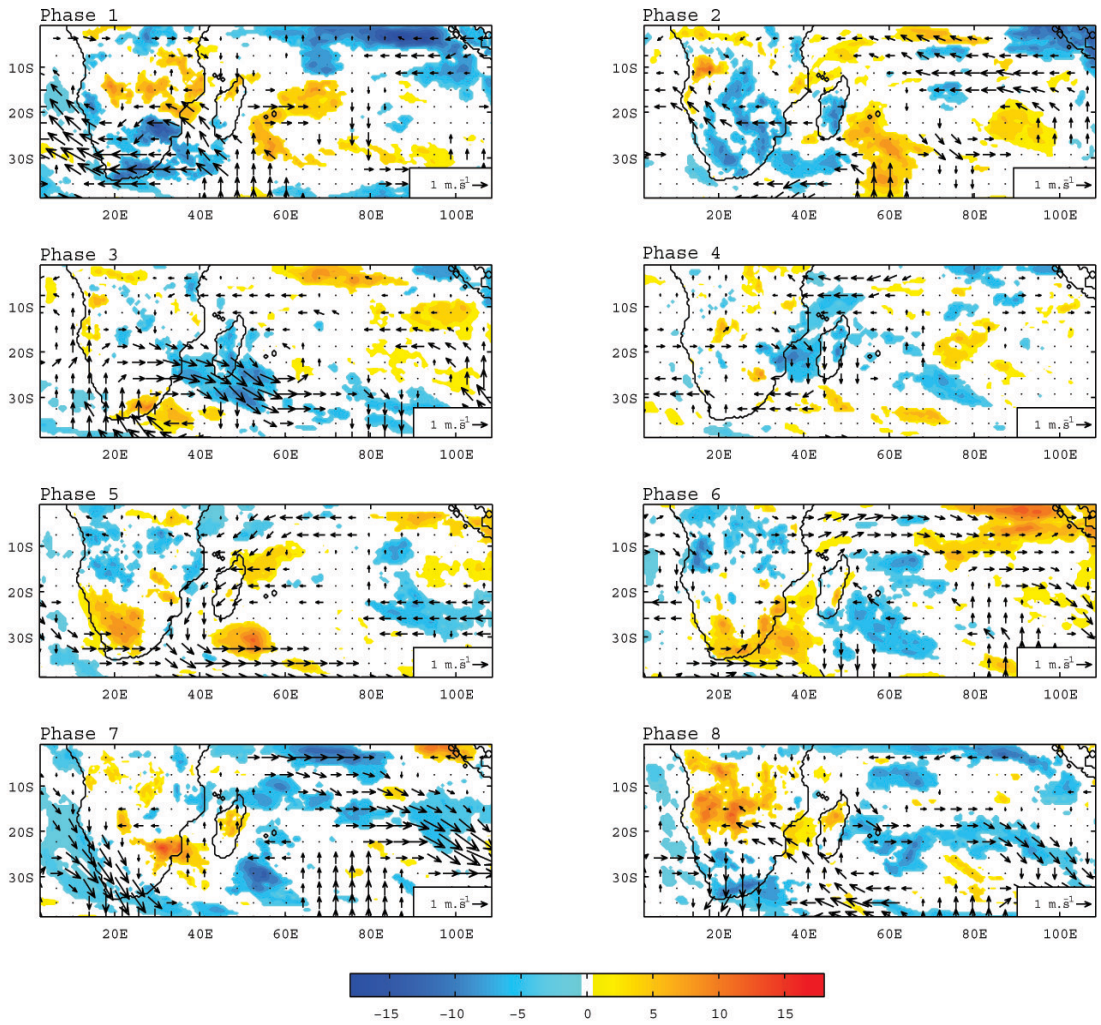

Figure 3.17 a) Same as Figure 3.16a but for RegCM4.

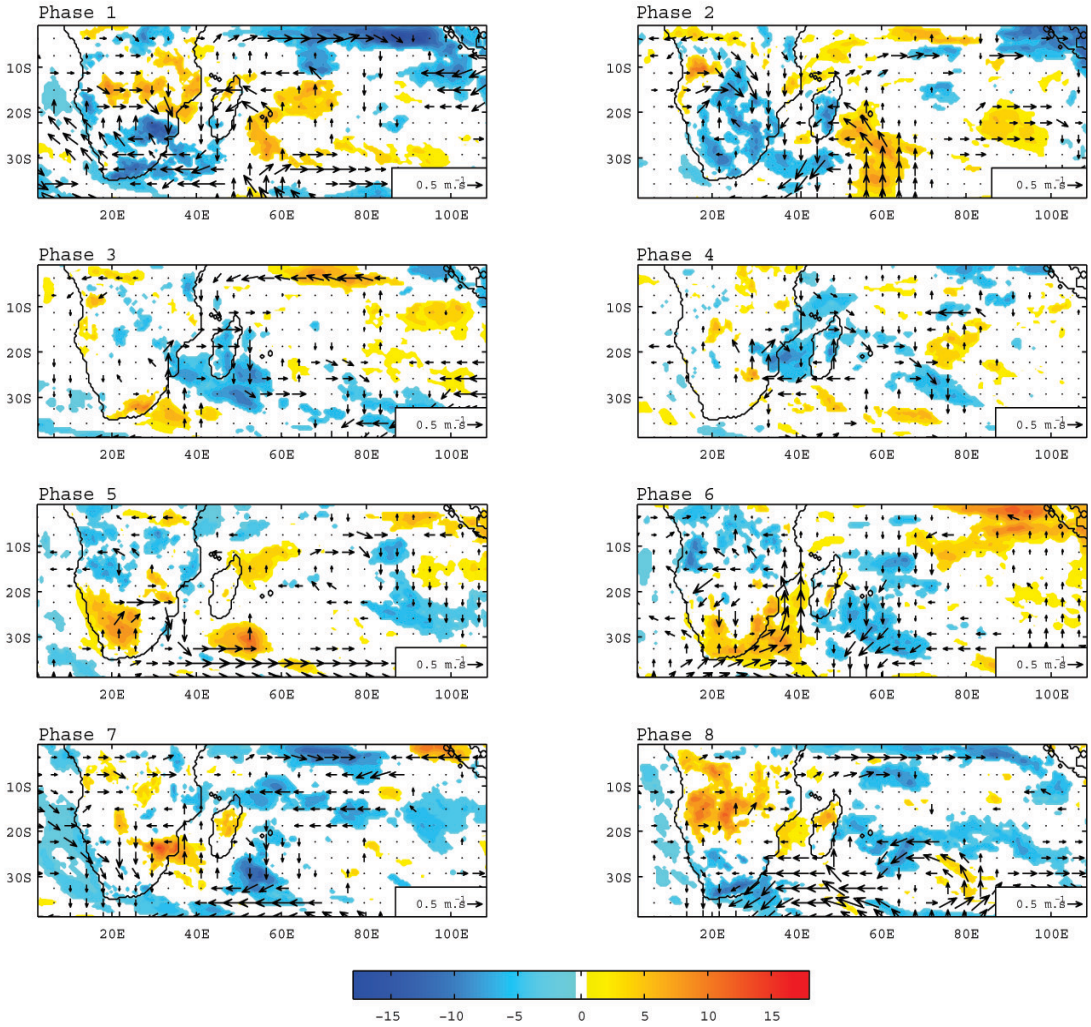

Figure 3.17 b) Same as Figure 3.16b but for RegCM4.

3.3 Synoptic climate variability of surface solar radiation

The analysis of TTTs through the recurrent outgoing longwave radiation (OLR) patterns over the domain (0°-40°S, 0°-100°E) is conducted with the objective to study the synoptic climate variability of SSR over this domain. Based on the results of Fauchereau et al. (2009), we first construct the TTTs patterns over the region by examining NOAA OLR. We then check whether ERA-Interim and RegCM4 are able to represent such patterns. This will help validating the ability of RegCM4 to simulate the synoptic climate variability. Finally, we focus on the relationship between SSR and TTTs.

In this part, the dynamical clustering (K-means clustering) is applied on the daily OLR anomalies over the SWIO and Southern Africa. K-means clustering here essentially follows that of Cheng and Wallace (1993) and Michelangeli et al. (1995). Given a previously fixed number of regimes, k, the aim of the regime analysis algorithm is to obtain a partition, P, of the observations (days) into k regimes that minimizes the sum of the intra-regime variances, V. The Euclidian distance is used to

measure the similarity between two observations, X and Y. The overall minimum of the function V(P) corresponds to the partition that best separates the different points. When the classification is applied to large samples, climatological series as we use, this overall minimum cannot be found in practice because of the huge number of different possibilities to explore. The algorithm defines n iterative partitions, P(n), for which V[P(n)] decreases with n and eventually converges to a local minimum of the Function, V(P). The overall minimum of V(P) is surrounded by many local minima that differ from it by only a few observations, exchanged from one regime to another and essentially found at the periphery of them. The latter may largely depend on the analyzed sample, the algorithm being initialized by a random draw of the k regimes. The reproducibility of the obtained partitions should therefore be tested. If the distribution of the climatological dataset is uniform, the final partition is assumed to be largely dependent on the initial randomly chosen seeds. In contrast, when the dataset is distributed into well-defined regimes, two different initial draws should theoretically lead to roughly similar final partitions. The dependence of the final result on the initial random draw may thus be sued as an indicator of the degree of classifiability of the dataset into k regimes (Fauchereau et al. 2009).

3.3.1 Recurrent OLR regimes over the region

To be sure that the k-means clustering applied to ERA-Interim and RegCM4 OLR could give a reasonable classification as NOAA, we first present in Figure 3.18, the mean OLR field from NOAA and ERA-Interim over the studied period (November to February summer seasons from 1999 to 2008). The mean OLR patterns from the two datasets are similar, both showing high (low) values over the western part of South Africa and the subtropical Indian Ocean (DR Congo and Angola). This at least confirms that these two datasets show similar patterns for OLR and they should give comparable classification. Then we apply the k-means clustering method to NOAA, ERA-Interim and RegCM4 OLR data. Figure 3.19 shows the classifiability index c as a function of the number of clusters k along with the significance levels computed from the first-order Markov process for RegCM4 OLR. It shows a clear and significant (at the 95% level) peak for k=6. The results for NOAA and EAR-Interim OLR both give a peak for k=7 (the figures are similar to Figure 3.19, so they are not shown here). Larger numbers of regimes are also determined as presenting a high degree of robustness among the regime analysis based initiated with different random draws. However, with regard to the results of Fauchereau et al. (2009) and to make the comparison between the three datasets easier, we choose hereafter a seven-regime partition because this value of the classifiability index is the largest and is the one that provides the best and compact summary of the information among those that reach significance considering those three datasets.

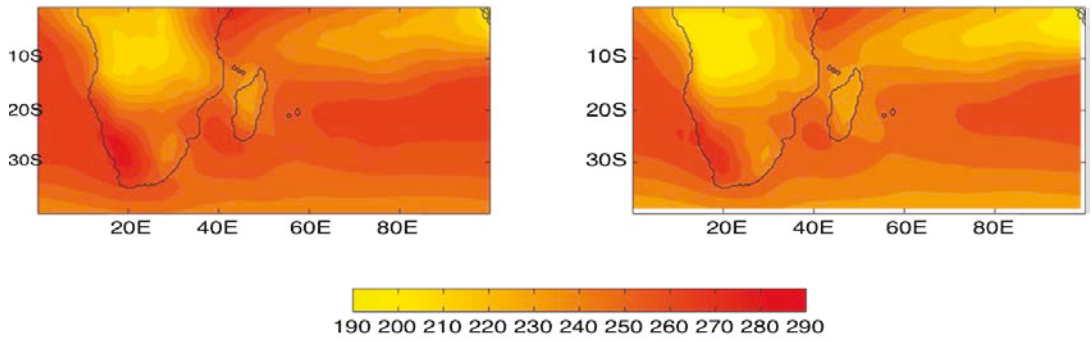

Figure 3.18 Average of OLR during Nov to Feb 1999-2008 for NOAA (left) and ERA-Interim (right) daily datasets (W/m^2).

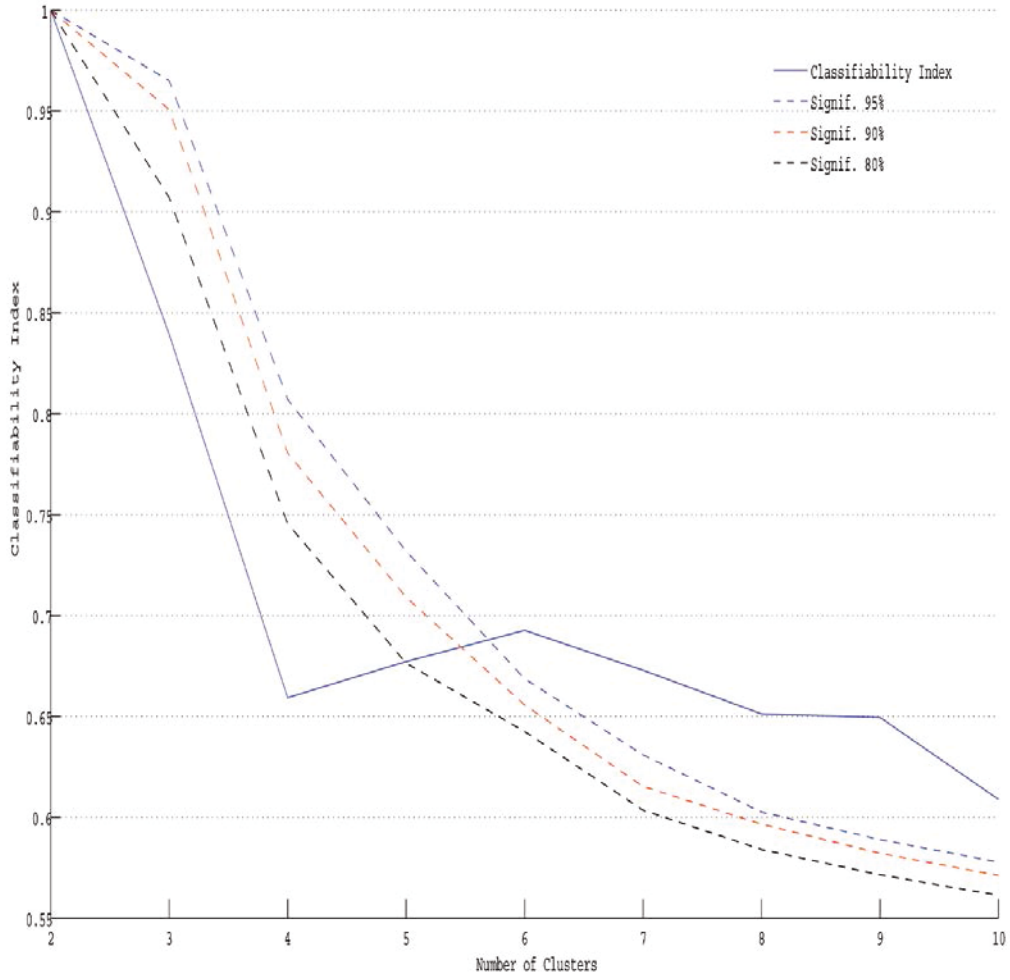

Figure 3.19 Classifiability index c as a function of the number of regimes k (solid line). The significance levels at 95%, 90% and 80% (dashed lines) are computed according to a first-order Markov process.

Figure 3.20 presents the composite mean of NOAA OLR according to the results of the k-means clustering analysis applied onto NOAA OLR and Figure 3.21 is for the OLR composite anomalies respectively. Only the anomalies significant at the 95-% level according to a Student's t-test are displayed. Three regimes (Figure 3.21e-g; regimes #5, #6, #7) are characterized by a NW/SE band extending from the southern African subcontinent or Madagascar at tropical latitudes to the mid-latitudes of the SWIO (south of 30°S). These bands are rooted in southern Africa respectively over northeastern South Africa, Mozambique and Madagascar for regimes #5, #6, #7. Figures 3.21e-g show the strong negative OLR anomalies which should be associated with the mean cloud band and this kind of band may extend similarly in a NW-SE direction. These three regimes are thus chosen as representative of TTTs systems. The remaining four regimes are not obviously associated with tropical-temperate linkages, even though negative OLR anomalies exhibited by regimes #2 (Figure 3.21b) and #4 (Figure 3.21d) present a somewhat NW-SE structure. The composite anomalies show that regime #1 represents a pattern of overall increased convection (negative OLR anomalies) over the regime analysis domain, except a small region over Mozambique. Regime #2 indicates large increased convective activity east of Madagascar, around 25°-30°S, while convection is reduced (positive OLR anomalies) over the southwestern southern Africa (Figure 3.21b). Regime #3 shows a large region of increased convection over the continent south of 10°S as well as the adjacent Atlantic Ocean (Figure 3.21c). During occurrences of regime #4 (Figure 3.21d), convection is increased over the oceanic region as well as the northeastern southern Africa, while decreased convective activity occurs over South Africa, Botswana and Namibia region.

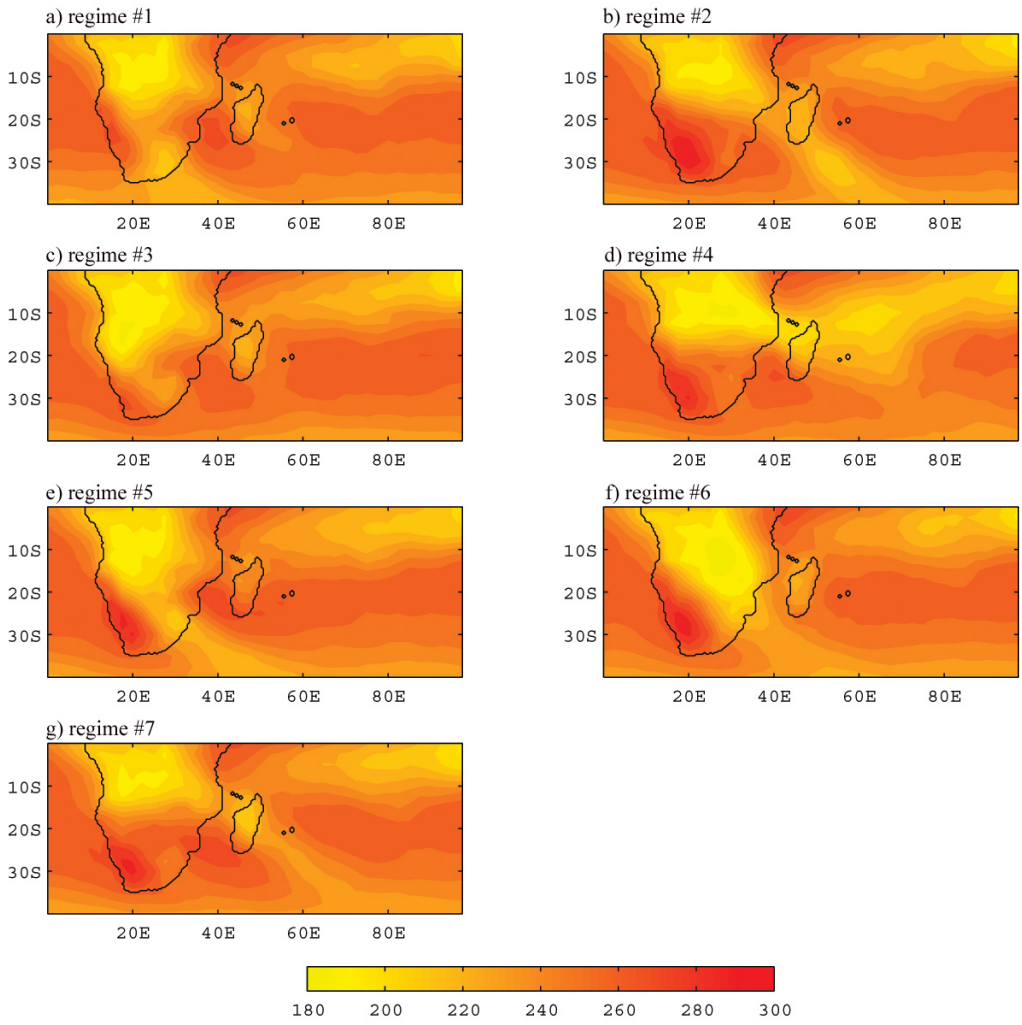

Figure 3.20 NOAA OLR regimes for NDJF: composite means (W/m^2).

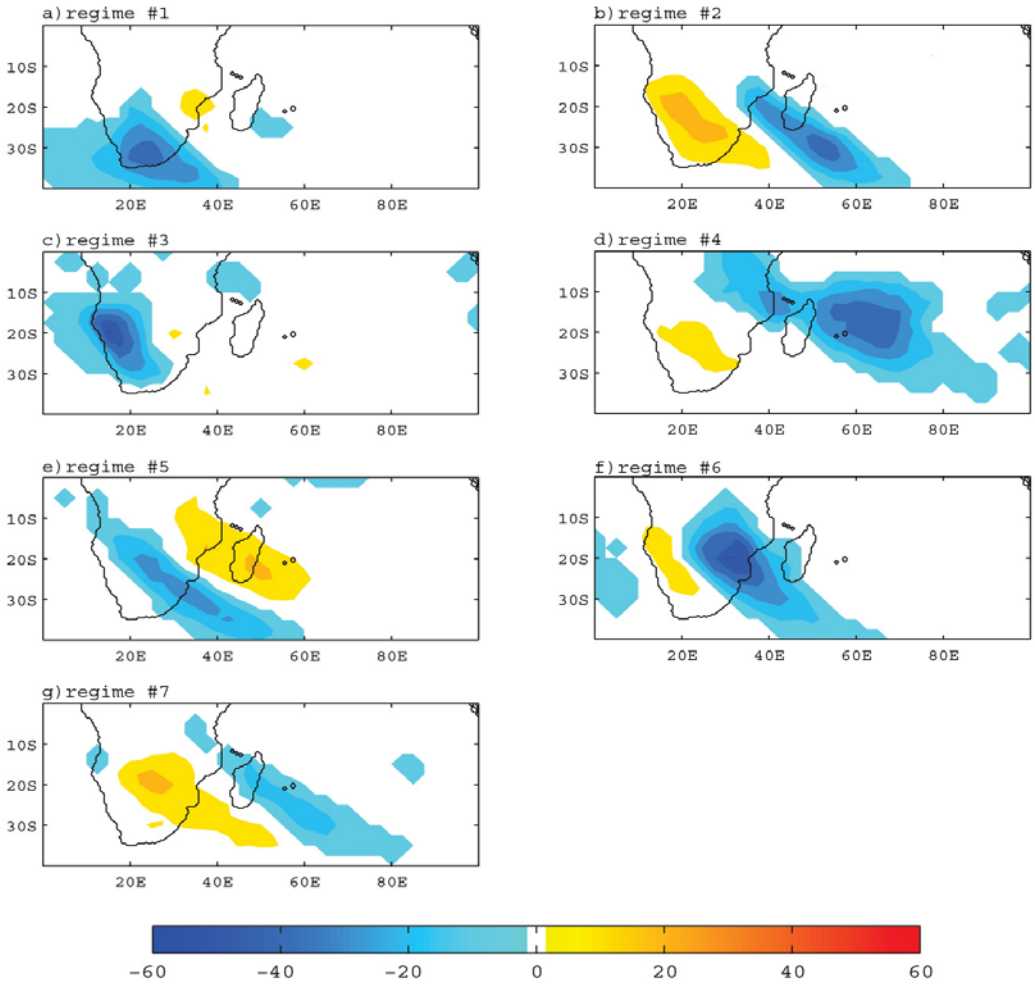

Figure 3.21 Composites of NOAA OLR (W/m^2) anomalies for NDJF 1999-2008 in the 7 TTTs regimes. Only 95% significant anomalies according to a t-test are displayed.

K-means clustering is then applied onto ERA-Interim and RegCM4 OLR data (Figures 3.22 and 3.23 respectively). Resulting regimes are re-ordered by calculating the Euclidean distance between them and those from NOAA OLR separately. The minimum of distance is considered to be the similar corresponding regime. Three regimes of ERA-Interim OLR (Figure 3.22e-g; regimes #5, #6, #7) and RegCM4 OLR (Figure 3.23e-g; regimes #5, #6, #7) give a similar NW/SE band extending from the southern African subcontinent or Madagascar at tropical latitudes to the mid-latitudes of the SWIO (south of 30°S) as NOAA OLR, which indicates that both RegCM4 input (i.e., ERA-Interim) and output data present a characterization of the TTTs. RegCM4 model is able to represent the synoptic climate variability of radiation over the SWIO and southern Africa region. The other regimes (a-e; #1-#4) in Figures 3.22 and 3.23 show similar anomalies patterns as NOAA OLR (Figure 3.21). We won't give further details on those regimes hereafter.

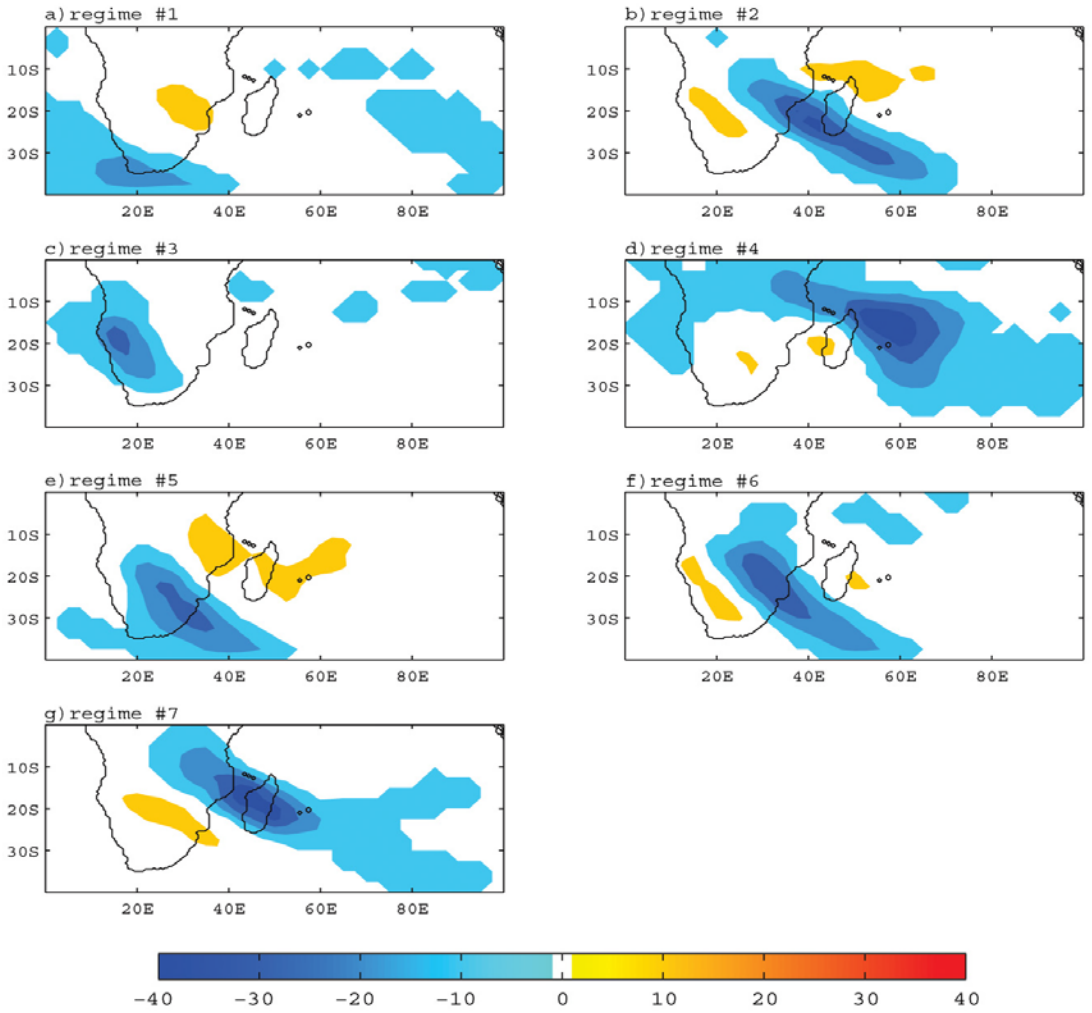

Figure 3.22 Same as Figure 3.21 but for ERA-Interim OLR.

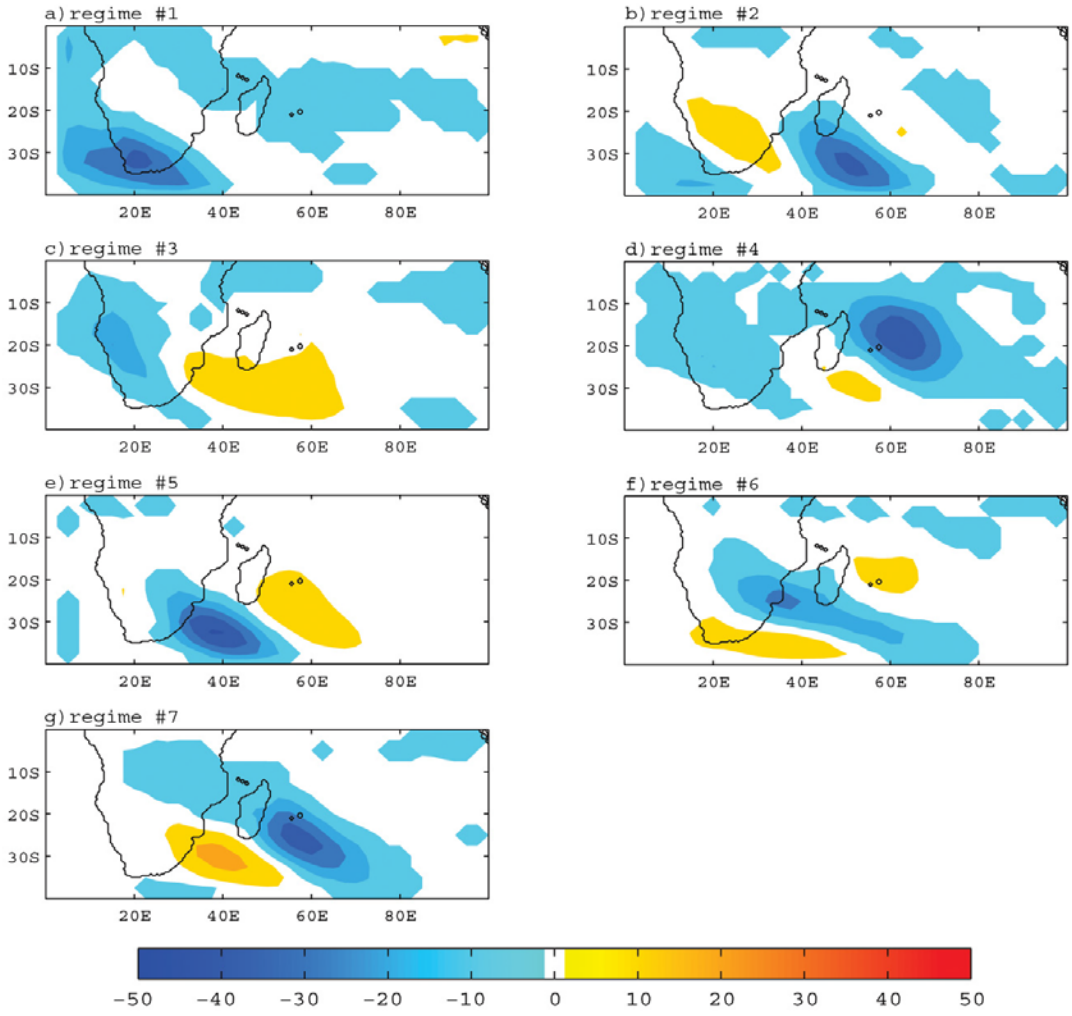

Figure 3.23 Same as Figure 3.21 but for RegCM4 OLR.

Table 3.1 gives the number of occurrences of each regime from NOAA followed by the same or another regime from ERA-Interim. The columns show days' distribution of the 7 regimes from ERA-Interim in each regime from NOAA, and the rows present days' distribution of the 7 regimes from NOAA in each regime from ERA-Interim, where the days with the same regime numbers are indicated in red. This table could be seen as the conditional probabilities of regime transitions and also the agreement of each regime between NOAA and ERA-Interim. More days observed on the diagonal are all more than 30% in each cluster and they give an indication on the persistence of each regime in NOAA and ERA-Interim. It can be seen that more same days laying between the TTTs regimes (regimes #5, #6, #7).

Figure 3.24 shows the OLR bias of each regime between RegCM4 and NOAA. RegCM4 simulates more OLR (~40-60W/m^2) than NOAA in each regime over northern southern Africa region, which corresponds to the results of bias between RegCM4 and CERES in chapter 2 (Figure 2.18) With regard to RegCM4 OLR anomaly composites (Figure 3.23), negative bias bands in Figure 3.24e-g (regime #5,

#6, #7) are associated with the TTTs systems.

Table 3.1 Number of occurrences of each regime in NOAA followed by the same or another regime in ERA-Interim (days)

		ERA-Interim						
NOAA	**Clusters**	**1**	**2**	**3**	**4**	**5**	**6**	**7**
	1	**70**	4	19	1	28	0	12
	2	13	**65**	8	12	0	26	14
	3	8	5	**108**	7	3	6	13
	4	18	2	11	**51**	3	1	28
	5	23	3	31	6	**89**	22	3
	6	9	20	2	1	25	**91**	3
	7	44	16	57	24	4	5	**66**

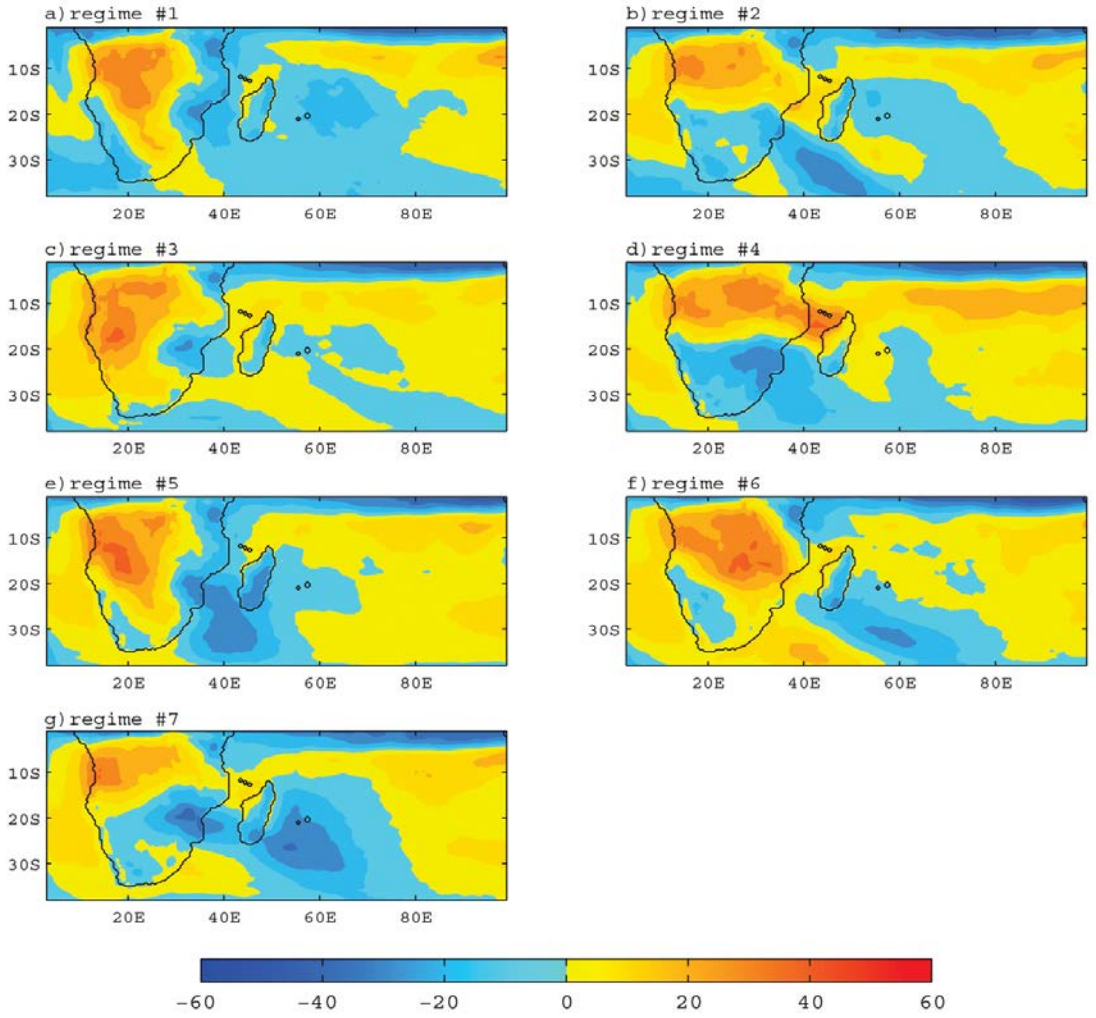

Figure 3.24 Composites of RegCM4 bias (W/m^2) with regard to NOAA for the 7 regimes constructed from OLR for the austral summer months (NDJFMA) over the period 1999-2008.

3.3.2 Relationship to the daily surface solar radiation

In this section, daily SSR anomaly composites for RegCM4 are computed according to the above classification (Figure 3.25), thus showing the daily anomalies associated with the occurrences of the regimes. Regime #1 (Figure 3.25a) is associated with cloudy conditions over South Africa and the adjacent Atlantic Ocean, where we find negative anomalies of SSR. Regime #2 (Figure 3.25b) presents significant positive (negative) SSR anomalies over South Africa (Mozambique Channel and Indian Ocean of south coast of Madagascar), indicating clear (cloudy) conditions over that region. In contrast to regime #2, regime #3 (Figure 3.25c) is a regime during which we get more (less) SSR over the Mozambique Channel and Indian Ocean of south coast of Madagascar (western of southern Africa). During regime #4 (Figure 3.25d) cloudy conditions generally prevail so that negative SSR anomalies appear over southern Africa and the Indian Ocean, with the exception of a small area in the south of Madagascar. In regime #5 (Figure 3.25e), strong negative SSR anomalies (cloudy

conditions) are experienced over the eastern of South Africa and the adjacent Mozambique Channel while positive SSR anomalies (clear sky conditions) occur over the southern of Madagascar and the Indian Ocean adjacent to eastern coast of Madagascar. The occurrence of regime #6 (Figure 3.25f) is associated with cloudy conditions over the northeast of South Africa, south of Mozambique, Zimbabwe, Zambia and Botswana, while regime #7 (Figure 3.25g) is related to large negative (positive) SSR anomalies prevailing over the Indian Ocean, Madagascar and north of southern Africa (eastern of South Africa and Mozambique Channel). Three regimes (Figure 3.25e-g; #5, #6, #7) present negative anomalies bands as observed in the TTTs systems from RegCM4 OLR, explaining thus the synoptic climate variability of SSR over the SWIO and southern Africa.

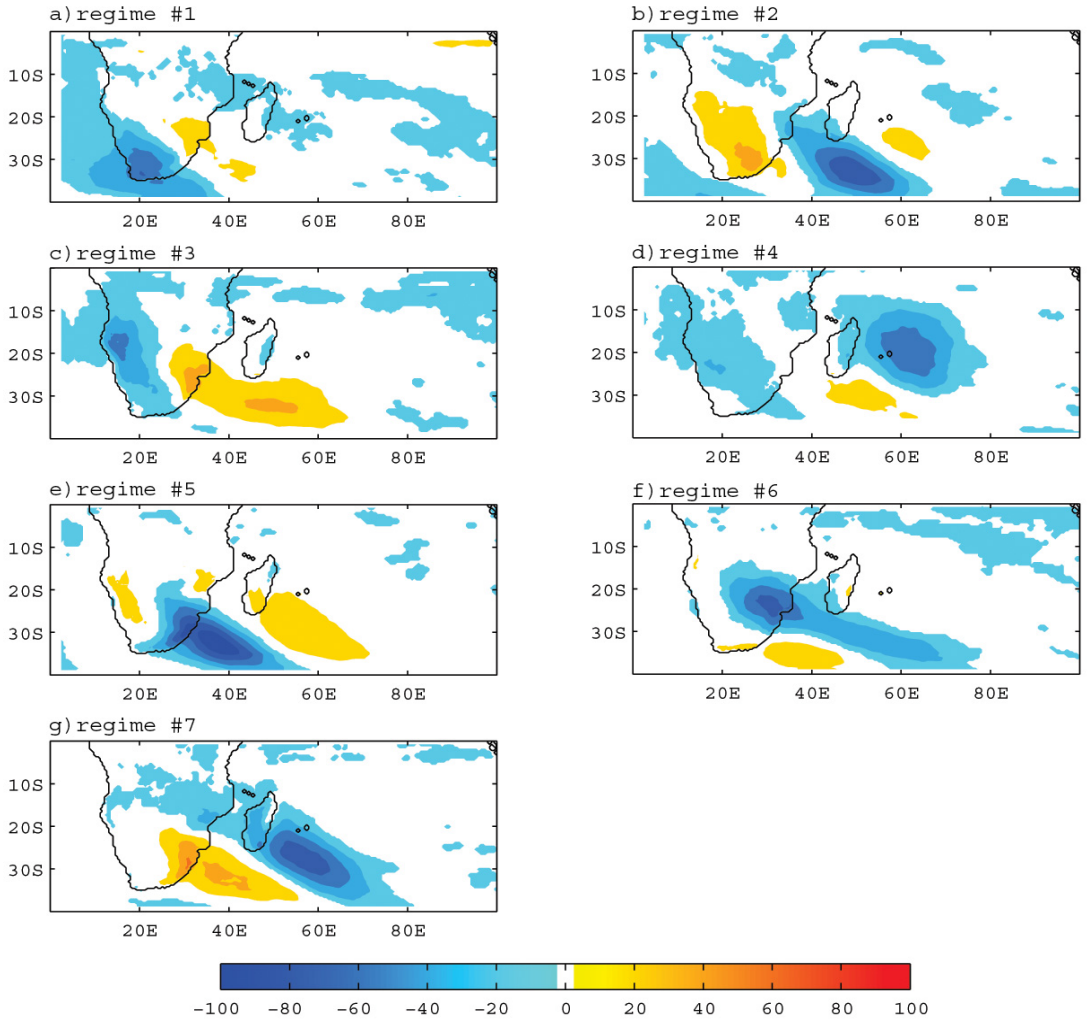

Figure 3.25 Composites of RegCM4 surface solar radiation (SSR) anomalies (W/m^2) for the 7 regimes obtained from the classification of RegCM4 NDJFMA OLR for the period 1999-2008 (Figure 3.23). Only the anomalies significant at the 95% level according to a Student's t-test are displayed.

3.4 Summary and discussion

A RCM should be able to simulate correctly the regional climate variability, as it has been developed for that. However, climate models are imperfect due to the needed discretization in both time and space of continuous processes and mechanisms. Both the forcing global model and the forced regional model contain errors that can sometimes lead to an unrealistic simulated regional climate, if they give very different natural solutions between the two models. In this Chapter, we have characterized the simulated climate variability and assess the overall performance of the regional climate model RegCM. We have considered the effects at regional scales of several modes of large-scale climate variability known to affect the SWIO: ENSO and IOD at the interannual time scales, MJO at the intraseasonal time scale, and TTT at the synoptic time scale. Indeed, our main goal was to check whether the model forced by ERA-Interim reanalyses was able to maintain the ENSO, IOD, MJO and TTT signals,

under the condition that ERA-Interim forcing data would capture those signals. Firstly, several ERA-Interim parameters (U, V, T and RH) along with the corresponding RegCM output data are analyzed. Secondly, simulated SSR in association with the different modes of variability was examined.

To examine the interannual variability associated with ENSO and the IOD, we first calculated the correlation between SSR and the Multivariate ENSO Index (MEI) and the Dipole Mode Index (DMI) separately for austral summer months (NDJF; 1999-2008) from the input (ERA-Interim) and output data from RegCM4 with regard to the related atmospheric parameters. We showed that RegCM4 is able to simulate the anticyclonic circulation in the lower levels over Southern Africa, with lower-air level divergence, and upper-air level convergence, associated with suppressed convection there. Because of drier air subsiding there, the cloud cover is reduced and more SSR can reach the surface and warm it. As expected, the situation is reversed over the SWIO, with enhanced convection there over a warmer ocean that releases more latent heat to the atmosphere, that is an increase in the RH, more clouds and less SSR.

To analyze the intraseasonal variability associated with the MJO, we constructed an index based on RMM1 & RMM2 to define the 8 phases describing the life cycle of an MJO event. We computed SSR anomaly composites in those 8 different phases for both the input (ERA-Interim) and output data of RegCM4 for austral summers (NDJFMA 1999-2008). In the upper atmosphere, we found positive RH anomalies at places where we would find negative SSR anomalies. These anomalies are moving eastward as the MJO shifts. At the lower atmosphere, SSR anomalies can be related to the RH anomalies patterns in each phase, with obvious negative (positive) RH anomalies over South Africa (Madagascar and Mozambique Channel) in phase 5 at places where we would find positive (negative) SSR anomalies. Regard to the air temperature, there are areas where the patterns are inverted with regard to SSR.

Finally we applied k-means clustering onto the daily OLR from ERA-Interim and RegCM4 to identify the TTTs systems according to NOAA OLR patterns. RegCM4 SSR gives similar anomalies distribution according to the classification of OLR, which present kind of synoptic climate variability. Daily SSR anomaly composites for RegCM4 are computed according to the classification, showing the daily anomalies associated with the occurrences of the regimes. Three regimes present negative anomalies bands as observed in the TTTs systems from RegCM4 OLR, explaining thus the synoptic climate variability of SSR over the SWIO and southern Africa.

In general, RegCM4 appears to be able to simulate the temporal variability of SSR based on the analysis of interannual variability, intraseasonal variability and synoptic climate variability. However, there is still some future work needed to study. The 10-year period analyzed in our study doesn’t contain any major ENSO and IOD events. Though the model achieved a good performance in reproducing the

interannual climate variability over this period, it would be interesting to run one simulation of the model over a much longer period (about 30 years) containing several major events, and look at the way the model reproduces those events. As ENSO and IOD are not independent, a partial correlation technique could be used to distinguish the impact of one phenomenon on the other. The modulation of the MJO by ENSO could also be studied in a future study. To define whether the model's good performance due to the intrinsic qualities of model itself or the lateral forcing, it would be interesting to run the tropical band of the model (Coppola et al. 2012) to see how the model effectively maintain the MJO signal when only forced at the northern and southern boundaries of the domain.

Appendix (Figures for MJO composites)

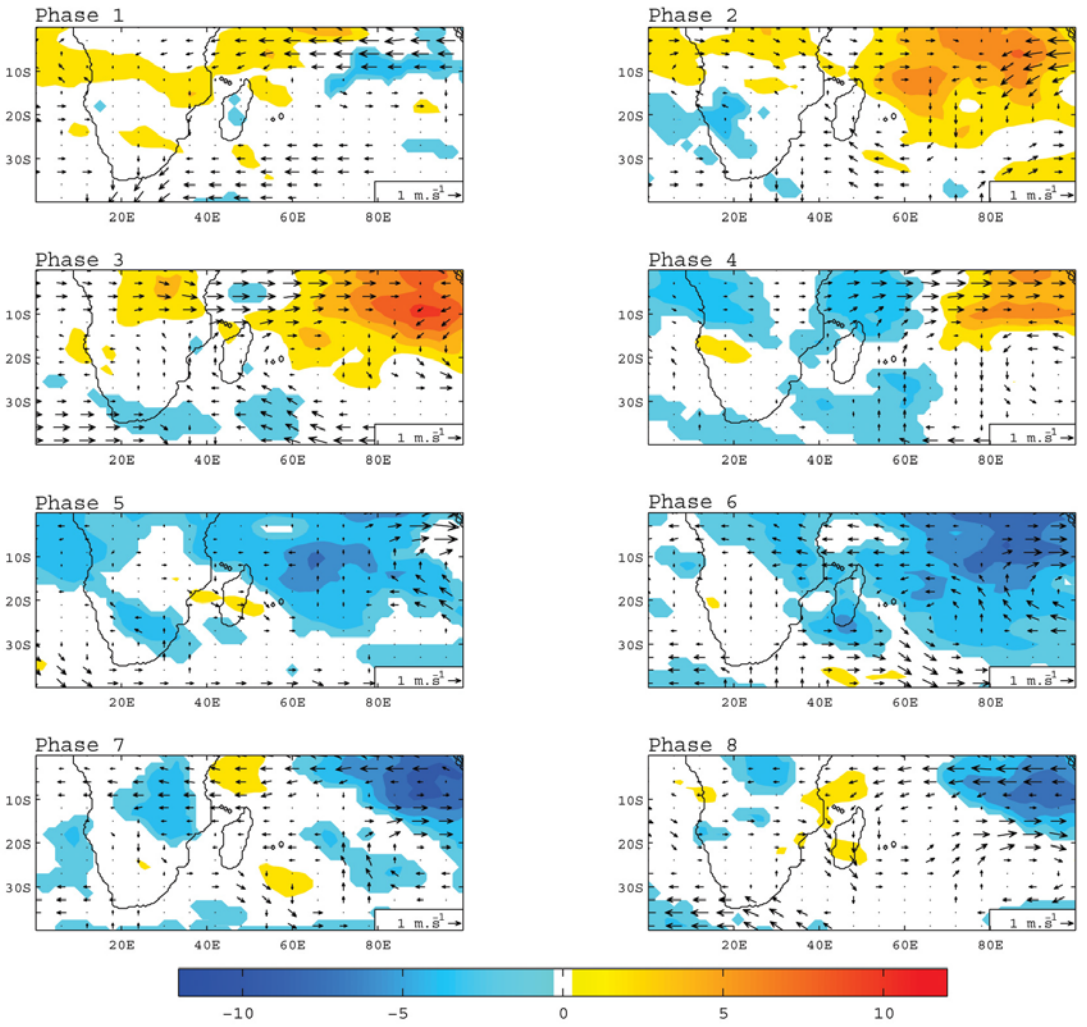

Figure A1) composite of RH (ERA-Interim) anomalies at 8 phases with band-pass 20-100days associated with wind anomalies at 500hPa during Nov to Apr 1999-2008

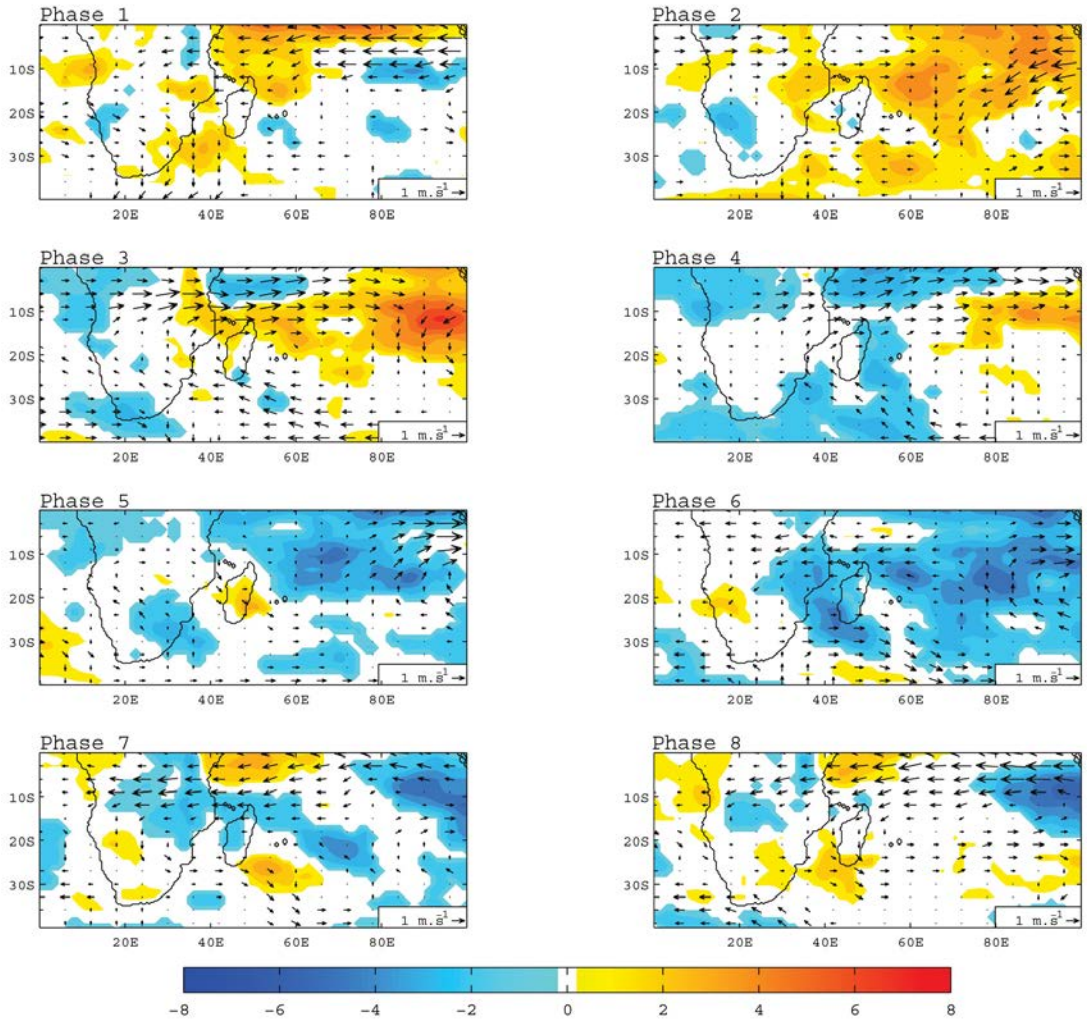

Figure A2) composite of RH (ERA-Interim) anomalies at 8 phases with band-pass 20-100days associated with wind anomalies at 700hPa during Nov to Apr 1999-2008

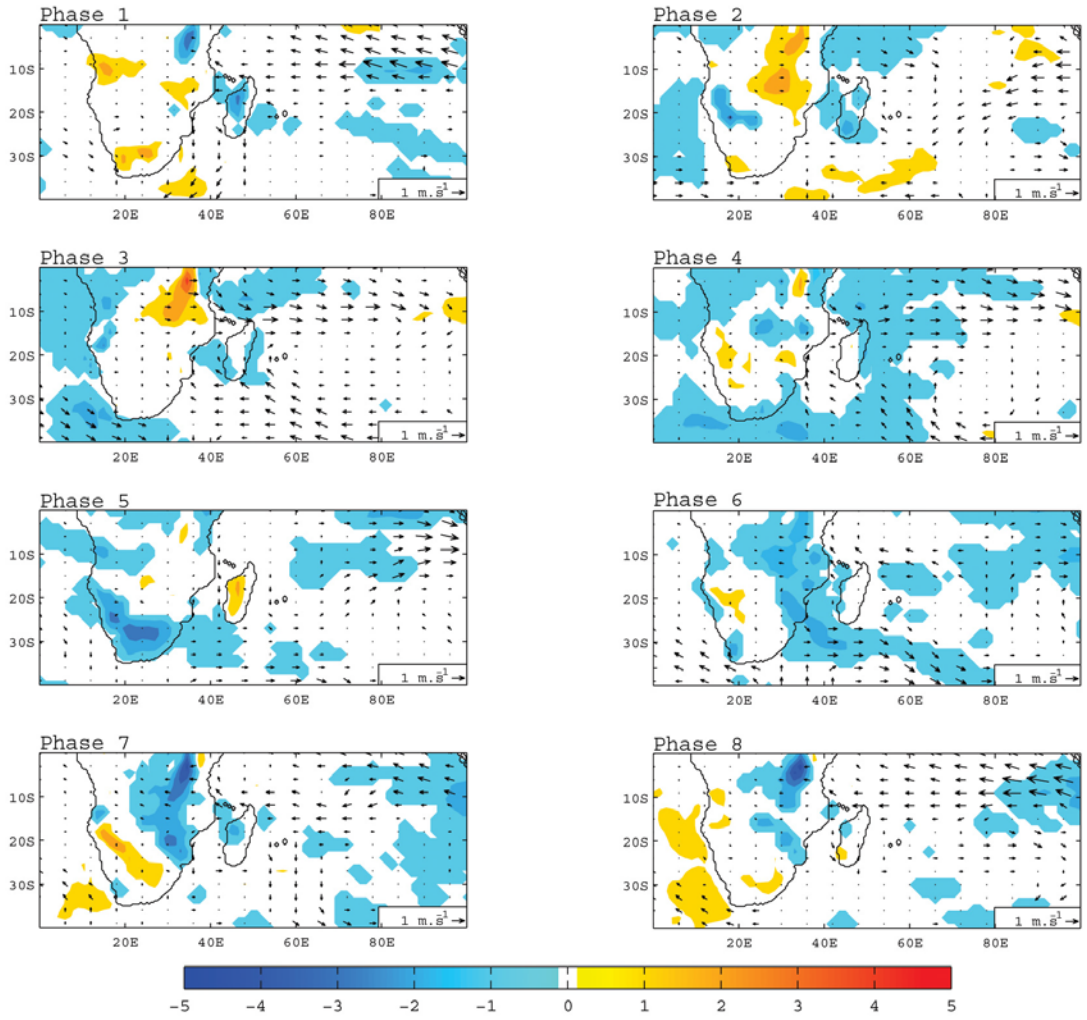

Figure A3) composite of RH (ERA-Interim) anomalies at 8 phases with band-pass 20-100days associated with wind anomalies at 1000hPa during Nov to Apr 1999-2008

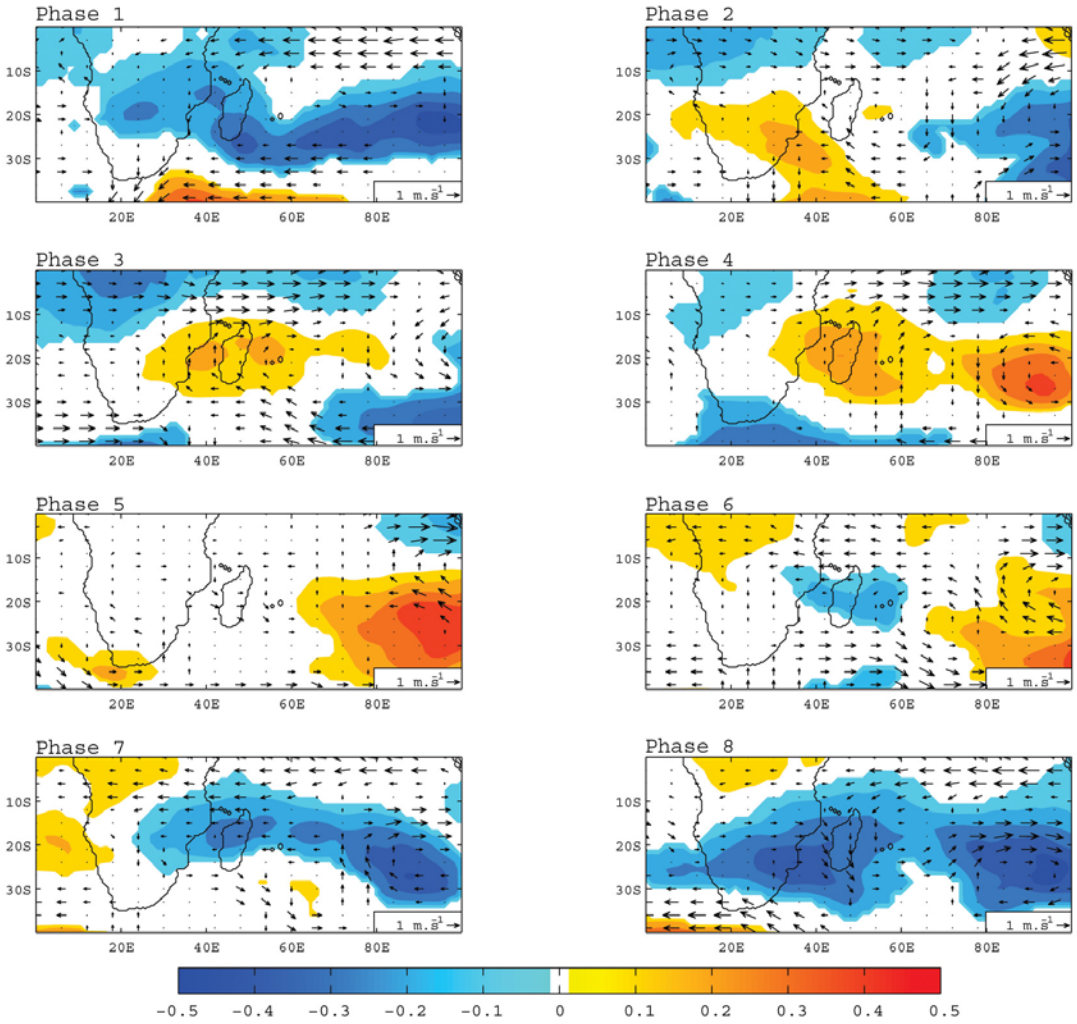

Figure A4) composite of T (ERA-Interim) anomalies at 8 phases with band-pass 20-100days associated with wind anomalies at 500hPa during Nov to Apr 1999-2008

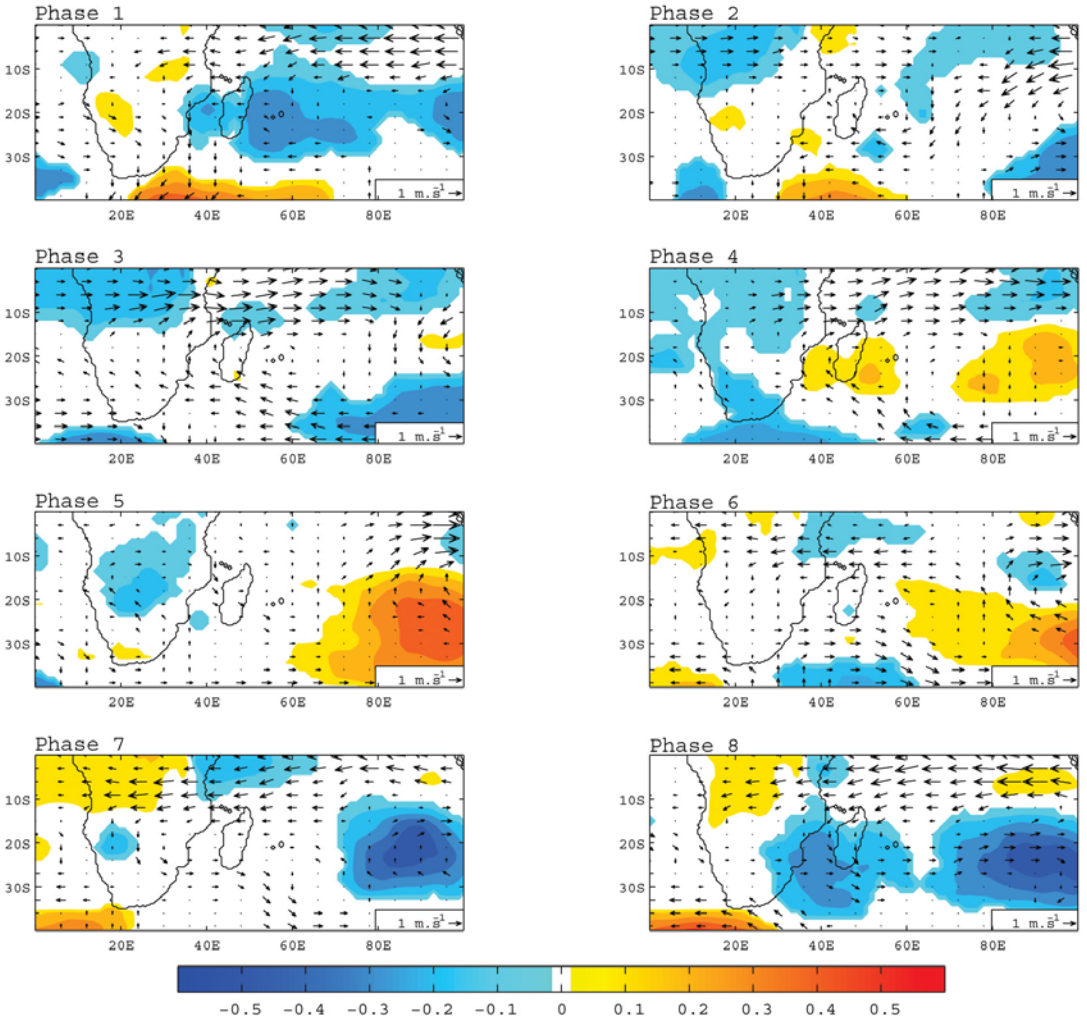

Figure A5) composite of T (ERA-Interim) anomalies at 8 phases with band-pass 20-100days associated with wind anomalies at 700hPa during Nov to Apr 1999-2008

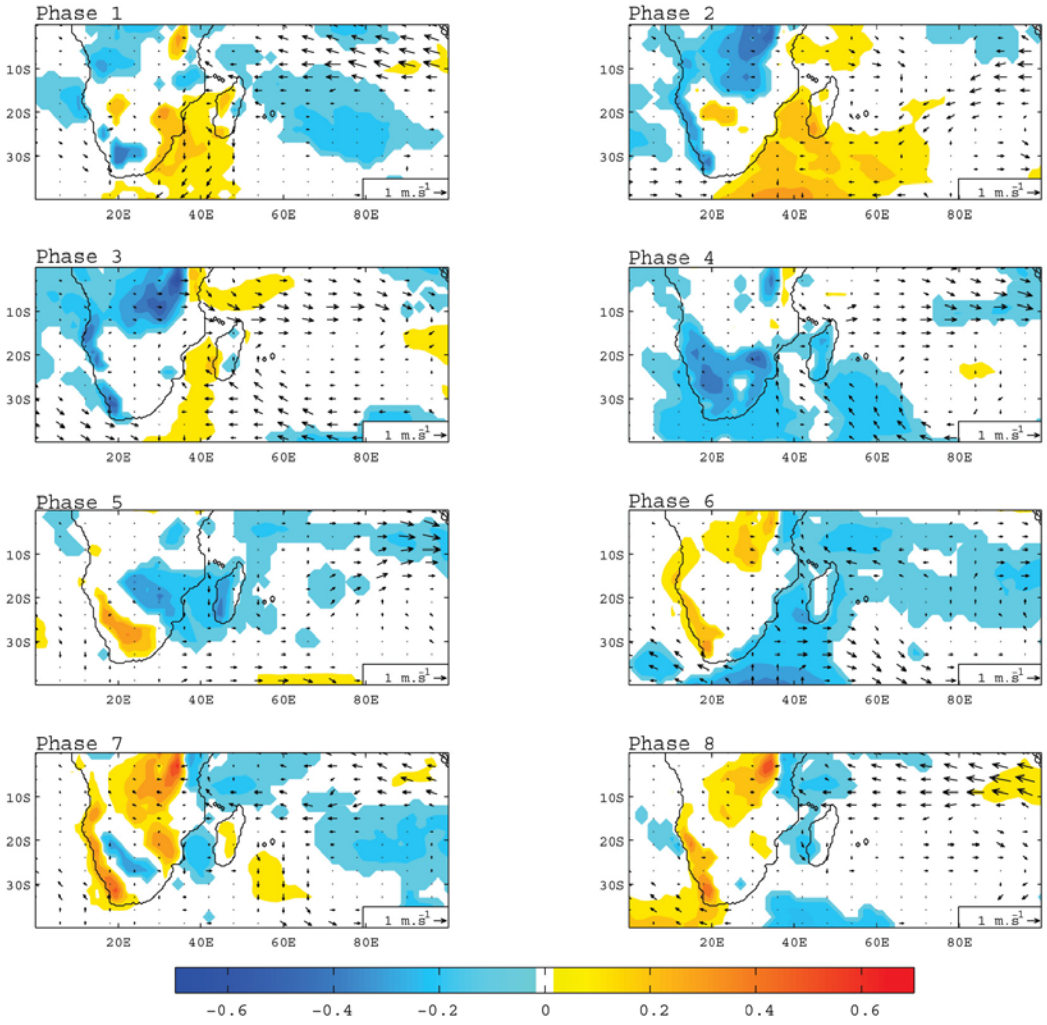

Figure A6) composite of T (ERA-Interim) anomalies at 8 phases with band-pass 20-100days associated with wind anomalies at 1000hPa during Nov to Apr 1999-2008

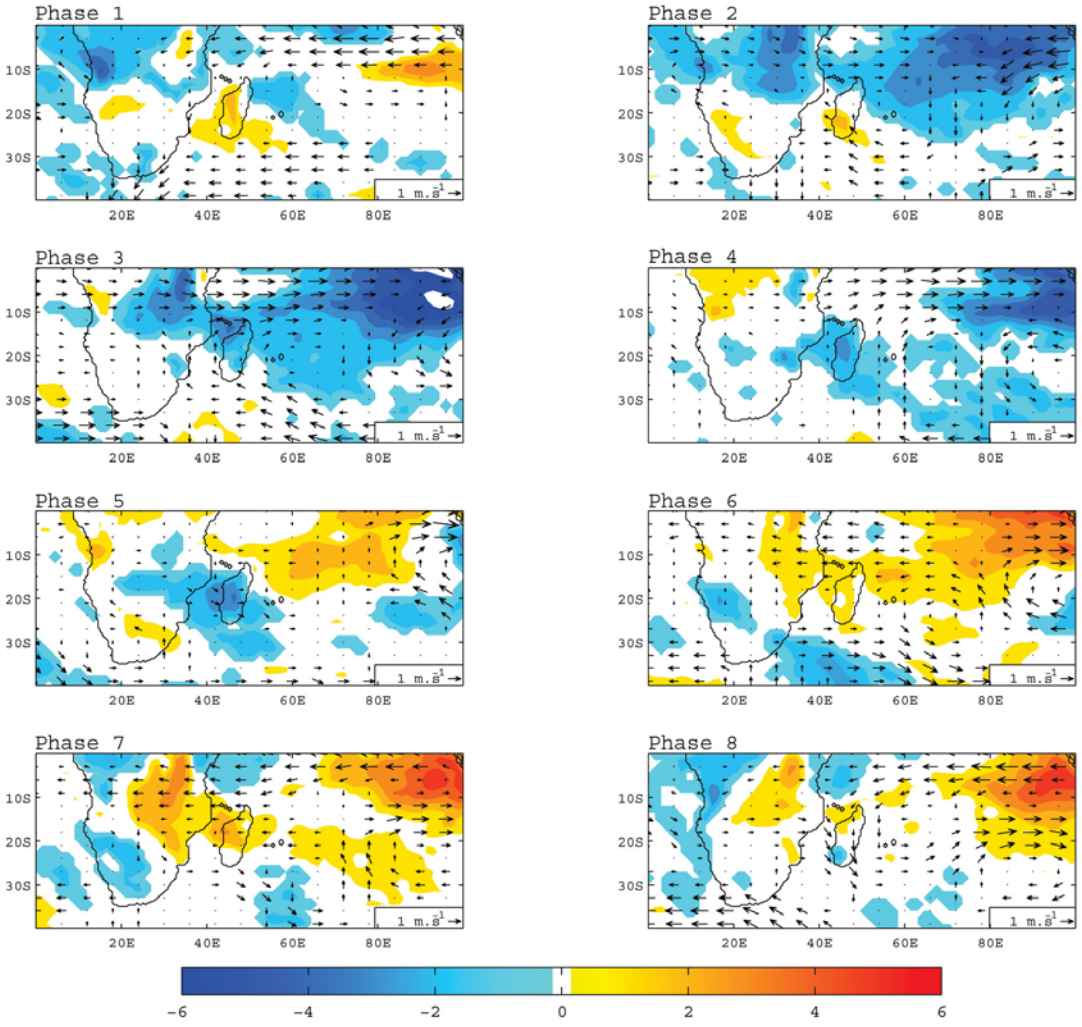

Figure A7) composite of SSR (ERA-Interim) anomalies at 8 phases with band-pass 20-100days associated with wind anomalies at 500hPa during Nov to Apr 1999-2008

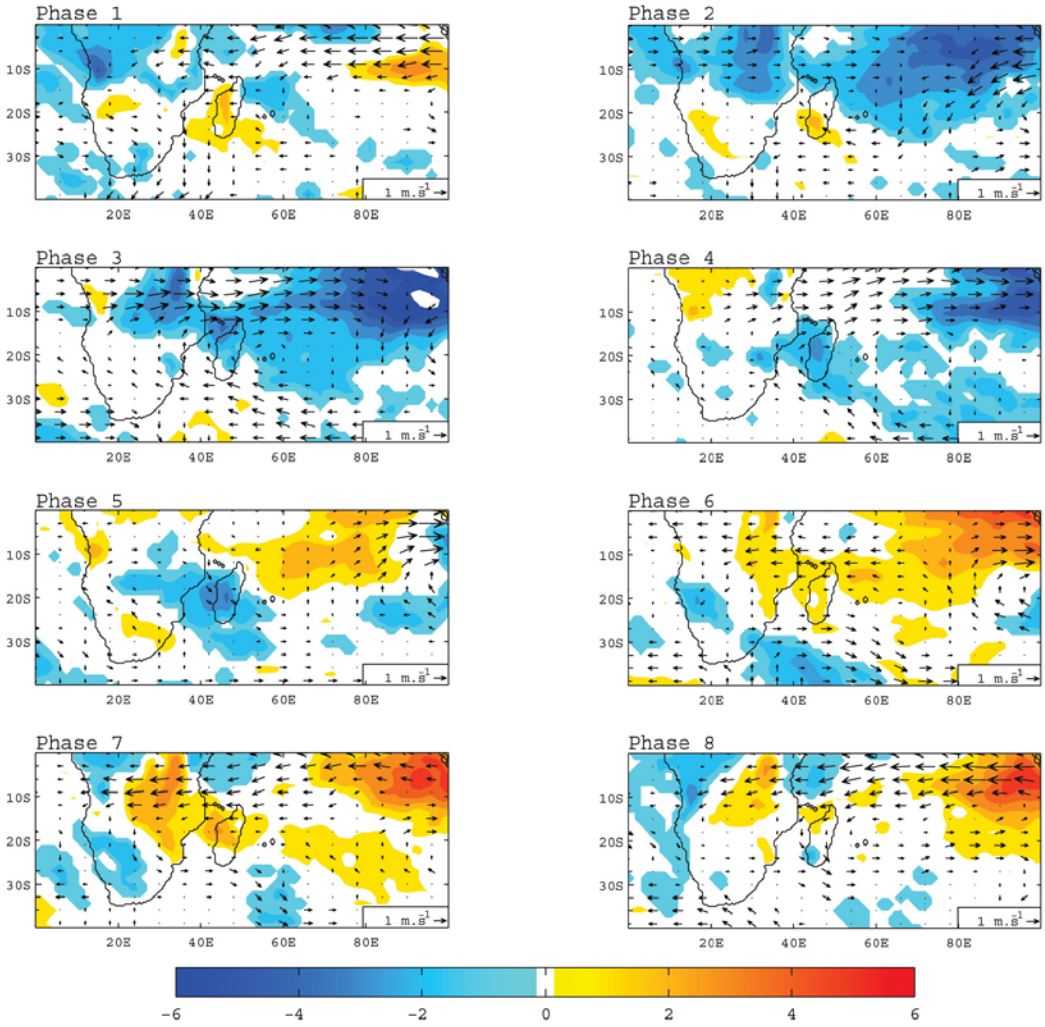

Figure A8) composite of SSR (ERA-Interim) anomalies at 8 phases with band-pass 20-100days associated with wind anomalies at 700hPa during Nov to Apr 1999-2008

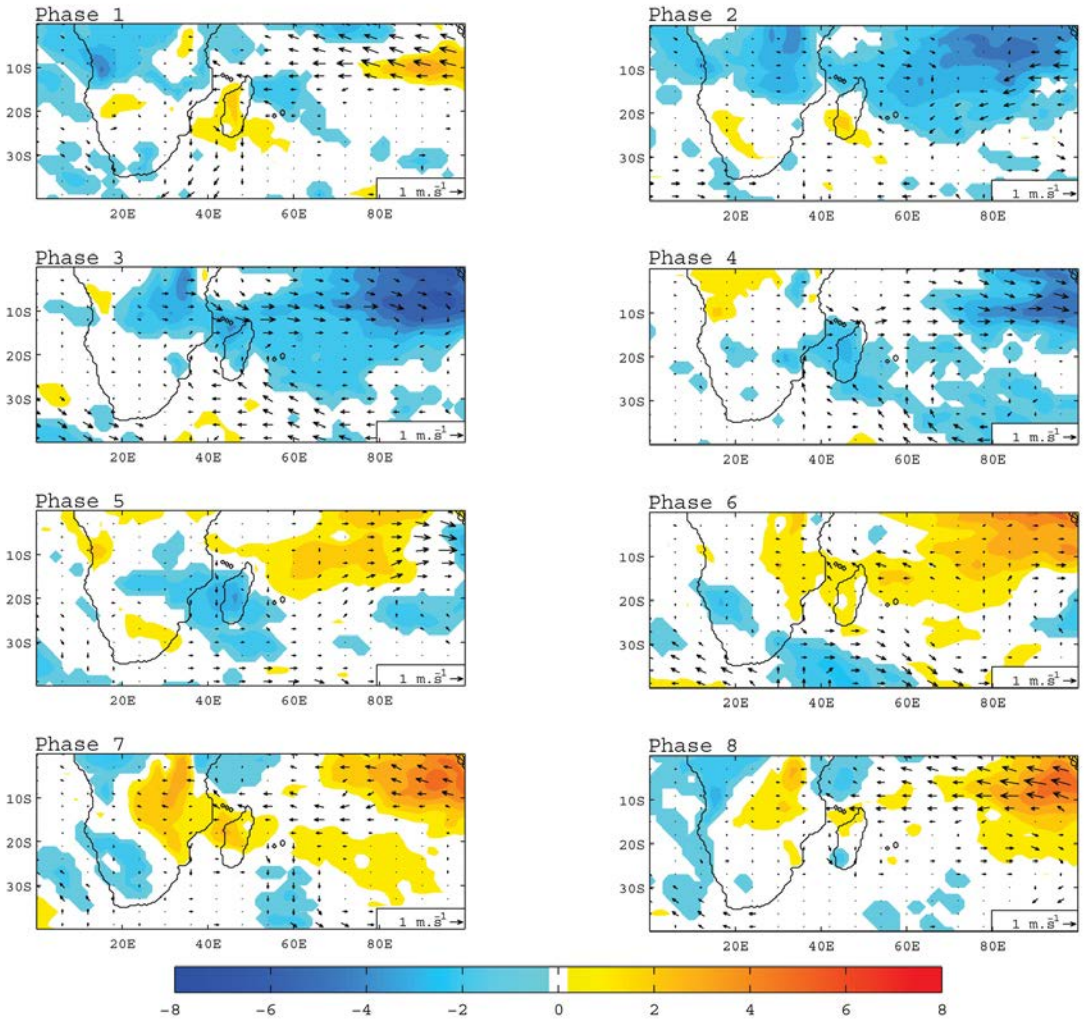

Figure A9) composite of SSR (ERA-Interim) anomalies at 8 phases with band-pass 20-100days associated with wind anomalies at 1000hPa during Nov to Apr 1999-2008

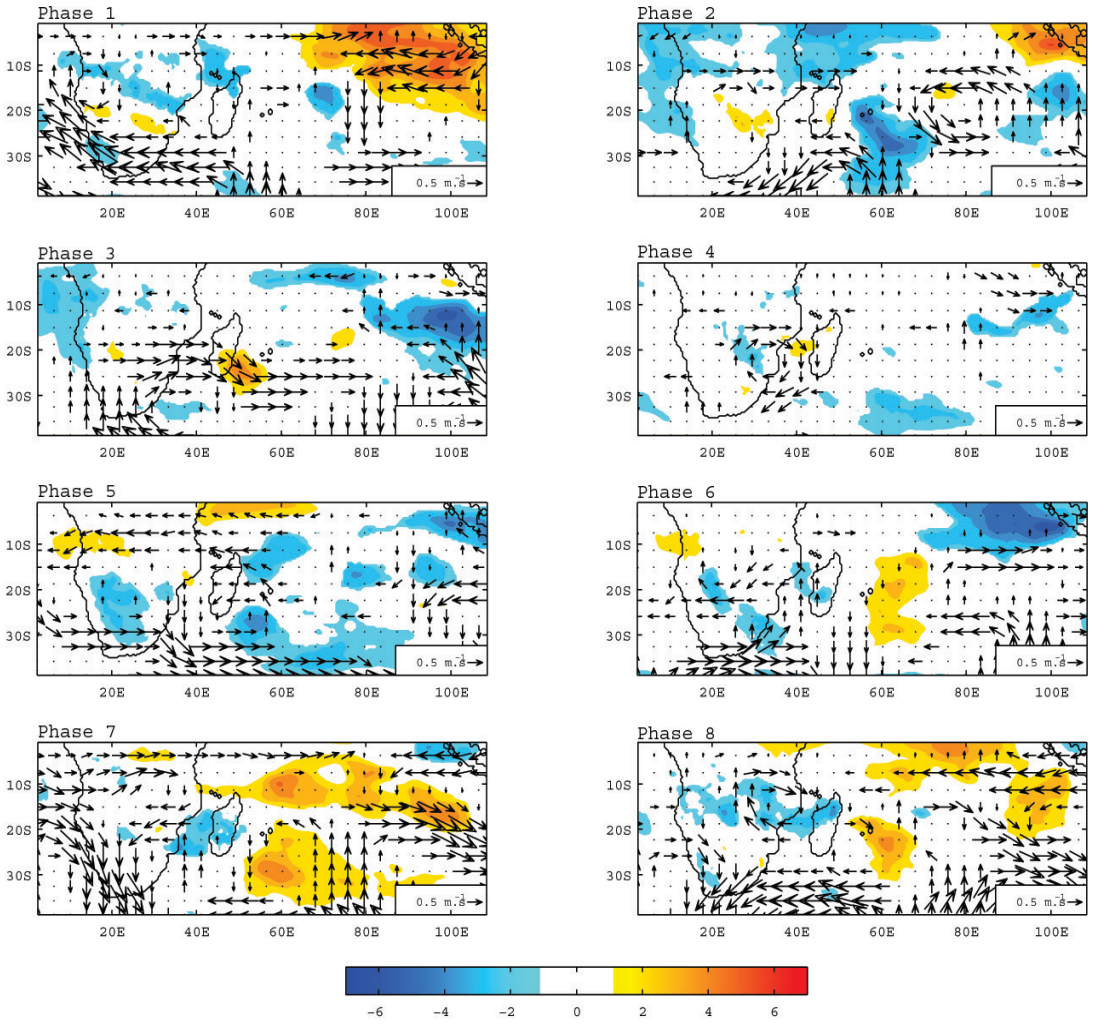

Figure A10) composite of RH (RegCM4) anomalies at 8 phases with band-pass 20-100days associated with wind anomalies at 500hPa during Nov to Apr 1999-2008

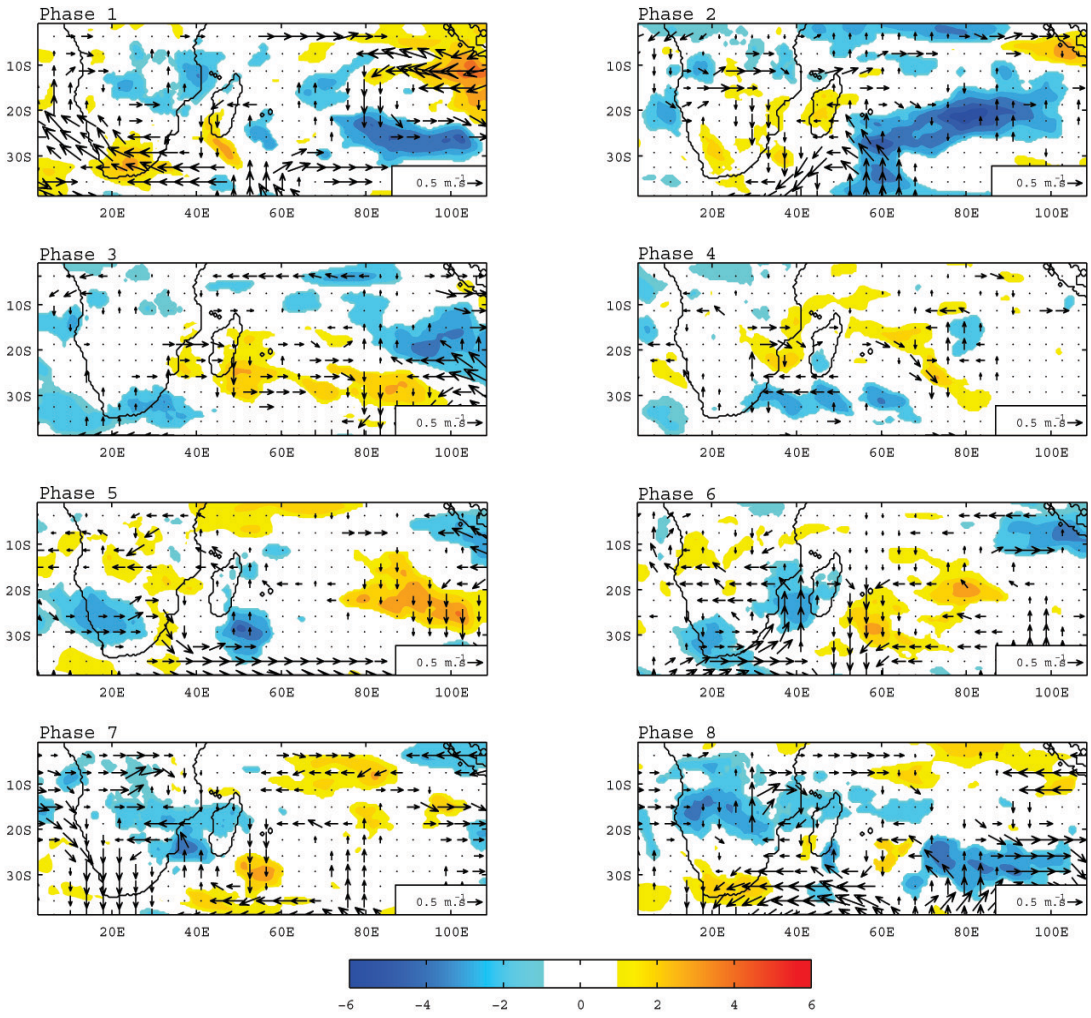

Figure A11) composite of RH (RegCM4) anomalies at 8 phases with band-pass 20-100days associated with wind anomalies at 700hPa during Nov to Apr 1999-2008

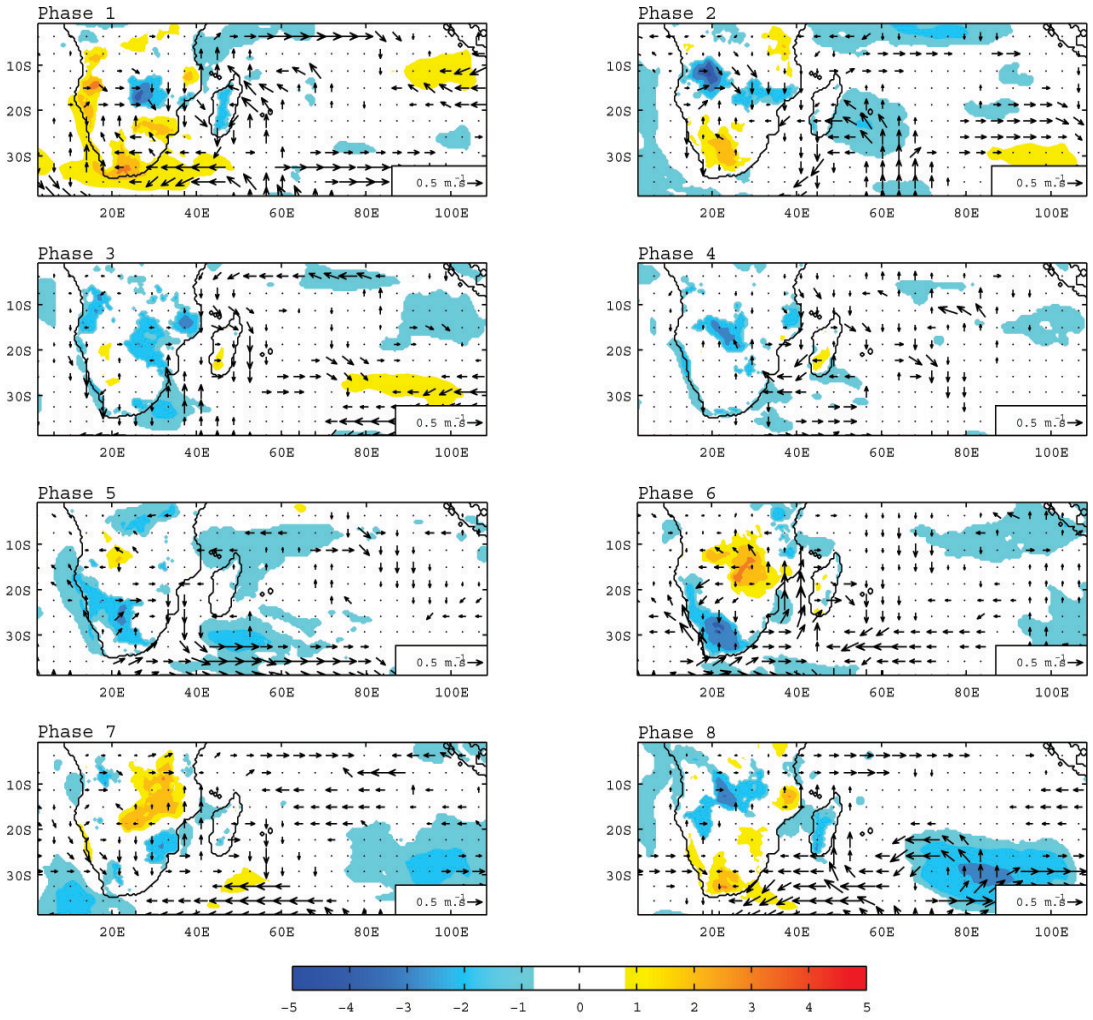

Figure A12) composite of RH (RegCM4) anomalies at 8 phases with band-pass 20-100days associated with wind anomalies at 1000hPa during Nov to Apr 1999-2008

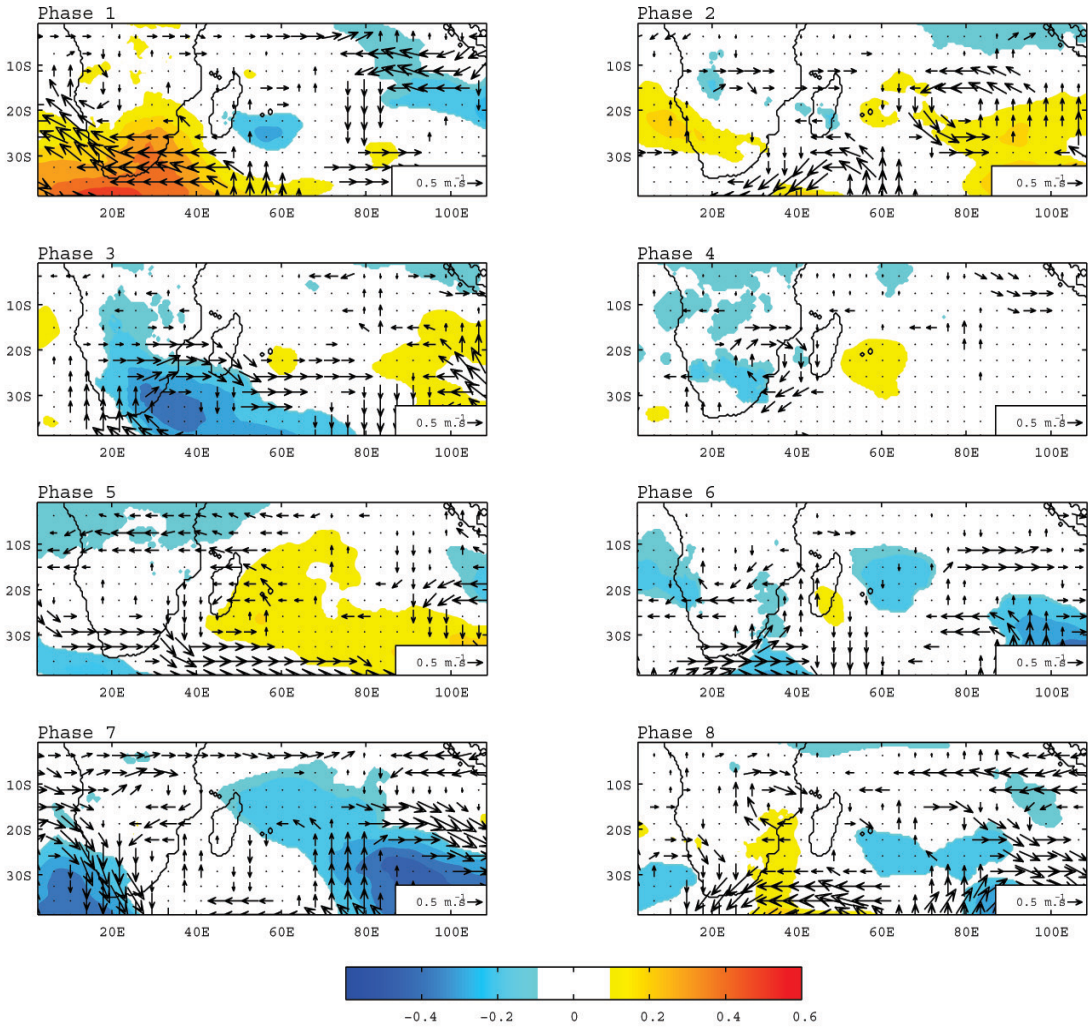

Figure A13) composite of T (RegCM4) anomalies at 8 phases with band-pass 20-100days associated with wind anomalies at 500hPa during Nov to Apr 1999-2008

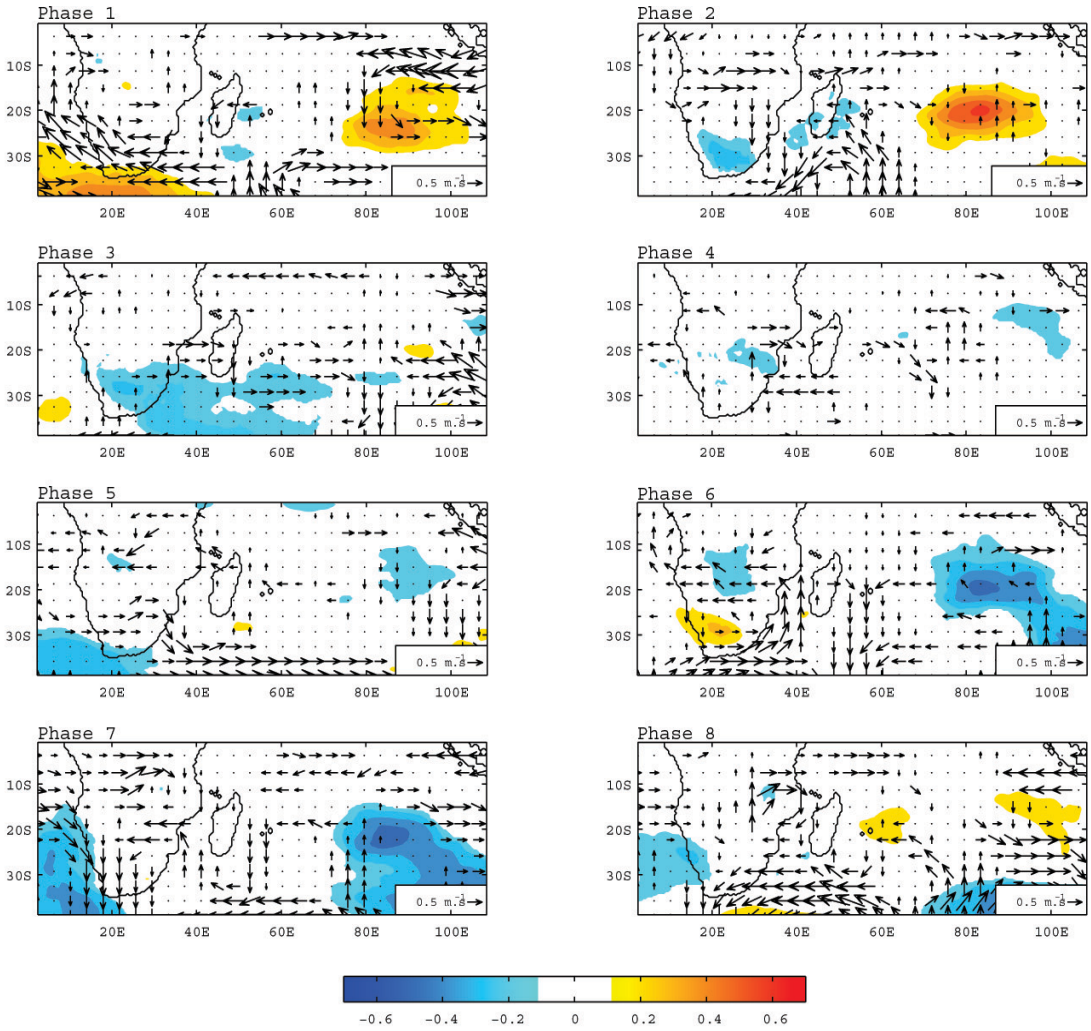

Figure A14) composite of T (RegCM4) anomalies at 8 phases with band-pass 20-100days associated with wind anomalies at 700hPa during Nov to Apr 1999-2008

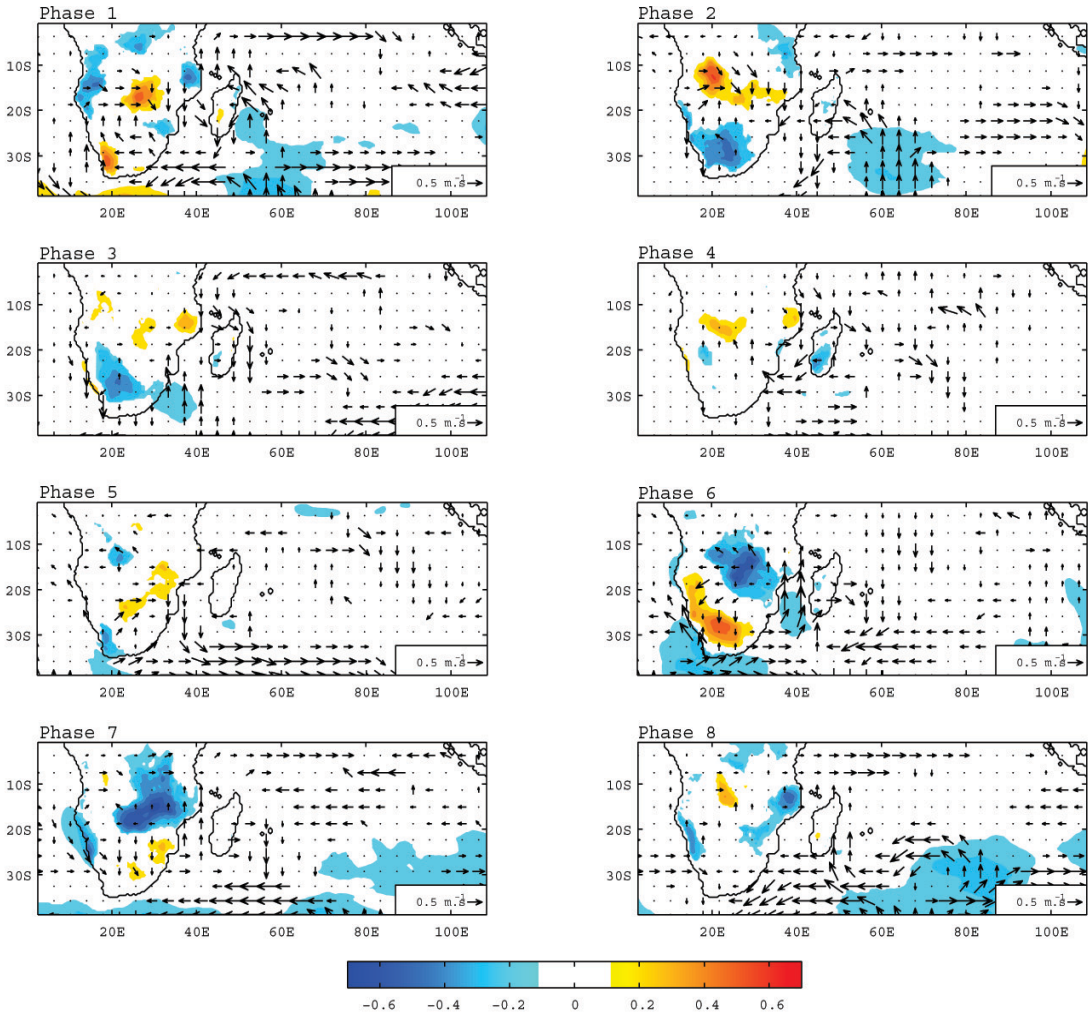

Figure A15) composite of T (RegCM4) anomalies at 8 phases with band-pass 20-100days associated with wind anomalies at 1000hPa during Nov to Apr 1999-2008

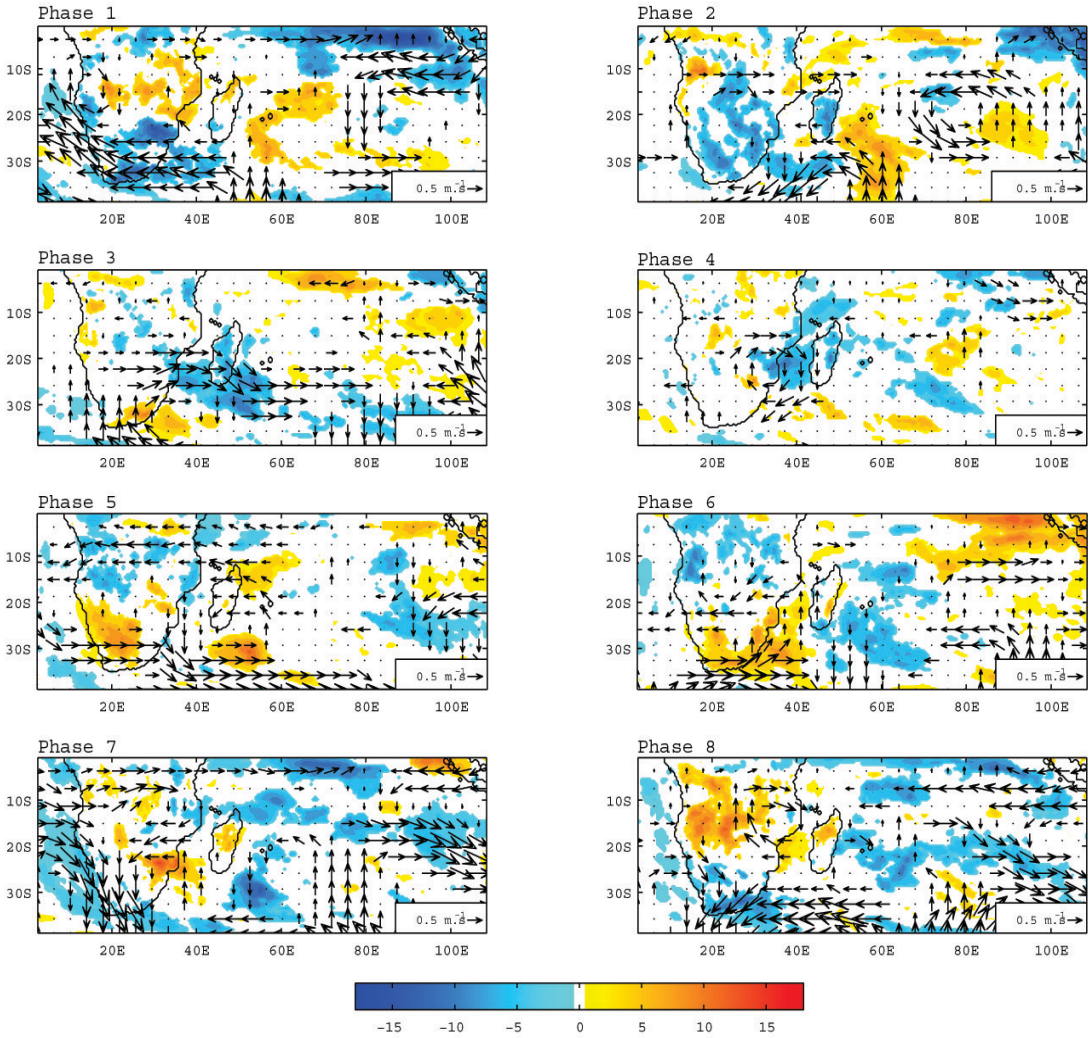

Figure A16) composite of SSR (RegCM4) anomalies at 8 phases with band-pass 20-100days associated with wind anomalies at 500hPa during Nov to Apr 1999-2008

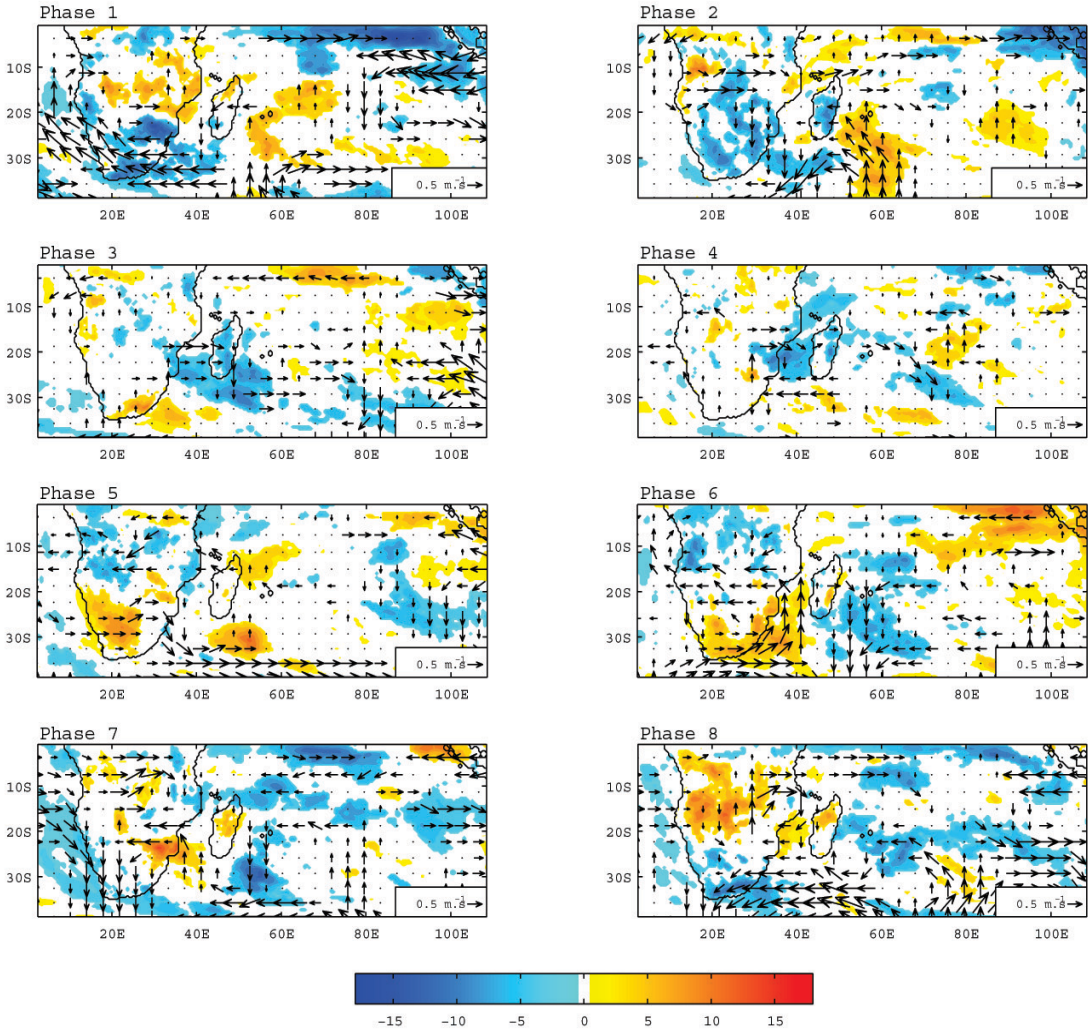

Figure A17) composite of SSR (RegCM4) anomalies at 8 phases with band-pass 20-100days associated with wind anomalies at 700hPa during Nov to Apr 1999-2008

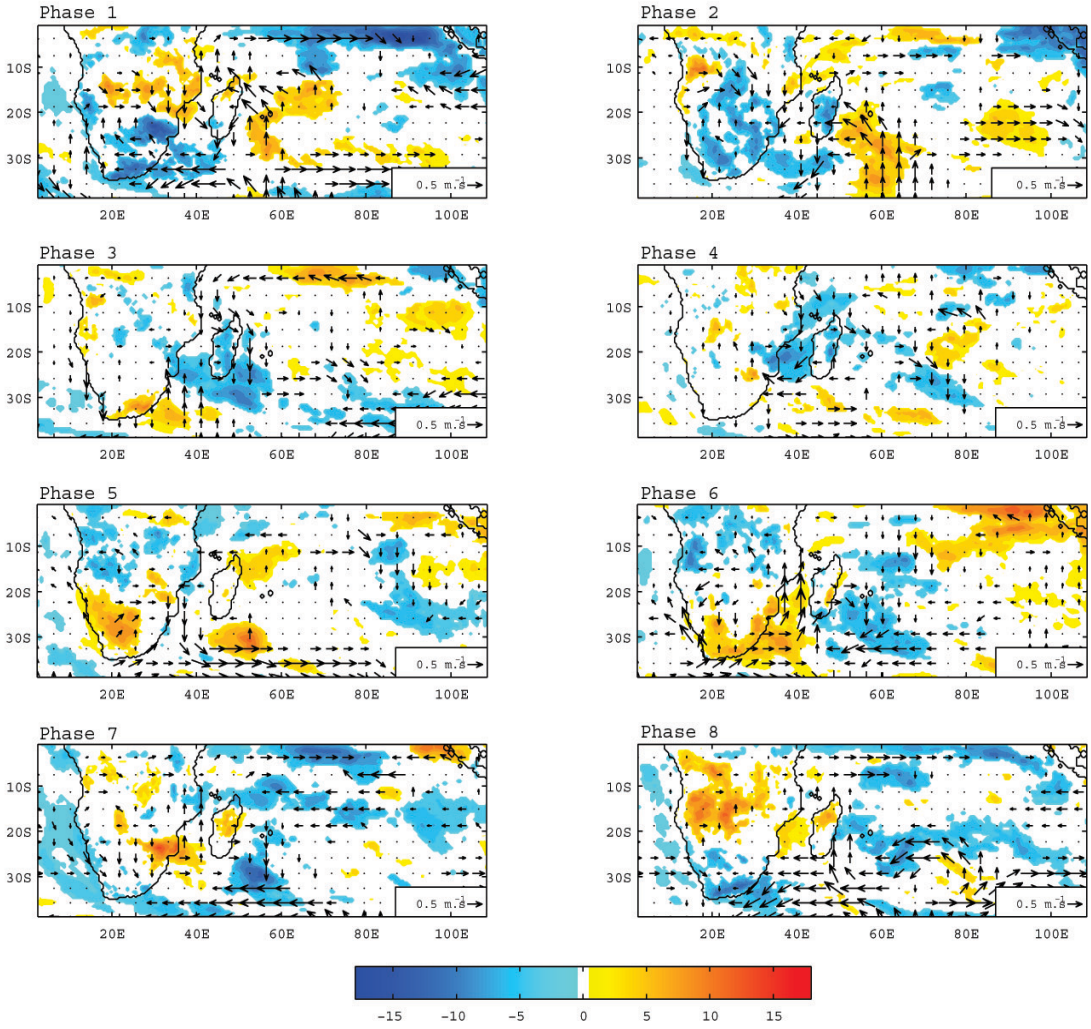

Figure A18) composite of SSR (RegCM4) anomalies at 8 phases with band-pass 20-100days associated with wind anomalies at 1000hPa during Nov to Apr 1999-2008

Chapter 4

Spatial Variability of Surface Solar Radiation over Reunion

Morel et al. (2014) documented the capabilities of WRF RCM to regionalize associated rainfall at very high resolution (680m): this good performance was notably due to a nudging technique guiding the RCM towards the large-scale atmospheric configurations derived from the forcing ERA-Interim reanalyses. In this Chapter, we conduct ensemble simulations to assess the capability, usefulness and limitations of WRF to regionalize SSR over Reunion Island at very high resolution (a few hundreds of meters). Time scales considered in this work range from seasonal differences between two contrasted rainy seasons on the one hand, to daily SSR on the other hand. Seasonal means and intraseasonal variability are also documented. Following the work of Morel et al. (2014), two contrasted wet seasons (November–April) are selected: 2000–2001 (abnormally dry) and 2004–2005 (abnormally wet). To evaluate the RCM skill, we utilize the satellite products at 3-km resolution provided by CM_SAF along with the ground-based measurements from the network of about 39 radiometers maintained by Météo France. Because a direct comparison on a ‘‘grid by point’’ basis may provide intrinsic errors due to the potentially high local variability of clouds on oceanic tropical islands, a ‘‘grid to grid’’ comparison, which accounts for this local variability, should be preferred (Morel et al. 2014). However, 23 of the 39 Météo France stations are located below 500m above sea level, 8 of them between 500 and 1000m above sea level, and the remaining 8 above 1000m above sea level, and we therefore haven’t tried to statistically interpolate the observations onto WRF grid.

4.1 Seasonal mean

Figure 4.1 shows seasonal mean SSR for austral summer as simulated by WRF for the two time periods: 2000-2001 and 2004-2005 over Reunion Island, along with CM_SAF and Météo France data. The two WRF simulated means look fairly similar with generally more SSR along the coast and in the inner part of the island where values can reach as much as 300W/m^2. This pattern is presumably driven by the topography, though the differences between the two periods are likely due to differences in the climatology of the two periods. Indeed, the highest values of SSR (about 320 W/m^2) are found along the south-west coast of the island and at a few locations inland (Piton de La Fournaise, Cirques of Mafate and Cilaos; Figure 1.3) in 2000-2001. This is consistent with the observed spatial patterns as obtained from Météo France, though WRF tends to produce higher values of SSR on the coast and inland and lower ones at mid-level altitudes.

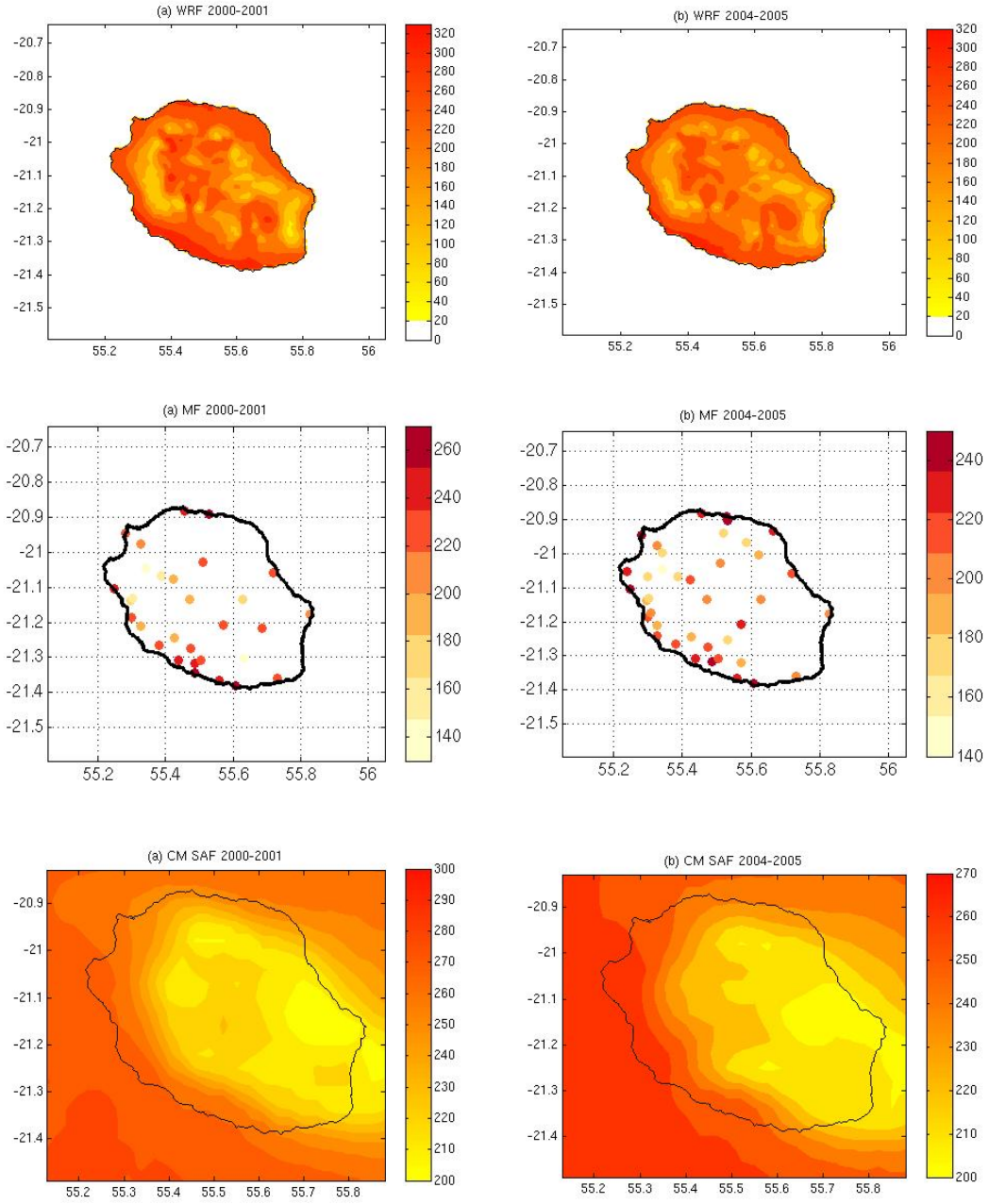

Figure 4.1 a) WRF simulated seasonal SSR at 750-m spatial resolution, Météo France observed seasonal SSR and CM SAF seasonal SSR (3km) for 2000-2001; b) same as a), but for 2004-2005 (W/m^2).

WRF SSR seasonal mean from the five ensemble members is interpolated onto the CM SAF grid (0.03°×0.03°) and the error is calculated between them for austral summer 2000 to 2001 and 2004 to 2005 (Figure 4.2). The shift of CM SAF patterns could be noted in Figure 4.2 when comparing to the WRF SSR for two seasons. CM SAF simulates more SSR than WRF over the Reunion, except at a few locations

inland (Piton de La Fournaise, Cirques of Mafate and Cilaos). WRF seems able to produce fine contrasts with small patches of higher SSR along the edges of the Cirques due to its higher resolution.

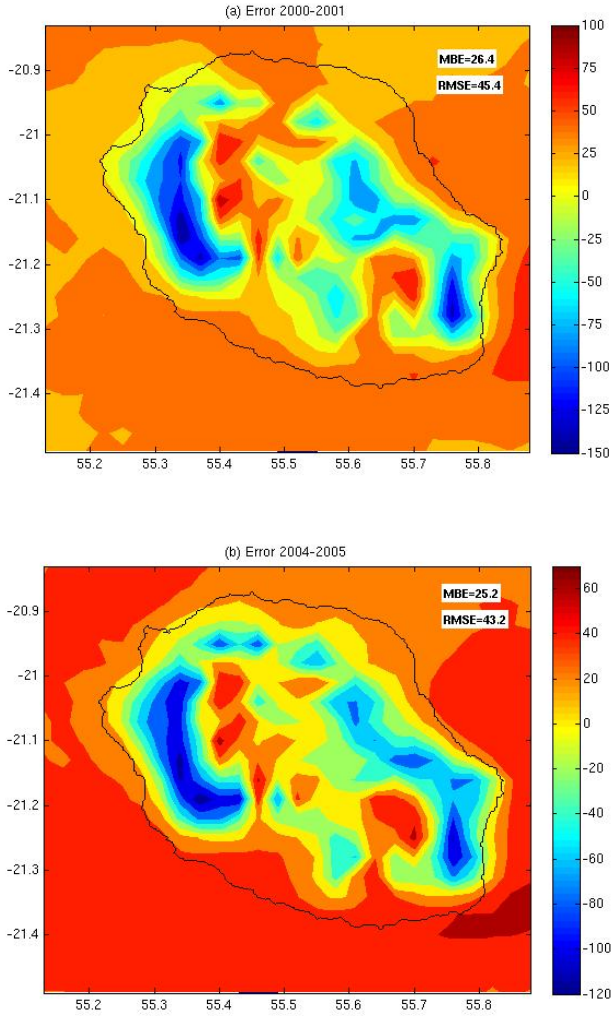

Figure 4.2 a) SSR errors between WRF and CM SAF for austral summer 2000-2001; b) same as a), but for 2004-2005 (W/m^2).

Simulated monthly SSR of WRF and CM_SAF are also compared to Météo France at 5 stations for austral summer 2004-2005 individually in Figure 4.3. These plots show that apart Gillot (coastal site, about 0m above sea level) at which WRF and CM_SAF give reduced errors, they both have difficulties in reproducing the irradiance at every other site considered, probably because of the topography effects (CM_SAF at only 3-km resolution and WRF though run at 750-m resolution may not properly represents orographic clouds).

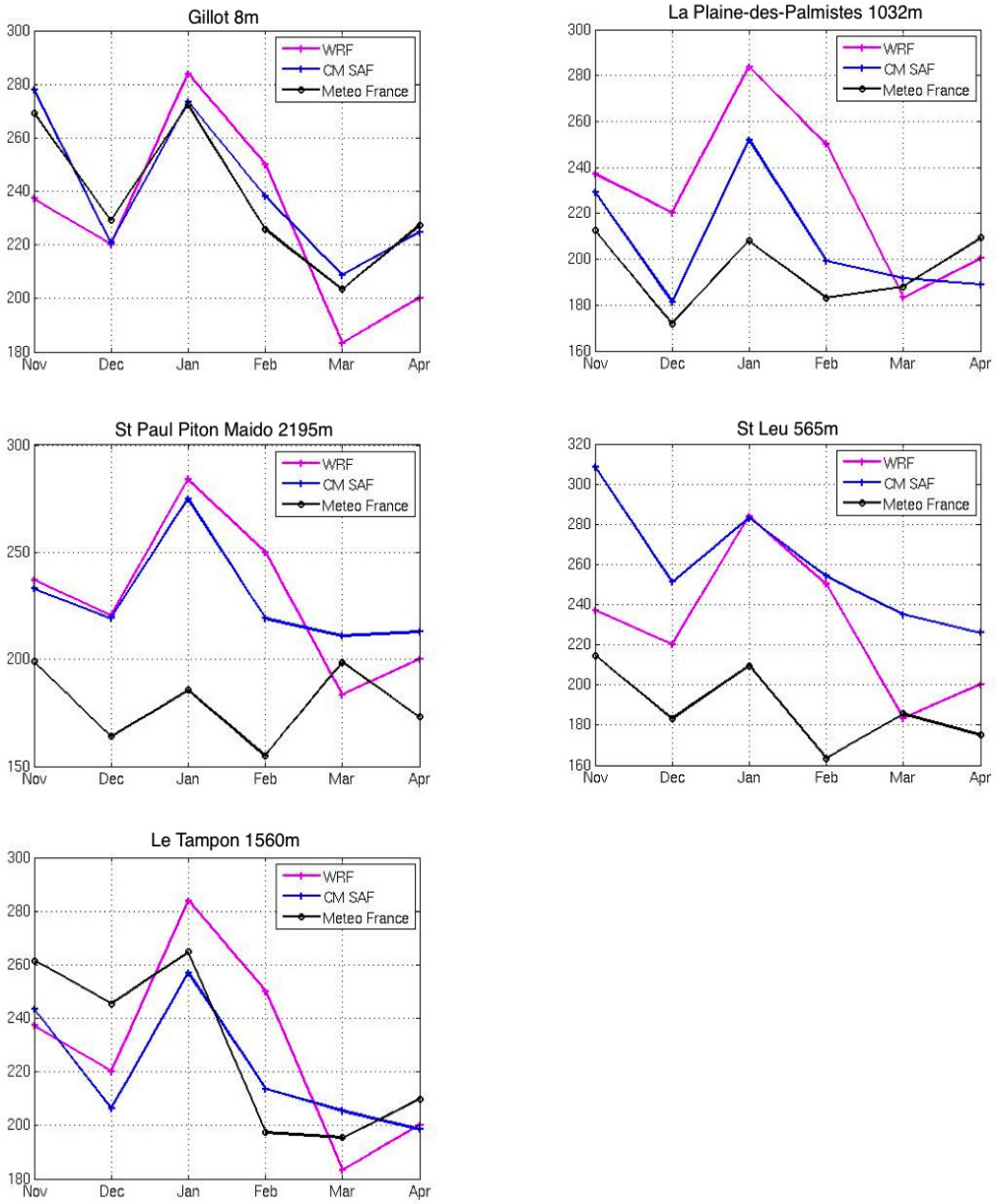

Figure 4.3 WRF simulated monthly means and CM SAF compared to Météo France data at 5 stations separately for austral summer 2004-2005 (W/m^2).

With regard to the total cloud cover (TCC) simulated by WRF for two seasons (Figure 4.4) and the MODIS cloud image for Nov 2007 to Apr 2015 (Figure 4.5; from Mike Douglas, NOAA), more SSR along the south-west coast of the island and the inland area is associated to the TCC. Where Figure 4.4 and 4.5 show less TCC, there is more SSR. At the same time, SSR patterns are consistent with the rainfall patterns in Morel et al. (2014) for two seasons. There is more TCC for 2004-2005 (Figure 4.4b) than 2000-2001, indicating 2000-2001 is drier than 20004-2005, which is found in Morel et al. (2004). Even though the time period of MODIS TCC is different with that we study, WRF still could give the similar patterns regard to its multi-year average for 8

years.

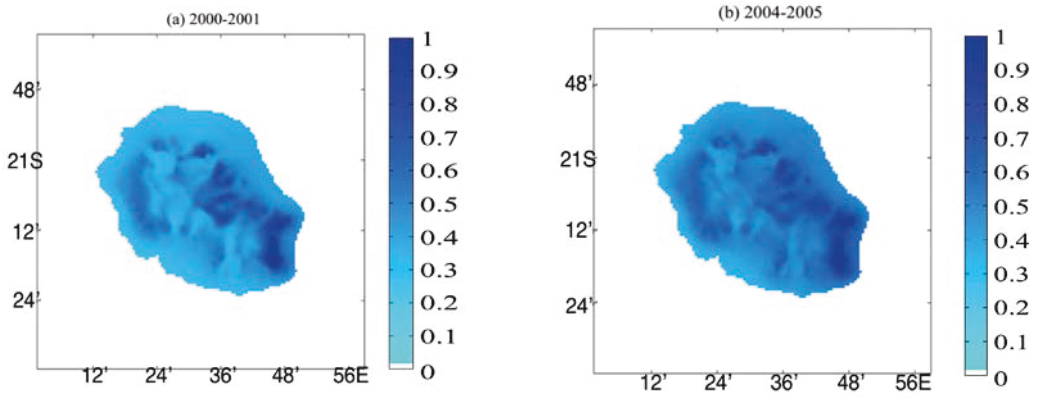

Figure 4.4 a) WRF seasonal total cloud cover for austral summer 2000-2001; b) same as a), but for 2004-2005.

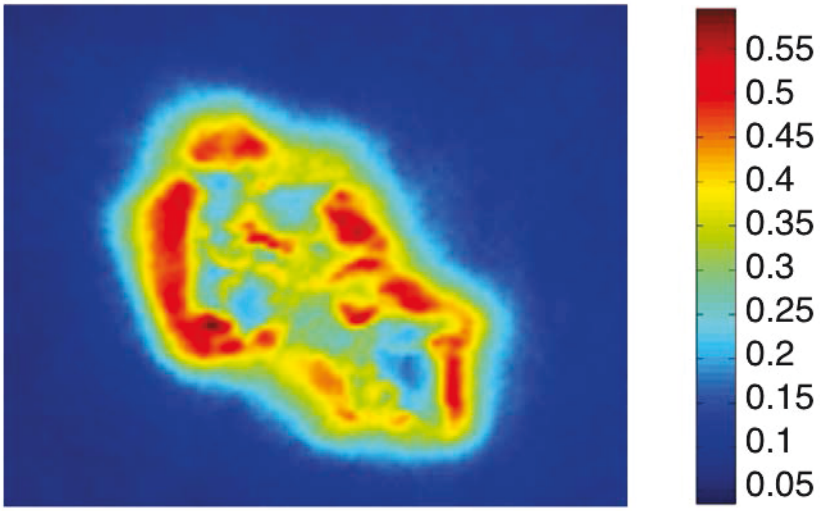

Figure 4.5 MODIS mean season total cloud cover (250m pixel) for Nov 2007- Apr 2015 (image from Mike Douglas, NOAA).

4.2 Intraseasonal variability

This part focuses on the WRF-simulated daily SSR patterns obtained by AHC for the summer period over Reunion (domain #3) during Nov to Apr. The spatial characteristics of WRF-simulated daily SSR patterns are described, related to the large-scale atmospheric circulation, and statistically discussed in terms of frequency of occurrence, and in-phase variability between clusters and members. Because of the amplitude of the seasonal cycle of SSR, AHC is applied to the daily anomalies, which are defined as the difference between the daily values and the seasonal mean for each period (Figure 4.1).

4.2.1 Austral summer 2000-2001

Figure 4.6 presents the dendrogram summarizing the successive groupings produced by the AHC procedure performed on WRF SSR anomalies over Reunion during the period Nov 2000 to Apr 2001. Five clusters were retained because they appeared to be the most robust statistically, i.e. they were those representing a reasonable compromise between detailed partitioning and compactness. The 905 days (5 ensemble simulations times 181 days) are distributed unequally within the 5 clusters; Figure 4.7 shows these 5 clusters' intra-class variability by computing the spatial average of each day ascribed to each cluster. Cluster #4, which accounts for 17% (155 days) of the total, shows the largest positive anomalies, indicating that days with higher values of SSR (i.e. less clouds) were simulated by WRF. Cluster #5 absolutely represents the cloudy days with less SSR. It concentrates the largest number of days: 234 days out of 905 (26%).

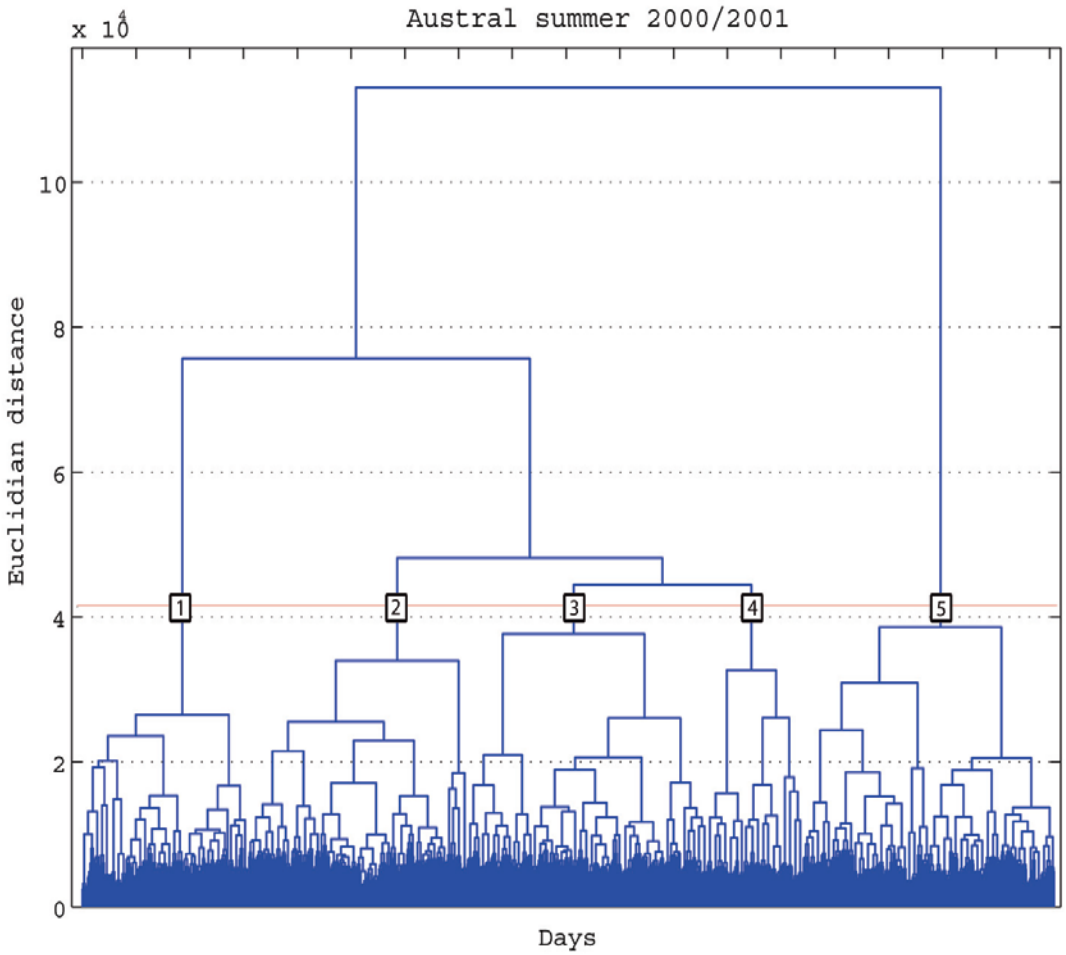

Figure 4.6 Dendrogram (Clustering tree) of the hierarchical ascending classification performed on WRF-simulated daily SSR anomalies fields (domain #3), Nov 2000 to Apr 2001 period. The red line shows the truncation for the 5 clusters used in this study.

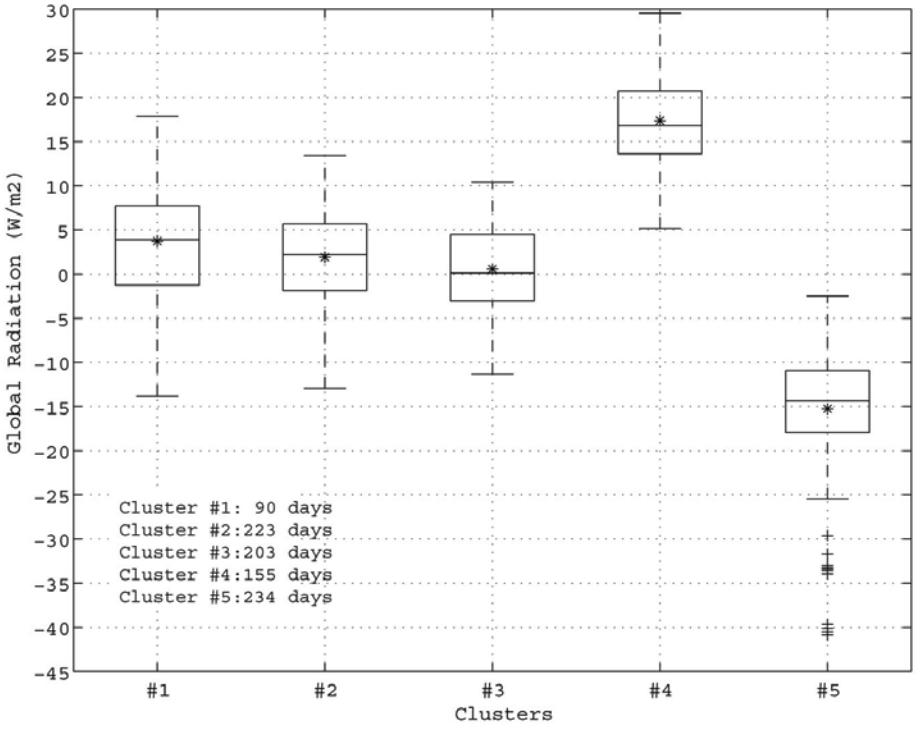

Figure 4.7 Box-and-whisker plots for the spatial average SSR anomalies amount for 5 clusters (intra-class variability) Nov 2000 to Apr 2001. The boxes have lines at the lower quartile, median and upper quartile values. Cluster sizes are labeled on the figure.

The spatial patterns associated with the 5 clusters are shown in Figure 4.8. Cluster #1 shows strong positive SSR anomalies (i.e. more SSR) over the northern part of Reunion, and negative ones (i.e. less SSR) over the southern part. Clusters #2 and #3 show contrary patterns. Cluster #2 presents positive (negative) SSR anomalies, i.e. more (less) SSR, in the eastern (western) areas of the island. We find positive and negative SSR anomalies all over the island in Clusters #4 and #5, respectively. These two clusters represent two obvious opposite situations: the clear and cloudy days, confirming Figure 4.7.

To analyze the spatial variability of SSR over Reunion, the spatial patterns of cloud cover at Reunion associated to the 5 clusters obtained from SSR AHC are also examined. These are represented in Figure 4.9. In contrast to Figure 4.8, blue color here is associated with positive anomalies of total cloud cover. As for the seasonal mean (Figure 4.1), the spatial patterns of total cloud cover in each cluster are consistent with those of SSR, showing more (less) clouds all over Reunion in cluster #5 (#4), where less (more) SSR was found. In cluster #3, there are more clouds over the eastern part than the western part, which could explain the larger values of SSR anomalies there. The most striking differences are obtained in clusters 1 and 2, considering the SSR and cloud cover at the same time. The cloud spatial patterns

associated with all the other clusters correspond with SSR patterns well, which explain the spatial variability of SSR over Reunion.

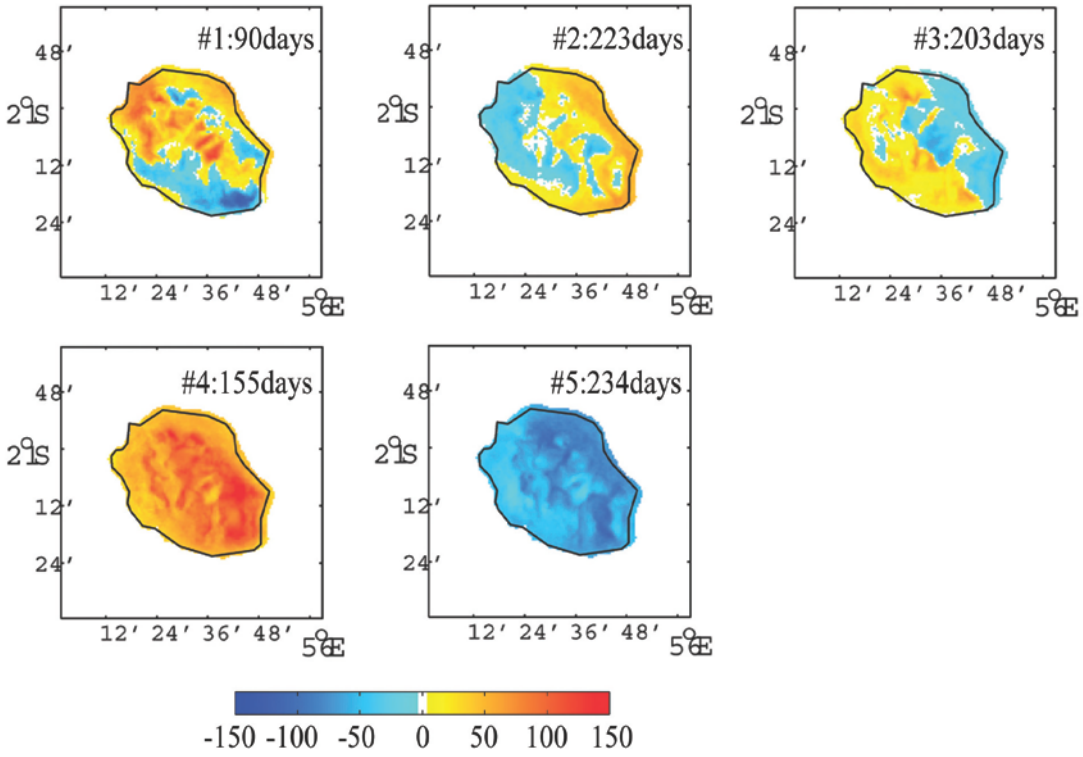

Figure 4.8 Spatial distribution of composite SSR anomalies (W/m^2) associated with the 5 clusters for Nov 2000 to Apr 2001. The number of days for each cluster is labeled on the figure.

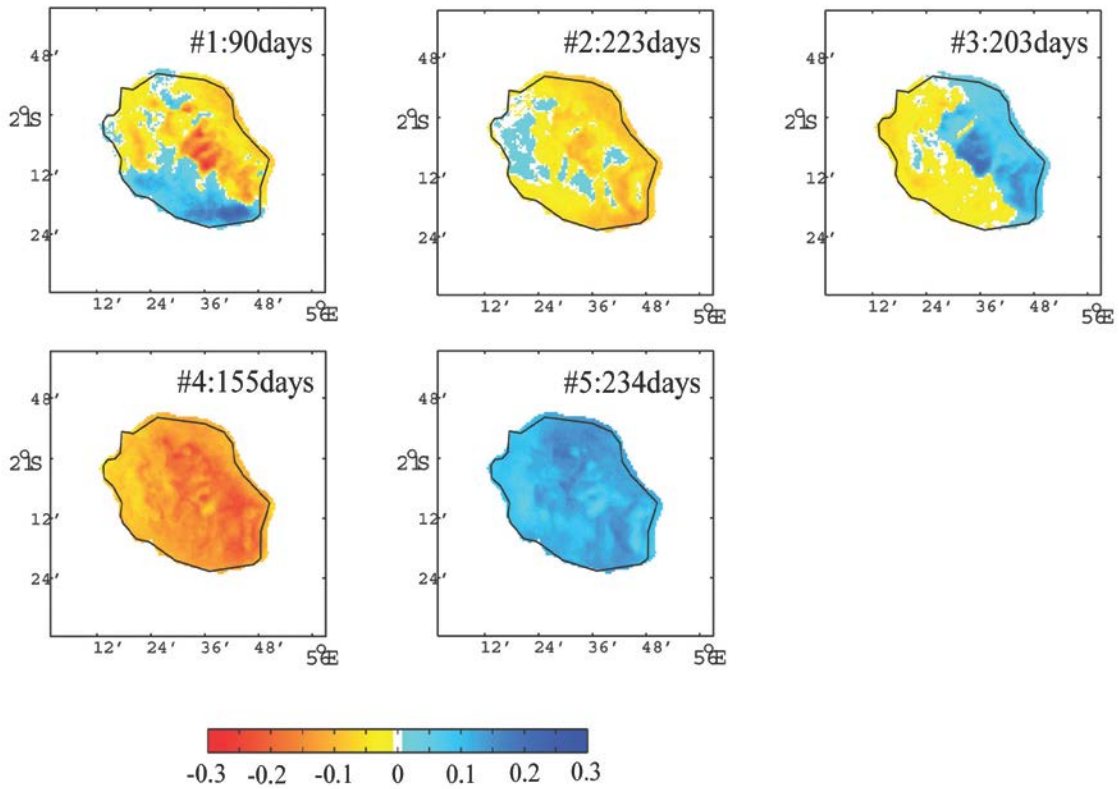

Figure 4.9 Spatial distribution of composite total cloud cover (TCC) anomalies associated with the 5 clusters for Nov 2000 to Apr 2001. The number of days for each cluster is labeled on the figure.

In order to find out the influence of the large-scale atmospheric circulation over domain #1 on SSR over domain #3, the individual contribution of several parameters from WRF outputs over domain #1 on SSR over domain #3 is evaluated through SVD.

Parameters associated to the large scale circulation, namely U and V at 500hPa, U and V at 10m,, vertical velocity of the wind, air temperature at 2 meters, temperature, specific humidity and geopotential height are tested on the modes of covariance with SSR at local scale through SVD. All the data used from domain #1 and #3 are ensemble mean of the 5 simulation members. Though we applied SVD to all the aforementioned atmospheric parameters, only the patterns of Q2 with UV10 and SSR are shown here in Figure 4.6, because they have higher correlations with SSR over Reunion. The specific humidity and synoptic wind near the surface were also chosen as the most relevant parameters to study the influence of the large-scale atmospheric circulation onto SSR (Badosa et al. 2015) and precipitation (Morel et al. 2014) at local scale. Q2 with UV10 will then be chosen as the variables to study the SSR in

clustering classification analysis in the following section. Here we just briefly descript the results of this method as the basis of the following parts.

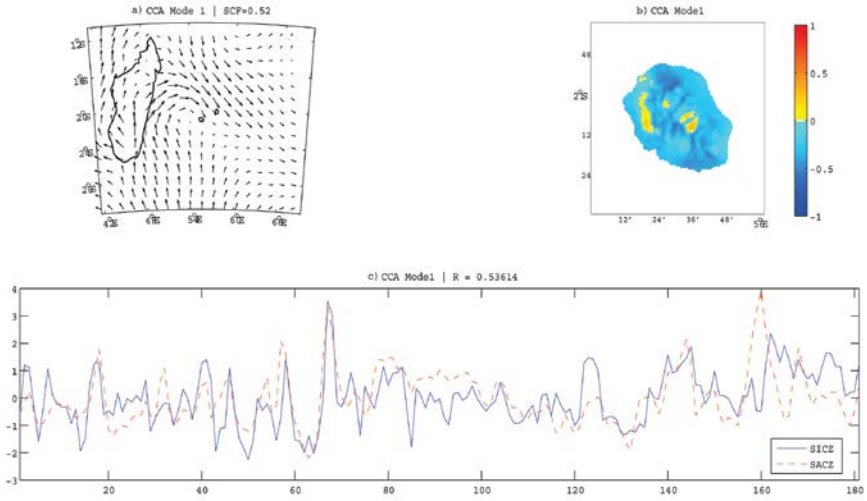

Figure 4.10 SVD analysis applied to Q2 with UV10 anomalies in domain #1 and SSR anomalies in domain #3 Nov 2000 to Apr 2001, first mode displayed through heterogeneous correlation maps: a) for Q2 with UV10; b) for SSR; c) Q2 with UV10 (SACZ) and SSR (SICZ) convection indices in Nov 2000 to Apr 2001. The correlation value between the two indexes is labeled on the figure.

The correlation between Q2 and UV10 anomalies (Nov 2000 to Apr 2001) over domain #1 is presented in Figure 4.10a, which shows the humidity and surface winds moving northeastward over Reunion (domain #3). The associated SSR correlation patterns in Figure 4.10b are kind of consistent with the circulation, which present negative (positive) correlation over southeast (northwest) area of Reunion. However, these correlations are not strong and significant. In addition, the Squared Covariance Fraction (SCF) value is 0.52. Figure 4.10c gives domain #1 and domain #3 convection indices for the period Nov 2000 to Apr 2001 (the correlation between the two indices is 0.54). Two indices consistent well during the time period, indicating that Q2 with UV10 could be used as atmospheric parameters to study SSR over Reunion. Similar results were obtained for the time period Nov 2004 to Apr 2005 (not shown).

In the following, we then relate the spatial patterns of SSR over Reunion to Q2 with UV10, evaluating the influence of the atmospheric circulation in domain #1 over SSR in domain #3. Figure 4.11 presents Q2 anomalies in shading along with UV10 anomalies in vectors.

In Cluster #4, there is weak easterly wind diverging over Reunion Island in line with less humidity there (Figure 4.11), which is consistent with less TCC in Figure 4.9 and more SSR in Figure 4.8. In Cluster #5, weak northwesterly wind transporting humidity from the north over Reunion, is associated with generally higher TCC and lower SSR covering the whole of Reunion. In Cluster #3, strong

southeasterly-easterly wind with less humidity coincides with less TCC (more SSR) on the western part of Reunion, and more TCC (less SSR) on the eastern part of Reunion (Figures 4.9 & 4.8). In Cluster #1, cyclonic circulation located south of Reunion generates strong northwesterly-westerly wind conveying large amount of humidity from the tropical latitudes. This produces less TCC on the north of Reunion, and more SSR over the south of the island.

In Cluster #2, weak thermal winds (Badosa et al. 2015) combine to create an inland flow forcing air up the slope and cloud formation, associated with higher TCC on the western side at midlevel altitudes (Figure 4.9).

Based on the analysis of Q2 with UV10 at large scales with TCC and SSR at local scales over Reunion Island, a clear relationship is found between them. When there is more humidity conveyed by the synoptic wind, there is more cloud and less SSR generated at local scales. This has been obtained in our results too and proves that the cluster classification applied here on the WRF output data over domain #3 achieves a good performance in representing the spatial variability of surface solar radiation at a high resolution (750m) in association with the atmospheric circulation during Nov 2000 to Apr 2001.

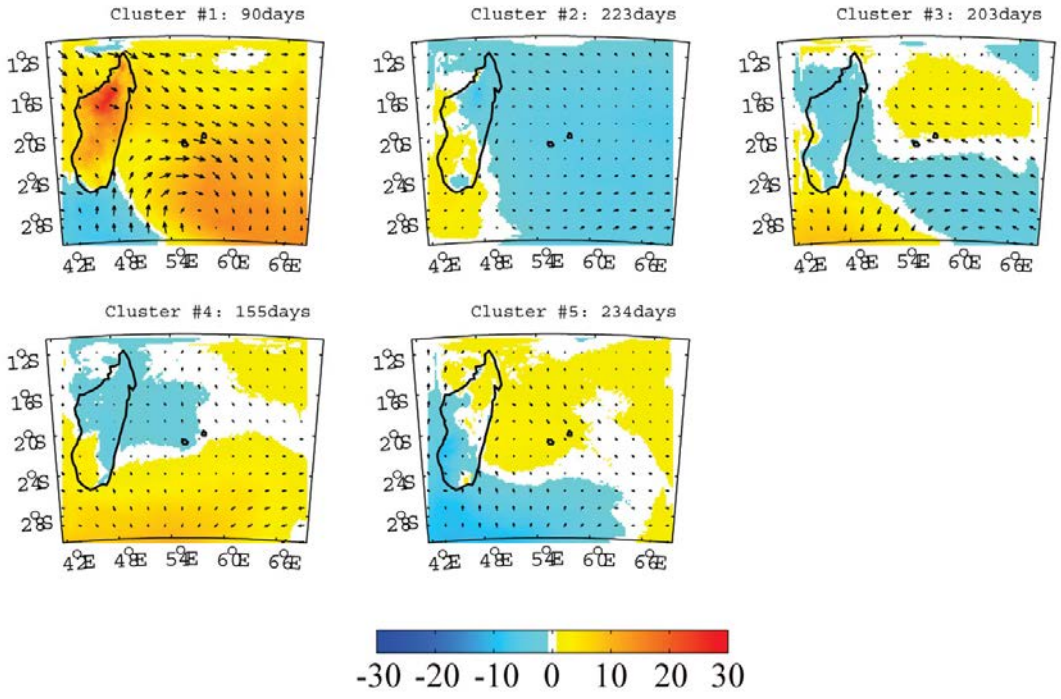

Figure 4.11 Spatial distribution of composite Q2-UV10 anomalies (10^{-4}·kg/kg; m/s) associated with the 5 clusters for Nov 2000 to Apr 2001. The number of days for each cluster is labeled on the figure.

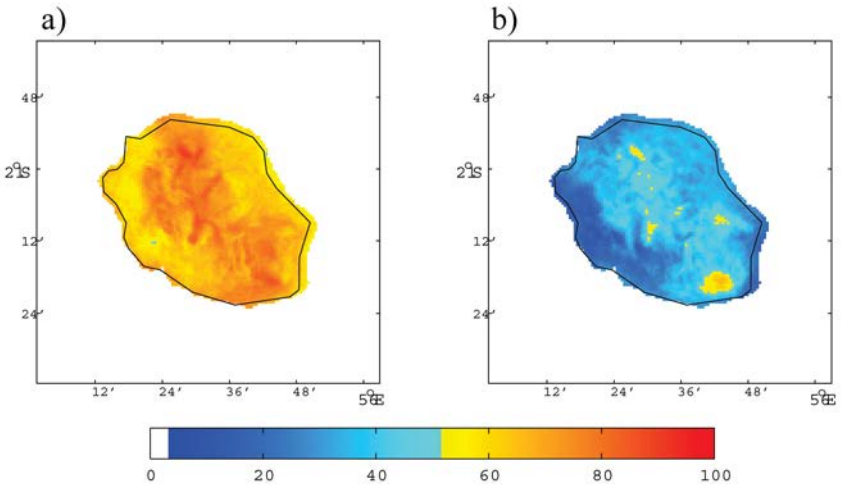

Figure 4.12 Fraction of the daily variability of simulated SSR (%) explained by the 5 members (a) and WRF clusters (b) Nov 2000 to Apr 2001

The spatial distribution of the total variance explained by the 5 ensemble simulations and the clustering approach is presented in Figure 4.12. The 5 ensemble simulations (Figure 4.12 a) explain larger fraction of SSR total variance than the 5 clusters (Figure 4.12 b) over Reunion, but both of them explain smaller variance over the coastal area than the central area. Figure 4.12 a) gives inter-member variation fraction of SSR, which indicates model's internal variability and uncertainties' spatial distribution.

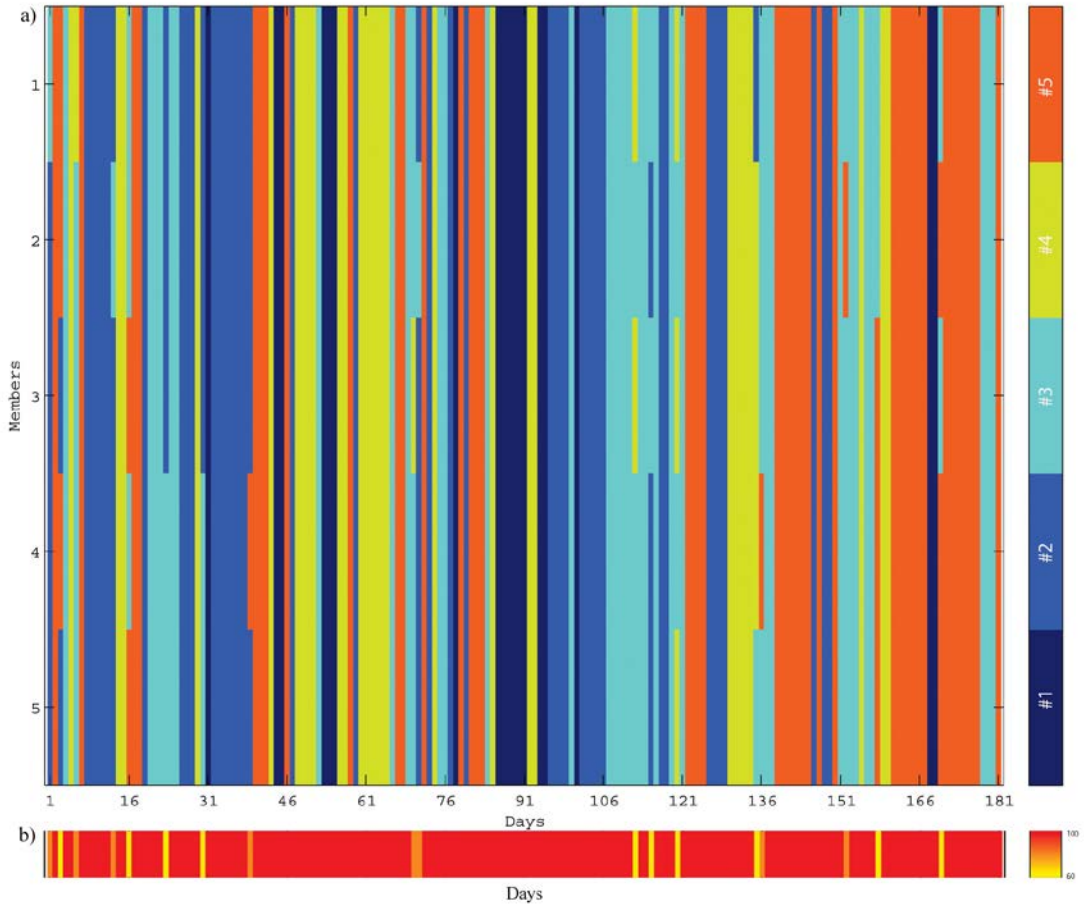

Figure 4.13 a) Succession of the clusters for each day of the Nov 2000 to Apr 2001 season and the 5 members (y-axis). b) Associated intermember agreement expressed as the percentage of the 5 members converging towards the same cluster (%).

Figure 4.13a shows the temporal distribution of the five clusters, for each member (rows) and each day of the period (columns). From one member to another, the timing of the five clusters appears as highly reproducible during the overall period (Figure 4.13a, b), 90% of the members converging towards the same solution during 163 days out of 181. The succession of the clusters over the time almost gives reproducible features on the date and duration for all members.

4.2.2 Austral summer 2004-2005

The same analysis methods are applied to the period from Nov 2004 to Apr 2005. Figure 4.14 presents the dendrogram summarizing the successive groupings produced by the AHC procedure performed on WRF SSR anomalies at Reunion during the period from Nov 2004 to Apr 2005. Four clusters are chosen and the 905 days are distributed unequally within the 4 clusters (Figure 4.15). Cluster #3 shows the largest positive anomalies which indicate more SS during this period and it account for 15% (136 days) of the total. Cluster #4 absolutely represents the cloudy days with least SSR. It concentrates a large number of days: 338 days out of 905 (37%), which is more than Nov 2000 – Apr 2001 (26%). This is consistent with the analysis of Morel

et al. (2014) that 2004-2005 austral summer is wetter than that of 2000-2001.

Figure 4.16 presents the spatial patterns of SSR anomalies in domain #3 associated to the 4 clusters. Cluster #1 shows strong positive (negative) SSR anomalies over the western (eastern) part of Reunion. Cluster #2 presents positive SSR anomalies almost over the whole island, but these anomalies are as strong as in cluster #3 in which large amounts of SSR are simulated everywhere except over Saint Leu. Cluster #4 gives contrary patterns with regard to cluster #3. All over the Reunion is distributed with negative SSR anomalies for cluster #4. These two clusters represent two obvious different situations: the clear and the cloudy days, which are corresponding to the intra-class variability patterns in Figure 4.15.

The spatial patterns of cloud cover over Reunion associated to the 4 clusters obtained from SSR AHC are also examined to analyze the spatial variability of SSR. The spatial patterns of cloud are consistent with SSR spatial patterns very well. Cluster # 2 (weak) and Cluster #3 (strong) show less cloud over Reunion, which is consistent with the more SSR for them in Figure 4.16. Cluster #4 presents more cloud over Reunion which receives less SSR there. In Cluster #1, there is more cloud over the east than the west, which could explain the larger values of SSR anomalies found there (Figure 4.17). In general, all the clusters for cloud spatial patterns correspond with SSR clusters patterns well, which explain the spatial variability of SSR over Reunion.

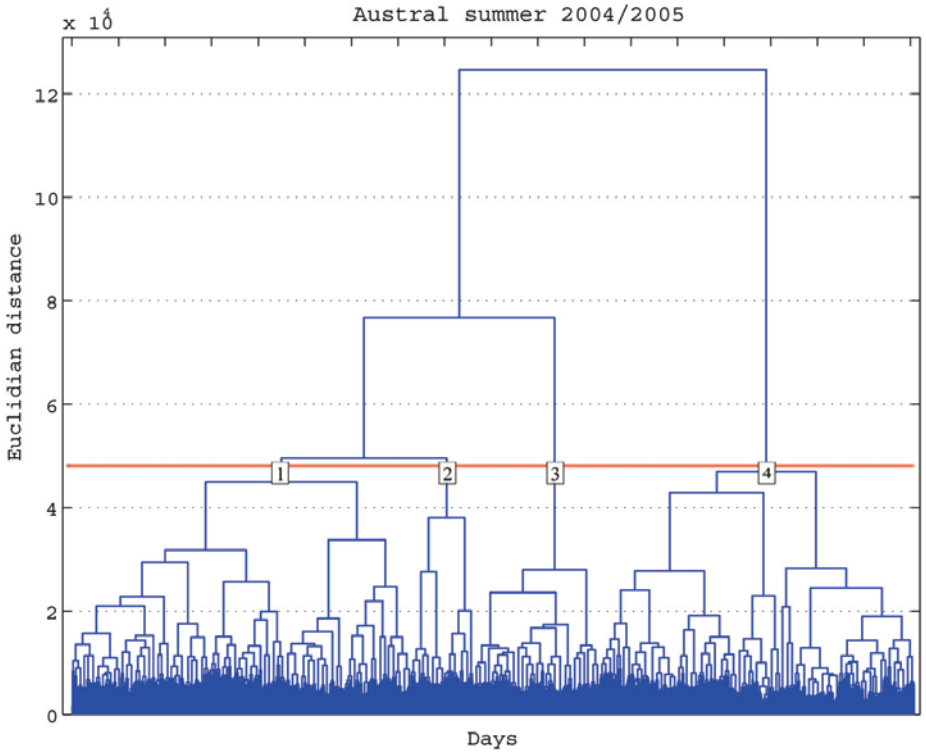

Figure 4.14 Dendrogram (Clustering tree) of the hierarchical ascending classification performed on WRF-simulated daily SSR anomalies fields (domain #3), Nov 2004 to Apr 2005 period. The red line shows the truncation for 4 clusters used in this study.

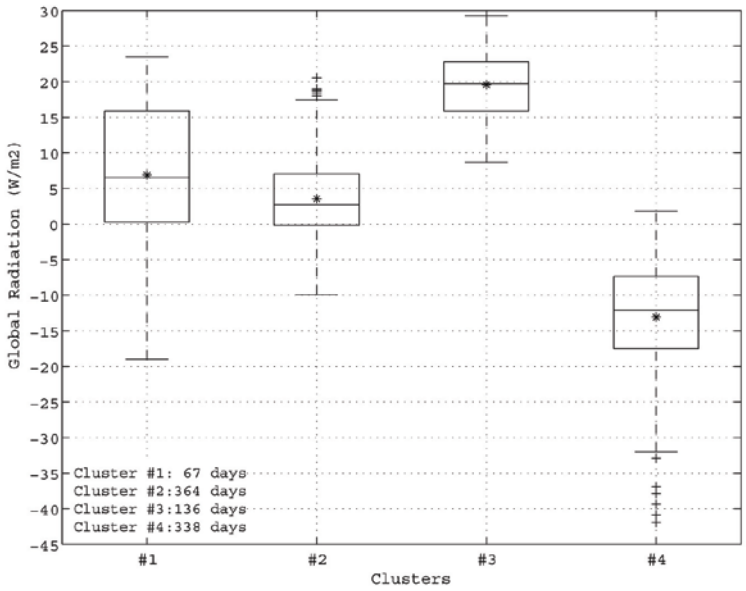

Figure 4.15 Box-and-whisker plots for the spatial average SSR anomalies amount for 4 clusters (intra-class variability) Nov 2004 to Apr 2005. The boxes have lines at the lower quartile, median and upper quartile values. Cluster sizes are labeled on the figure.

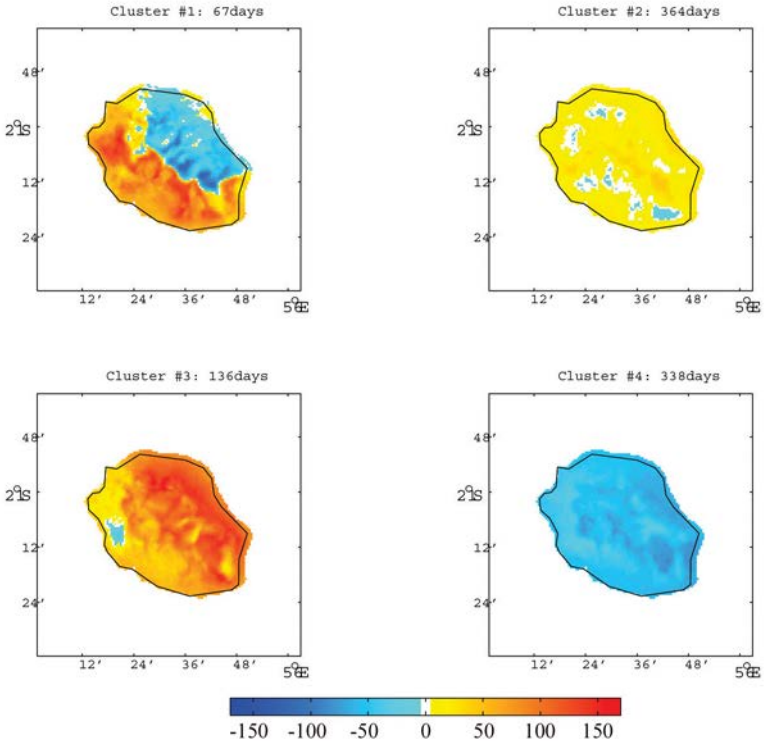

Figure 4.16 Spatial distribution of composite SSR anomalies (W/m^2) associated with the 4 clusters for Nov 2004 to Apr 2005. The number of days for each cluster is labeled on the figure.

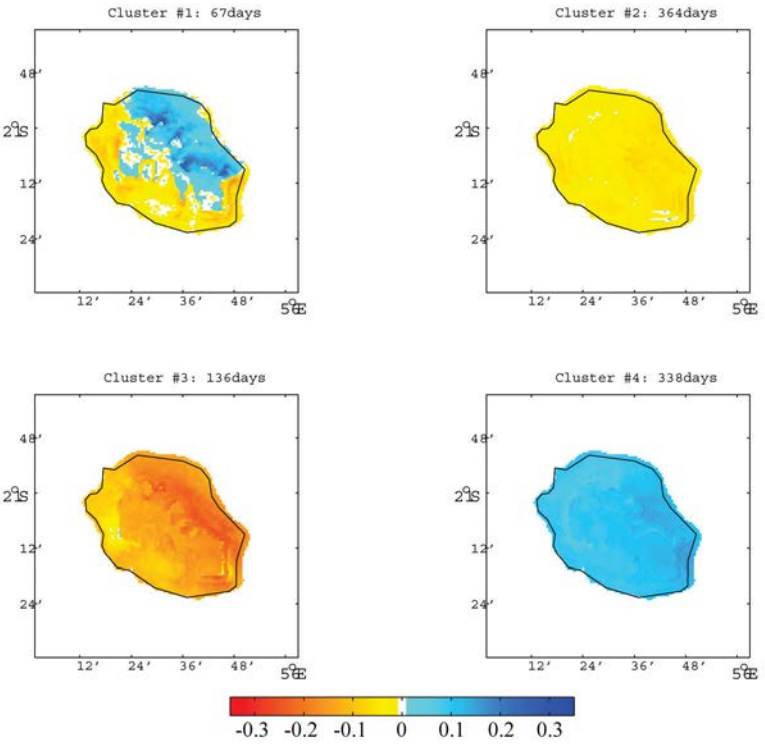

Figure 4.17 Spatial distribution of composite total cloud cover (TCC) anomalies associated with the 4 clusters for Nov 2004 to Apr 2005. The number of days for each cluster is labeled on the figure.

Q2 with UV10 are related to the spatial patterns of SSR and TCC over Reunion (Figure 4.18). In Cluster #1, cyclonic circulation located southwest of Reunion generates strong northerly wind transporting large amount of humidity there. Less TCC and more SSR are found on the western and southern parts of Reunion, and more TCC and less SSR on the eastern and northern parts of this island. In Cluster #2, southwesterly synoptic wind with weak humidity conveyed over Reunion at the large scale, creates less TCC and more SSR over the whole island. In Cluster #3, the anticyclone is located southeast of Reunion generating strong easterly wind which doesn't bring much humidity. The whole island is covered by large amount of TCC, with less SSR reaching the surface. In Cluster #4, the synoptic wind is weak with more TCC forming over the whole island, and less SSR received at the surface.

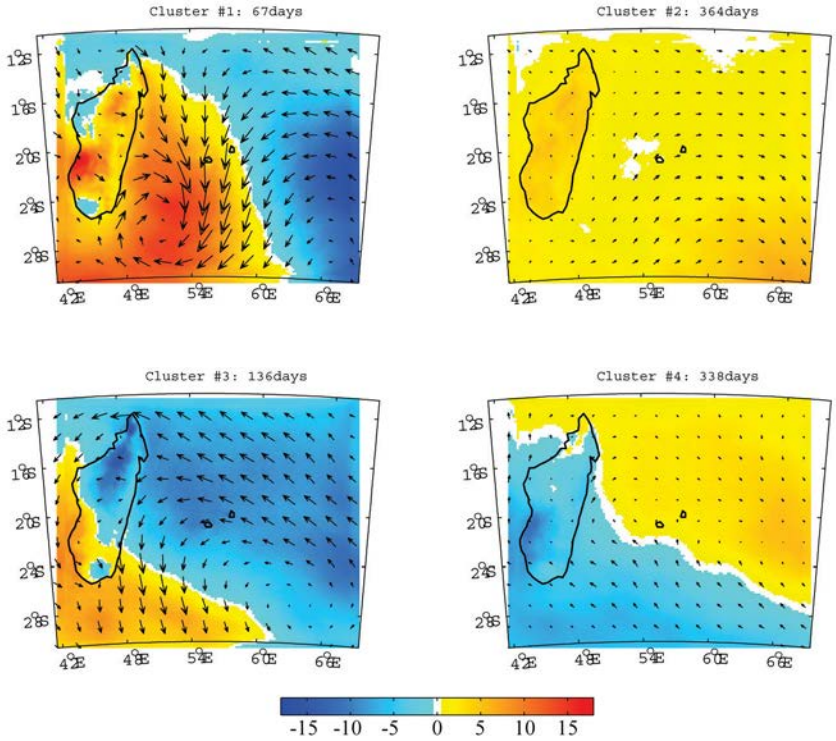

Figure 4.18 Spatial distribution of composite Q2-UV10 anomalies (10^{-4}·kg/kg; m/s) associated with the 4 clusters for Nov 2004 to Apr 2005. The number of days for each cluster is labeled on the figure.

The spatial distribution of the total variance explained by the 5 ensemble simulations (a) and the clustering approach (b) is presented respectively in Figure 4.19. The 5 ensemble simulations of WRF explain larger fraction of total SSR variance than the 4

clusters over the coastal area of Reunion, and both of them explain larger variance over the Piton de la Fournaise, Piton des Neiges and other high elevation areas. Figure 4.19 a) gives inter-member variation fraction of SSR, which indicates model's internal variability and uncertainties' spatial distribution.

Figure 4.20a shows the temporal distribution of the four clusters, for each member (rows) and each day of the period (columns). From one member to another, the timing of the five clusters appears as highly reproducible during the overall period (Figure 4.20a, b), 90% of the members converging towards the same solution during 162 days out of 181. The succession of the clusters over the time almost gives reproducible features on the date and duration for all members. This high degree of reproducibility is also related to the SSR's variability over spatial scale as discussed above.

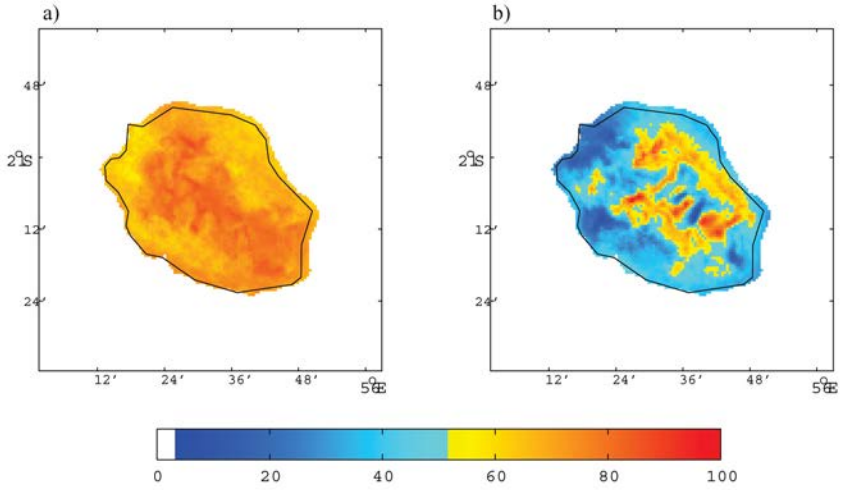

Figure 4.19 Fraction of the daily variability of simulated SSR (%) explained by the 5 members (a) and WRF clusters (b) Nov 2004 to Apr 2005

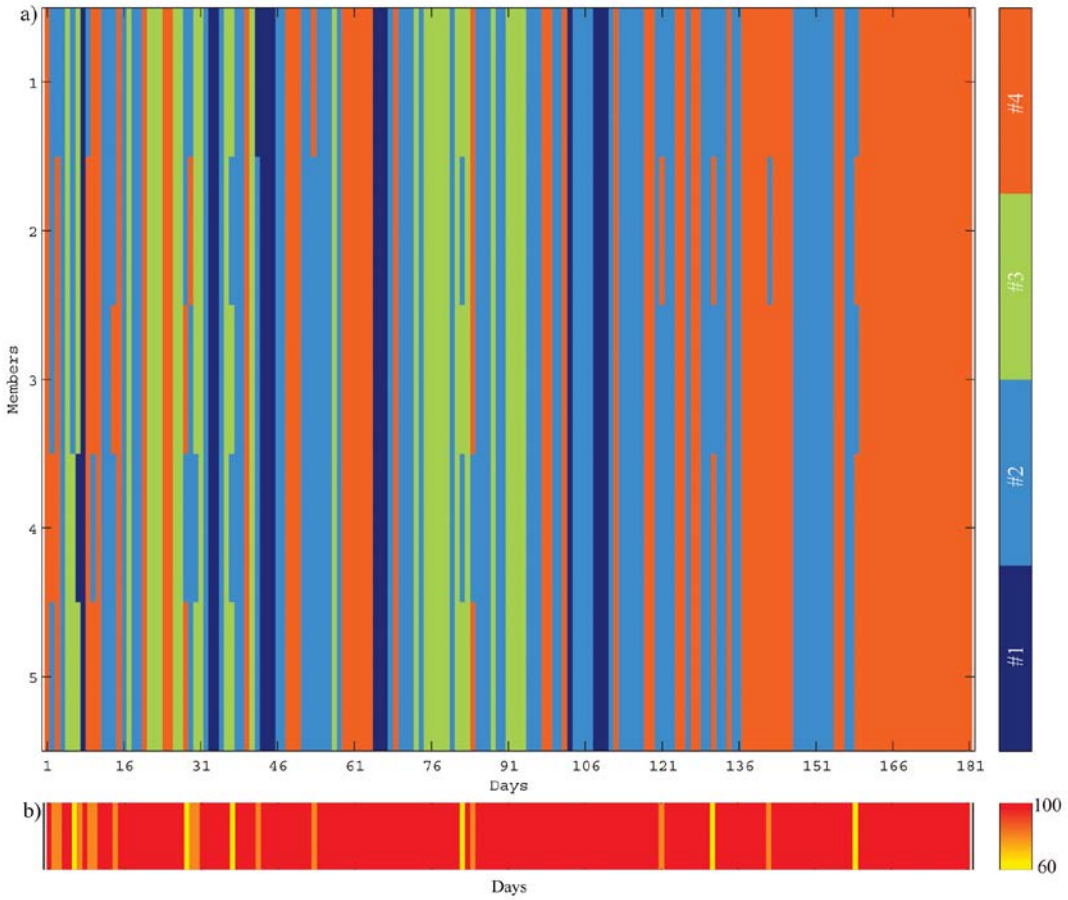

Figure 4.20 a) Succession of the clusters for each day of the Nov 2004 to Apr 2005 season and the 5 members (y-axis).b) Associated intermember agreement expressed as the percentage of the 5 members converging towards the same cluster (%).

4.2.3 Comparison to Météo France observations and CM_SAF products

Though the SSR measurement from stations is insufficient over Reunion, a comparison between these measurements (Figure 2.6) and corresponding nearest grid points in WRF outputs has been performed. Results are presented in Figures 4.21 and 4.22 for the two periods: 2000-2001 and 2004-2005, respectively. The nearest grid point from WRF output is calculated the bias with the each station of Météo France, and the average of bias over each WRF cluster is shown. Though the five members of WRF simulations were examined here, only the results for member 1 are presented because results for all the members are similar. This is not surprising given the fact the intra-member variability is small (see previous section).

As shown Figure 4.21 and 4.22, WRF simulates more SSR than Météo France at all stations for the two seasons (2000-2001; 2004-2005). The five clusters all gives large positive biases for Nov 2000 to Apr 2001 (MBE>75 W/m^2; RMSE>83 W/m^2) and for Nov 2004 to Apr 2005 (MBE>61 W/m^2; RMSE>65 W/m^2).

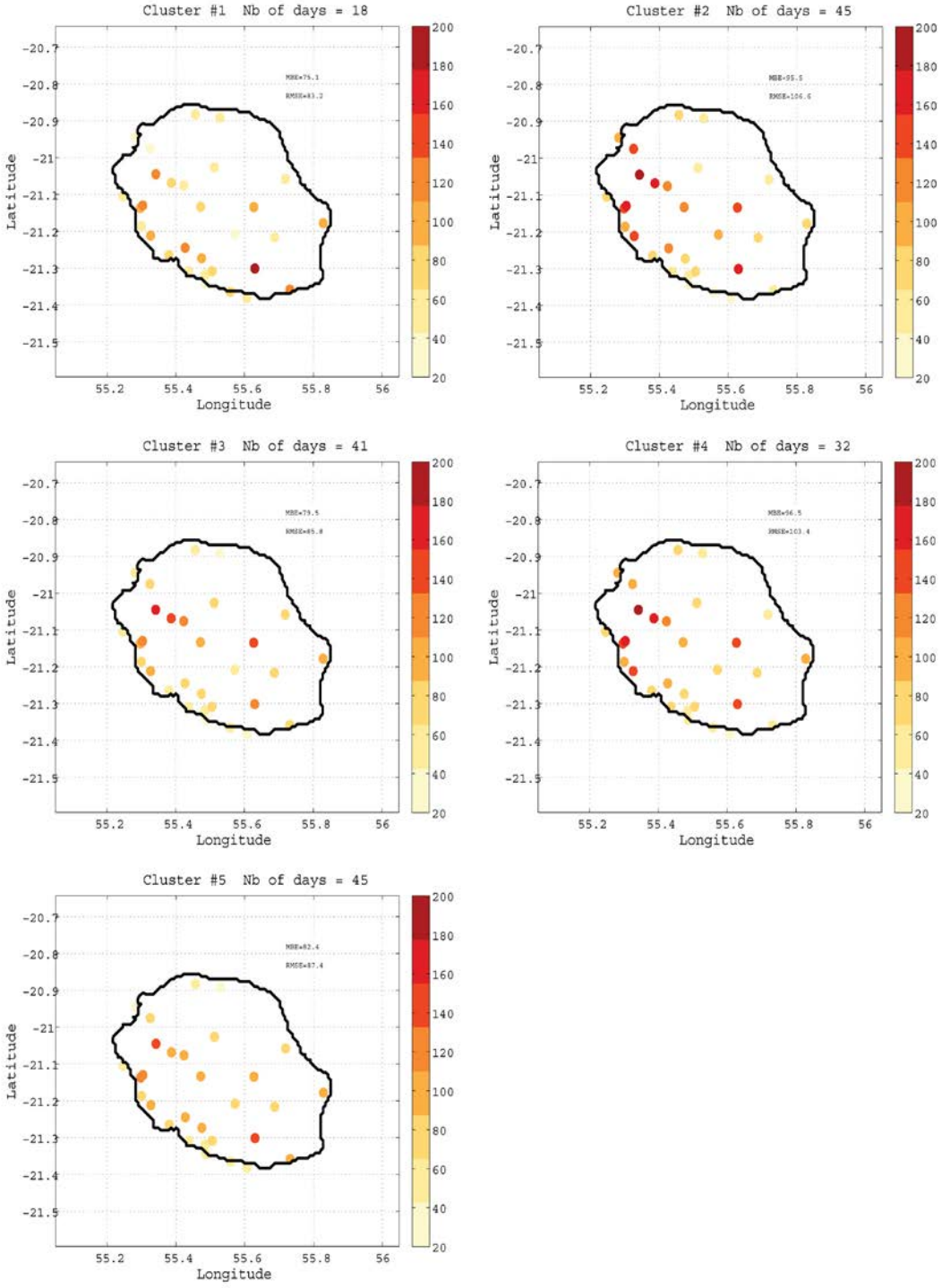

Figure 4.21 Member 1's bias (W/m^2) between measurement at Météo France stations and the corresponding points in WRF for each cluster (row) Nov 2000 to Apr 2001. MBE and RMSE statistics are labeled on the figure.

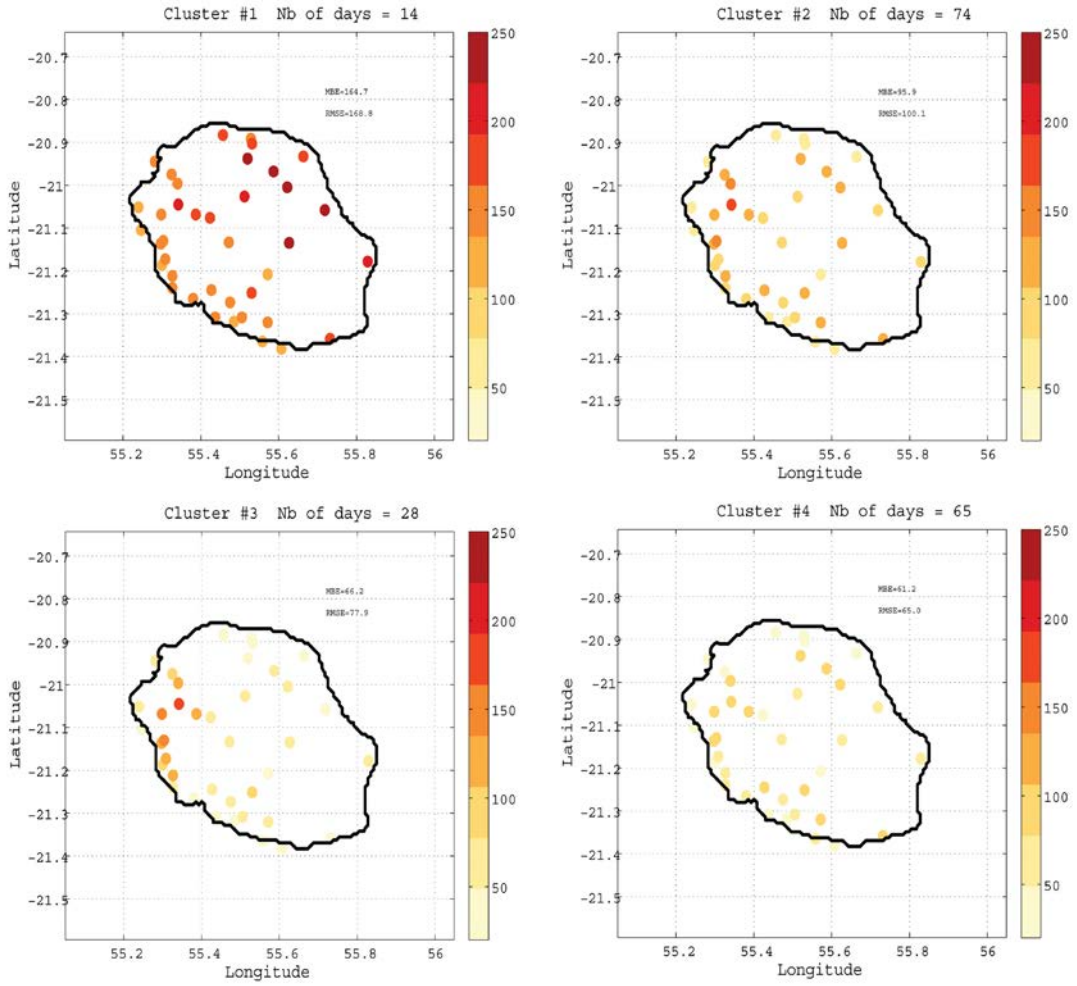

Figure 4.22 same as Figure 4.21, but for Nov 2004 to Apr 2005.

CM SAF satellite data are compared to the WRF simulations over domain #3 at 3 different time scales: 1) seasonal: 5-member seasonal mean (based on 905 days) is compared with CM_SAF seasonal mean for the two austral summer seasons studied (done in first section); 2) intra-seasonal: CM_SAF are used to valid the clustering results through considering the clusters of WRF simulation. Mean Bias Error (MBE) and Root Mean Square Error (RMSE) are calculated in Table 4.1 and 4.2; 3) daily: shown in next section.

At the clustering scale, SSR of CM SAF considers the cluster choice of WRF at each member. The MBE and RMSE between them for each cluster are calculated. Results are summarized in Table 4.1 for austral summer 2000 to 2001 and in Table 4.2 for austral summer 2004 to 2005. For each cluster, values of MBE and RMSE are similar from one member to the other in spite of some differences illustrating once again the model internal variability. However, the error between WRF and CM SAF is big at a large resolution difference. For cluster #1 to #4, WRF SSR is larger than CM SAF SSR over the domain area. In contrast, CM SAF gives higher values of SSR (negative values of MBE) than WRF for cluster #5 during 2000-2001 and for cluster #4 during

2004-2005. According to the clustering analysis in the section before, these are the clusters regrouping the cloudy days.

Table 4.1 MBE and RMSE between WRF and CM SAF for 2000 to 2001 (W/m^2)

Cluster / Member	#1		#2		#3		#4		#5	
	MBE	RMSE	MBE	RMSE	MBE	RMSE	MBE	RMSE	MBE	RMSE
1	44.4968	91.1701	43.213	93.97	24.586	76.547	78.9474	101.3928	-31.5961	77.8395
2	44.8724	89.6305	46.3953	95.5498	27.7384	79.3396	75.0188	99.5528	-31.203	76.9281
3	45.5281	91.6473	43.3541	94.1004	25.8491	75.8847	75.1617	98.3712	-31.3812	78.1122
4	48.4351	92.8612	44.3499	94.5916	31.1366	79.832	73.9	97.4231	-31.9549	76.5895
5	46.6702	92.5747	43.1868	94.4948	27.9001	77.5983	75.7639	99.4943	-32.7336	78.1705

Table 4.2 MBE and RMSE between WRF and CM SAF for 2004 to 2005 (W/m^2)

Cluster / Member	#1		#2		#3		#4	
	MBE	RMSE	MBE	RMSE	MBE	RMSE	MBE	RMSE
1	55.5391	102.9996	43.1612	88.4527	93.6984	122.1058	-30.6188	77.6937
2	57.8947	105.3416	43.9402	88.4918	90.9518	120.2840	-25.8088	76.8526
3	57.4372	103.5910	43.9473	88.3156	92.8485	120.4035	-33.6604	78.8463
4	62.7962	105.6830	44.7007	89.2885	92.1298	121.2747	-26.0740	76.8338
5	57.1864	105.4487	42.9693	88.5753	95.3841	122.6616	-27.4098	77.1309

4.3 Daily variability

To observe the daily SSR variance of errors between WRF and CM SAF, CM SAF is compared to each member individually. Five members' daily errors (MBE) for austral summer 2000 to 2001 and for austral summer 2004 to 2005 are presented in Figures 4.23 and 4.24, respectively. Firstly, five members give reproducible daily errors for both seasons, except at the 14th day (14th Nov) for member 3 during the period 2004-2005, which has big difference and largest MBE (-243.0144 W/m^2). Secondly, most of the daily MBE value is large for these two seasons and there is no significant difference for each member during the summer season.

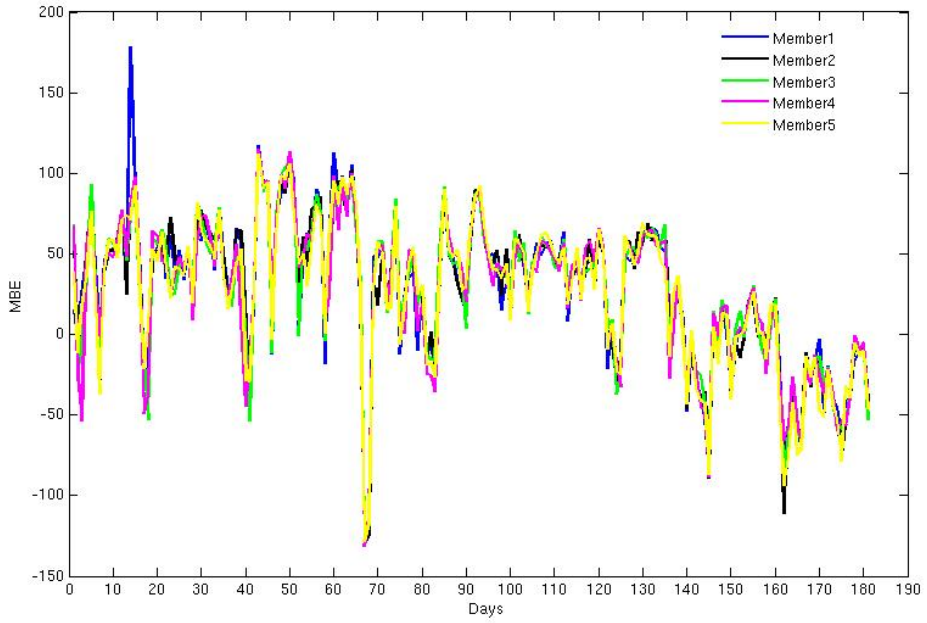

Figure 4.23 Daily MBE of SSR between WRF and CM SAF for austral summer 2000 to 2001 (W/m^2).

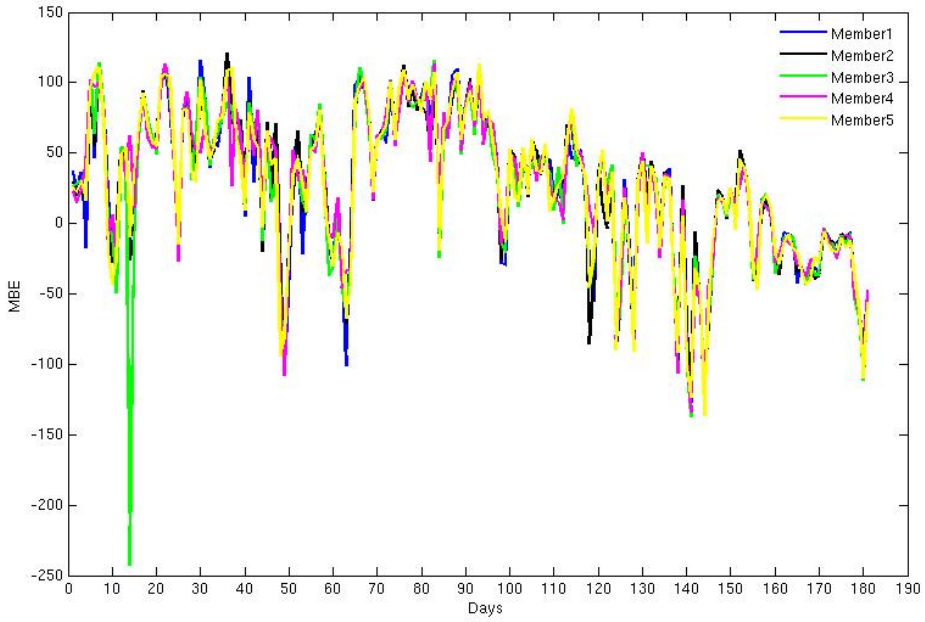

Figure 4.24 Daily MBE of SSR between WRF and CM SAF for austral summer 2004 to 2005 (W/m^2).

4.4 Summary and discussion

In this chapter, SSR spatial variability is analyzed through three aspects: seasonal, intraseasonal, and daily scales. At the seasonal state, simulated SSR of WRF for two contrasted wet seasons: austral summer 2000-2001 and 2004-2005 are evaluated by the CM SAF satellite products along with Météo France measurements. The two WRF simulated seasonal means give similar values with more SSR along the coast and in the inner part of the island, which is consistent with the observed spatial patterns from Météo France, even though WRF tends to produce higher values of SSR on the coast and inland and lower ones at mid-level altitudes. CM SAF simulates more SSR than WRF over the Reunion, except at a few locations inland (Piton de La Fournaise, Cirques of Mafate and Cilaos), though CM SAF patterns are shift. WRF seems able to produce fine contrasts with small patches of higher SSR along the edges of the Cirques due to its higher resolution. Simulated monthly SSR of WRF and CM_SAF are also compared to Météo France at 5 stations for austral summer 2004-2005 individually. The Gillot station located at coastal site give reduced errors for WRF and CM SAF. The difficulties in reproducing the irradiance at other considered stations are probably from the topography effects. Then the simulated total cloud cover is analyzed with regard to the MODIS product, even though the time period is different. SSR studied before is associated with TCC patterns and also consistent with the rainfall patterns produced by Morel et al. (2014). This indicates the topography's effect on the SSR and the spatial variability of SSR at seasonal scale.

At intraseasonal scale, the AHC methodology performed on WRF outputs during the austral summers 2000-2001 and 2004-2005. The AHC classifies the daily SSR

patterns in domain #3. The relationship with the larger-scale circulation in domain #1 is further analyzed by considering the specific humidity and the horizontal wind at 10 meters in each cluster. Five clusters and four clusters are obtained for 2000-2001 and 2004-2005 separately. Three clusters represent the same spatial patterns: totally overcast, clear sky, overcast on the windward (eastern) side of the island with orographic clouds forming as the synoptic wind slows down, clear on the leeward side in spite of the presence of some locally-formed clouds induced by the topography. Though these clusters are similar in the spatial patterns of SSR and TCC, the large-scale atmospheric circulation is somehow slightly different. The frequency of occurrence and in-phase variability between clusters and members are then statistically discussed to analyze the spatial characteristics of WRF-simulated daily SSR patterns. The 5 ensemble simulations of WRF explain larger fraction of total SSR variance than the 5 clusters over Reunion, but both of them explain smaller variance over the coastal area than the central area. The inter-member variation fraction of SSR indicates model's internal variability and the uncertainties of spatial distribution. The succession of the clusters over the time almost gives reproducible features on the date and duration for all members (90% of the members converging towards the same solution). The clustering results are compared with Météo France observations and CM SAF products. WRF simulates more SSR than Météo France at all stations for the two seasons. All the clusters give large positive biases (MBE>60 W/m^2). The MBE and RMSE between SSR WRF and CM SAF for each cluster are calculated. Even the error is kind of large, the display of positive and negative error over different clusters is correspond to the TCC and SSR clustering before.

At the daily scale, the daily SSR variance of errors between WRF and CM SAF is examined through showing five members' daily MBE for two seasons. Five members give reproducible daily errors, but the MBE is large showing that CM SAF products is not fully satisfactory here for its coarse resolution at local scale.

In general, WRF has the ability of simulating SSR's spatial variability over Reunion with regard to the cloud cover and atmospheric circulation. But we still need to find high resolution products from satellite and ground stations to validate the model. Cloud cover of MODIS gives a satisfied pattern which is associated to SSR in WRF even at a different time period. It could be interesting to perform a different time period simulation using WRF corresponding to the time period of MODIS.

Chapter 5

Conclusion and Perspectives

5.1 Conclusion

As the objective of this thesis is to study the temporal and spatial variability of SSR over the SWIO and Reunion Island, regional climate models are applied to perform simulations for SSR analysis, considering the insufficient ground stations and complex geography condition over the domain field.

The first part is analyzing the temporal variability of SSR through regional climate model RegCM4 over the SWIO centered on Reunion Island. For RegCM4 is the first one that focuses on the solar radiation research over SWIO region, a first series of test experiments with RegCM4 to illustrate the model performance and sensitivity to the choice of the physical parameterizations are performed, which include domain size, resolution, radiative scheme, and convective scheme tests. The default CCM radiative and the mixed convective scheme: Grell scheme over land and Emanuel scheme over ocean give better performance compared to the others options over the SWIO area.

To check whether the RegCM4 model forced by ERA-Interim reanalyses is able to maintain the ENSO, IOD, MJO and TTT signals, several ERA-Interim parameters (U, V, T and RH) along with the corresponding RegCM4 output data are analyzed at the first step. Secondly, simulated SSR in association with the different modes of variability was examined. RegCM4 is able to simulate the temporal variability of SSR based on the analysis of interannual variability, intraseasonal variability and synoptic climate variability.

To examine the interannual variability associated with ENSO and the IOD, we first calculated the correlation between SSR and the Multivariate ENSO Index (MEI) and the Dipole Mode Index (DMI). The anticyclonic circulation in the lower levels over Southern Africa, with lower-air level divergence, and upper-air level convergence associated with suppressed convection there could be simulated associated with ENSO. As the drier air subsiding there, the cloud cover is reduced and more SSR can reach the surface and warm it. This situation is reversed over the SWIO, with enhanced convection there over a warmer ocean that releases more latent heat to the atmosphere, that is an increase in the RH, more clouds and less SSR.

To analyze the intraseasonal variability associated with the MJO, we constructed an index based on RMM1 & RMM2 to define the 8 phases describing the life cycle of an MJO event. In the upper atmosphere, we found positive RH anomalies at places where we would find negative SSR anomalies. These anomalies are moving eastward as the MJO shifts. At the lower atmosphere, SSR anomalies can be related to the RH anomalies patterns in each phase. K-means clustering is applied onto the daily OLR from ERA-Interim and RegCM4 to identify the TTTs systems according to NOAA OLR patterns. RegCM4 SSR gives similar anomalies distribution according to the classification of OLR, which present kind of synoptic climate variability. Daily SSR anomaly composites for RegCM4 are computed according to the classification, showing the daily anomalies associated with the occurrences of the regimes. Three

regimes present negative anomalies bands as observed in the TTTs systems from RegCM4 OLR, explaining thus the synoptic climate variability of SSR over the SWIO and southern Africa.

SSR's spatial variability is analyzed through three aspects: seasonal, intraseasonal, and daily scales. At the seasonal scale, WRF simulated seasonal means give more SSR along the coast and in the inner part of the island, which is consistent with the observed spatial patterns from Météo France, even though WRF tends to produce higher values of SSR on the coast and inland and lower ones at mid-level altitudes. CM SAF simulates more SSR than WRF over the Reunion, except at a few locations inland (Piton de La Fournaise, Cirques of Mafate and Cilaos), though CM SAF patterns are shift. The simulated total cloud cover is analyzed with regard to the MODIS product, even though the time period is different. SSR studied before is associated with TCC patterns and also consistent with the rainfall patterns produced by Morel et al. (2014). This indicates the topography's effect on the SSR and the spatial variability of SSR at seasonal scale. At intraseasonal scale, clustering analysis shows the clear relationship for SSR and TCC at local scale and their relations with the large-scale circulation. Even SSR of WRF over Reunion has large bias with Météo France observations and CM SAF, they could also give some spatial variability information by clustering comparing. At the daily scale, the daily SSR variance of errors between WRF and CM SAF is examined through showing five members' daily MBE for two seasons. Five members give reproducible daily errors, but the MBE is large showing that CM SAF products are not fully satisfactory for its coarse resolution at local scale. Based on this analysis, WRF could be regarded to have the ability of simulating SSR's spatial variability over Reunion.

5.2 Perspectives

Even though the thesis has been finished, there is still space to do further research.

Firstly, RegCM4 has some new updating characteristics, so the sensitivity tests may cover the new options to discover the model changes on radiative scheme as RRTM is a more sophisticated scheme than CCM. The 10-year period analyzed in our study by RegCM4 doesn't contain any major ENSO and IOD events. Though the model achieved a good performance in reproducing the interannual climate variability over this period, it would be interesting to run one simulation of the model over a much longer period (about 30 years) containing several major events, and look at the way the model reproduces those events. As ENSO and IOD are not independent, a partial correlation technique could be used to distinguish the impact of one phenomenon on the other. And also the modulation of the MJO by ENSO could be studied in future too. To define model's good performance due to the intrinsic qualities of model itself or the lateral forcing, it would be interesting to run the tropical band of the model (Coppola et al. 2012) to see how the model effectively maintain the MJO signal when only forced at the northern and southern boundaries of the domain. CM SAF could also be useful to validate simulation results of RegCM4 for a different time period

over large domain.

It is still need to find high resolution products from satellite and ground stations to validate SSR of WRF model at local scale. Cloud cover of MODIS gives a satisfied pattern which is associated to SSR in WRF even at a different time period. It could be interesting to perform a different time period simulation using WRF corresponding to the time period of MODIS.

References

Abiodun BJ, Pal JS, Afiesimama EA, Gutowski WJ, Adedoyin A (2008) Simulation of West African monsoon using RegCM3. II. Impacts of deforestation and desertification. Theor Appl Climatol 93: 245-261.

Adler RF, Huffman GJ, Chang A, Ferraro R and others (2003) The version-2 Global Precipitation Climatology Project (GPCP) monthly precipitation analysis (1979-Present). J Hydrometeor 4: 1147-1167.

Allan RJ (2000) ENSO and climatic variability in the past 150 years. In: Diaz HF, Markgraf V (eds) El Niño and the Southern Oscillation-multiscale variability and global and regional impacts. Cambridge, New York, p 3-55.

Anthes RA, Hsie EY, Kuo YH (1987) Description of the Penn State/NCAR Mesoscale Model Version 4 (MM4). NCAR Tech Note NCAR/TN-282+STR, NCAR, Boulder, CO.

Anthes RA, Kuo YH, Hsie EY and others (1989) Estimation of skill and uncertainty in regional numerical models. Quart J Roy Meteorol Soc 115: 763-806.

Anyah RO, Semazzi FHM (2007) Variability of East African rainfall based on multi-year RegCM3 model simulations. Int J Climatol 27: 357-371.

Artale V, Calmanti S, Carillo A, Dell'Aquila A and others (2010) An atmosphere-ocean regional climate model for the Mediterranean area: assessment of a present climate simulation. Clim Dyn 35: 721-740.

Avery WH, Wu C (1994) Renewable energy from the ocean: a guide to OTEC. New York: Oxford Universigy Press.

Badosa J, Haeffelin M, Chepfer H (2013) Scales of spatial and temporal variation of solar irradiance on Reunion tropical island. Solar Energy 88: 42-56.

Badosa J, Haeffelin M, Kalecinski N, Bonnardot F and others (2015) Reliability of day-ahead solar irradiance forecasts on Reunion Island depending on synoptic wind and humidity conditions. Solar Energy 115: 306-321.

Baldacci A, Burgassi PD, Dickson MH, Fanelli M (1998) Non-electric utilization of geothermal energy in Italy. World Renewable Energy Congress V, Part I, Pergamon, Florence, Italy, 2795p.

Baldy S, Ancellet G, Bessafi M and others (1996) Field observations of the vertical distribution of tropospheric ozone at the island of Reunion (southern tropics). J

Geophys Res 101: 23835-23849.

Barbier E (1997) Nature and technology of geothermal energy. Renew Sustain Energy Rev 1(1/2): 1-69.

Barbier E (2002) Geothermal energy technology and current status: an overview. Renew Sustain Energy Rev 6: 3-65.

Barker HW, Stephens HW and others (2003) Assessing 1D atmospheric solar radiative transfer models: interpretation and handling of unresolved clouds. J Clim 16: 2676-2699.

Bechini L, Ducco G, Donatelli M, Stein A (2000) Modelling, interpolation and stochastic simulation in space and time of global solar radiation. Agric Ecosyst Environ 81: 29-42.

Bessafi M, Morel M and others (2013) A method for mapping monthly solar irradiation over complex areas of topography: Reunion Island's case study. In: Fiho WL, Mannke F, Mohee R et al (eds) Climate-Smart Technologies: Integrating Renewable Energy and Energy Efficiency in Mitigation and Adaptation Responses. Springer Science & Business, p 295-305.

Bishop JKB, Rossow WB (1991) Spatial and temporal variability of global surface solar irradiance. J Geophys Res 96: 16839-16858.

Boes EC (1981) Fundamentals of solar radiation. In Kreider JF and Kreith F, editors, Solar Energy Handbook, chapter 2. McGraw-Hill, New York.

Bojanowski JS (2014) Quantifying solar radiation at the earth surface with meteorological and satellite data. Ph.D. Thesis.University of Twente: Netherlands.

Boyle G (1996) Renewable energy: power for a sustainable future. Oxford: Oxford University Press.

Bretherton CS, McCaa JR, Grenier H (2004) A new parameterization for shallow cumulus convection and its application to marine subtropical cloud-topped boundary layers. I. Description and 1D results. Mon Weather Rev 132: 864-882.

Briegleb BP (1992) Delta-Eddington approximation for solar radiation in the NCAR Community Climate Model. J Geophys Res 97: 7603-7612.

Brisson A, Borgne PL, Marsouin A (1999) Development of algorithms for surface solar irradiance retrieval at O&SI SAF low and mid latitudes. Météo-France/SCEM/CMS

O&SI SAF Low and Mid Latitudes.

Cheng X, Wallace JM (1993) Regime analysis of the Northern Hemisphere wintertime 500-hPa height field: spatial patterns. J Atmos Sci 50: 2674-2696.

Chiacchio M, Vitolo R (2012) Effect of cloud cover and atmospheric circulation patterns on the observed surface solar radiation in Europe. J Geophys Res 117: D18.

Christensen JH, Christensen OB (2007) A summary of the PRUDENCE model projections of changes in European climate by the end of this century. Climatic Change 81: 7-30.

Christian AG, Stephen MW (2011) Assessment of spatial and temporal variability in the US solar resource from radiometric measurements and predictions from models using ground-based or satellite data. Solar Energy 85: 1068-1084.

Clough SA, Kneizys FX, Rothman LS, Gallery WO (1981) Atmospheric spectral transmittance and radiance: FASCODE1B. Proc Soc Photo Opt Instrum Eng 277: 152-166.

Clough SA, Shephard MW, Mlawer EJ and others (2005) Atmospheric radiative transfer modeling: a summary of the AER code. J Quant Spectrosc Radiat Transf 91(2): 233-244.

Cook KH (2000) The South Indian convergence zone and interannual rainfall variability over Southern Africa. J Clim 13: 3789-3804.

Coppola E, Giorgi F, Mariotti L, Bi X (2012) RegT-Band: a tropical band version of RegCM4. Clim Res 52: 115-133.

Crétat J, Macron C, Pohl B, Richard Y (2011) Quantifying internal variability in a regional climate model : a case study for Southern Africa. Clim Dyn 37: 1335-1356.

Crétat J, Pohl B, Smith CC, Vigaud N, Richard Y (2014) An original way to evaluate daily rainfall variability simulated by a regional climate model: the case of South African austral summer rainfall. Int J Climatol 35: 2485-2502.

Crétat J, Richard Y, Pohl B, Rouault M and others (2012) Recurrent daily rainfall patterns over South Africa and associated dynamics during the core of the austral summer. Int J Climatol 32: 261-273.

Crimp SJ, Lutjeharms JRE, Mason SJ (1998) Sensitivity of a tropical-temperate trough to sea-surface temperature anomalies in the Agulhas retroflection region. Water SA 24:

93-101.

Davy RJ, Troccoli A (2012) Interannual variability of solar energy generation in Australia. Solar Energy 86: 3554-3560.

Dee DP, Uppala SM, Simmons AJ and others (2011) The ERA-Interim reanalysis: configuration and performance of the data assimilation system. Q J R Meteorol Soc 137: 553-597.

Dehne K, Wild M (1998) Baseline Surface Radiation Network (BSRN/WCRP): new precision radiometry for climate research. Bulletin of the American Meteorological Society 79: 2115-2136.

Diagne M, David M, Boland J, Schmutz N, Lauret P (2014) Postprocessing of solar irradiance forecasts from WRF model at Reunion Island. Sol Energy 105: 99-108.

Dickinson RE, Errico RM, Giorgi F, Bates GT (1989) A regional climate model for the Western United States. Clim Change 15: 383-422.

Dickinson RE, Henderson-Sellers A, Kennedy P (1993) Biosphere-atmosphere transfer scheme (BATS) version 1e as coupled to the NCAR community climate model. Tech Rep, National Center for Atmospheric Research Tech Note NCAR. TN-387+STR, NCAR, Boulder, CO.

Dincer I (2000) Renewable and sustainable development: a crucial review. Renew Sustain Energy Rev 4: 157-175.

Dudhia J (1989) Numerical study of convection observed during the winter monsoon experiment using a mesoscale two-dimensional model. J Atmos Sci 46: 3077-3107.

Dudhia J, Hong SY, Lim KS (2008) A new method for representing mixed-phase particle fall speeds in bulk microphysics parameterizations. J Met Soc Japan 86A: 33-44.

Emanuel KA (1991) A Scheme for Representing Cumulus Convection in Large-Scale Models. J Atmos Sci 48: 2313-2329.

Emanuel KA, Zivkovic-Rothman M (1999) Development and evaluation of a convection scheme for use in climate models. J Atmos Sci 56: 1766-1782.

Ertekin C, Evrendilek F (2007) Spatio-temporal modeling of global solar radiation dynamics as a function of sunshine duration for Turkey. Agric Forest Meteorol 145: 36-47.

Fairall CW, Bradley EF, Godfrey JS, Wick GA, Edson JB, Young GS (1996) Cool-skin and warm-layer effects on sea surface temperature. J Geophys Res 101: 1295-1308.

Fauchereau N, Pohl B, Reason CJC and others (2009) Recurrent daily OLR patterns in the Southern Africa/Southwest Indian Ocean region, implications for South African rainfall and teleconnections. Clim Dyn 32: 575-591.

Field CB, Campbell JE, Lobell DB (2008) Biomass energy: the scale of the potential resource. Trends Ecol Energy 23: 65-72.

Flato GM (2011) Earth system models: an overview, WIREs Clim Change 2: 783-800.

Fritsch JM, Chappell CF (1980) Numerical prediction of convectively driven mesoscale pressure systems, part i: Convective parameterization. J Atmos Sci 37: 1722-1733.

Fu Q, Yang P, Sun WB (1998) An accurate parameterization of the infrared radiative properties of cirrus clouds for climate models. J Clim 9: 2058-2082.

Garci L (2003) Renewable energy applications in desalination: state of the art. Solar Energy 75: 381-393.

Gates WL (1992) AMIP: The atmospheric intercomparison project. Bull. Am Met Soc 73: 1962-1970.

Gilgen H, Wild M, Ohmura A (1998) Means and trends of shortwave irradiance at the surface estimated from global energy balance archive data. J Clim 11(8): 2042-2061.

Giorgi F (2008) Regionalization of climate change information for impact assessment and adaptation. WMO Bulletin 57: 86-92.

Giorgi F, Anyah RO (2012) The road towards RegCM4. Clim Res 52: 3-6.

Giorgi F, Bates GT (1989) The climatological skill of a regional model over complex terrain. Mon Wea Rev 117: 2325-2347.

Giorgi F, Bates GT, Nieman S (1993a) The multi-year surface climatology of a regional atmospheric model over the Western United States. J Clim 6: 75-95.

Giorgi F, Coppola E, Solmon F, Mariotti L and others (2012) RegCM4: model description and preliminary tests over multiple CORDEX domains. Clim Res 52: 7-29.

Giorgi F, Franclsco R, Pal JS (2003) Effects of a sub-grid scale topography and landuse scheme on surface climate and hydrology. I. Effects of temperature and water vapor disaggregation. J Hydrometeorol 4: 317-333.

Giorgi F, Jones C, Asrar G (2009) Addressing climate information needs at the regional level: the CORDEX FRAMEWORK. WMO Bull 58: 175-183.

Giorgi F, Marinucci MR (1996) An investigation of the sensitivity of simulated precipitation to the model resolution and its implications for climate studies. Mon Wea Rev 124: 148-166.

Giorgi F, Marinucci MR, Bates GT (1993b) Development of a second generation regional climate model (RegCM2). Part I: Boundary layer and radiative transfer processes. Mon Wea Rev 121: 2794-2813.

Giorgi F, Marinucci MR, Bates GT, DeCanio G (1993c) Development of a second generation regional climate model (RegCM2). Part II: Convective processes and assimilation of lateral boundary conditions. Mon Wea Rev 121: 2814-2832.

Giorgi F, Mearns LO (1999) Introduction to special section: regional climate modeling revisited. J Geophys Res 104: 6335-6352.

Giorgi F, Shields C (1999) Tests of precipitation parameterizations available in latest version of NCAR regional climate model (RegCM) over continental United States. J Geophys Res 104: 6353-6375.

Giorgi G (1990) Simulation of regional climate using a limited area model nested in a general circulation model. J Clim 3: 941-963.

Gong X, Richman MB (1995) On the application of cluster analysis to growing season precipitation data in North America east of the Rockies. J Clim 8: 897-931.

Grell G (1993) Prognostic evaluation of assumptions used by cumulus parameterizations. Mon Wea Rev 121: 764-787.

Grell G, Dudhia J, Stauffer DR (1994) A description of the fifth generation Penn State/NCAR Mesoscale Model (MM5). NCAR Tech Note NCAR/TN-398+STR, NCAR, Boulder, CO.

Grenier H, Bretherton CS (2001) A moist PBL parameterization for large scale models and its application to subtropical cloud-topped marine boundary layers. Mon Wea Rev 129: 357-377.

Gueymard CA, Myers DR (2008b) Solar radiation measurement: progress in radiometry for improved modeling. V. Badescu (Ed.), Modeling Solar Radiation at the Earth's Surface, Springer.

Harangozo S, Harrison MSJ (1983) On the use of synoptic data indicating the presence of cloud bands over southern Africa. S Afr J Sci 79: 413-414.

Harrison MSJ (1984) A generalized classification of South African rain-bearing synoptic system. J Climatol 4: 547-560.

Harrison MSJ (1986) A synoptic climatology Of South African rainfall variations. Ph.D. dissertation, University of Witwatersrand, 341pp.

Hart NCG, Reason CJC (2012) Cloud bands over southern Africa: seasonality, contribution to rainfall variability and modulation by the MJO. Climate Dyn 41: 1199-1212.

Hart NCG, Reason CJC, Fauchereau N (2010) Tropical extratropical interactions over southern Africa: three cases of heavy summer season rainfall. Mon Wea Rev 138: 2608-2623.

Heavens NG, Ward DS, Natalie MM (2013) Studying and projecting climate change with Earth System Models. Nature Education Knowledge 4(5): 4.

Holtslag AAM, de Bruijn EIF, Pan HL (1990) A high resolution air mass transformation model for short-range weather forecasting. Mon Weather Rev 118: 1561-1575.

Hong SY (2007) Stable Boundary Layer Mixing in a Vertical Diffusion Scheme. The Korea Meteor Soc, Fall conference, Seoul, Korea, Oct. 25-26.

Hong SY, Dudhia J, Chen SH (2004) A revised approach to ice microphysical processes for the bulk parameterization of clouds and precipitation. Mon Wea Rev 132: 103-120.

Hong SY, Lim JOJ (2006) The WRF Single-Moment 6-Class Microphysics Scheme (WSM6). J Korean Meteor Soc 42(2): 129-151.

Hong SY, Noh Y, Dudhia J (2006) A new vertical diffusion package with an explicit treatment of entrainment processes. Mon Wea Rev 134: 2318-2341.

Hong SY, Pan HL (1996) Nonlocal boundary layer vertical diffusion in a

medium-range forecast model. Mon Wea Rev 124: 2322-2339.

Hostetler SW, Bates GT, Giorgi F (1993) Interactive nesting of a lake thermal model within a regional climate model for climate change studies. J Geophys Res 98: 5045-5057.

Hu YX, Stamnes K (1993) An accurate parameterization of the radiative properties of water clouds suitable for use in climate models. J Clim 6: 728–742.

Hunt LA, Kuchar L, Swanton CJ (1998) Estimation of solar radiation for use in crop modeling. Agric. Forest Meteorol 91: 293-300.

Hussain M, Rahman L, Rahman MM (1999) Techniques to obtain improved predictions of global radiation from sunshine duration. Renewable Energy 18: 263-275.

Janowiak J (1988) An investigation of interannual rainfall variability in Africa. J Climate 1: 240-255.

Jia B, Xie Z, Dai A, Shi C, Chen F (2013) Evaluation of satellite and reanalysis products of downward surface solar radiation over East Asia: spatial and seasonal variations. J Geophys Res Atmos 118. http://dx.doi.org/10.1002/jgrd.50353.

Jones RG, Murphy JM, Noguer M (1995) Simulation of climate change over Europe using a nested regional-climate model. I: assessment of control climate, including sensitivity to location of lateral boundaries. Quart J Roy Meteor 121: 1413-1449.

Kagatuke MM, Landman WA, Beraki A, Mbedzi MP (2008) The internal variability of the RegCM3 over South Africa. Int J Climatol 28: 505-520.

Kain JS (2004) The Kain-Fritsch convective parameterization: An update. J Appl Meteor 43: 170-181.

Kain JS, Fritsch JM (1990) A one-dimensional entraining/ detraining plume model and its application in convective parameterization. J Atmos Sci 47: 2784-2802.

Kain JS, Fritsch JM (1993) Convective parameterization for mesoscale models: The Kain-Fritcsh scheme, The representation of cumulus convection in numerical models. Emanuel KA and Raymond DJ, Eds, Amer Meteor Soc, 246 pp.

Karakoti I, Das PK, Singh SK (2012) Predicting monthly mean daily diffuse radiation for India. Applied Energy 91: 412-425.

Kato S, Leob NG, Rose FG, Doelling DR and others (2013) Surface irradiances consistent with CERES-Derived top-of-atmosphere shortwave and longwave

irradiances. J Climate 26: 2719-2740.

Kaunda CS, Kimambo CZ, Nielsen TK (2012) Hydropower in the context of sustainable energy supply: a review of technologies and challenges. Int Sch Res Netw Renew Energy. Article ID: 730631.

Kemp D (2011) Climate Models and Uncertainty - Model Types, General circulation models, Evaluation and Reliability, Models of intermediate complexity, energy balance models.

Kennedy A, Dong X, Xi B and others (2011) A comparison of MERRA and NARR reanalyses with the DOE ARM SGP data. J Clim 24: 4541-4557.

Kiehl JT, Hack JJ, Bonan GB, Boville BA and others (1996) Description of the NCAR community climate model (CCM3). NCAR/TN-4201STR, 152, MCAR, Boulder, CO.

Kiladis GN, Dias J, Straub KH and others (2014) A comparison of OLR and circulation based indices for tracking the MJO. Mon Wea Rev 142: 1697-1715.

Kim D, K Sperber, W Stern, D Waliser and others(2009) Application of MJO simulation diagnostics to climate models. J Clim 22: 6413-6436.

Kothe S, Ahrens B (2010) On the Radiation Budget in Regional Climate Simulations for West Africa. J Geophys Res 115: D23120.

Kothe S, Dobler A, Beck A, Ahrens B (2011) The radiation budget in a regional climate model. Clim Dyn 36: 1023-1036.

Lacis AA, Hansen JE (1974) A parameterization for the absorption of solar radiation in the earth's atmosphere. J Atmos Sci 35: 118-133.

Laprise R, Kornic D, Rapaić M and others (2012) Considerations of domain size and large-scale driving for nested regional climate models: impact on internal variability and ability at developing small-scale details. Climate Change, Part 4, 181-199, doi: 10.1007/978-3-7091-0973-1_14.

Lara-Fanego V, Ruiz-Arias JA, Pozo-Vázquez D, and others (2012) Evaluation of the WRF model solar irradiance forecasts in Andalusia (southern Spain). Solar Energy 86: 2200-2217.

Laszlo I, Ciren P, Liu H and others (2008) Remote sensing of aerosol and radiation from geostationary satellites. Adv. Space Res 41: 1882-1893.

Latif M, Dogmmenget D, Dima M, Grotzner A (1999) The role of Indian Ocean Sea Surface Temperature in forcing east african rainfall anomalies during December-January 1997/98. J Climate 12: 3497-3504.

Leduc M, Laprise R (2009) Regional climate model sensitivity to domain size. Clim Dyn 32: 833-854.

Leduc M, Laprise R, Moretti-Poisson M, Morin JP (2011) Sensitivity to domain size of mid-latitude summer simulations with a regional climate model. Clim Dyn 37: 343-356.

Li H, Ma WB, Wang XL, Lian YW (2011) Estimating monthly average daily diffuse solar radiation with multiple predictors: a case study. Renewable Energy 36: 1944-1948.

Liebmann B, Smith CA (1996) Description of a complete (interpolated) outgoing longwave radiation dataset. Bull Am Meteorol Soc 77: 1275-1277.

Lin JL, GN Kiladis, BE Mapes, KM Weickmann and others (2006) Tropical intraseasonal variability in 14 IPCC AR4 climate models. Part I: Convective signals. J Climate 19: 2665-2690

Lin YL, Farley RD, Orville HD (1983) Bulk parameterization of the snow field in a cloud model. J Climate Appl Meteor 22: 1065-1092.

Lohmann S, Schillings C, Mayer B, Meyer R (2006) Long-term variability of solar direct and global radiation derived from ISCCP data and comparison with reanalysis data. Solar Energy 80: 1390-1401.

Luo JJ, Zhang R, Behera SK and others (2010) Interaction between El Niño and extreme Indian Ocean dipole. J Climate 23: 726-742.

Ma LM, Tan ZM (2009) Improving the behavior of the cumulus parameterization for tropical cyclone prediction: convection trigger. Atmos Res 92: 190-211.

Macron C, Pohl B, Richard Y, Bessafi M (2014) How do tropical-temperate troughs form and develop over southern Africa. Journal of Climate 27: 1633-1647.

Madden R, Julian P (1971) Detection of a 40-50 day oscillation in the zonal wind in the tropical Pacific. J Atmos Sci 28: 702-708.

Madden R, Julian P (1972) Description of global-scale circulation cells in the tropics

with a 40-50 day period. J Atmos Sci 29: 1109-1123.

Makarau A, Jury MR (1997) Predictability of Zimbabwe summer rainfall. Int J Climatol 17: 1421-1432.

Marchant R, Mumbi C, Behera S, Yamagata T (2007) The Indian Ocean dipole- The unsung driver of climatic variability in East Africa. African Journal of Ecology 45: 4-16.

Mariotti L, Coppola E, Sylla MB, Giorgi F, Piani C (2011) Regional climate model simulation of projected 21st century climate change over an all-Africa domain: Comparison analysis of nested and driving model results. J Geophys Res: 116, D15111.

Markovic M, Jones CG, Vaillancourt PA, Paquin D, Winger K, Paquin-Ricard D (2008) An evaluation of the surface radiation budget over North America for a suite of regional climate models against surface station observations. Clim Dyn 31: 779-794.

Martínez-Castro D, Porfirio da Rocha R, Bezanilla-Morlot A, Alvarez-Escudero L and others (2006) Theor Appl Climatol 86: 5-22.

Mearns LO (2012) The North American Regional Climate Change Assessment 730 Program: Overview of Phase I Results. Bull Amer Meteor Soc 93: 1337-1362.

Michelangeli P, Vautard R, Legras B (1995) Weather regime occurrence and quasi-stationarity. J Atmos Sci 52: 1237-1256.

Misra V (2003) The influence of Pacific SST variability on the precipitation over Southern Africa. J Climate 16: 2408-2418.

Mlawer EJ, Clough SA (1998) Shortwave clear-sky model measurement intercomparison using RRTM. Proc. 8th ARM Science Team Meeting, Tucson, Arizona, USA. Dept. of Energy: 513-516.

Mlawer EJ, Taubman SJ, Brown PD and others (1997) Radiative transfer for inhomogeneous atmospheres: RRTM, a validated correlated-k model for the longwave. J Geophys Res: Atmospheres 102: 16663-16682.

Mlawer EJ, Tobin D, Clough SA (2003) A new water vapor continuum model: MT_CKDD_1.0. Proc. 13th ARM Science Team Meeting, Broomfield, CO, U.S. Dept. of Energy.

Monforti F, Huld T, Bódis K, and others (2014) Assessing complementarity of wind and solar resources for energy production in Italy: a Monte Carlo approach. Renewable Energy 63: 576-586.

Morel B, Pohl B, Richard Y and others (2014) Regionalizing rainfall at very high resolution over La Réunion Island using a regional climate model. Mon Wea Rev 142: 2665-2686.

Moron V, Plaut G (2003) The impact of El Niño-Southern Oscillation upon weather regimes over Europe and the North Atlantic during Boreal winter. Int J Climatol 23: 363-379.

Muñoz-Díaz D, Rodrigo FS (2004) Spatio-temporal patterns of seasonal rainfall in Spain (1912–2000) using cluster and principal component analysis: comparison. Ann Geophys 22: 1435-1448.

Muñoz-Díaz D, Rodrigo FS (2006) Seasonal rainfall variations in Spain (1912–2000) and their links to atmospheric circulation. Atmos Res 81(1): 94-110.

Murphy JM (1999) An evaluation of statistical and dynamical techniques for downscaling local climate. J Clim 12: 2256-2284.

Nicholson S (2003) Comments on "The South Indian Convergence Zone and interannual rainfall variability over southern Africa" and the questions of ENSO's influence on southern Africa. J Climate 16: 555-562.

Nikulin G, Jones C, Giorgi F, Asrar G and others (2012) Precipitation climatology in an ensemble of CORDEX-Africa regional climate simulations. J Climate 25: 6057-6078.

Noh Y, Cheon WG, Hong SY, Raasch S (2003) Improvement of the K-profile model for the planetary boundary layer based on large eddy simulation data. Bound Layer Meteor 107: 401-427.

North GR, Cahalan RF, Coakley JA (1981) Energy balance climate models. Rev Geophys Space Phys 19: 91-121.

Oehler JF, Lénat JF, Labazuy P (2008) Growth and collapse of the Reunion Island volcanoes. Bull Volcanol 70: 717-742.

Ohmura A, Dutton EG, Forgan B and others (1998) Baseline surface radiation network (bsrn/wcrp): new precision radiometry for climate research. Bull Am Meteorol Soc 79(10): 2115-2136.

Ohmura A, Gilgen H, Wild M (1989) Global energy balance archive GEBA, worl climate program-water project a7. Zuercher Geografische Schriften 34. Zuerich.

Omer AM (2008) Energy, environment and sustainable development. Renew Sustain Energy Rev 12: 2265-2300.

Orlanski I (1981) The quasi-hydrostatic approximation. J Atmos Sci 38(3): 572-582.

Otieno VO, Anyah RO (2012) Effects of land use changes on climate in the Greater Horn of Africa. Clim Res 52: 77-95.

Pal JS, Giorgi F, Bi XQ and others (2007) Regional climate modeling for the developing world: the ICTP RegCM3 and RegCNET. Bull Am Meteorol Soc 88: 1395-1409.

Pal JS, Small E, Eltahir E (2000) Simulation of regional-scale water and energy budgets: representation of subgrid cloud and precipitation processes within RegCM. J Geophys Res 105: 29579-29594.

Pelc R, Fujita RM (2002) Renewable energy from the ocean. Marine Policy 26: 471-479.

Perdigão J, Salgado R, Dasari H, Costa MJ (2011) Inter annual variability of surface solar radiation over Iberian Peninsula. Proceedings of the Global Conference on Global Warming, 11-14 July, Lisbon, Portugal.

Perez R, Hoff T (2013) Solar resource variability, in: Solar Resource Assessment and Forecasting (Editor Jan Kleissl), Elsevier.

Perez R, Lorenz E, Pelland S, and others (2013) Comparison of numerical weather prediction solar irradiance forecasts in the US, Canada and Europe. Solar Energy 94: 305-326.

Philippon N, Rouault M, Richard Y, Favre A (2012) The influence of ENSO on winter rainfall in South Africa. Int J Climatol 32: 2333-2347.

Pierce DW, Barnett TP, Santer BD, Gleckler PJ (2009) Selecting global climate models for regional climate change studies. Proceedings of the National Academy of Sciences 106(21): 8441-8446.

Pincus R, Barker HW, Morcrette JJ (2003) A fast, flexible, approximate technique for computing radiative transfer through global arrays of 2D clouds. J Geophys Res 108(D): 4376, doi:10.1029/2002JD003322.

Pohl B, Fauchereau N, Richard Y and others (2009) Interactions between synoptic, intraseasonal, and interannual convective variability over southern Africa. J Climate 33: 1033-1050.

Pohl B, Rouault M, Roy SS (2014) Simulation of the annual and diurnal cycles of rainfall over South Africa by a Regional Climate Model. Climate Dynamics 43: 2207-2226.

Posselt R, Mueller R, Trentmann J and others (2012a) Extension of the CM SAF surface radiation climatology beyond Meteosat first generation satellites. In: 12th EMS Annual Meeting & 9th European Conference on Applied Climatology (ECAC), Poland.

Posselt R, Müller R, Stöckli R, Trentmann J (2011) Spatial and temporal homogeneity of solar surface irradiance across satellite generations. Remote Sensing 3(5): 1029-1046.

Praene JP, David M, Sinama F, and others (2012) Renewable energy: progressing towards a net zero energy island, the case of Reunion Island. Renewable and Sustainable Energy Reviews 16: 426-442.

Qian Y, Giorgi F (1999) Interactive coupling of regional climate and sulfate aerosol models over eastern Asia. J Geophys Res 104: 6477-6499.

Ramos MC (2001) Divisive and hierarchical clustering techniques to analyse variability of rainfall distribution patterns in a Mediterranean region. Atmos Res 57: 123-138.

Randall DA, Wood RA, Bony S and others (2007) Climate models and their evaluation. Cambridge University Press, Cambridge, United Kingdom.

Rao SA, Behera SK, Masumoto Y, Yamagata T (2002) Interannual subsurface variability in the tropical Indian Ocean with a special emphasis on the Indian Ocean dipole. Deep Sea Res, Part II 49: 1549-1572.

Rapaić M, Leduc M, Laprise R (2010) Evaluation of the internal variability and estimation of the downscaling ability of the Canadian regional climate model for different domain sizes over the north Atlantic region using the Big-Brother experimental approach. Clim Dyn 36: 1979-2001.

Ratna SB, Behera S, Ratnam JV and others (2012) An index for tropical temperate troughs over southern Africa. Climate Dyn 41: 421-441.

Ratnam JV, Giorgi F, Kaginalkar A, Cozaini S (2009) Simulation of the Indian monsoon using the RegCM3-ROMS regional coupled model. Clim Dyn 33: 119-139.

Rauscher SA, Seth A, Qian JH, Camargo SJ (2006) Domain choice in an experimental nested modeling prediction system for South America. Theor Appl Climatol 86: 229-246.

Reason CJC (2001) Subtropical Indian Ocean SST dipole events and southern African rainfall. Geophysical Research Letters 28: 2225-2227.

Reynolds R, Rayner N, Smith TM, Stokes D, Wang W (2002) An improved in situ and satellite SST analysis for climate. J Clim 15: 1609-1625.

Rocha A, Simmonds I (1997a) Interannual variability of southeastern African summer rainfall. Part I: Relationships with air-sea interaction processes. Int J Climatol 17: 235-265.

Ropelewski CF, Halpert MS (1989) Precipitation patterns associated with the high index phase of the Southern Oscillation. J Climate 2: 268-284.

Rui H, Wang B (1990) Development characteristics and dynamic structure of tropical intraseasonal convection anomalies. J Atmos Sci 47: 357-379.

Ruiz-Arias JA, Dudhia J, Santos-Alamillos FJ, Pozo-Vázquez D (2013a) Surface clear-sky shortwave radiative closure intercomparisons in the weather research and forecasting model. J Geophys Res Atmos 118 (17): 9901-9913.

Ruiz-Arias JA, Pozo-Vázquez D, Lara-Fanego V, Santos-Alamillos FJ, Tovar-Pescador J (2011b) A high-resolution topographic correction method for clear-sky solar irradiance derived with a numerical weather prediction model. J Appl Meteorol Clim 50(12): 2460-2472.

Ruiz-Arias JA, Quesada-Ruiz S, Fernández EF, Gueymard CA (2015) Optimal combination of gridded and ground-observed solar radiation data for regional solar resource assessment. Solar Energy 112: 411-424.

Rummukainen M (2010) State-of-the-art with regional climate models. WIREs Climate Change 1: 82-96.

Saji NH, Goswami BN, Vinayachandran PN, Yamagata T (1999) A dipole mode in the tropical Indian Ocean. Nature 401: 360-363.

Schneider E, Lindzen RS (1976) A discussion of the parameterization of momentum exchange by cumulus convection. J Geophys Res 81: 3158-3160.

Simmons A, Dee D, Uppala S, Kobayashi S (2007) Era-interim: new ecmwf reanalysis products from 1989 onwards. In: ECMWF Newsl, 110. ECMWF, p 29-35.

Skamarock WC, Klemp JB (2008) A time-split nonhydrostatic atmospheric model for weather research and forecasting applications. J Comput Phys 227: 3465-3485.

Slade R, Bauen A, Gross R (2014) Global bioenergy resources. Nat Clim Change 4: 99-105.

Small EE, Sloan LC, Hostetler SW, Giorgi F (1999) Simulating the water balance of the Aral Sea with a coupled regional climate-lake model. J Geophys Res 104: 6583-6602.

Soler O (2000) Atlas climatique de la Réunion. Météo France, Direction interrégionale de la Rénion: 79.

Solmon F, Elguindi N, Mallet M (2012) Radiative and climatic effects of dust over West Africa, as simulated by a regional climate model. Clim Res 52: 7-29.

Solmon F, Giorgi F, Liousse C (2006) Aerosol modeling for regional climate studies: application to anthropogenic particles and evaluation over a European/African domain. Tellus Ser B Chem Phys Meterol 58: 51-72.

Solomon S, Qin D, Manning M and others (2007) IPCC fourth assessment report of working group 1: climate change 2007-the physical science basis. Cambridge University Press, Cambridge.

Stenier AL, Pal JS, Rauscher SA, Bell JL and others (2009) Land surface coupling in regional climate simulations of the West Africa monsoon. Clim Dyn 33: 869-892.

Stephens GL (1978) Radiation profiles in extended water clouds. Part II: Parameterization schemes. J Atmos Sci 35: 2123-2132.

Sundqvist H, Berge E, Kristjansson JE (1989) The effects of domain choice on summer precipitation simulation and sensitivity in a regional climate model. J Climate 11: 2698-2712.

Sylla MB, Coppola E, Mariotti L, Giorgi F and others (2010) Multiyear simulation of the African climate using a regional climate model (RegCM3) with the high resolution ERA-interim reanalysis. Clim Dyn 35: 231-247.

Sylla MB, Giorgi F, Stordal F (2012) Large-scale origins of rainfall and temperature bias in high resolution simulations over southern Africa. Clim Res 52: 193-211.

Taylor KE (2001) Summarizing multiple aspects of model performance in a single diagram. J Geophys Res 106: 7183-7192.

Tennant WJ, Hewitson BC (2002) Intra-seasonal rainfall characteristics and their importance to the seasonal prediction problem. Int J Climatol 22: 1033-1048.

Tiedtke M (1989) A comprehensive mass flux scheme for cumulus parameterization on large scale models. Mon Wea Rev 117: 1779-1800.

Todd M, Washington R (1999) Circulation anomalies associated with tropical-temperate troughs in Southern Africa and the South West Indian Ocean. Clim Dyn 15: 937-951.

Todd M, Washington R, Palmer P (2004) Water vapour transport associated with tropical-temperate trough systems over South Africa and the Southwest Indian Ocean. Int J Climatol 24: 555-568.

Trenberth KE, Caron JM (2000) The Southern Oscillation revisited: sea level pressures, surface temperatures, and precipitation. J Clim 13: 4358-4365.

Tyson PD, Preston-White RA (2000) The weather and climate of southern Africa. Oxford University Press, 396pp.

Ulgen K, Hepbasli A (2009) Diffuse solar radiation estimation models for Turkey's big cities. Energy Conversion and Management 50: 149-156.

Ventrice MJ, Wheeler MC, Hendon HH, and others (2013) A modified multivariate Madden-Julian Oscillation index using velocity potential. Mon Wea Rev 141: 4197-4120.

Vigaud N, Pohl B, Crétat J (2012) Tropical-temperate interactions over southern Africa simulated by a regional climate model. Clim Dyn 39: 2895-2916.

Vinayachandran PN, Francis PA, Rao SA (2009) Indian Ocean dipole: processes and impacts. In: Current trends in science, platinum jubilee special volume of the Indian Academy of Sciences, Indian Academy of Science, Bangalore, India, pp569-589.

Wang YQ, Leung LR, and others (2004) Regional Climate Modeling: progress, challenges, and prospects. Journal of the Meteorological Society of Japan 82: 1599-1628.

Washington R, Todd M (1999) Tropical–temperate links in Southern Africa and

Southwest Indian Ocean satellite-derived daily rainfall. Int J Climatol 19: 1601-1616.

Wheeler MC, Hendon HH (2004) An all-season real-time multivariate MJO index: development of an index for monitoring and prediction. Mon Wea Rev 132: 1917-1932.

Wild M, Folini D, Schär C and others (2013) The global energy balance from a surface perspective. Clim Dyn 40: 3107-3134.

Wild M, Truessel B, Ohmura A and others (2009) Global dimming and brightening: an update beyond 2000. J Geophys Res Atoms 114: D00d13.

Wolter K, Timlin MS (1993) Monitoring ENSO in COADS with a seasonally adjusted principal component index. Proc. of the 17th Climate Diagnostics Workshop, Norman, OK, NOAA/N MC/CAC, NSSL, Oklahoma Clim. Survey, CIMMS and the School of Meteor., Univ. of Oklahoma, 52-57.

Wolter K, Timlin MS (1998) Measuring the strength of ENSO – how does 1997/98 rank? Weather 53: 315-324.

Wyser K, Jones C, Du P, and others (2008) An evaluation of Arctic cloud and radiation processes during the SHEBA year: simulation results from eight Arctic regional climate models. Clim Dyn 30(2–3): 203-223.

Yohanna JK, Itodo IN, Umogbi VI (2011) A model for determining the global solar radiation for Makurdi, Nigeria. Renewable Energy 36: 1989-1992.

Zakey AS, Giorgi F, Bi X (2008) Modeling of sea salt in a regional climate model: fluxes and radiative forcing. J Geophys Res 113: D14221, doi: 10.1029/2007JD009209.

Zakey AS, Solmon F, Giorgi F (2006) Implementation and testing of a desert dust module in a regional climate model. Atmos Chem Phys 6: 4687-4704.

Zamora RJ, Dutton EG, Trainer M, McKeen SA, Wilczak JM, Hou YT (2005) The accuracy of solar irradiance calculations used in mesoscale numerical weather prediction. Mon Weather Rev 133: 783-792.

Zeng X, Beljaars A (2005) A prognostic scheme of sea surface skin temperature for modeling and data assimilation. Geophys Res Lett 32: L14605, doi: 10.1029/2005 GL023030.

Zeng X, Zhao M, Dickinson RE (1998) Intercomparison of bulk aerodynamic algorithms for the computation of sea surface fluxes using TOGA COARE and TAO data. J Clim 11: 2628-2644.

Zhang C (2005) Madden-Julian Oscillation. Reviews of Geophysics 43: 1-36.

Zhang C, Dong M, Gualdi S, Hendon HH, Maloney and others (2006) Simulations of the Madden-Julian oscillation by four pairs of coupled and uncoupled global models. Clim Dyn DOI: 10.1007/s00382-006-0148-2.

Appendix A --- List of Acronyms

AGCM	Atmospheric General Circulation Models
AHC	Agglomerative Hierarchical Clustering
AHC	Ascending Hierarchical Clustering
ARW	Advanced Research WRF
BEST	Bivariate ENSO Timeseries
BSRN	Baseline Surface Radiation Network
BSRN	Baseline Surface Radiation Network
CCM	Community Climate Model
CERES	Clouds and Earth's Radiant Energy System
CLM	Community Land Model
CM SAF	Satellite Application Facility on Climate Monitoring
CMIP	Climate Model Intercomparison Project
CO2	Carbon Dioxide
CORDEX	Coordinated Regional Downscaling Experiment
COV	Coefficient Of Variation
CV	Coefficient of Variation
DEM	Digital Elevation Model
DMI	Dipole Mode Index
DNI	Direct Normal Irradiance
EBAF	Energy Balanced and Filled
ECMWF	The European Centre for Medium-Range Weather Forecasts
ENSO	El Niño Southern Oscillation
EOFs	Empirical Orthogonal Functions
ESM	Earth System Model
ESP	Earth System Physics
GCM	Global Climate Models
GEBA	Global Energy Balance Archive
GERRI	Green Energy Revolution-Reunion Island
GHG	Greenhouse Gases
GHI	Global Horizontal Irradiance
GPCP	Global Precipitation Climatology Project
GTI	Global Tilt Irradiance
ICTP	International Centre for Theoretical Physics
IOD	Indian Ocean Dipole
ISCCP	International Satellite Cloud Climatology Project
IV	Internal Variability
LBLRTM	Line-By-Line Radiative Transfer Model
LSM	Land Surface Model
LW	Long-wave
LWN	Longwave Net
MBE	Mean Bias Error
McICA	Monte-Carlo Independant Column Approximation
MEI	Multivariate ENSO Index

MJO	Madden–Julian oscillation
MRF	Medium Range Forecast
NARCCAP	North American Regional Climate Change Assessment Program
NCAR	National Center for Atmospheric Research
NCEP	National Centers for Environmental Prediction
NDJF	November December January February
NDJFMA	November December January February March April
NOAA	National Oceanic and Atmospheric Administration
NSRDB	National Solar Radiation Database
NWP	Numerical Weather Prediction
OLR	Outgoing Longwave Radiation
PBL	Planetary Boundary Layer
PC	Principal Component
PFT	Plant Functional Type
PRERURE	Plan Régional des Énergies Renouvelables et de l'Utilisation Rationnelle de l' Énergie
Q2	Specific Humidity at 2 meter
RCM	Regional Climate Models
RegCM2	Regional Climate Model Version 2
RegCM2.5	Regional Climate Model Version 2.5
RegCM3	Regional Climate Model Version 3
RegCM4	Regional Climate Model Version 4
RH	Relative Humidity
RMM	Real-time Multivariate MJO
RMM1	Real-time Multivariate MJO series 1
RMM2	Real-time Multivariate MJO series 2
RMSD	Root Mean Standard Deviation
RRTM	Rapid Radiative Transfer ModelRRTMG
SCF	Squared Covariance Fraction
SD	Standard Deviation
SID	Surface Incoming Direct
SIS	Surface Incoming Solar
SRB	Surface Radiation Budget
SSR	Surface Solar Radiation
SST	Sea Surface Temperature
SUBEX	Subgrid Explicit Moisture Scheme
SVD	Singular Value Decomposition
SW	Short-wave
SWIO	South West Indian Ocean
SWN	Shortwave Net
T	Air Temperature
TKE	Turbulent Kinetic Energy
TOA	Top of Atmosphere

TTT	Tropical Temperate Trough
U	Zonal wind component
UV10	Zonal and Meridional wind component at 10m
V	Meridional wind component
WCRP	World Climate Research Programme
WRF	Weather Research and Forecasting
WSM6	WRF Single-moment Microphysics scheme 6-class
YSU	Yonsei University (Korea)

Appendix B --- Conferences Attended

Sixth ICTP Workshop on the Theory and Use of Regional Climate Models
7 -18 May 2012 Trieste, Italy

Europe Geosciences Union General Assembly
7-12 April 2013 Vienna, Austria

XXVIIe Colloque de l'Association Internationale de Climatologie (AIC)
2-5 July 2014 Dijon, France

Appendix C --- List of Publications

Li P, Morel B, Solmon F, Chiacchio M, Bessafi B. Radiation Budget in the Regional Climate Model RegCM4: Simulation Results from Two Different Radiative Schemes over the South West Indian Ocean (submitted to Journal of Climate Research in review).

Li P, Morel B, Solmon F, Pohl B, Bessafi M (2014) Estimation du rayonnement solaire dans le Sud-Ouest de l'Océan Indien et à la Réunion: modélisation régionale du climat. XXVIIe Colloque de l'Association Internationale de Climatologie, 2-5 July, Dijon, France.

Li Q, Bessafi M, Delage O, Chabriat JP, Li P (2015) Intermittency study of global solar radiation on Reunion Island using Hilbert-Huang Transform. Third Southern African Solar Energy Conference, 11-13 May, Kruger National Park, South Africa.

ESTIMATION DU RAYONNEMENT SOLAIRE DANS LE SUD-OUEST DE L'OCÉAN INDIEN ET À LA RÉUNION : MODÉLISATION RÉGIONALE DU CLIMAT

LI P. [(1)], MOREL B. [(1)], SOLMON F. [(2)], POHL B. [(3)], BESSAFI M. [(1)]

(1) Laboratoire d'Énergétique, d'Électronique et des Procédés, Université de La Réunion, 15 avenue René Cassin CS 92003, 97744 Saint-Denis de La Réunion cedex, France [peng.li@univ-reunion.fr ; Beatrice.Morel@univ-reunion.fr ; Miloud.Bessafi@univ-reunion.fr]

(2) ICTP (UNESCO-IAEA), Strada Costiera 1, 34014 Trieste, Italy [fsolmon@ictp.it]

(3) Centre de Recherches de Climatologie / Biogéosciences, UMR 6282 CNRS / université de Bourgogne, 6 bd Gabriel, 21000 Dijon, France [benjamin.polh@u-bourgogne.fr]

Résumé *– On analyse ici la capacité du modèle climatique régional RegCM4 à simuler les champs radiatifs, la température de surface et les précipitations sur un domaine couvrant l'Afrique australe et le sud-ouest de l'océan Indien (0-40°S ; 0-100°E), centré sur La Réunion. Les données produites par le modèle sont confrontées aux données d'observations CERES pour les paramètres du rayonnement (ondes courtes et longues) et GPCP pour les précipitations, et aux données des réanalyses ERA-Interim pour la température. Six simulations ont été conduites, chacune avec un schéma de convection différent, afin de tester la sensibilité des résultats à la physique du modèle.*

Le schéma mixte de Grell sur les terres et Emanuel sur les océans, donne les résultats les plus satisfaisants du point de la vue de la température, des précipitations et du rayonnement solaire (ondes courtes), malgré des biais humides et froids plus marqués sur l'Afrique de l'Est et Madagascar et des biais importants pour ce qui concerne le rayonnement solaire partout sur le domaine. Une raison possible viendrait du fait que les simulations produites dans ce travail ne prennent pas en compte le forçage par les aérosols. La bonne performance du modèle est toutefois à noter pour une zone à l'est de Madagascar, incluant l'île de La Réunion.

Mots-clés : *rayonnement solaire, température, précipitation, modèle régional de climat, sud-ouest de l'océan Indien, moyennes saisonnières.*

Abstract – Estimating solar radiation over the south-west Indian ocean and Reunion Island: regional climate modelling. *We analyse the capabilities of the regional climate model RegCM4 in simulating the radiative fields, temperature and precipitations over a domain covering Southern Africa and the south-western Indian ocean [0-40°S ; 0-100°E], centered on Reunion. Model outputs are compared to observational data as taken from CERES for the long and short wave radiative parameters and GPCP for the precipitation, and to ERA-Interim reanalyses for the temperature. In order to assess the sensitivity of the results to the physical package of the model, six simulations are conducted, each with a different convective scheme.*

Results from the mixed convection scheme Grell over the lands and Emanuel over the oceans, are the most satisfatory in terms of temperature, precipitation and solar irradiation, in spite of marked wet and cold biases over Eastern Africa and Madagascar and strong biases in solar irradiation throughout the domain. This may be due to the fact that the simulations performed in this work do not take into account forcing by the aerosols. The good performance of the model is however to be noticed for the area eastward of Madagacar, including Reunion Island.

Keywords: *solar irradiation, temperature, precipitation, regional climate model, south-west Indian ocean, seasonal means.*

Introduction

La région sud-ouest de l'océan Indien, par sa localisation subtropicale, dispose en théorie d'un fort potentiel en matière de gisement solaire. À cet égard, l'île de La Réunion par exemple, qui vise l'autonomie énergétique à l'horizon 2030, s'est engagée activement en faveur du développement des systèmes utilisant l'énergie solaire. Pour le dimensionnement et le déploiement de ces systèmes, une connaissance très approfondie du potentiel solaire de l'île est toutefois indispensable.

Le rayonnement solaire reçu au sol présente en effet une forte variabilité spatiale et temporelle en lien avec le climat. La répartition du rayonnement solaire à la surface est conditionnée généralement par la nébulosité et la hauteur du soleil. Les principales causes de nébulosité qui prévalent dans la région sud-ouest de l'océan Indien sont les perturbations tropicales (alizés, zone de convergence intertropicale, cyclones tropicaux, mousson indienne, ondes tropicales, MJO, ENSO). Les effets du relief, si ceux-ci sont très marqués — comme c'est le cas à La Réunion — peuvent également moduler le rayonnement solaire reçu au sol *via* des processus connus tels que les brises de mer et de terre et les effets de pente.

SASEC2015
Third Southern African Solar Energy Conference
11 – 13 May 2015
Kruger National Park, South Africa

INTERMITTENCY STUDY OF GLOBAL SOLAR RADIATION ON REUNION ISLAND USING HILBERT-HUANG TRANSFORM

LI Qi, BESSAFI Miloud, DELAGE Olivier, CHABRIAT Jean-Pierre, LI Peng

Laboratory of Energy, Electronic and Process (LE^2P),
University of Reunion Island,
15 Avenue Rene Cassin,
CS 92003, 97 744 Saint-Denis Cedex 9,
Reunion Island, France

E-mail: richie.qili@gmail.com

ABSTRACT

The characterization of the solar radiation variability is a fundamental step before prediction and is crucial to transform an intermittent source of energy into a stable one. As solar irradiance result from a nonlinear and non-stationary process, we use a multifractal approach based on the Hilbert-Huang Transform (HHT) consisting of an empirical mode decomposition (EMD) followed by a spectral analysis. In this paper, we will briefly introduce the HHT data analysis method. Such a recent adaptive data analysis method has been applied to Reunion Island global solar radiation time series of measurements with a sampling rate of 1/60 Hz over six years. Through the EMD, daily global solar radiation data were decomposed into several intrinsic mode functions (IMF). For each IMF, we estimate the amplitude, instantaneous frequency and Hilbert spectrum for the original data. From the comparison of Hilbert Spectrum and Fourier Spectrum, we find the calculated solar radiation power spectrum follows a power law behavior close to the Kolmogorov law. The method described in this paper provides an amplitude frequency representation of the global solar radiation sequences resulting in a probability density function and a scaling coefficient. The multifractal approach allows to extract parameters connected to the multifractal properties of the global solar radiation.

INTRODUCTION

With the rapid development of the global economy and society, requirements for renewable energy increase remarkably. Solar energy is considered as one of the most promising alternative energy resources. However, the spatial and temporal variability of solar radiation over various time scales is difficult for computing, controlling and balancing. Solar radiation shows the characteristics, nonlinear, nonstationary and intermittency in various process [1].

Intermittency is the irregular alternation of phases of apparently periodic and chaotic dynamics or different forms of chaotic dynamics (crisis-induced intermittency) [2 3]. In the area of solar radiation, Tarroja et al. give the concept of intermittency the same meaning that to the concept of fluctuation, defining the severity of the intermittency as the change in the magnitude of the total irradiation on a surface over a given time interval [4]. Thus, this meaning is agreed with the concept of variability. On the contrary, Davis et al. import the notion of intermittency from turbulence, though they analyze radiation data artificially generated from cloud data [5]. This one is the sense given to the concept of intermittency in the present work, that is, intermittency refers to the changes of the variability of daily solar radiation according to the scale considered. In this sense, intermittency and multifractality are synonym.

Intermittency and multiscaling properties have been found in many fields, such as rainfall [11], finance [9 10], turbulence [6-8 15], and geophysical fields [12 13 28].

Multiscaling intermittency is often characterized using a structure function of order $q > 0$ as the statistical moment of the fluctuations $\Delta X_\tau = |X(t+\tau) - X(t)|$ [6 15]

$$\langle (\Delta X_\tau)^q \rangle \sim C_q \tau^{\zeta(q)} \qquad (1)$$

where C_q is a constant and $\zeta(q)$ is a scale invariant moment function; it is also a cumulant generating function, which is nonlinear and concave and fully characterizes the scale-invariant properties of intermittency.

For this global solar radiation study, we consider the scaling exponent $\zeta(q)$ that characterizes the scaling behavior or measures the distance between a monofractal and multifractal